Institute of Fundamental Technological Research
Polish Academy of Sciences

PhD Thesis

Atomistic Simulation of Crack Propagation in Irradiated Materials

by

Hojjat Mousavisogolitappeh

Supervisor

dr hab. Aneta Ustrzycka

Warsaw 2026

Abstract

Structural materials in nuclear reactors are exposed to extreme conditions where neutron irradiation alters their microstructure and mechanical behavior. The accumulation of radiation-induced defects progressively suppresses ductile deformation mechanisms and promotes the ductile-to-brittle transition (DBT), leading to reduced fracture resistance. Austenitic stainless steels, including 310S, are widely used in such environments due to their high-temperature strength, corrosion resistance, and irradiation stability. This thesis investigates irradiation-induced degradation mechanisms in Fe–Ni–Cr alloy, representative of 310S steel.

Molecular dynamics simulations were used to qualitatively examine the interactions between radiation-induced defects, crack propagation, and plastic deformation mechanisms, and to quantitatively evaluate fracture resistance through energy-based criteria. Fracture resistance was assessed using two complementary methods: a global energy-based approach incorporating the critical energy release rate, as a sum of the energy associated with surface formation and the plastic work, and a local traction–separation analysis providing atomic-scale fracture energies. The influence of crystallographic orientation on the DBT was also examined.

Results show that both radiation-induced defect accumulation and crystallographic orientation significantly affect post-irradiation fracture behavior. Radiation-induced defects alter the dominant orientation-dependent deformation mechanisms, reducing plasticity and thereby driving the transition in the material's response from ductile to brittle.

The novelty of this thesis lies in establishing an atomistic framework that integrates radiation-induced defect evolution, orientation-dependent deformation mechanisms, and crack propagation behavior, supported by energy-based fracture metrics, to elucidate the mechanisms underlying the ductile-to-brittle transition in irradiated austenitic alloys. This framework clarifies the microstructure–fracture relationships governing irradiation-assisted embrittlement, including the ductile-to-brittle transition, and provides a transferable methodology for evaluating these mechanisms and post-irradiation fracture resistance.

Streszczenie

Materiały konstrukcyjne stosowane w reaktorach jądrowych poddawane są ekstremalnym warunkom eksploatacyjnym, w których napromieniowanie neutronowe prowadzi do istotnych zmian mikrostruktury oraz właściwości mechanicznych. Akumulacja defektów radiacyjnych stopniowo ogranicza aktywność mechanizmów odkształcenia plastycznego i sprzyja wystąpieniu przejścia ciągliwo–kruchego (ductile-to-brittle transition, DBT), skutkując obniżeniem odporności na pękanie. Austenityczne stale, w tym 310S, są szeroko stosowane w takich warunkach ze względu na wysoką wytrzymałość w podwyższonych temperaturach, odporność na korozję oraz odporność na promieniowanie. Niniejsza rozprawa dotyczy mechanizmów degradacji wywołanej promieniowaniem w stopie Fe–Ni–Cr, reprezentatywnym dla stali 310S.

Symulacje dynamiki molekularnej zostały wykorzystane do jakościowego zbadania oddziaływań między defektami radiacyjnymi, propagacją pęknięć i mechanizmami odkształceń plastycznych oraz ilościowo ocenić odporność na pękanie w oparciu o kryteria energetyczne. Odporność na pękanie określano dwiema metodami: globalnym podejściem energetycznym, obejmującym krytyczny współczynnik uwalniania energii (sumę energii powierzchniowej i pracy plastycznej), oraz lokalną analizą traction–separation, dostarczającą energii pękania w skali atomowej. Zbadano także wpływ orientacji krystalograficznej na zjawisko DBT.

Wyniki pokazują, że zarówno akumulacja defektów radiacyjnych, jak i orientacja krystalograficzna istotnie wpływają na charakter pękania materiałów napromieniowanych. Defekty radiacyjne zmieniają dominujące mechanizmy deformacji, ograniczając plastyczność i powodując przejście materiału od ciągliwego do kruchego.

Nowatorstwo niniejszej rozprawy polega na opracowaniu atomistycznego modelu łączącego ewolucję defektów radiacyjnych, mechanizmy deformacji zależne od orientacji oraz zachowanie propagującej szczeliny, wspieranego energetycznymi miarami pękania, w celu wyjaśnienia przejścia DBT w napromieniowanych stopach austenitycznych. Opracowane podejście pozwala powiązać mikrostrukturę z procesami pękania odpowiedzialnymi za kruchość wspomaganą napromieniowaniem, w tym przejście ciągliwo–kruche, oraz dostarcza uniwersalnej metody oceny mechanizmów i odporności materiału na pękanie po napromieniowaniu.

Acknowledgements

First and foremost, I would like to express my sincere gratitude to my supervisor, dr. hab. Aneta Ustrzycka, for her invaluable mentorship, guidance, and continuous support throughout the course of this research. I am deeply thankful for the opportunity to work under her supervision and for her trust in allowing me to develop this work with scientific independence and rigor.

I would also like to extend my heartfelt thanks to prof. dr hab. inż. Stanisław Stupkiewicz for his insightful discussions, constructive feedback, and the generous time he devoted to closely following and supporting this research. His scientific perspective and thoughtful comments significantly strengthened the quality of this dissertation.

My sincere appreciation goes to dr. hab. Francisco Javier Domínguez-Gutiérrez for his effective collaboration, particularly in the irradiation simulation studies. His expertise and cooperative spirit contributed greatly to the advancement of this work.

Beyond the academic sphere, I owe my deepest gratitude to my parents and my siblings for their unconditional love, encouragement, and unwavering belief in me throughout my entire life. Their support has been the foundation upon which all my achievements are built. I am equally thankful to my parents-in-law and siblings-in-law for their encouragement and support, especially while I was far from our hometown and pursuing this journey abroad.

Finally, and most importantly, I wish to express my profound gratitude to my wife, Sanam — my friend, my love, and my constant companion on this path. Her endless patience, unwavering support, and unconditional love, in both the good times and the difficult moments, have sustained me throughout this journey. Her presence has been my greatest source of strength and stability, and this achievement would not have been possible without her.

Funding

This work was supported by the National Science Centre, Poland, under Grant No. UMO-2020/38/E/ST8/00453. We gratefully acknowledge the Polish high-performance computing infrastructure PLGrid (HPC Center at ACK Cyfronet AGH) for providing computer facilities and support within the computational Grant No. PLG/2024/017084.

Contents

Chapter 1

Introduction

1.1 Scientific context

Materials in nuclear environments are subjected to some of the harshest service conditions encountered in engineering applications. These environments are characterized by sustained exposure to high temperatures, complex mechanical stresses, corrosive coolant chemistries, and intense irradiation by energetic particles (Zinkle and Busby, 2009; Zinkle and Ghoniem, 2011). The ability of structural materials to resist these demanding conditions over extended lifetimes is central to the safety, efficiency, and economic viability of current and future nuclear energy systems.

Under prolonged irradiation, materials experience progressive degradation of their mechanical and physical properties. Radiation-induced damage manifests through mechanisms such as hardening (Renault-Laborne et al., 2018; Monnet and Mai, 2019; Cui et al., 2024; Ustrzycka et al., 2024), volumetric swelling (Xiao, 2019; Griffiths et al., 2022), irradiation creep (Ustrzycka, 2021; Ortner, 2023), and embrittlement (Xu et al., 2018; Yang, 2022; Ustrzycka et al., 2025). Among these effects, embrittlement represents one of the most severe threat, as it leads to the loss of ductility and fracture toughness, thereby increasing the probability of crack initiation and unstable crack propagation (Stephenson and Was, 2015). This reduction in fracture resistance poses a fundamental challenge to maintaining the structural integrity of nuclear components throughout their operational lifetime.

Fracture mechanics provides a robust theoretical framework for analyzing such degradation phenomena. It accounts for the presence of flaws and defects in real materials and predicts failure conditions through a stress-intensity-based and energy-based description of crack growth (Griffith, 1921; Orowan, 1949; Anderson, 2005). This framework is particularly important for nuclear applications, where radiation-induced defects act as stress concentrators and crack initiation sites, profoundly modifying the fracture resistance and failure behavior of structural materials (Little, 1986; Zinkle and Was, 2013).

Defects generated under irradiation, typically of nanometric dimensions, progressively accumulate and lead to material degradation. Radiation-induced defects differ fundamentally from conventional defects introduced during manufacturing processes, not only in their characteristic types but also in their spatial scale. While manufacturing-related defects are generally larger and more extended, radiation-induced defects form at nanometric length scales, are randomly

distributed within the crystalline lattice. Their evolution and interactions with dislocations, slip and twinning systems, and developing crack-tip stress fields under mechanical loads disrupt the underlying deformation mechanisms, thereby reducing resistance to crack initiation. Although these defects originate at the nano-scale, their collective influence governs macroscopic mechanical degradation, ultimately resulting in reduced ductility and fracture toughness in irradiated materials (Zinkle, 2012; Nordlund et al., 2018a; Ustrzycka et al., 2024).

To capture the impact of radiation-induced defects on fracture behavior, models must extend beyond continuum descriptions. Atomistic simulations provide a unique insight into defect structures and crack-tip mechanisms. By explicitly modeling atomic interactions, they provide both qualitative and quantitative insights into how radiation-induced defects influence material behavior during crack initiation and propagation (Krull and Yuan, 2011; Li et al., 2020; Chang et al., 2020). This approach enables systematic investigations of radiation-induced microstructures under controlled conditions, contributing to a physical understanding of defect-driven mechanisms that influence macroscopic mechanical degradation in nuclear materials (Zeng et al., 2018).

1.2 Research motivation, goals, and scope

The motivation for this research arises from the need to ensure the structural reliability of nuclear energy systems under extreme service conditions, particularly regarding radiation-induced embrittlement. Experimental studies have provided valuable insight into radiation effects at the nanoscale, including partial observation of defect structures and their evolution; however, they are inherently limited in capturing the full atomistic mechanisms governing defect formation, interactions, and crack propagation. Resolving this knowledge gap is essential for understanding how radiation-induced microstructures compromise fracture behavior and material performance, which is critical for enhancing the longevity and safety of current fission reactors and guiding material selection and design in advanced systems, including Generation IV fission technologies and fusion power plants.

At the nanoscale, radiation effects originate from the formation and evolution of defects, which strongly affect the material's physical and mechanical response under loading. This study aims to elucidate the physical mechanisms by which radiation-induced defects interact with propagating cracks and to develop a systematic method for analyzing the evolution of defect populations near the crack tip. Particular emphasis is placed on how different defect types can either accelerate or impede crack growth, and on how their competing effects govern crack propagation rates, fracture resistance, and overall structural integrity.

The primary objective of this work is to develop an atomistic framework integrating defect evolution, orientation-dependent deformation, and crack propagation to elucidate the mechanisms of the ductile-to-brittle transition and enable evaluation of irradiation-induced embrittlement.

To guide this investigation, the study addresses the following key questions:

- Do radiation-induced interstitial defect clusters (dislocation loops and stacking fault tetrahedra), acting as strong inclusions, effectively decelerate macrocrack propagation in fcc crystals, and under which irradiation doses does this crack-shielding mechanism prevail?
- To what extent do vacancy-type defects (voids) promote crack acceleration through stress concentration and local lattice weakening, and how do their growth and coalescence compete with crack-arresting mechanisms induced by interstitial defect clusters?
- Which defect population dominates the fracture response at increasing irradiation levels: void-assisted crack acceleration or interstitial-cluster-induced crack shielding, and how is this balance controlled by defect density, spatial distribution, and crystallographic orientation?
- Under what conditions can interstitial defect clusters be considered beneficial for material lifetime by delaying crack advance, despite their role in radiation hardening and suppression of dislocation mobility?
- How do orientation-dependent slip activity and crack-tip plasticity mediate the transition from a defect-shielded regime to a void-dominated brittle fracture regime in irradiated materials?
- Can the observed competition between crack acceleration and crack shielding be quantitatively resolved through mechanical responses and energy-based fracture metrics, thereby identifying the governing mechanisms of radiation-induced ductile-to-brittle transition?

The scope of this study is focused on atomistic-scale simulations of fracture under mode-I tensile loading in irradiated materials. Radiation damage is represented by defect populations generated via overlapping collision cascades, enabling systematic analysis of their interaction with advancing cracks, their influence on local deformation, and the resulting mechanical response. By investigating these processes, the research provides fundamental insights and quantitative data on defect-crack interactions. These results are vital for informing and validating higher-scale models to enable predictive assessments of structural degradation in irradiated environments.

1.3 Outline of the thesis

The remainder of this thesis is organized as follows.

Chapter 2 establishes the scientific background necessary for the analysis of fracture in irradiated materials. The chapter begins by outlining the irradiation environments relevant to structural materials, highlighting the fundamental challenges imposed by energetic particle exposure. Within this context, the $Fe_{55}Ni_{19}Cr_{26}$ alloy is introduced as the model material system adopted in this work, based on its properties and applications. Following this, the chapter reviews

the fundamental mechanisms of radiation damage, including displacement cascades, defect formation, and defect evolution, together with a visualization of radiation-induced defects using transmission electron microscopy for context. It then reviews atomistic simulation approaches for modeling radiation damage through overlapping collision cascades and discusses their relevance for reproducing defect accumulation under controlled conditions. The chapter further introduces the essential principles of plastic deformation in fcc metals and the atomistic concepts of fracture mechanics, with emphasis on crack–defect interactions, crystallographic orientation effects, and crack-tip plasticity.

Chapter 3 presents the methodological framework and computational tools employed throughout this thesis. It introduces the molecular dynamics approach used to model atomic motion and material response under irradiation and mechanical loading, and outlines the theoretical foundations linking classical mechanics, statistical mechanics, and thermodynamic interpretation. The chapter describes the thermodynamic ensembles adopted to control temperature, pressure, and energy during different stages of the simulations, together with the numerical integration schemes used to generate stable atomic trajectories. It further clarifies the evaluation of macroscopic mechanical and thermodynamic quantities from atomistic data, including stress, pressure, and temperature, and discusses their physical interpretation within the virial formalism. The chapter also discusses the interatomic potentials used to represent metallic bonding in Fe–Ni–Cr alloys, as well as the procedures for energy minimization, system relaxation, and boundary-condition selection. Finally, it outlines the overall simulation workflow and data-processing pipeline, providing a unified methodological basis for the irradiation and fracture simulations presented in the subsequent chapters.

Chapter 4 presents an atomistic investigation of radiation-induced embrittlement in austenitic $Fe_{55}Ni_{19}Cr_{26}$ alloy, focusing on the mechanisms governing the irradiation-assisted ductile-to-brittle transition. The chapter examines how irradiation-driven defect accumulation modifies crack-tip deformation and fracture behavior by systematically comparing pristine and irradiated microstructures. MD simulations are employed to generate irradiated configurations, model crack propagation, and resolve crack–defect interactions at the atomic scale. Particular attention is given to the roles of radiation-induced voids, dislocation loops, and defect clustering in suppressing plastic deformation, altering crack paths, and promoting crack acceleration and branching. The fracture response is further quantified using an energy-based framework, in which the critical energy release rate (G_c) is decomposed into surface-formation and plastic-dissipation contributions to clarify how irradiation redistributes the fracture energy balance. Together, the mechanistic observations and energetic analyses establish a direct link between radiation-induced microstructural evolution and the emergence of embrittlement in fcc $Fe_{55}Ni_{19}Cr_{26}$ alloy. This chapter is extracted from the paper by Ustrzycka et al. (2025).

Chapter 5 investigates the role of crystallographic orientation in governing irradiation-assisted fracture behavior in austenitic $Fe_{55}Ni_{19}Cr_{26}$ alloy. While irradiation generates broadly similar

defect populations across orientations, the interaction of these defects with crack-tip plasticity is strongly conditioned by lattice geometry and slip-system accessibility. This chapter shows that the transition from ductile to brittle behavior under irradiation is influenced by crystallographic orientation. Using orientation-controlled MD simulations, crack propagation is examined in single crystals oriented along (001), (011), and (111), enabling a systematic comparison of deformation mechanisms, crack–defect interactions, and fracture resistance under identical irradiation conditions. The analysis combines atomistic visualization with quantitative metrics, including stress–strain response, crack-growth kinetics, traction–separation (T-S) behavior, and fracture energy (g_f). Together, these results establish how crystallography modulates the balance between plastic accommodation and defect-driven crack advance, and identify orientation-dependent signatures of the irradiation-induced ductile to brittle transition in the selected alloy. This chapter is extracted from the paper by Mousavi et al. (2026).

The main results of the thesis are summarized in Chapter 6. The thesis is further supplemented by seven appendices that provide additional supporting material and technical details.

Chapter 2

Background and state of the art

2.1 Radiative environments: properties of functional materials

Structural materials employed in advanced technologies that operate under radiation exposure are subjected to various forms of irradiation, each presenting critical challenges to their performance and reliability. These environments include nuclear fission and fusion reactors, particle accelerators, and space applications. In fission reactors such as light water reactors (LWRs), sodium-cooled fast reactors (SFRs), and very high temperature reactors (VHTRs), components like cladding, core internals, and pressure vessels operate under high temperatures (300–1000 °C), corrosive coolants, and intense neutron fluxes that can generate significant displacement damage in structural materials (Zinkle and Busby, 2009; Zinkle and Was, 2013; Zinkle et al., 2016).

Fusion systems present additional complexity, as illustrated by large-scale fusion devices such as ITER, DEMO, and stellarator concepts (Fig. 2.1), where 14 MeV neutrons create nuclear transmutation reactions, producing significant helium that accelerates swelling, embrittlement, and phase instabilities (Lucon et al., 2006; Stork et al., 2014; Hosemann et al., 2018). Similarly, accelerator- and detector-based facilities, such as CERN and KEK (Fig. 2.1), expose

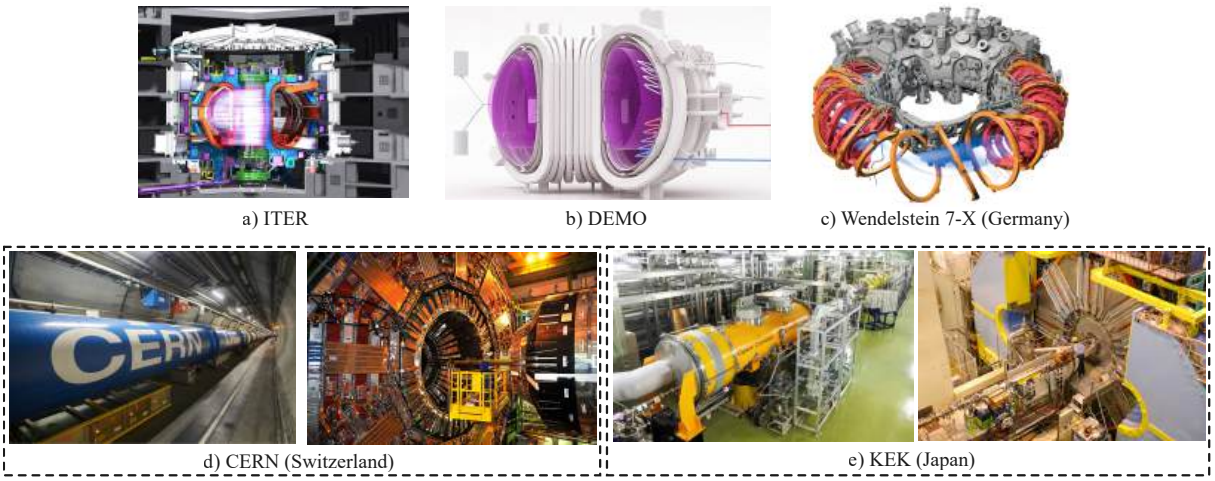

a) ITER b) DEMO c) Wendelstein 7-X (Germany)

d) CERN (Switzerland) e) KEK (Japan)

Figure 2.1: Representative accelerator- and fusion-related facilities operating in radiation-intensive environments: (a) ITER, an international tokamak fusion reactor (source link: ITER Organization); (b) DEMO, a conceptual demonstration fusion power plant (source link: EUROfusion); (c) Wendelstein 7-X (Germany), a stellarator-type fusion device (source link: Max Planck Institute for Plasma Physics); (d) CERN (Switzerland) (source link: CERN) and (e) KEK (Japan) (source link: KEK), illustrating large-scale particle accelerator and detector infrastructures.

structural and functional materials to high-energy particles, leading to radiation damage that limits operational lifetime and reliability (Will, 2021). These irradiation environments promote microstructural evolution in metals and alloys through the formation and accumulation of radiation-induced defects, which govern subsequent changes in mechanical behavior (Kinchin and Pease, 1955; Norgett et al., 1975; Boisson et al., 2019).

Fig. 2.2 shows the MARIA reactor at the National Center for Nuclear Research (NCBJ), the only operating nuclear research reactor in Poland, which provides a unique national irradiation capability. The MARIA reactor enables studies of material behavior under intense neutron irradiation relevant to nuclear applications. While the present work does not involve direct reactor-based experiments, close collaboration with NCBJ researchers allows relevant experimental insights from fission irradiation systems to be incorporated into the analysis (Nowak et al., 2023; Ustrzycka et al., 2024, 2025).

In nuclear structural environments, including high-temperature components in both fission and fusion systems, austenitic stainless steels (ASSs) are frequently employed due to their high-temperature strength, corrosion resistance, and ductility. These properties are closely related to the face-centered cubic (fcc) crystal structure of ASSs, which provides phase stability and good toughness over a wide temperature range (Hasanzadeh et al., 2019).

Among this class of materials, 310S stainless steel is frequently considered for high-

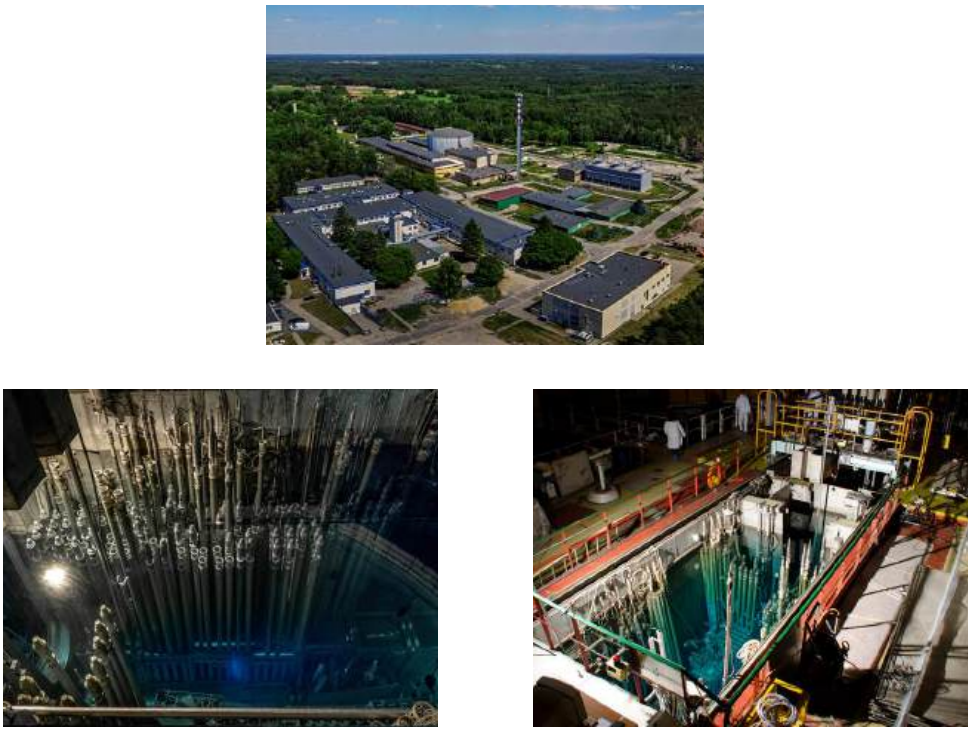

Figure 2.2: Representative views of the MARIA research reactor at the National Centre for Nuclear Research (NCBJ), Poland. The images depict the reactor core (bottom left and right) and the facility layout (top). Images provided by the National Centre of Nuclear Research (NCBJ Otwock-Świerk).

temperature components such as piping, heat exchangers, and structural supports, and it is commonly employed as a reference alloy in irradiation studies. Although 310S is not used as a primary load-bearing material in reactor cores or fusion plasma-facing regions, its chemical composition confers excellent oxidation resistance and microstructural stability, while its low carbon content limits carbide precipitation and associated embrittlement (Ortner, 2023). These characteristics make 310S a suitable model system for systematically investigating radiation-induced defect formation, defect evolution, and the resulting changes in mechanical behavior. The nominal chemical composition of 310S stainless steel is summarized in Table 2.1.

Table 2.1: Chemical composition of 310S stainless steel (in wt%).

C	S	P	Mn	Si	Cr	Ni	N	Fe
0.08	0.015	0.045	2.0	0.75	24.0–26.0	19.0–22.0	0.11	Balance

In fission irradiation environments, austenitic stainless steels located outside the reactor core may still experience neutron exposure sufficient to induce the formation and accumulation of nanoscale defects (Zinkle and Was, 2013; Zinkle et al., 2016). These irradiation-driven microstructural changes progressively modify the mechanical response, commonly leading to hardening, reduced ductility, and diminished fracture resistance as a direct consequence of defect accumulation. Experimental studies have consistently demonstrated that neutron irradiation alone can produce significant hardening and ductility loss in austenitic stainless steels, independent of specific reactor configurations (Zinkle et al., 2016; Hosemann et al., 2018). These observations underscore the relevance of 310S as a controlled model alloy for elucidating the fundamental mechanisms governing radiation-induced embrittlement.

Accordingly, the selection of 310S in this dissertation enables a focused investigation of atomic-scale processes governing defect generation, defect–defect interactions, and defect–crack interactions under irradiation. Its well-documented irradiation response and stable austenitic microstructure provide a robust material platform for atomistic simulations aimed at clarifying the physical mechanisms that link radiation-induced microstructural evolution to degradation in mechanical and fracture behavior.

2.2 Radiation defects: formation and identification

At the atomic level, the radiation process begins when an energetic particle (typically a neutron, proton, or ion) collides with a lattice atom, transferring sufficient energy to displace it from its equilibrium site to interstitial position and generate a primary knock-on atom (PKA), as shown in Fig. 2.3. The schematic illustrates this process within a multicomponent Fe–Ni–Cr matrix, where Fe (blue), Ni (yellow), and Cr (green) atoms form the crystalline framework. Upon collision, the energetic particle (red sphere) transfers its kinetic energy to the lattice atoms, producing PKAs (orange atoms) that cascade through the Fe–Ni–Cr lattice. These PKAs initiate a series of atomic collisions that eject neighboring atoms from their sites, generating a dense region

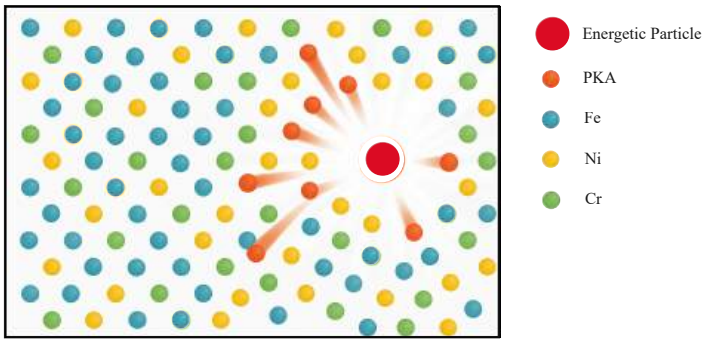

Figure 2.3: Schematic representation of the irradiation process. An energetic particle transfers its kinetic energy to a lattice atom, generating a primary knock-on atom (PKA). The PKA moves through the lattice, displacing surrounding atoms and initiating a displacement cascade that creates point defects.

of atomic disorder composed of vacancies and interstitials, collectively referred to as Frenkel pairs. As illustrated in Fig. 2.4, the initially generated Frenkel pairs evolve through migration, recombination, and clustering during the cascade and subsequent equilibration stages. Vacancy-rich regions may condense into vacancy clusters and eventually collapse into vacancy-type dislocation loops or voids. In contrast, self-interstitial atoms aggregate to form interstitial clusters that can evolve into interstitial-type dislocation loops. These defect structures constitute the fundamental microstructural features governing radiation-induced evolution in Fe–Ni–Cr alloys.

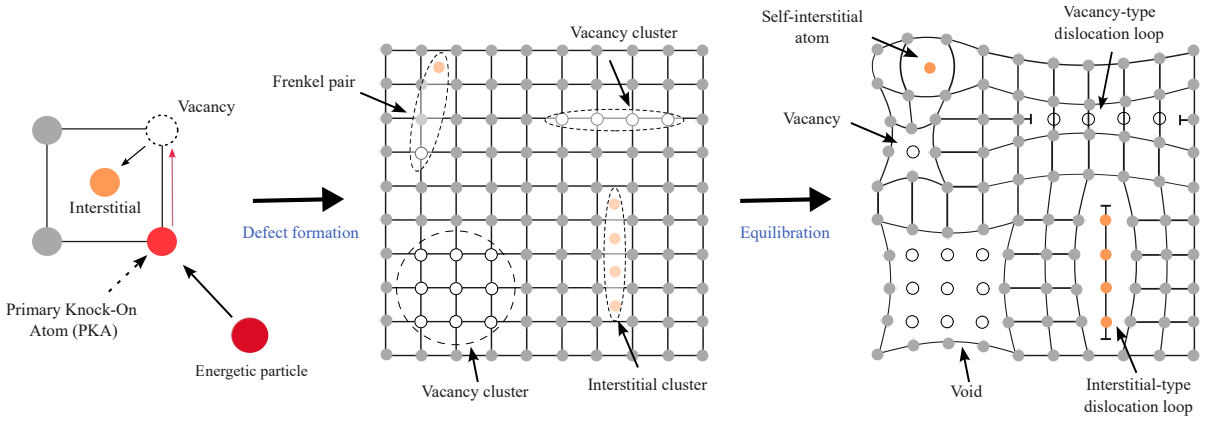

Figure 2.4: Schematic representation of radiation-induced defect formation and evolution. An energetic particle creates a primary knock-on atom (PKA), initiating displacement cascades and generating Frenkel pairs. Subsequent defect migration and clustering during equilibration result in vacancy clusters (voids) and interstitial aggregates, which may evolve into vacancy-type and interstitial-type dislocation loops.

The extent of this damage is measured by the displacements per atom (dpa), a metric that estimates the number of atomic displacements per lattice atom as a result of collisions with energetic particles. The dpa metric originates from the early work of Kinchin and Pease (1955) on primary point-defect production. The number of displacements caused by a PKA, denoted $N_{\mathrm{d}}(T_{\mathrm{d}})$, is described by the Norgett–Robinson–Torrens (NRT) model (Nordlund et al., 2018a,b) as follows:

$$N_{\mathrm{d}}(T_{\mathrm{d}}) = \begin{cases} 0 & T_{\mathrm{d}} < E_{\mathrm{d}} \\ 1 & E_{\mathrm{d}} \leq T_{\mathrm{d}} < \frac{2E_d}{0.8} \\ \frac{0.8\,T_{\mathrm{d}}}{2E_{\mathrm{d}}} & \frac{2E_{\mathrm{d}}}{0.8} \leq T_{\mathrm{d}} < \infty. \end{cases} \tag{2.1}$$

In Eq. 2.1, T_{d} is the damage energy of the PKA, and E_{d} is the threshold displacement energy (TDE), which is the minimum recoil energy required to displace an atom and form a stable Frenkel pair (Nordlund et al., 2018b; Ustrzycka et al., 2024). The dpa parameter, derived from the NRT model, quantifies the cumulative radiation damage throughout the material. It accounts for the damage energy, T_{d}, which is the portion of the PKA's energy that contributes to atomic displacements after subtracting energy lost to electronic interactions. The dpa is given by:

$$\mathrm{dpa} = \frac{N_{\mathrm{d}}(T_{\mathrm{d}})}{N} = \frac{1}{N}\frac{0.8\,(T_{\mathrm{PKA}} - S_{\mathrm{E}})}{2E_{\mathrm{d}}}, \tag{2.2}$$

where N is the total number of atoms in the material, T_{PKA} denotes the energy of PKA, and S_{E} is the electronic stopping power correction. The energy loss associated with electronic interactions, represented by S_{E}, corresponds to a retarding force arising from inelastic interactions between the energetic atom and the electronic subsystem of the material (Ustrzycka et al., 2024).

Advanced microscopy methods provide direct experimental validation of these defect types and their spatial distributions. Transmission electron microscopy (TEM) has long been the primary technique for identifying cascade-produced defect clusters, such as vacancy-type voids, dislocation loops, and SFTs, which form during irradiation and evolve under subsequent mechanical loading (Zinkle and Singh, 2006). TEM investigations reveal how these defects act as effective obstacles to dislocation motion, thereby enhancing hardening and altering slip behavior, often leading to localized deformation in the form of cleared dislocation channels (Briceño et al., 2011). The use of in-situ TEM has been particularly valuable, allowing direct visualization of dynamic interactions between moving dislocations and radiation-induced defect populations. Such studies demonstrate that dislocations are frequently pinned, depinned, or deflected by dislocation loops and voids, resulting in intermittent and jerky motion that is characteristic of irradiated microstructures (Fukumoto et al., 2022).

Complementary approaches such as 3D atom probe tomography (APT) and electron backscatter diffraction (EBSD) provide further insight into chemical and crystallographic features associated with irradiation damage. APT can resolve solute clustering at the nanoscale, linking defect structures with local compositional changes, while EBSD enables phase mapping and characterization of crystallographic orientation effects on defect accumulation and recovery processes (Lin et al., 2024b). X-ray diffraction (XRD), with its sensitivity to lattice strains and defect-induced peak broadening, is widely employed to quantify radiation-induced changes in microstrain and to monitor recovery during annealing (Chauhan et al., 2021). These complemen-

tary techniques extend the interpretive framework beyond direct imaging and allow correlation of defect populations with bulk material response.

Radiation-induced defects must be clearly distinguished from microstructural features introduced during conventional manufacturing processes, as their origin, characteristic length scale, and mechanical implications differ fundamentally. Fig. 2.5 presents representative microscopy images illustrating the characteristic differences between radiation-induced defects and processing-related microstructural features. Radiation-induced defects (Fig. 2.5(a)) are predominantly nanometric in scale and consist of dense populations of dislocation loops, vacancy clusters, and stacking fault tetrahedra (SFTs) formed under far-from-equilibrium irradiation conditions. In contrast, manufacturing-induced microstructural features (Fig. 2.5(b)) generally occur at the micrometer scale and include inclusions, microcracks, pores, and deformation-induced dislocation structures associated with thermo-mechanical processing history. This marked difference in characteristic length scale and spatial distribution reflects the distinct origins and evolution pathways of radiation-induced and manufacturing-related defects.

As illustrated in Fig. 2.6, TEM provides nanoscale evidence of defect clustering and their direct interactions with dislocations. Recent work has demonstrated that voids and dislocation

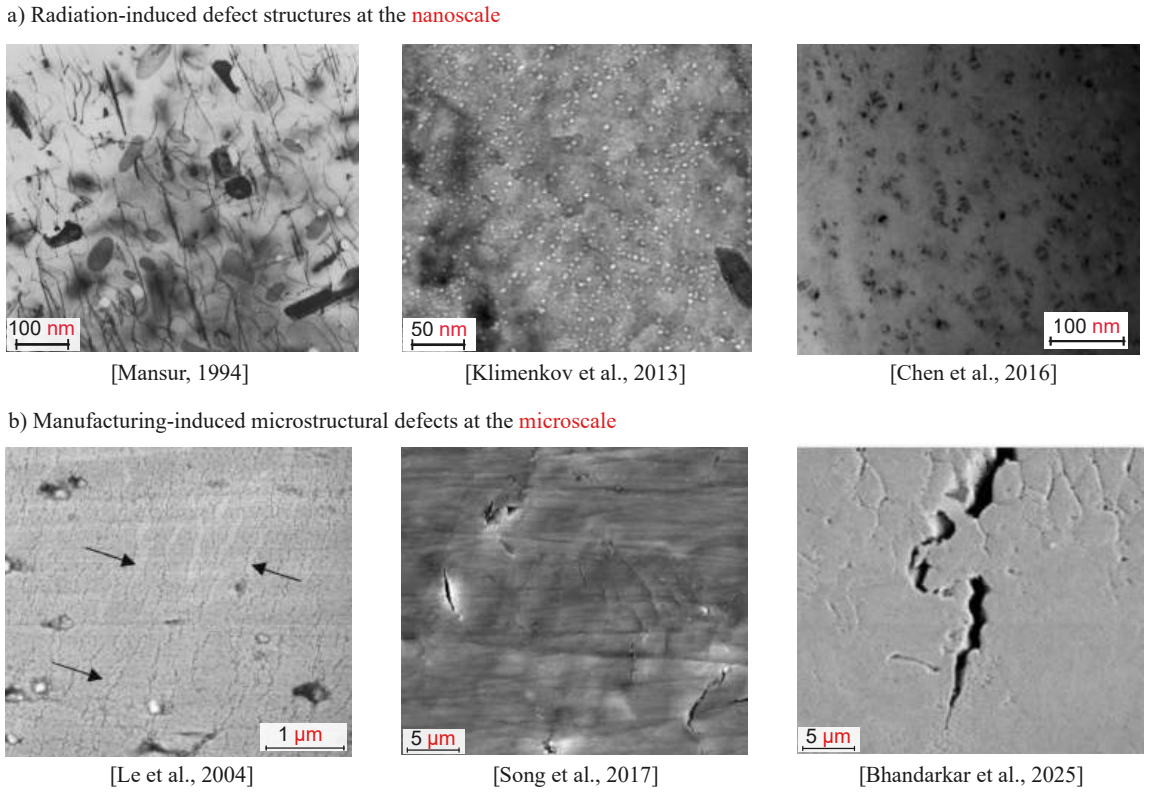

Figure 2.5: Experimental comparison of defect classes in steels: (a) Radiation-induced defect structures at the nanoscale revealed by TEM, showing dense populations of defects after irradiation (reproduced from Mansur, 1994; Klimenkov et al., 2013; Chen et al., 2016). (b) Manufacturing-induced microstructural defects at the microscale, including micro-cracks, inclusions, and deformation features observed by SEM and optical microscopy (reproduced from Le et al., 2004; Song et al., 2017; Bhandarkar et al., 2025).

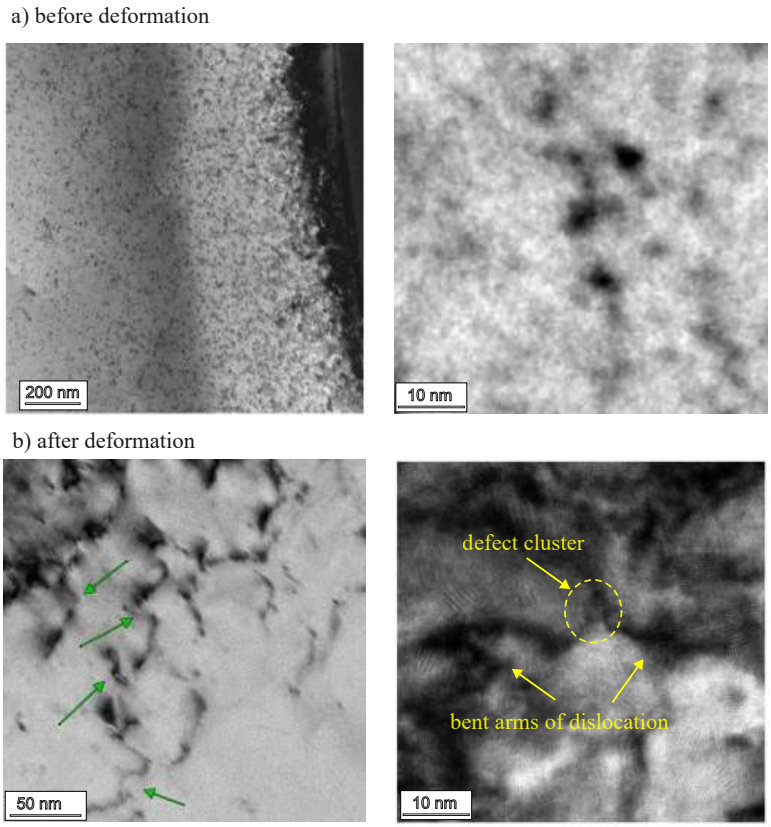

Figure 2.6: Transmission electron microscopy (TEM) analysis of austenitic stainless steel irradiated to 0.12 dpa (reproduced from Ustrzycka et al., 2024), showing (a) radiation-induced porosity in the form of defect clusters at varying magnifications. (b) TEM images further illustrate the dislocation-blocking mechanism, where a dislocation line encircles radiation defects at different magnifications. These images depict the irradiated material after deformation, highlighting the interaction between dislocations and radiation-induced defects.

loops not only coexist but also compete as barriers to plastic deformation, with voids often acting as stronger obstacles than loops of comparable size (Ustrzycka et al., 2024). Such observations highlight the role of defect morphology and spatial distribution in dictating mechanical behavior. Post-deformation imaging reveals how dislocations bypass or encircle clusters, leaving characteristic signatures that confirm their interaction mechanisms. These insights are critical for developing mechanistic models that connect defect structure to macroscopic hardening and embrittlement.

Experimental studies also emphasize the complex hierarchy of defect evolution under irradiation. Small interstitial clusters coalesce into dislocation loops, vacancy clusters grow into resolvable voids, and helium or hydrogen atoms introduced during irradiation stabilize bubbles that further exacerbate hardening and promote localized fracture modes (Zinkle and Was, 2013; Lin et al., 2021). The stability and growth of these defects under thermal and mechanical driving forces have been directly monitored by ex-situ and in-situ annealing experiments, which show shrinkage, coarsening, or collapse of defect populations, together with partial recovery of

mechanical properties (Chauhan et al., 2021). These results demonstrate the competing processes of defect production and recovery, and their balance defines the steady-state microstructure of irradiated alloys.

Altogether, the experimental body of work converges on the view that radiation-induced defects form a dynamic and interacting system of obstacles that fundamentally alter plasticity. Dislocation loops, voids, bubbles, and SFTs each play distinctive roles in strengthening and channeling dislocation motion, as well as in controlling strain localization during deformation. High-resolution methods such as TEM, APT, EBSD, and XRD continue to expand understanding by linking nanoscale defect structures with macroscopic hardening, fracture resistance, and radiation-induced embrittlement (Vo et al., 2017; Howard et al., 2018; Li et al., 2025). This multi-technique framework establishes the experimental foundation upon which predictive models of irradiation damage are built, underscoring the importance of direct observation in advancing the mechanistic understanding of defect evolution in nuclear structural materials. The growth, clustering, and interactions of these nanoscale defects ultimately govern the macroscopic behavior of structural materials. Understanding their dynamics is therefore essential for uncovering the origins of radiation-induced embrittlement and for guiding the design of radiation-tolerant alloys and optimized microstructures.

Despite advances in experimental techniques, critical questions remain regarding how complex defect environments interact with evolving cracks at the atomic scale. In irradiated materials, microstructural heterogeneity and defect clustering strongly influence crack initiation and propagation, underscoring the need for atomistic-level investigations to reveal the fundamental mechanisms governing fracture in defected systems. Bridging experimental observations with atomistic modeling is therefore a key step toward resolving these open questions and enabling predictive understanding of fracture in irradiated alloys.

2.3 Atomistic irradiation simulation via overlapping collision cascades

Molecular dynamics (MD) is a powerful atomistic simulation method widely used to investigate the effects of irradiation in structural materials, particularly those used in nuclear energy systems (Zhou, 2003; Osetsky et al., 2004; Stukowski and Albe, 2010). Since its development in the mid-20th century, MD has enabled researchers to capture the dynamic processes of defect generation, microstructural evolution, and property degradation at temporal and spatial resolutions inaccessible to experimental methods. With its ability to bridge the scale gap between quantum mechanical models and mesoscale approaches, MD plays a central role in advancing the understanding of irradiation phenomena relevant to irradiation environments (Nordlund et al., 2018a,b).

The simulation of radiation damage using MD began with the PKA approach, first introduced by Kinchin and Pease (1955) and later formalized by Norgett et al. (1975). Early implementations, such as by Mattei and Mazzone (1996), laid the groundwork for tracking defect initiation by imparting kinetic energy to a single atom to mimic the recoil from an energetic neutron.

Subsequent advances by Bacon et al. (1999) introduced overlapping cascade techniques, allowing cumulative damage and athermal recombination mechanisms to be examined across sequential PKA events.

A classical MD application in the study of radiation damage is presented by Park et al. (2007), who investigated displacement cascades in tungsten using a modified Finnis–Sinclair interatomic potential. Their work focused on the formation, evolution, and transformation of self-interstitial atoms (SIAs) during high-energy collision cascades.

Subsequently, more statistically robust approaches emerged in MD simulations of PKA-initiated cascades. These methods typically involve the PKA approach, where a selected atom is given an initial kinetic energy to initiate a cascade, mimicking the recoil from neutron or ion irradiation and leading to ballistic collisions followed by thermal spike and relaxation phases that produce stable defects. To simulate cumulative damage under higher-dose conditions, repeated PKA events with randomized recoil directions, energies, and (in alloys) atom types are employed, enabling statistically averaged defect production comparable to experimental dpa levels. Key studies, such as those by Stoller (2012), who reviewed primary damage formation in iron via MD cascades; Bukonte et al. (2013), comparing MD and binary collision approximation for cascades in silicon and tungsten; Nordlund et al. (2018a), introducing athermal recombination-corrected dpa models; Nordlund et al. (2018b), providing a comprehensive review of primary radiation damage understanding; Nordlund (2019), offering a historical perspective on simulation techniques; and Vázquez et al. (2021), extending cascade modeling to electronic effects in materials, have emphasized best practices for dpa estimation, cascade efficiency, and defect analysis. These efforts have established standardized protocols for MD simulations of collision cascades and cumulative radiation damage, particularly in metals and multicomponent alloys.

Building on developments in the analysis of radiation damage, Domínguez-Gutiérrez and von Toussaint (2020) demonstrated a novel fingerprint-like method to detect and classify material defects in crystalline solids following energetic particle irradiation. Their approach is based on computing a rotation-invariant descriptor vector for each atom, which characterizes its local environment. This method, which is generalizable, easy to use, does not require extreme computational resources, and is largely independent of the sample material and temperature. They applied this methodology to MD simulations of collision cascades in both pristine and deuterated tungsten, successfully identifying and quantifying standard point defects as well as discovering a new type of defect configuration. Their analysis revealed that deuterated tungsten samples consistently exhibited more defects than pristine ones.

In a subsequent study, von Toussaint et al. (2021) explored the analysis of defects and their dynamics in crystalline materials, highlighting their significance for both fundamental science and various engineering applications. The research addresses the increasing complexity of interpreting MD simulation data as system sizes grow. The authors propose a semi-automatic workflow for identifying and classifying defects in crystalline structures, featuring a novel defect

description method. This approach overcomes challenges such as the small volume fraction of altered regions, thermal motion, and the emergence of unexpected atomic configurations post-irradiation. By converting the local atomic environment into a rotation-invariant descriptive vector, the method enables comparison with known defect types and facilitates the detection of new defects using a distance-based classification metric. Unmatched vectors suggest the presence of novel defect types.

Following a similar approach, Ustrzycka et al. (2024) employed sequential MD simulations incorporating PKAs to model the accumulation of radiation-induced defects in Fe–Ni–Cr alloys under neutron-equivalent ion irradiation conditions. Their study focused on the nucleation and evolution of dislocation loops and voids formed via overlapping displacement cascades. An illustrative sequence of such a displacement cascade is shown in Fig. 2.7. Snapshots of the cascade development from 0.1 ps to 10 ps (Fig. 2.7a–h) reveal the successive stages of defect evolution. The first defects appear in the direction of the projectile velocity at 0.1 ps, while the maximum defect production occurs between 0.4–0.7 ps, corresponding to the heat spike stage in which atoms can temporarily reach supersonic velocities. Beyond this point, the system undergoes recovery and recrystallization from 1 ps to 10 ps, leading to the formation of stable Frenkel pairs during thermalization. The final microstructure contains SIAs and vacancies that survive recombination. These defects mark the initiation of stable defects in irradiated crystalline solids (Ustrzycka et al., 2024). The resulting defect morphologies and

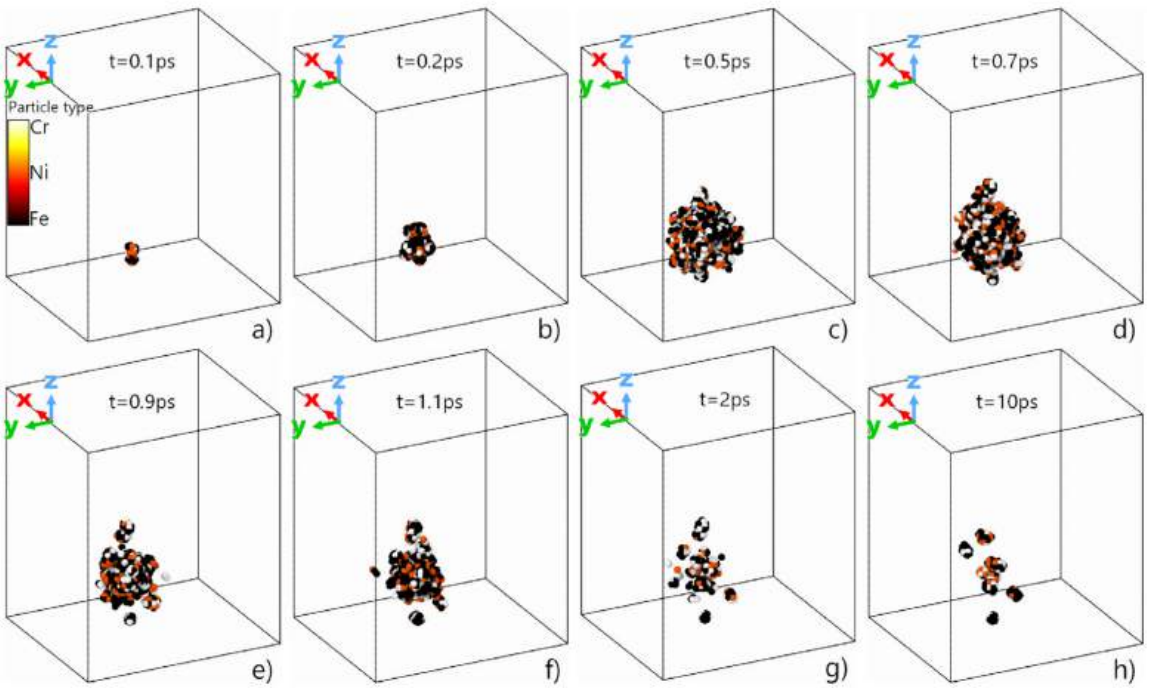

Figure 2.7: Time evolution of a collision cascade induced by a 5 keV PKA in an Fe–Ni–Cr alloy, obtained from MD simulations (Ustrzycka et al., 2024).

densities were systematically validated through TEM observations of Ni-ion-irradiated Fe–Ni–Cr samples, confirming the predictive accuracy of MD simulations in capturing radiation-induced microstructural evolution.

As irradiation proceeds beyond individual displacement cascades, many displaced atoms recombine or return to near-equilibrium positions during cascade stabilization. At the same time, the surviving point defects accumulate, migrate, and interact, progressively driving the formation of more complex and stable microstructural features at higher irradiation doses. As shown in Fig. 2.8, vacancy clusters tend to collapse into well-defined stacking fault tetrahedra (SFTs), a characteristic defect structure in fcc systems such as Ni-based and austenitic Fe–Ni–Cr alloys (Zinkle, 2012; Aidhy et al., 2016; Zhao et al., 2019). The relatively low stacking fault energy in fcc metals facilitates the formation of SFTs (Kai Nordlund, 1999). Simultaneously, dislocation loops, such as Frank loops, can evolve and interconnect, forming entangled dislocation networks that significantly hinder dislocation glide. The coexistence of these defects, including SFTs, Frank loops, entangled dislocation segments, and voids, collectively contributes to the radiation-induced embrittlement observed in fcc metals by reducing dislocation mobility and altering the pathways of plastic deformation.

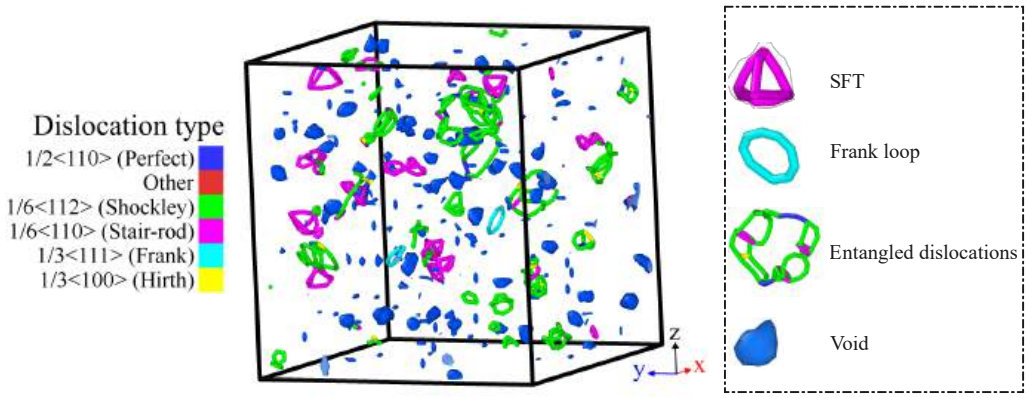

Figure 2.8: Typical defect structures generated after 200 cascades (0.076 dpa) of irradiation in Fe–Ni–Cr alloys. Prominent features include SFTs, Frank loops, entangled dislocations, and vacancy clusters (voids), which represent the dominant radiation-induced defect morphologies in fcc systems. Visualization generated using OVITO (Stukowski and Albe, 2010).

MD simulations have evolved from simulating single cascade events to comprehensive modeling of defect formation, evolution, and mechanical degradation. It now serves as a cornerstone in nanoscale modeling frameworks aimed at predicting material performance in nuclear environments. Nevertheless, simulating radiation-assisted fracture remains a developing area, with limited MD studies capturing the transition from microstructural damage to fracture.

2.4 Plastic deformation mechanisms at crack tips in fcc metals

The mechanical behavior of metals is fundamentally governed by the nature of metallic bonding, in which delocalized valence electrons provide non-directional cohesion between atomic cores. Stronger interatomic cohesion corresponds to higher resistance against elastic deformation, while the absence of directional bonding constraints enables atoms to rearrange under applied stress without immediate fracture (Ashby and Jones, 2012). As a result, metals typically exhibit moderate elastic stiffness combined with a pronounced capacity for irreversible plastic deformation once resistance to atomic motion is overcome. This bonding character permits relative atomic displacement under applied stress without immediate bond rupture, thereby enabling plastic deformation rather than brittle fracture.

In an ideal crystal, atoms occupy perfectly periodic lattice positions defined by the crystal structure (e.g., fcc or bcc); however, real crystalline solids invariably contain imperfections that dominate their mechanical response. Rather than being limited by the intrinsic strength of atomic bonds, plastic deformation is controlled by the nucleation, motion, and interaction of crystal defects. Among these, dislocations act as the primary carriers of plastic deformation. A dislocation is a one-dimensional lattice imperfection around which atomic planes are misaligned, producing long-range stress fields that interact with applied loads and other defects (Hirth and Lothe, 1992; Hull and Bacon, 2011). The ability of dislocations to glide allows adjacent atomic planes to shear past one another at stresses orders of magnitude lower than those required for homogeneous lattice shear, thereby enabling plastic flow in crystalline metals.

In crystalline metals, the atomic arrangement further dictates how plastic deformation is accommodated. Face-centered cubic (fcc) metals are characterized by a high atomic packing density and a large number of crystallographically equivalent deformation systems, which together promote high ductility and fracture resistance. In fcc metals such as Cu, Ni, Al, and austenitic Fe–Ni–Cr alloys, dislocation-mediated plasticity is particularly efficient due to the dense atomic packing and the presence of multiple equivalent slip systems. The dominant slip systems in fcc lattices consist of the close-packed $\{111\}$ planes and the $\langle 110\rangle$ directions, yielding twelve independent slip systems capable of accommodating arbitrary plastic strain, as schematically illustrated in the left panel of Fig. 2.9 (Hirth and Lothe, 1992; Hull and Bacon, 2011). A perfect dislocation in an fcc crystal has a Burgers vector $\mathbf{b} = \frac{a_0}{2}\langle 110\rangle$, where a_0 denotes the lattice parameter.

In many fcc alloys, particularly those with low to intermediate stacking fault energy (SFE), perfect dislocations dissociate into two Shockley partial dislocations separated by a stacking fault in order to reduce the elastic energy of the system:

$$\frac{a_0}{2}\langle 110\rangle \;\rightarrow\; \frac{a_0}{6}\langle 112\rangle + \mathrm{SF} + \frac{a_0}{6}\langle 211\rangle. \tag{2.3}$$

The SFE controls both the equilibrium separation of the partial dislocations and their mobility.

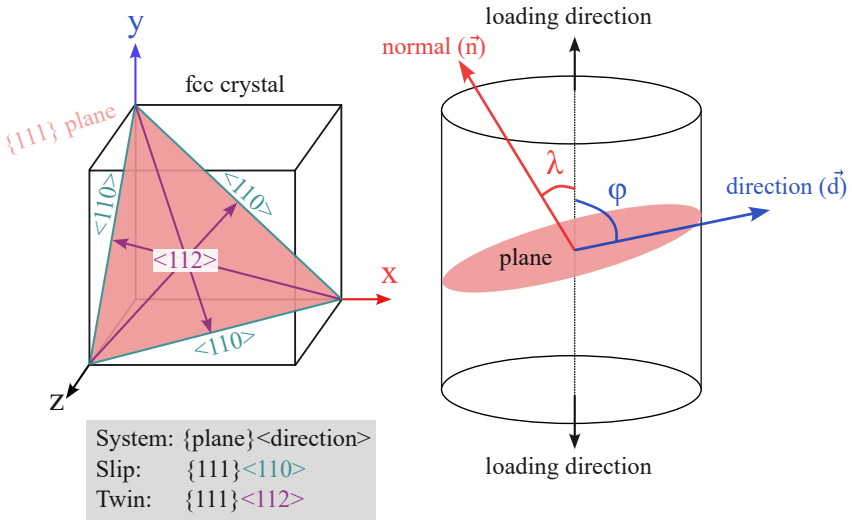

Figure 2.9: Schematic illustration of crystallographic deformation systems and Schmid factor geometry in fcc metals. Left: Representation of slip and twinning systems in the fcc lattice, highlighting the $\{111\}\langle 110\rangle$ slip systems and the $\{111\}\langle 112\rangle$ twinning systems. Right: Definition of the Schmid factor, showing the angles ϕ between the loading direction and the plane normal, and λ between the loading direction and the slip or twinning direction used to evaluate the resolved shear stress (Xu et al., 2014).

Low-SFE materials, such as austenitic stainless steels and Cu-based alloys, exhibit extended stacking fault ribbons and planar slip, whereas high-SFE materials, such as Al, favor compact dislocation cores and frequent cross-slip (Christian and Mahajan, 1995).

A crack represents an extreme crystallographic imperfection, introducing a highly localized stress field with steep gradients. Near the crack tip, the resolved shear stress acting on specific crystallographic systems can significantly exceed the applied far-field stress, making the crack tip a preferential site for the activation of plastic deformation mechanisms that dissipate energy and reduce the crack driving force.

In fcc metals, crack-tip plasticity is primarily governed by two closely related but distinct mechanisms: dislocation slip and deformation twinning. Both mechanisms originate from the emission of Shockley partial dislocations on $\{111\}$ planes, but they differ in their crystallographic directions and atomic-scale evolution. Dislocation slip proceeds when a leading partial dislocation is followed by the emission of a trailing partial on the same $\{111\}$ plane, restoring the perfect fcc stacking sequence and producing a full dislocation. In contrast, deformation twinning occurs when successive partial dislocations of identical Burgers vectors are emitted on adjacent $\{111\}$ planes, generating a coherent twin boundary and a mirror-symmetric lattice orientation across the twin plane (Warner et al., 2007).

The geometric conditions governing the activation of slip and twinning are illustrated schematically in Fig. 2.9. The figure highlights the crystallographic distinction between the $\{111\}\langle 110\rangle$ slip systems and the $\{111\}\langle 112\rangle$ twinning systems in fcc crystals, as well as the angular definitions required to evaluate their resolved shear stresses under an applied load.

These two mechanisms constitute complementary pathways for plastic deformation and energy dissipation at crack tips (Andric and Curtin, 2017). Slip-dominated plasticity generally promotes crack-tip blunting and stable crack growth, whereas deformation twinning can either enhance plastic accommodation or, under certain conditions, lead to localized strain concentration (Mousavi et al., 2026). The competition between slip and twinning is sensitive to crystallographic orientation, loading rate, and local stress state.

The activation of plastic deformation mechanisms at crack tips is governed by the resolved shear stress acting on a given crystallographic deformation system, which is commonly quantified using the Schmid factor. In its general form, the Schmid factor (Schmid and Boas, 1968) is expressed as

$$m = \cos\phi \cos\lambda, \tag{2.4}$$

where ϕ is the angle between the loading direction and the normal to the active deformation plane, and λ is the angle between the loading direction and the corresponding deformation direction.

For dislocation slip in fcc crystals, the Schmid factor is evaluated over all $\{111\}\langle 110\rangle$ slip systems. In this case, ϕ represents the angle between the loading direction and the normal to a $\{111\}$ slip plane, while λ is the angle between the loading direction and a $\langle 110\rangle$ slip direction lying within that plane. The maximum slip Schmid factor, $m_{\max}^{\text{slip}}$, is obtained by identifying the most favorably oriented slip system among all crystallographically equivalent candidates.

Deformation twinning in fcc metals is described within the same geometric framework but involves crystallographically distinct $\{111\}\langle 112\rangle$ twinning systems. For twinning, ϕ is defined with respect to the normal of the twinning plane, and λ corresponds to the angle between the loading direction and the $\langle 112\rangle$ twinning direction. The maximum twinning Schmid factor, $m_{\max}^{\text{twin}}$, reflects the most favorably oriented twinning system for a given crystallographic orientation.

Although slip and twinning share the same $\{111\}$ habit planes in fcc crystals, they differ fundamentally in their deformation directions, $\langle 110\rangle$ for slip and $\langle 112\rangle$ for twinning. This directional distinction imposes different geometric constraints on the resolved shear stress and explains why, for certain crystallographic orientations, the maximum Schmid factor for twinning can exceed that for slip. Consequently, the relative magnitudes of $m_{\max}^{\text{slip}}$ and $m_{\max}^{\text{twin}}$ provide a robust, orientation-dependent criterion for anticipating the dominant plastic deformation mechanism at crack tips.

2.5 Atomistic fracture mechanics

Fracture mechanics provides the theoretical foundation for understanding crack initiation and propagation in structural materials. At the engineering scale, it relates the interplay between stress intensity, crack geometry, and component configuration to the onset of fracture. However, fracture is inherently a multiscale process (see Fig. 2.10), bridging continuum-scale stress

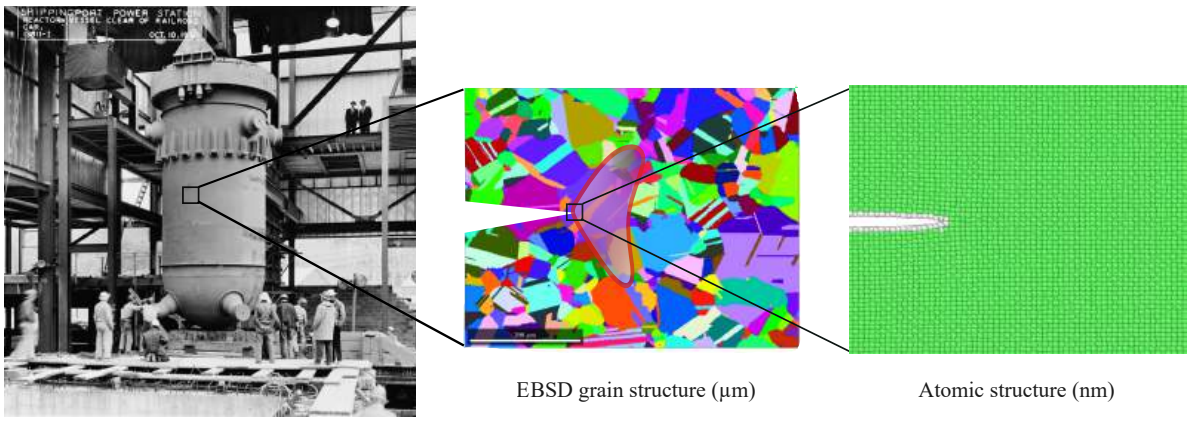

Figure 2.10: Multiscale representation of fracture from the engineering scale (reactor vessel) through the microstructural scale (polycrystalline grains) down to the atomic scale (crack tip in MD simulation).

analysis with grain-level microstructure and atomic bonding at crack tips. While continuum-based theories successfully describe macroscopic fracture behavior, they cannot resolve the discrete atomic events that govern crack nucleation and early-stage crack propagation. To address this limitation, atomistic simulations, particularly MD, offer a powerful framework to capture fracture processes at the atomic scale and to connect microscopic mechanisms with macroscopic mechanical response.

2.5.1 Theoretical basis of atomistic fracture methods

MD simulations have evolved from qualitative visualization tools into quantitative methods capable of capturing the mechanical response of materials at the atomic scale. The classical stress–strain response obtained from MD under uniaxial or shear loading provides access to elastic moduli, yield strength, and ultimate tensile strength, thus revealing the deformation mechanisms preceding fracture. In addition to stress–strain behavior, MD enables the evaluation of advanced fracture mechanics metrics such as the stress intensity factor (SIF) (Wilson et al., 2019; Fu et al., 2025), adapted from continuum theory to the atomistic scale.

However, the absence of true stress singularities and the discrete nature of atomic lattices limit the direct applicability of linear elastic fracture mechanics (LEFM) at the nanoscale (Jung et al., 2018). Energy-based quantities such as the J-integral (Kim et al., 2021; Jia et al., 2022; Stepanova and Mushankova, 2024), originally formulated within classical LEFM, are adapted to estimate the total energy dissipation during crack propagation in atomistic simulations. These adaptations are necessary because discrete atomic configurations do not provide a unique continuum stress field, making the direct application of LEFM ambiguous (Xu and Demkowicz, 2020).

The classical theory of fracture introduced by Griffith (1921) established that crack propagation occurs when the energy release rate G exceeds a critical value G_c, corresponding to the surface energy required to form new fracture surfaces. As shown schematically in Fig. 2.11,

this condition is equivalent to the stress intensity factor K_I reaching a critical threshold K_{Ic}, beyond which unstable crack growth occurs. While this framework successfully captures brittle fracture, its assumptions, linear elasticity, sharp cracks, and reversible deformation, restrict its applicability to ductile materials, where plastic dissipation plays a major role near the crack tip.

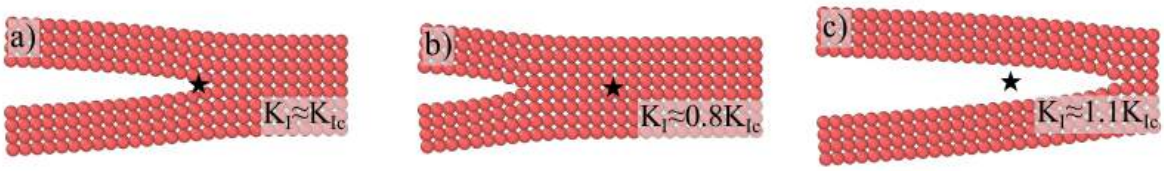

Figure 2.11: Schematic illustration of crack opening and closure behavior for different applied stress intensity factors K_I, showing the transition from subcritical to unstable crack propagation. At $K_I \approx 0.8K_{Ic}$ the crack remains stable, while at $K_I \gtrsim K_{Ic}$ catastrophic propagation occurs. Adopted from Andric (2019).

At the atomistic level, fracture is often preceded by plastic relaxation processes such as dislocation nucleation, which dissipate part of the applied energy before cleavage occurs. An additional threshold, K_{Ie}, represents the critical stress intensity required for dislocation emission from the crack tip. When $K_{Ie} < K_{Ic}$, dislocation emission precedes cleavage, blunting the crack and stabilizing it through plastic relaxation. Conversely, when $K_{Ie} > K_{Ic}$, dislocation emission is suppressed, leading to brittle cleavage. As shown in Fig. 2.12, these two competing mechanisms delineate the transition between the ductile and brittle regimes: the former dominated by dislocation-mediated plasticity, and the latter by direct bond rupture and surface formation.

From a methodological perspective, MD simulations allow direct quantification of the total fracture energy G_c and its decomposition into cleavage and plastic contributions (Xu and Demkowicz, 2020). The plastic term represents irreversible dislocation activity near the tip of the crack, while the cleavage term represents the surface energy associated with the creation of new fracture surfaces. This framework has been extended in recent studies (Xu and Demkowicz, 2020; Barik et al., 2024; Lin et al., 2025) to capture the continuous transition from ductile to brittle fracture by evaluating how the relative contributions of the plastic and cleavage energies

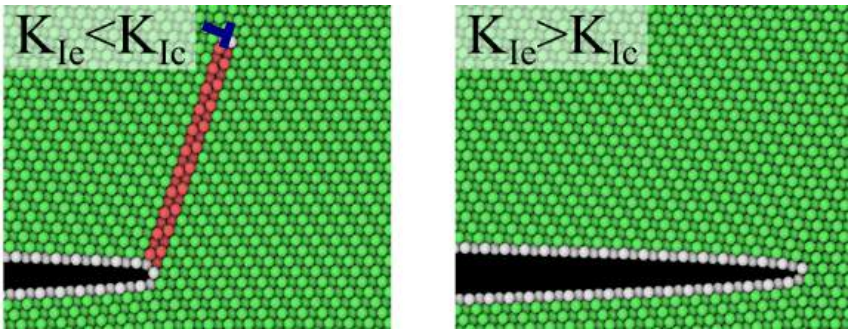

Figure 2.12: Evolution of an atomically sharp crack in a metallic lattice under different loading conditions: dislocation emission for $K_{Ie} < K_{Ic}$ (ductile regime, left) and cleavage-dominated propagation for $K_{Ie} > K_{Ic}$ (brittle regime, right). Adopted from Andric and Curtin (2017).

evolve with temperature, strain rate, or defect density.

In a broader context, the ductile-to-brittle transition (DBT) reflects a temperature- and microstructure-dependent shift in the dominant fracture mechanism. At higher temperatures or in defect-free materials, plasticity near the crack tip blunts and stabilizes the crack, delaying catastrophic failure. In contrast, at low temperatures or in defect-hardened microstructures, reduced dislocation mobility favors brittle cleavage characterized by rapid crack advance and minimal energy dissipation. This temperature- and defect-sensitive behavior of G_c offers a unified energy-based framework for quantifying the DBT in irradiated and non-irradiated systems.

To localize fracture processes, the traction–separation (T–S) law provides an effective framework for incorporating atomistic fracture data into continuum cohesive zone models (CZMs). By extracting atomic-scale traction–displacement data near crack tips, MD simulations facilitate the parameterization of T–S curves representing intergranular or transgranular decohesion. Several studies have implemented this approach to define critical traction, separation length, and total fracture energy for various materials, including aluminum (Yamakov et al., 2006), NiTi (Guiqiu et al., 2021), and ceramics (Wang et al., 2021). These atomistically derived T–S laws show strong consistency with both predictions of the continuum finite element method (FEM) and experimental observations.

2.5.2 Crack-defect interaction

Crack-defect interactions have been widely explored through atomistic simulations to elucidate how pre-existing microstructural features influence fracture behavior at the nanoscale. The presence of defects such as voids, vacancies, dislocation loops, and stacking faults modifies the local atomic arrangement and alters the pathways of crack propagation. These interactions can lead to either crack arrest, deflection, or accelerated propagation, depending on the defect type, size, and spatial distribution.

Wang et al. (2015) analyzed the interaction between cracks and voids in single-crystal silicon and found that void location and ligament distance strongly affect crack arrest or acceleration. Voids aligned along the crack path facilitate coalescence, while those positioned off-axis tend to blunt crack propagation. Similarly, Chandra et al. (2016) investigated single-crystal aluminum and demonstrated that the presence of vacancy clusters near the crack tip can either reduce or enhance fracture toughness depending on their spacing and configuration. In fcc Ni, Zhang and Ghosh (2013) showed that crack growth is coupled with dislocation emission and twin formation, where the evolution of stacking faults and partial dislocations mediates the fracture process. Moreover, Velilla-Díaz and Zambrano (2021) examined grain boundary effects in bi-crystals and reported that the interaction between propagating cracks and boundaries can enhance fracture toughness compared to single crystals.

The interaction between cracks and dislocations has also been investigated as a key mechanism controlling fracture behavior in crystalline materials. Early theoretical analyses by

Ohr (1987) demonstrated that dislocations in the vicinity of a crack tip can significantly modify the local stress field, leading to either crack shielding or amplification depending on the dislocation character and spatial arrangement. Direct atomistic evidence for these mechanisms was later provided by MD simulations of crack–dislocation interactions by Bitzek and Gumbsch (2008), who showed that dislocations approaching a crack tip may be absorbed, blocked, or transmitted, resulting in crack-tip blunting or localized stress concentration. These studies established that fracture at the atomic scale is governed by the competition between bond breaking and dislocation-mediated plastic relaxation, providing a fundamental framework for interpreting crack propagation in defected and irradiated microstructures.

In the context of the present work, attention is directed toward radiation-induced defects that accumulate during irradiation and strongly affect crack–defect interactions. By modeling defects such as voids, dislocation loops, and SFTs within the crack vicinity, this study aims to quantify their influence on crack propagation dynamics and associated energy dissipation mechanisms. These defects modify the local atomic configuration in distinct ways, thereby altering the crack's propagation path, deformation mode, and the balance between cleavage and plastic blunting.

2.5.3 Crystallographic orientation

Crystallographic orientation exerts a decisive influence on crack propagation behavior, deformation mechanisms, and overall fracture resistance in crystalline materials. At the atomic level, the alignment of the crack plane relative to the crystal lattice governs the available slip systems and, consequently, the competition between cleavage and plastic deformation. MD simulations have consistently shown that variations in crack orientation can lead to markedly different crack-tip responses, including dislocation emission, twinning, and cleavage along preferred crystallographic planes.

Singh et al. (2019) revealed that in single crystals of bcc niobium and hcp zirconium, fracture resistance is highly dependent on crack orientation, with dislocation nucleation or twinning emerging as dominant deformation mechanisms on specific planes. Gupta et al. (2020) further demonstrated that in fcc nickel, the orientation of the crack relative to the $\{111\}$ and $\langle 110 \rangle$ systems determines the activation of slip and the resulting ductility, while the presence of defects amplifies this anisotropic behavior. Similarly, Chang et al. (2020) studied crack propagation in single-crystal Cu and found that certain orientations promote dislocation emission and crack blunting, whereas others favor brittle cleavage. Orientation-dependent fracture behavior was also reported in nanocrystalline Ni by Xie et al. (2023), who showed that the dominant propagation mode, cleavage or plastic blunting, changes with grain orientation. Huang et al. (2023) confirmed that crack propagation velocity, energy absorption, and fracture morphology all vary with crystallographic orientation, particularly under dynamic loading conditions.

As illustrated in Fig. 2.13, the crystallographic alignment between the crack front and the lattice determines whether the fracture proceeds through direct atomic separation or through

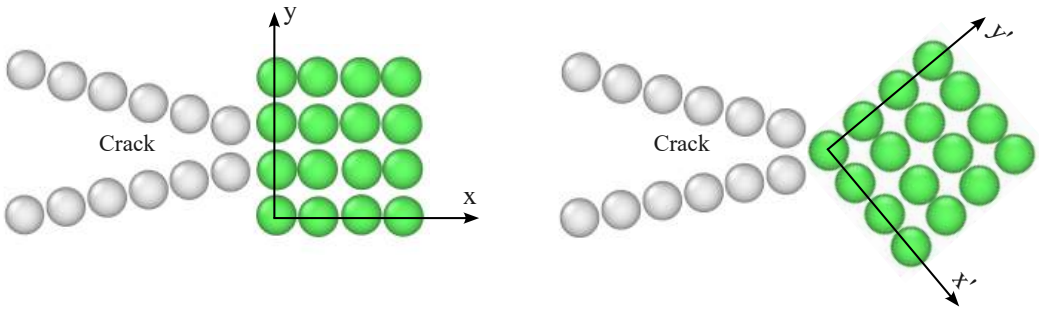

Figure 2.13: Schematic 2D representation of crack propagation relative to crystallographic orientation.

energy dissipation via dislocation processes. When the crack plane coincides with low-index lattice planes, bond breaking occurs along energetically favorable paths, resulting in cleavage (compare Fig. 2.13, left side). However, when the crack orientation is misaligned with these planes, additional shear components promote the nucleation and glide of dislocations, leading to blunting and enhanced toughness (compare Fig. 2.13, right side). This anisotropic behavior forms the physical basis for understanding orientation-dependent fracture responses in fcc metals.

2.5.4 Mechanisms of dislocation emission and crack-tip plasticity

Building on the principles of dislocation-mediated plasticity discussed in Section 2.4, this subsection focuses on the atomic-scale mechanisms governing plastic deformation near the crack tip. When a material containing a pre-existing crack is subjected to external loading, atomic bonds in the vicinity of the crack front become stretched and distorted, leading to localized rearrangements of atoms. These atomic-scale processes determine whether the crack advances through brittle cleavage or becomes stabilized by dislocation-mediated plasticity.

Plastic relaxation initiates when the applied driving force exceeds the nucleation barrier for defect formation. Partial dislocations are typically emitted from atomic ledges along the crack front and glide along the energetically favorable $\{111\}$ slip planes. This process accommodates shear deformation, redistributes strain energy, and promotes crack-tip blunting rather than direct cleavage. The balance between dislocation activity and crack propagation defines the fracture mode: frequent dislocation emission and motion correspond to ductile behavior, whereas their suppression results in brittle fracture.

The crystallographic orientation of the crack relative to active slip systems governs the emission geometry and subsequent plastic zone morphology. When the crack is aligned with one or more $\{111\}$ slip planes, partial dislocations are emitted symmetrically, producing stacking faults that extend away from the crack tip. With increasing deformation, additional dislocations nucleate, interact, and can transform into twin faults, further enhancing plastic accommodation and blunting of the crack front.

As illustrated in Fig. 2.14, the evolution of crack-tip plasticity follows a strain-dependent sequence. At low strain levels, partial dislocation emission produces isolated stacking faults that

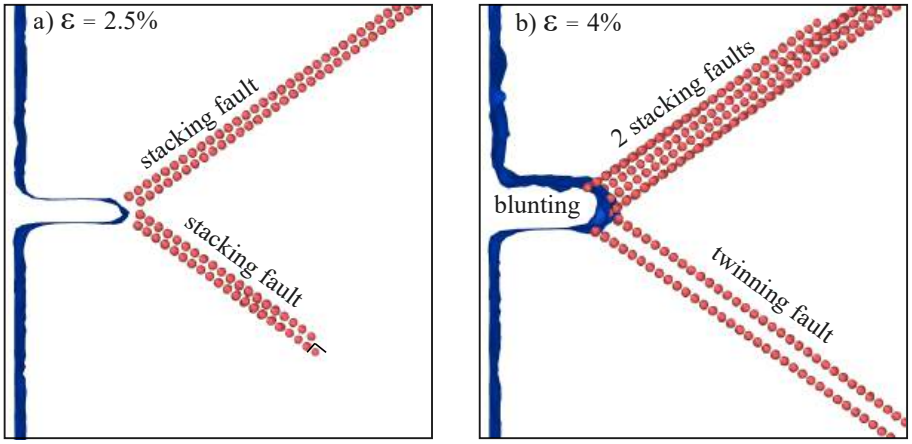

Figure 2.14: Atomistic visualization of crack-tip plasticity evolution in an fcc crystal under increasing strain. (a) At $\varepsilon = 2.5\%$, partial dislocation emission generates two symmetric stacking faults along $\{111\}$ planes. (b) At $\varepsilon = 4\%$, continued deformation leads to the formation of multiple stacking faults and a twinning fault, resulting in pronounced crack-tip blunting. The transition from isolated stacking faults to twin-assisted deformation reflects enhanced plastic energy dissipation at higher strain. Only hcp atoms are presented and colored red according to Common Neighbour Analysis (CNA) (Stukowski, 2010).

provide limited shear accommodation. As strain increases, additional dislocations are generated, leading to twin fault formation and more substantial lattice rearrangement near the crack tip. This twin-mediated plasticity intensifies crack blunting and delays unstable crack advance, thereby increasing the effective fracture toughness of the material.

The emitted dislocations subsequently interact through glide, pinning, and pile-up mechanisms, producing a discrete plastic zone surrounding the crack front. This region accommodates irreversible atomic rearrangements and serves as the primary source of plastic energy absorption. The extent of blunting and fault formation observed in these atomistic simulations directly correlates with the material's ductility and provides insight into the microscopic origins of fracture resistance in fcc alloys.

The present research employs atomistic simulations to investigate these phenomena in irradiated fcc systems. By explicitly modeling the interaction between advancing cracks and radiation-induced defects, this work aims to quantify how microstructural disorder alters dislocation activity, energy dissipation, and the overall fracture response. Such an atomistic perspective provides a mechanistic understanding of irradiation-assisted embrittlement and establishes a predictive framework for identifying the conditions leading to DBT in irradiated materials.

Chapter 3

Methodology

3.1 Molecular dynamics framework

Molecular Dynamics (MD) simulation provides a fundamental bridge between the microscopic world of atomic motion and the macroscopic behavior of materials. It represents a computational realization of classical mechanics, enabling the direct observation of how atoms evolve over time according to well-defined physical laws. As depicted schematically in Fig. 3.1, the MD framework follows a continuous theoretical chain that links several key components: the description of atomic motion through analytical mechanics, the representation of system states within phase space, the use of statistical ensembles for averaging, the ergodic principle for connecting time and ensemble averages, the numerical integration of equations of motion, and finally, the derivation of thermodynamic quantities and macroscopic observables from atomic trajectories.

In practice, the simulation process begins with the construction of an initial configuration, where each atom is assigned a position $\vec{r}_i(t_0)$ and velocity $\vec{v}_i(t_0)$ according to the chosen lattice structure or a pre-equilibrated configuration, with $i = 1, 2, \ldots, N$. Here, i denotes the atomic

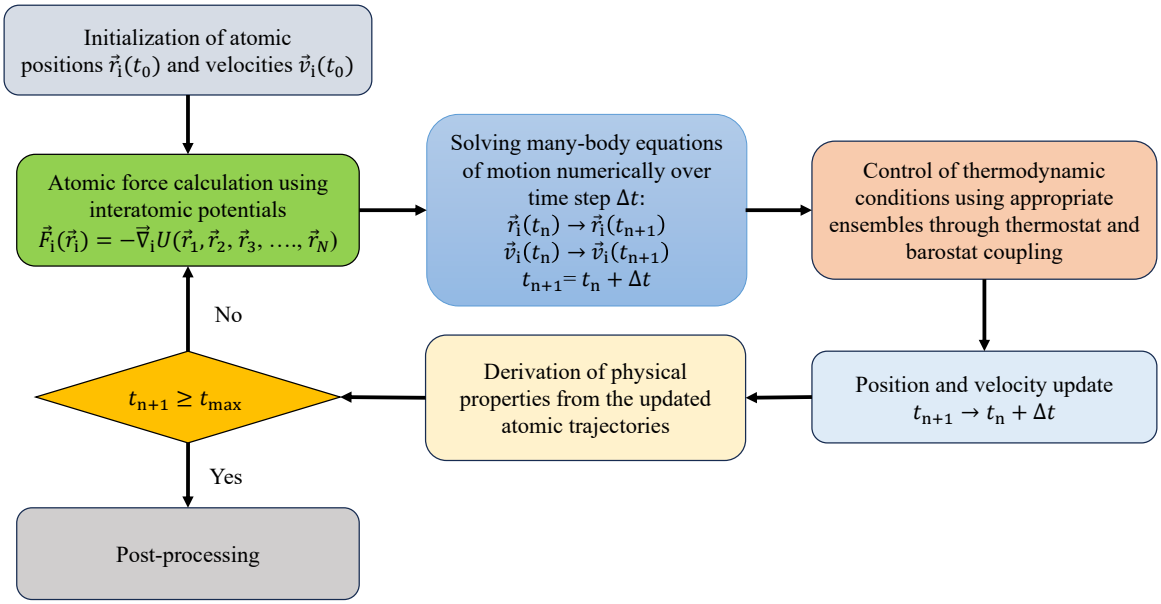

Figure 3.1: General flowchart illustrating the effective theoretical chain of MD simulation, connecting classical mechanics, statistical ensembles, ergodicity, and thermodynamic interpretation.

index, N is the total number of atoms in the simulation, and t_0 represents the initial time.

The interatomic forces $\vec{F}_\mathrm{i}$ acting on each atom are computed from the total potential energy $U(\vec{r}_1, \vec{r}_2, \ldots, \vec{r}_\mathrm{N})$ of the system and are then used to integrate Newton's equations of motion over discrete time steps Δt, updating atomic positions and velocities throughout the simulation.

Statistical ensembles are used to model systems under specific thermodynamic constraints, enabling the study of microscopic behavior and the prediction of macroscopic properties by controlling variables such as the number of particles, volume, temperature, and energy. This iterative process (Fig. 3.1) continues until the total simulation time t_max is reached, producing atomic trajectories that form the basis for post-processing. The resulting trajectories provide the basis for computing a wide range of structural, thermodynamic, and mechanical properties.

MD simulations provide atomistic insight into the mechanisms governing material behavior under controlled thermodynamic and mechanical conditions. Its key strength lies in the ability to capture fast, localized phenomena, such as atomic rearrangements, defect nucleation, dislocation motion, and crack propagation, with spatial and temporal resolutions far beyond those achievable by continuum models. This capability makes MD an indispensable method for investigating defect dynamics, radiation-induced damage, and fracture processes in crystalline materials.

Following the general overview presented in Fig. 3.1, each stage of the MD process can be understood through its underlying physical and mathematical principles. The subsequent sections 3.2 and 3.3 systematically elaborates on these principles, starting from classical mechanics and phase-space conservation, and extending through statistical mechanics, ergodic sampling, numerical integration, and the thermodynamic interpretation of simulation results.

3.2 Statistical mechanics in molecular dynamics

At the most fundamental level, MD simulations are governed by the principles of *classical mechanics*, which describe the time evolution of atoms under the influence of interatomic forces (Tuckerman, 2023). For a system consisting of N atoms, each atom i is characterized at any time t by three fundamental quantities: its position vector $\vec{r}_\mathrm{i}(t)$, the velocity vector $\dot{\vec{r}}_\mathrm{i}(t)$, and the acceleration vector $\ddot{\vec{r}}_\mathrm{i}(t)$. Here, the overdot notation denotes differentiation with respect to time.

The motion of each atom in MD simulations is governed by Newton's second law:

$$m_\mathrm{i}\ddot{\vec{r}}_\mathrm{i} = \vec{F}_\mathrm{i}, \tag{3.1}$$

where m_i represents the atomic mass of the ith atom. The interatomic force $\vec{F}_\mathrm{i}$ is derived from the potential energy function $U(\vec{r}_1, \vec{r}_2, \ldots, \vec{r}_\mathrm{N})$, which depends on the instantaneous positions of all N atoms.

The force on atom i is obtained as the negative spatial gradient (i.e., derivative with respect

to $\vec{r}_\mathrm{i}$) of this potential energy:

$$\vec{F}_\mathrm{i} = -\nabla_\mathrm{i} U(\vec{r}_1, \vec{r}_2, \ldots, \vec{r}_\mathrm{N}), \tag{3.2}$$

The potential energy U typically incorporates all relevant interatomic interactions, including pairwise, three-body, or many-body terms, depending on the chosen potential model.

Alternatively, the dynamics of atoms can be expressed through the *Hamiltonian formalism*, which reformulates the equations of motion in terms of generalized coordinates and their conjugate momenta. The canonical momentum of each atom i is defined as

$$\vec{p}_\mathrm{i} = m_\mathrm{i} \dot{\vec{r}}_\mathrm{i}, \tag{3.3}$$

and the total energy (Hamiltonian) of the system is given by

$$H(\vec{r}^\mathrm{N}, \vec{p}^\mathrm{N}) = K + U = \sum_{\mathrm{i}=1}^{\mathrm{N}} \frac{\vec{p}_\mathrm{i}^{\,2}}{2m_\mathrm{i}} + U(\vec{r}_1, \vec{r}_2, \ldots, \vec{r}_\mathrm{N}), \tag{3.4}$$

where we shall usually abbreviate this as $\vec{r}^\mathrm{N} = (\vec{r}_1, \vec{r}_2, \ldots, \vec{r}_\mathrm{N})$ and $\vec{p}^\mathrm{N} = (\vec{p}_1, \vec{p}_2, \ldots, \vec{p}_\mathrm{N})$, which collectively denote the full set of atomic positions and conjugate momenta. Within the framework of classical mechanics, particles are distinguishable and may therefore be individually labeled, allowing each coordinate and momentum to be uniquely associated with a specific atom (Andersen and Chandler, 1970). The Hamiltonian H thus represents the total mechanical energy of the system expressed in phase-space coordinates.

The time evolution of the system follows from Hamilton's canonical relations, obtained by taking partial derivatives of the Hamiltonian with respect to coordinates and momenta:

$$\dot{\vec{r}}_\mathrm{i} = \frac{\partial H}{\partial \vec{p}_\mathrm{i}}, \tag{3.5a}$$

$$\dot{\vec{p}}_\mathrm{i} = -\frac{\partial H}{\partial \vec{r}_\mathrm{i}}. \tag{3.5b}$$

These equations ensure that, in the absence of external coupling, the total energy H remains constant over time (Tuckerman and Martyna, 2000).

Although the Newtonian and Hamiltonian formulations are mathematically equivalent for closed classical systems, they play conceptually distinct roles in MD simulations. The Newtonian formulation is primarily employed as a computational tool, providing explicit equations of motion that are numerically integrated to generate atomic trajectories in real space. The Hamiltonian formulation provides a phase-space description of the system that forms the basis for the statistical-mechanical interpretation of MD simulations. In this framework, the Hamiltonian defines the conserved quantities of the system, such as the total energy. It uniquely specifies

Table 3.2: Comparison of Newtonian and Hamiltonian formulations and their respective roles in MD simulations.

Aspect	**Newtonian formulation**	**Hamiltonian formulation**
Description	Atomic trajectories in real space	System evolution in phase space (positions and momenta)
Primary role in MD	Computational framework for integrating equations of motion	Theoretical framework for statistical mechanics, energy conservation, and ensemble definition
Configuration space	Real space (particle positions)	Phase space (positions and conjugate momenta)
Implementation in MD codes	Explicitly integrated via force-based time-stepping algorithms	Reflected implicitly through symplectic integrators and statistical interpretation

the statistical ensemble sampled by the dynamics, while also providing the theoretical basis for symplectic integration schemes that preserve the geometric structure of phase-space flow and ensure stable long-time behavior. A concise comparison of the roles of the Newtonian and Hamiltonian formalisms in MD is provided in Table 3.2.

Numerical Integration of Equations of Motion

As summarized in Table 3.2, the Newtonian formulation provides the computational basis for MD simulations through the explicit integration of the equations of motion. To compute atomic trajectories, the continuous equations of motion (Eq 3.1) are integrated numerically in discrete time steps Δt. Since analytical solutions are generally impossible for interacting many-body systems, numerical integration algorithms are employed to advance atomic positions and velocities in time while maintaining accuracy, stability, and energy conservation. Among these, the *velocity–Verlet* and *leap-frog* schemes are the most widely used in MD (Frenkel and Smit, 2023).

The velocity–Verlet algorithm is particularly favored for its simplicity, time reversibility, and symplectic nature. It updates atomic positions and velocities according to

$$\vec{r}_{\mathrm{i}}(t+\Delta t) = \vec{r}_{\mathrm{i}}(t) + \vec{v}_{\mathrm{i}}(t)\Delta t + \tfrac{1}{2}\vec{a}_{\mathrm{i}}(t)\Delta t^2, \tag{3.6}$$

$$\vec{v}_{\mathrm{i}}(t+\Delta t) = \vec{v}_{\mathrm{i}}(t) + \tfrac{1}{2}\left[\vec{a}_{\mathrm{i}}(t) + \vec{a}_{\mathrm{i}}(t+\Delta t)\right]\Delta t, \tag{3.7}$$

where $\vec{a}_{\mathrm{i}}(t) = \vec{F}_{\mathrm{i}}(t)/m_{\mathrm{i}}$ is the instantaneous acceleration of atom i. This method preserves the total energy of the system to within small numerical fluctuations, ensuring physically meaningful trajectories over long simulation times.

Several numerical schemes can be written in forms equivalent to the Verlet integrator. One of the most straightforward is the *leap-frog* method, which updates velocities at half-time increments and then uses these staggered velocities to advance the atomic positions. In this formulation, the

dynamical variables evolve according to

$$\vec{v}_{\mathrm{i}}\left(t+\tfrac{1}{2}\Delta t\right)=\vec{v}_{\mathrm{i}}\left(t-\tfrac{1}{2}\Delta t\right)+\vec{a}_{\mathrm{i}}(t)\,\Delta t, \tag{3.8}$$

$$\vec{r}_{\mathrm{i}}(t+\Delta t)=\vec{r}_{\mathrm{i}}(t)+\vec{v}_{\mathrm{i}}\left(t+\tfrac{1}{2}\Delta t\right)\,\Delta t, \tag{3.9}$$

where the acceleration $\vec{a}_{\mathrm{i}}(t)$ is evaluated from the forces at the current configuration. When velocities at integer times are required (for example, for thermostatting or output), they are obtained by the midpoint average

$$\vec{v}_{\mathrm{i}}(t)=\frac{1}{2}\left[\vec{v}_{\mathrm{i}}\left(t+\tfrac{1}{2}\Delta t\right)+\vec{v}_{\mathrm{i}}\left(t-\tfrac{1}{2}\Delta t\right)\right] \tag{3.10}$$

Although the leap-frog and velocity–Verlet schemes differ in how they store and update velocities, they are formally equivalent, both providing second-order accuracy and symplectic time evolution. Both approaches maintain time reversibility and symplectic integration, which are essential for conserving total energy and momentum in long MD trajectories.

It is essential to note that the velocity–Verlet and leap–frog schemes are general numerical integration methods, and therefore, they apply to all statistical ensembles.

Phase-Space Representation

Following the conceptual distinction between the Newtonian and Hamiltonian formulations (Table 3.2), although atomic trajectories in MD simulations are generated by direct integration of Newton's equations of motion, their interpretation within a statistical-mechanical context relies on the Hamiltonian phase-space description. In particular, it introduces the concept of *phase space*, which forms the foundation for relating microscopic dynamics to macroscopic thermodynamic observables.

Phase space provides a complete representation of all possible states of the system and enables ensemble averaging over these states, which is essential for the derivation of thermodynamic quantities (Haile, 1992; Frenkel and Smit, 2023). For a system of N atoms in a d-dimensional space, the corresponding phase space is a $2dN$-dimensional manifold that comprises the generalized coordinates and conjugate momenta of all atoms. Each point in this space uniquely specifies the instantaneous microscopic state of the system and is represented by

$$\Gamma=(\vec{r}^{\,\mathrm{N}},\vec{p}^{\,\mathrm{N}},\{\chi\}), \tag{3.11}$$

where $\{\chi\}$ represents a generalized parameter (or set of parameters) associated with the external environment of the system. The variable $\{\chi\}$ accounts for additional degrees of freedom that may be introduced to control thermodynamic conditions, and its form depends on the statistical ensemble selected for the simulation. For instance, it may correspond to parameters that regulate temperature or pressure, thereby extending the phase-space dimensionality.

Liouville Equation and Probability Density

To describe the statistical behavior of a system within this extended phase space, it is convenient to define a *probability density function* $\rho(\Gamma,t)$. This function represents the probability of finding the system in a particular microscopic state $\Gamma = (\vec{r}^{\,\mathrm{N}}, \vec{p}^{\,\mathrm{N}}, \{\chi\})$ at time t. For an ensemble of identical systems, $\rho(\Gamma,t)\,d\Gamma$ gives the fraction of systems whose states lie within an infinitesimal volume element $d\Gamma$ around Γ at that instant. The normalization condition ensures that the system must exist somewhere in the accessible region of phase space:

$$\int \rho(\Gamma,t)\,d\Gamma = 1. \tag{3.12}$$

The time evolution of this probability density is governed by the *Liouville equation*, which expresses the conservation of probability in phase space:

$$\frac{\partial \rho}{\partial t} + (\nabla_\Gamma \rho)\cdot\dot{\Gamma} + \rho\,\kappa(\Gamma,t) = 0. \tag{3.13}$$

In this relation, ∇_Γ denotes the gradient operator in phase space, $\dot{\Gamma}$ is the phase-space velocity vector that represents the time derivatives of all dynamical variables, and $\kappa(\Gamma,t)$ is the *phase-space compressibility*, defined as

$$\kappa(\Gamma,t) = \nabla_\Gamma \cdot \dot{\Gamma}. \tag{3.14}$$

The first term in Eq. (3.13) describes the explicit time dependence of the probability density, the second term accounts for the convection or transport of probability through phase space due to the motion of the representative phase-space point along trajectories generated by the equations of motion, and the third term quantifies any local expansion or contraction of the phase-space volume. These terms ensure that the total probability within phase space is conserved over time, providing the fundamental statistical foundation for MD simulations and ensemble averaging (Tuckerman and Martyna, 2000).

Ergodicity and Ensemble Averaging

The Liouville equation provides a geometric framework for describing the evolution of probability density in phase space. However, to extract physically meaningful macroscopic quantities from MD simulations, this geometric conservation must be connected to a statistical interpretation. This connection is established through the concept of *ergodicity*, which bridges the microscopic dynamics of particles with macroscopic thermodynamic observables, as illustrated in Fig. 3.2.

The *ergodic hypothesis* provides the conceptual bridge between deterministic mechanics and statistical thermodynamics (Frenkel and Smit, 2023; Tuckerman, 2023). It postulates that, over a sufficiently long time, a system evolving under deterministic dynamics will explore all accessible microstates consistent with its total energy and constraints. Consequently, the

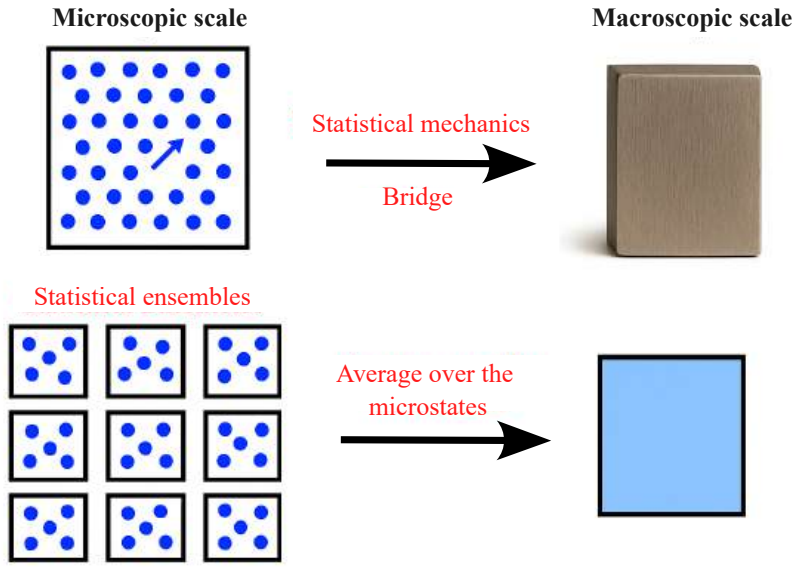

Figure 3.2: Schematic representation of the statistical mechanics concept linking microscopic and macroscopic descriptions. The microscopic scale (top left) consists of individual atomic configurations, while the macroscopic scale (right) represents the averaged behavior of the system. At the bottom, a set of statistical ensembles illustrates how different microstates are averaged to yield the corresponding macroscopic observable. This averaging process, governed by statistical mechanics, serves as the bridge between atomic motion and thermodynamic properties.

ensemble average of any observable $A(\Gamma)$, obtained by averaging over all possible microstates weighted by the probability distribution $\rho(\Gamma)$, can be replaced by the time average of the same observable computed along a single MD trajectory:

$$\langle A \rangle_\rho = \frac{\int_\Gamma A(\Gamma)\,\rho(\Gamma)\,d\Gamma}{\int_\Gamma \rho(\Gamma)\,d\Gamma} \iff \bar{A} = \lim_{t_{\max}\to\infty} \frac{1}{t_{\max}} \int_0^{t_{\max}} A(\Gamma_t)\,dt. \tag{3.15}$$

In Eq. (3.15), Γ_t denotes the time-evolved phase-space point of the system. The numerator represents the weighted average of the observable $A(\Gamma)$ over all accessible microstates, while the denominator ensures proper normalization of the probability density $\rho(\Gamma)$. The right-hand expression defines the time average $\bar{A}$, obtained by integrating the instantaneous value of the observable along a trajectory of duration $t_{\max}$. Under the assumption of ergodicity, these two averages become equivalent in the limit of sufficiently long simulation time, allowing macroscopic thermodynamic observables to be evaluated directly from atomistic trajectories. Thus, while the Liouville equation ensures the conservation of probability in phase space, the ergodic principle provides the statistical foundation that enables MD simulations to reproduce equilibrium thermodynamic behavior.

3.3 Simulation ensembles

The concepts of phase space, probability density, and ergodicity provide the theoretical foundation for connecting atomic motion to macroscopic observables. In practical MD simulations, this connection is realized through the use of *statistical ensembles*, each representing a specific set of thermodynamic constraints imposed on the system. An ensemble specifies whether the system exchanges energy with an external heat reservoir and whether the system volume is fixed or allowed to fluctuate, while the number of particles is typically maintained constant. These constraints determine the form of the phase-space probability distribution $\rho(\Gamma)$. In general, three fundamental ensembles are commonly employed in MD simulations. Each ensemble imposes different constraints on the phase-space variables and requires specific algorithms to reproduce the correct thermodynamic behavior. The following subsections describe the physical assumptions, governing equations, and probability distributions associated with these three ensembles (Frenkel, 1931; Tuckerman and Martyna, 2000).

Microcanonical ensemble (NVE)

The microcanonical ensemble, denoted as NVE, describes an *isolated system* in which the number of particles (N), volume (V), and total energy (E) remain constant (Rapaport, 2004; Frenkel and Smit, 2023). No exchange of energy or matter with the surroundings is permitted, and the system evolves under deterministic Newtonian dynamics. From a theoretical perspective, the same dynamics can be formulated within the Hamiltonian framework, in which momenta are introduced as conjugate variables, and the equations of motion are obtained from derivatives of the Hamiltonian. In MD simulations, the NVE ensemble represents the most fundamental formulation, in which the total energy of the system is conserved throughout the time evolution, as illustrated schematically in Fig. 3.3.

In this isolated system, the state of all atoms is fully defined by the position and momentum

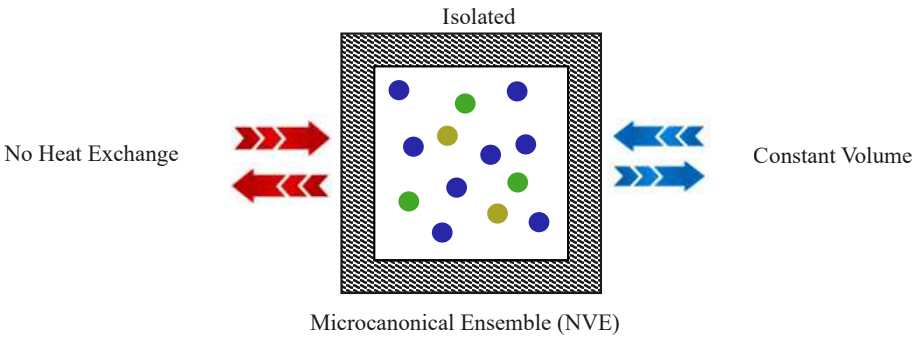

Figure 3.3: Microcanonical ensemble (NVE): isolated system with no heat exchange and constant volume; total energy (Hamiltonian) is conserved via Eq. (3.17).

coordinates in phase space:

$$\Gamma_{\mathrm{NVE}} = (\vec{r}^{\mathrm{N}}, \vec{p}^{\mathrm{N}}), \tag{3.16}$$

which corresponds to the generalized phase-space vector Γ introduced in Eq. (3.11) with the extended variables set to $\{\chi\} = 0$, reflecting the absence of external control parameters such as thermostats or barostats.

The system evolves according to the canonical equations of motion, derived from the Hamiltonian $H(\vec{r}^{\mathrm{N}}, \vec{p}^{\mathrm{N}})$ in Eq. (3.4) and explicitly written in Eq. (3.5), and these are equivalent to Newton's equations of motion for each atom (Eq. (3.1)). Under these relations, the time derivative of the Hamiltonian (Eq. (3.4)) can be expressed as

$$\frac{dH}{dt} = \sum_{\mathrm{i}=1}^{\mathrm{N}} \left(\frac{\partial H}{\partial \vec{r}_{\mathrm{i}}} \cdot \dot{\vec{r}}_{\mathrm{i}} + \frac{\partial H}{\partial \vec{p}_{\mathrm{i}}} \cdot \dot{\vec{p}}_{\mathrm{i}} \right) = \sum_{\mathrm{i}=1}^{\mathrm{N}} \left(\frac{\partial H}{\partial \vec{r}_{\mathrm{i}}} \frac{\partial H}{\partial \vec{p}_{\mathrm{i}}} - \frac{\partial H}{\partial \vec{p}_{\mathrm{i}}} \frac{\partial H}{\partial \vec{r}_{\mathrm{i}}} \right) = 0, \tag{3.17}$$

which confirms that the total energy (Hamiltonian) is conserved during the time evolution of an isolated system. This conservation property is a direct consequence of the Hamiltonian equations of motion and represents the defining characteristic of the NVE ensemble.

In the absence of any external coupling, the phase-space volume occupied by the system is also conserved. For an isolated NVE system, the Liouville equation (Eq. (3.13)) reduces to its expanded form:

$$\frac{\partial \rho}{\partial t} + \sum_{\mathrm{i}=1}^{\mathrm{N}} \left(\frac{\partial \rho}{\partial \vec{r}_{\mathrm{i}}} \cdot \dot{\vec{r}}_{\mathrm{i}} + \frac{\partial \rho}{\partial \vec{p}_{\mathrm{i}}} \cdot \dot{\vec{p}}_{\mathrm{i}} \right) = 0, \tag{3.18}$$

which expresses the conservation of the probability density $\rho(\Gamma, t)$ in an incompressible phase-space flow. Here, the first term represents the explicit time dependence of the probability density, while the summation term describes the convection of probability in the phase-space coordinates $(\vec{r}_{\mathrm{i}}, \vec{p}_{\mathrm{i}})$. Because $\nabla_{\Gamma} \cdot \dot{\Gamma}_{\mathrm{NVE}} = 0$ for Hamiltonian motion, the total probability within any region of phase space remains constant, ensuring that the system's evolution preserves both energy and volume in phase space.

The probability density for the microcanonical ensemble can therefore be written as

$$\rho(\Gamma_{\mathrm{NVE}}, t) \propto \delta\left(H(\vec{r}^{\mathrm{N}}, \vec{p}^{\mathrm{N}}) - E\right). \tag{3.19}$$

This distribution implies that only microstates consistent with the total energy contribute to the ensemble average. Accordingly, the ensemble average of any observable $A(\Gamma)$ in the NVE ensemble is given by

$$\langle A \rangle_{\mathrm{NVE}} = \frac{C_{\mathrm{N}}}{h^{3\mathrm{N}}\, \Omega(N, V, E)} \int d^{\mathrm{dN}}p \int_{D(V)} d^{\mathrm{dN}}r\, A(\vec{p}^{\mathrm{N}}, \vec{r}^{\mathrm{N}})\, \delta\left(H(\vec{p}^{\mathrm{N}}, \vec{r}^{\mathrm{N}}) - E\right), \tag{3.20}$$

where C_{N} is a normalization constant, h is Planck's constant (used for proper dimensionality),

$\Omega(N,V,E)$ is the density of accessible microstates, and $D(V)$ represents the configuration-space domain of volume V.

In this framework, the ergodic hypothesis ensures that the time average of a physical observable along a single MD trajectory is equivalent to its ensemble average (See Eq (3.15)). Thus, in the NVE ensemble, both the total energy and the phase-space volume are conserved, and the system samples all microstates consistent with its energy, providing the foundation for the equilibrium properties of isolated systems. When the system is no longer isolated but allowed to exchange energy with a thermal reservoir, the NVE ensemble generalizes into the canonical (NVT) ensemble.

Canonical ensemble (NVT)

The canonical ensemble, denoted as NVT, represents a system in thermal equilibrium with a heat reservoir at constant temperature T and fixed volume V. In contrast to the isolated microcanonical (NVE) case, the NVT ensemble allows for energy exchange with the external environment while maintaining a constant number of atoms (N) and volume (Nosé, 1984; Hoover, 1985). This condition is typically realized in MD simulations through the introduction of a *thermostat*, which dynamically adjusts the system's kinetic energy to achieve the desired temperature, as illustrated in Fig. 3.4.

In this ensemble, the extended phase-space vector is defined as

$$\Gamma_{\mathrm{NVT}} = (\vec{r}^{\mathrm{N}}, \vec{p}^{\mathrm{N}}, \zeta), \tag{3.21}$$

where ζ is an additional dynamical variable associated with the thermostat and represents the friction coefficient controlling the rate of heat exchange between the system and the thermal reservoir. Unlike the NVE ensemble, the inclusion of ζ introduces a *non-Hamiltonian* term into the equations of motion, allowing the system's total energy to fluctuate around a mean value consistent with the imposed temperature.

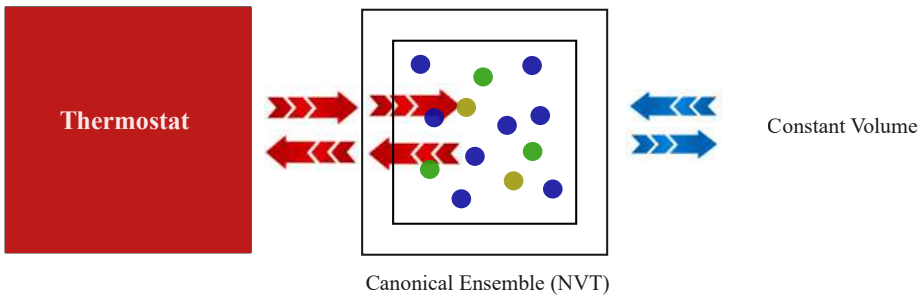

Figure 3.4: Canonical ensemble (NVT): system at constant volume coupled to a thermostat to maintain constant temperature, governed by the Nosé–Hoover equations (3.22).

The most widely used approach to realize this coupling in MD simulations is the Nosé–Hoover thermostat (Hoover, 1985), which ensures that the system samples configurations from the canonical distribution. The corresponding equations of motion are given by:

$$\dot{\vec{r}}_{\mathrm{i}} = \frac{\vec{p}_{\mathrm{i}}}{m_{\mathrm{i}}}, \tag{3.22a}$$

$$\dot{\vec{p}}_{\mathrm{i}} = \vec{F}_{\mathrm{i}} - \zeta\, \vec{p}_{\mathrm{i}}, \tag{3.22b}$$

$$\dot{\zeta} = \frac{1}{Q}\left(\sum_{\mathrm{i}=1}^{\mathrm{N}} \frac{\vec{p}_{\mathrm{i}}^{\,2}}{m_{\mathrm{i}}} - g k_{\mathrm{B}} T\right), \tag{3.22c}$$

where Q is a fictitious mass parameter that determines the coupling strength between the system and the thermostat, g denotes the number of degrees of freedom (typically $g = 3N$), and k_{B} is the Boltzmann constant. The first equation describes the atomic displacements, the second governs the momenta while incorporating a damping term proportional to ζ, and the third defines the evolution of the thermostat variable to maintain the target temperature. The presence of ζ introduces a controlled energy exchange mechanism that maintains thermal equilibrium, making this formulation inherently non-Hamiltonian.

The non-Hamiltonian nature of the Nosé–Hoover equations leads to a phase-space flow that is no longer incompressible. Consequently, the Liouville equation for the NVT ensemble includes an additional term associated with phase-space compressibility $\kappa(\Gamma_{\mathrm{NVT}}, t)$:

$$\frac{\partial \rho}{\partial t} + \sum_{\mathrm{i}=1}^{\mathrm{N}} \left(\frac{\partial \rho}{\partial \vec{r}_{\mathrm{i}}} \cdot \dot{\vec{r}}_{\mathrm{i}} + \frac{\partial \rho}{\partial \vec{p}_{\mathrm{i}}} \cdot \dot{\vec{p}}_{\mathrm{i}} \right) + \frac{\partial \rho}{\partial \zeta}\, \dot{\zeta} + \rho\, \kappa(\Gamma_{\mathrm{NVT}}, t) = 0, \tag{3.23}$$

where the compressibility term is given by

$$\kappa(\Gamma_{\mathrm{NVT}}, t) = \nabla_{\Gamma} \cdot \dot{\Gamma}_{\mathrm{NVT}} = -\zeta\, g. \tag{3.24}$$

This term reflects the contraction or expansion of the phase-space volume induced by the thermostat variable ζ, ensuring that the correct canonical distribution is sampled even though total energy is not conserved.

At equilibrium, the stationary probability density function for the canonical ensemble is expressed as

$$\rho(\Gamma_{\mathrm{NVT}}, t) \propto \exp\left[-\beta\, H(\vec{r}^{\,\mathrm{N}}, \vec{p}^{\,\mathrm{N}})\right], \tag{3.25}$$

where $\beta = 1/(k_{\mathrm{B}} T)$, and $H(\vec{r}^{\,\mathrm{N}}, \vec{p}^{\,\mathrm{N}})$ is the instantaneous Hamiltonian of the system. This exponential dependence ensures that states with higher energy are exponentially less probable, leading to thermal equilibrium consistent with Boltzmann statistics.

The ensemble average of any observable $A(\Gamma)$ in the canonical ensemble is given by the

integral over all accessible phase-space configurations weighted by the Boltzmann factor:

$$\langle A \rangle_{\mathrm{NVT}} = \frac{1}{Z(N,V,T)} \int d^{\mathrm{dN}}p \int_{D(V)} d^{\mathrm{dN}}r \, A(\vec{p}^{\,\mathrm{N}}, \vec{r}^{\,\mathrm{N}}) \exp[-\beta H(\vec{p}^{\,\mathrm{N}}, \vec{r}^{\,\mathrm{N}})], \tag{3.26}$$

where $Z(N,V,T)$ is the canonical partition function that serves as the normalization constant ensuring proper probability weighting.

Under the ergodic hypothesis, the time average of a physical observable along a sufficiently long Nosé–Hoover trajectory becomes equivalent to its ensemble average. This equivalence provides the foundation for extracting equilibrium thermodynamic observables from atomistic trajectories in NVT simulations.

Stochastic thermostats, such as the Langevin and Andersen methods, provide alternative mechanisms for sampling the canonical ensemble by introducing random forces or periodically rescaling velocities to maintain a constant temperature. In particular, the Langevin thermostat modifies the Newtonian equations of motion by adding both a damping term and a stochastic force:

$$m_{\mathrm{i}} \dot{\vec{v}}_{\mathrm{i}} = \vec{F}_{\mathrm{i}} - \gamma m_{\mathrm{i}} \vec{v}_{\mathrm{i}} + \vec{R}_{\mathrm{i}}(t), \tag{3.27}$$

where γ is a friction coefficient and $\vec{R}_{\mathrm{i}}(t)$ is a Gaussian random force that satisfies the fluctuation–dissipation theory. Unlike Nosé–Hoover, stochastic thermostats such as Langevin do not require an explicit additiequationsonal thermostat variable, and the system's energy fluctuates around the target temperature while ensuring proper canonical sampling.

Isothermal–isobaric ensemble (NPT)

The isothermal–isobaric ensemble, denoted as NPT, describes a system at constant number of particles (N), pressure (P), and temperature (T). In this ensemble, the system is allowed to exchange both energy and volume with an external reservoir, making it the most representative model for experimental conditions (Parrinello and Rahman, 1980, 1981). The NPT ensemble is typically realized in MD simulations by coupling the system simultaneously to a *thermostat* and a *barostat*, which maintain the desired temperature and pressure, respectively, as illustrated in Fig. 3.5.

The extended phase-space vector for the NPT ensemble is expressed as

$$\Gamma_{\mathrm{NPT}} = (\vec{r}^{\,\mathrm{N}}, \vec{p}^{\,\mathrm{N}}, \zeta, \eta), \tag{3.28}$$

where ζ and η are the thermostat and barostat variables, respectively. The variable ζ controls the rate of heat exchange with the thermal reservoir, ensuring constant temperature, while η regulates the isotropic scaling of the simulation box to maintain the external pressure P_0. As in the NVT ensemble, the introduction of ζ and η makes the dynamics *non-Hamiltonian*, since

energy is no longer conserved due to continuous coupling with the reservoirs.

The extended Nosé–Hoover equations of motion governing this ensemble are written as:

$$\dot{\vec{r}}_{\mathrm{i}} = \frac{\vec{p}_{\mathrm{i}}}{m_{\mathrm{i}}} + \eta\,\vec{r}_{\mathrm{i}}, \tag{3.29a}$$

$$\dot{\vec{p}}_{\mathrm{i}} = \vec{F}_{\mathrm{i}} - (\zeta + \eta)\,\vec{p}_{\mathrm{i}}, \tag{3.29b}$$

$$\dot{\eta} = \frac{1}{W}\left(P_{\mathrm{int}} - P_0\right), \tag{3.29c}$$

$$\dot{\zeta} = \frac{1}{Q}\left(\sum_{\mathrm{i}=1}^{\mathrm{N}} \frac{\vec{p}_{\mathrm{i}}^{\,2}}{m_{\mathrm{i}}} - g k_{\mathrm{B}} T\right), \tag{3.29d}$$

where Q and W are the fictitious masses associated with the thermostat and barostat, respectively, g is the number of degrees of freedom, k_{B} is Boltzmann's constant, and P_{int} is the instantaneous internal pressure. The inclusion of η allows the system volume V to fluctuate dynamically, enabling the simulation cell to expand or contract in response to the difference between P_{int} and P_0.

Because the NPT dynamics are non-Hamiltonian, the Liouville equation must be modified to include the full divergence of the extended phase-space flow. For the NPT ensemble, this takes the general form:

$$\frac{\partial \rho}{\partial t} + \sum_{\mathrm{i}=1}^{\mathrm{N}} \left(\frac{\partial \rho}{\partial \vec{r}_{\mathrm{i}}} \cdot \dot{\vec{r}}_{\mathrm{i}} + \frac{\partial \rho}{\partial \vec{p}_{\mathrm{i}}} \cdot \dot{\vec{p}}_{\mathrm{i}} \right) + \frac{\partial \rho}{\partial \zeta}\dot{\zeta} + \frac{\partial \rho}{\partial \eta}\dot{\eta} + \rho\,\kappa(\Gamma_{\mathrm{NPT}}, t) = 0, \tag{3.30}$$

where the phase-space compressibility $\kappa(\Gamma_{\mathrm{NPT}}, t)$ is given by

$$\kappa(\Gamma_{\mathrm{NPT}}, t) = \nabla_{\Gamma} \cdot \dot{\Gamma}_{\mathrm{NPT}} = -(3N+1)\eta - \zeta. \tag{3.31}$$

This term accounts for the non-zero divergence of the phase-space flow arising from volume and temperature fluctuations. Unlike in the NVE ensemble, where $\kappa = 0$, the presence of ζ and η

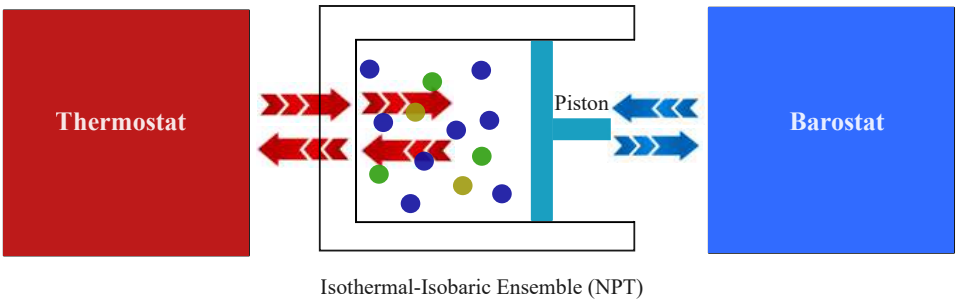

Figure 3.5: Isothermal–isobaric ensemble (NPT): system coupled to both thermostat and barostat to maintain constant temperature and pressure, governed by the extended Nosé–Hoover equations (3.29).

induces a compressible phase-space flow necessary for sampling the correct isothermal–isobaric distribution.

At equilibrium, the stationary phase-space probability density for the NPT ensemble is given by

$$\rho(\Gamma_{\mathrm{NPT}}, t) \propto V^{\alpha} \exp\left[-\beta\left(H(\vec{r}^{\mathrm{N}}, \vec{p}^{\mathrm{N}}) + P_0 V\right)\right], \tag{3.32}$$

where α is a constant dependent on the ensemble formulation (typically $\alpha = 1$ for isotropic volume scaling). This distribution shows that the probability of a given microstate decreases exponentially with increasing total enthalpy $H(\vec{r}^{\mathrm{N}}, \vec{p}^{\mathrm{N}}) + P_0 V$, consistent with the Boltzmann factor for the NPT ensemble.

The ensemble average of an observable $A(\Gamma)$ is then computed as

$$\langle A \rangle_{\mathrm{NPT}} = \frac{1}{\Delta(N,P,T)} \int dV \int d^{\mathrm{dN}}p \int_{D(V)} d^{\mathrm{dN}}r\, A(\vec{p}^{\mathrm{N}}, \vec{r}^{\mathrm{N}}, V) \exp[-\beta(H(\vec{p}^{\mathrm{N}}, \vec{r}^{\mathrm{N}}) + P_0 V)], \tag{3.33}$$

where $\Delta(N,P,T)$ is the isothermal–isobaric partition function ensuring normalization. The integration extends over all positions, momenta, and accessible volumes, reflecting the simultaneous sampling of thermal and volumetric fluctuations.

As in the previous ensembles, ergodicity is invoked through Eq. (3.15), ensuring that long-time trajectory averages reproduce isothermal-isobaric ensemble averages. This ergodic equivalence allows the evaluation of thermodynamic observables directly from MD trajectories, providing a complete statistical description of materials under experimental conditions of constant temperature and pressure. Several barostat algorithms have been developed in MD to realize this ensemble in practice, differing in their underlying dynamical formulations and statistical properties, but all designed to reproduce the correct isothermal–isobaric phase-space distribution.

3.4 Virial stress and thermodynamic quantities in molecular dynamics

In MD simulations, macroscopic mechanical and thermodynamic quantities emerge from the microscopic motion and interactions of atoms. These quantities, such as stress, pressure, temperature, and total energy, are emergent properties that arise from the microscopic dynamics and are obtained through appropriate temporal or ensemble averaging of atomic trajectories. This section describes how these observables are obtained and clarifies the physical interpretation of the underlying expressions.

Virial Stress

At the atomic scale, stress is evaluated using the *virial formulation*, which bridges microscopic dynamics with continuum-level quantities through appropriate spatial or temporal averaging (Irving and Kirkwood, 1950; Tsai, 1979). However, the virial stress is not identical to the true *mechanical* (Cauchy) stress defined in continuum mechanics. Their conceptual and mathematical foundations differ fundamentally.

In continuum mechanics, the *Cauchy stress tensor* σ represents the intensity of internal forces at a point within a deformable body, describing how normal and shear stresses are distributed on the coordinate planes of the current configuration (Zhou, 2003). The traction vector acting on an infinitesimal material surface with unit normal $\mathbf{n}$ is defined as

$$\mathbf{t} = \mathbf{n} \cdot \sigma, \tag{3.34}$$

In this definition, stress represents the internal mechanical force per unit area acting across material surfaces; it is thus independent of mass transport or particle motion.

In contrast, in atomistic simulations, the so-called *volume-averaged virial stress* tensor Π_{ij} is typically computed as

$$\Pi_{ij} = \frac{1}{V}\left(-\sum_{i} m_i \, \mathbf{v}_i \otimes \mathbf{v}_i + \frac{1}{2}\sum_{i}\sum_{j\neq i} \mathbf{r}_{ij} \otimes \mathbf{f}_{ij}\right), \tag{3.35}$$

where m_i and $\mathbf{v}_i = \dot{\mathbf{r}}_i$ are the mass and velocity of atom i, $\mathbf{r}_{ij} = \mathbf{r}_j - \mathbf{r}_i$ is the interatomic separation vector, and $\mathbf{f}_{ij}$ is the pairwise force acting on atom i due to atom j. Here, $\otimes$ denotes the tensor product of two vectors, and V is the volume over which the stress is defined (Zhou, 2003; Subramaniyan and Sun, 2008).

It is important to note that Eq. (3.35) corresponds to a *system-level* or *global* stress measure, as the summation is carried out over all atoms contained within the volume V. As such, the resulting virial stress represents an average over the entire system rather than a locally resolved stress field.

The first term in Eq. (3.35) represents the contribution of momentum flux due to *mass convection* across a fixed spatial surface, while the second term corresponds to *interatomic forces* that characterize the internal mechanical interactions. Hence, Π measures the *rate of momentum change within a stationary spatial region* rather than the true mechanical force per unit area acting between material surfaces.

Historic derivations of the virial stress include its generalization from the *virial theorem* of Clausius (1870), originally formulated for the pressure of gases, and later through solutions of the spatial form of the balance of linear momentum equation. This historical evolution links the statistical mechanical definition of pressure in molecular systems to the modern continuum representation of stress in atomistic simulations (Tsai, 1979).

Following the theoretical clarification proposed by Zhou (2003), the virial stress should be interpreted as a geometric measure of *spatial momentum flow*, not as a mechanical stress in the continuum sense. However, under appropriate conditions, a direct correspondence between the virial formulation and the Cauchy stress can be established.

Specifically, when the averaging volume moves with the material and macroscopic mass transport is negligible, the convective momentum flux term in Eq. (3.35) vanishes. In this limit,

the virial expression reduces to the interatomic force contribution,

$$\sigma_{ij} = \frac{1}{2V} \sum_{i} \sum_{j \neq i} \mathbf{r}_{ij} \otimes \mathbf{f}_{ij}, \tag{3.36}$$

which represents the true internal force transmission between atoms and satisfies the material form of the linear momentum balance. Under these conditions, Eq. (3.36) becomes physically equivalent to the Cauchy stress tensor defined in continuum mechanics.

This correspondence clarifies that the distinction between virial stress and Cauchy stress does not originate from the interatomic force contribution itself, but rather from the inclusion of convective momentum transport arising from fixed spatial averaging. The virial stress, therefore, characterizes momentum flow through a stationary control volume, whereas the Cauchy stress describes mechanical force transmission across material surfaces that deform and move with the body.

Figure 3.6 schematically illustrates this conceptual difference. Panel (a) illustrates the continuum definition of Cauchy stress, where the traction vector $\mathbf{t} = \mathbf{n} \cdot \sigma$ acts on a material surface that moves with the body. Panel (b) depicts the virial stress evaluated over a fixed spatial region, where $\mathbf{n} \cdot \Pi$ represents the total momentum flux, including both convective and interatomic contributions. The lower panels emphasize that the continuum body is treated as a homogeneous medium, while the atomistic representation consists of discrete particles interacting via interatomic forces. Here, the stress is defined with respect to an infinitesimal

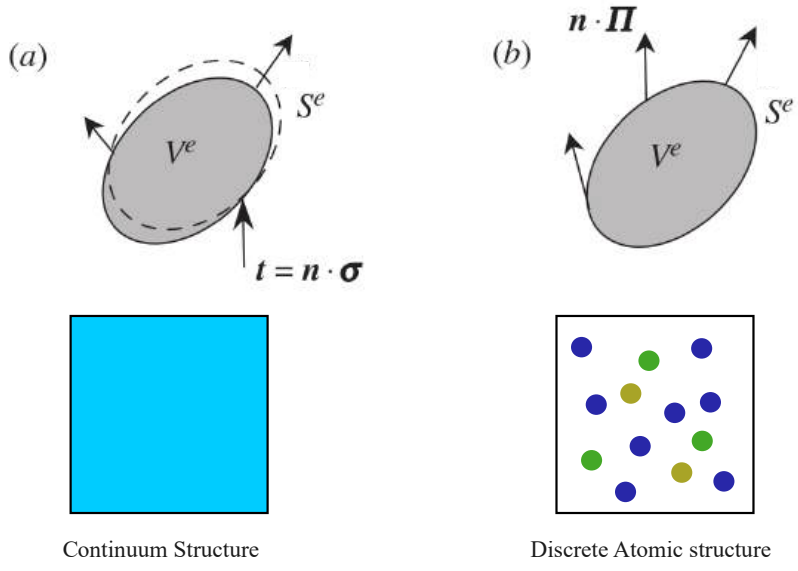

Figure 3.6: Comparison between (a) the Cauchy stress acting on a material volume element V^e bounded by surface S^e, and (b) the virial stress describing momentum flux across a stationary spatial surface. The lower panels illustrate the difference between the continuum and discrete atomic representations, adapted from Zhou (2003).

material volume element V^e and its enclosing material surface S^e, both of which deform and move with the body. The traction vector $\mathbf{t}$ represents the internal mechanical force transmitted across S^e per unit area, providing a local description of force transfer within the continuum.

Within the framework of MD simulations, the virial formulation provides a consistent and physically grounded means of evaluating stress from atomic trajectories and interatomic interactions. By accounting for both momentum transport and internal force contributions, the virial stress enables the quantitative assessment of stress evolution under mechanical loading.

In contrast to the interpretation proposed by Zhou (2003), who emphasized the conceptual distinction between spatial momentum flux and true mechanical stress, Subramaniyan and Sun (2008) provided a rigorous continuum-based derivation demonstrating that the virial stress can be fully consistent with the Cauchy stress tensor when formulated within a material description. In their theoretical framework, both the kinetic (convective) and potential (interatomic force) contributions naturally emerge from the balance of linear momentum when coarse-graining atomistic equations of motion. They argued that the kinetic term does not represent a non-mechanical artifact, but rather corresponds to the transport of momentum associated with particle motion relative to a reference frame. Through both analytical derivations and numerical simulations, they demonstrated that the total virial stress, including the kinetic component, converges to the continuum Cauchy stress when appropriate averaging procedures are applied. In particular, their numerical examples showed that neglecting the kinetic term in dynamic or non-equilibrium situations can lead to discrepancies in stress evaluation.

Considering the different theoretical interpretations discussed in the literature, the present study adopts the complete virial formulation, including both the kinetic and potential contributions, for stress evaluation in molecular dynamics simulations. This choice ensures consistency with the continuum balance of linear momentum under finite-temperature and dynamic conditions. By retaining both terms in the virial expression, the stress tensor reflects the total momentum transport within the system. It maintains general validity without relying on restrictive assumptions regarding mass convection or equilibrium conditions.

Thermodynamic Quantities

Macroscopic thermodynamic quantities in MD emerge from microscopic quantities computed along the simulation trajectory. The Hamiltonian in Eq. (3.4) provides the instantaneous kinetic and potential components of the system, while the ergodic principle in Eq. (3.15) justifies replacing ensemble averages with time averages once equilibrium is reached. Accordingly, temperature, pressure, and energy are evaluated from their microscopic definitions and subsequently averaged to obtain the corresponding macroscopic observables (Tadmor and Miller, 2011).

The temperature follows directly from the equipartition theorem, which states that each quadratic degree of freedom contributes $\frac{1}{2}k_{\mathrm{B}}T$ to the mean kinetic energy. For a system of N

atoms, the instantaneous kinetic energy is

$$K = \sum_{\mathrm{i}=1}^{\mathrm{N}} \frac{1}{2} m_{\mathrm{i}} v_{\mathrm{i}}^2, \tag{3.37}$$

where m_{i} and v_{i} are the mass and velocity magnitude of atom i. With g active degrees of freedom (after accounting for constraints and the removal of rigid-body translations and rotations; for an unconstrained atomic system without removed rigid-body motion, one has $g = 3N$.), equipartition gives $\langle K \rangle = \frac{g}{2} k_{\mathrm{B}} T$, leading to the instantaneous temperature estimator

$$T = \frac{2K}{g k_B} = \frac{1}{3N k_B} \sum_{i=1}^{N} m_i v_i^2. \tag{3.38}$$

This microscopic definition of temperature is identical across ensembles; however, the statistical properties and magnitude of fluctuations depend on the chosen ensemble. In NVE, the temperature fluctuates around a value determined by the conserved total energy. In NVT, the thermostat regulates kinetic energy to maintain a target temperature. In NPT, temperature is controlled together with pressure, with volume fluctuations naturally included.

The expression for pressure follows from the mechanical virial theorem. Introducing the Clausius virial $W = \sum_{\mathrm{i}} \vec{r}_{\mathrm{i}} \cdot \vec{F}_{\mathrm{i}}$, the relation

$$2\langle K \rangle + \langle W \rangle = 3PV \tag{3.39}$$

connects kinetic and configurational contributions. Combining this with Eq. (3.38) yields the working expression for the instantaneous pressure,

$$P = \frac{N k_{\mathrm{B}} T}{V} + \frac{1}{3V} \sum_{\mathrm{i}<\mathrm{j}} \mathbf{r}_{\mathrm{ij}} \cdot \mathbf{f}_{\mathrm{ij}}, \tag{3.40}$$

where the first term corresponds to the kinetic contribution and the second term arises from interatomic forces. Using Newton's third law, the Clausius virial can be transformed into the equivalent, frame-independent pairwise form $W = \sum_{\mathrm{i}<\mathrm{j}} \mathbf{r}_{\mathrm{ij}} \cdot \mathbf{f}_{\mathrm{ij}}$. In tensor form, the microscopic stress is given by the virial expression in Eq. (3.35), and the hydrostatic pressure follows from

$$P_{\mathrm{hyd}} = -\frac{1}{3} tr\,\Pi. \tag{3.41}$$

The total energy of the system, $E = K + U$, is conserved in the NVE ensemble, whereas it fluctuates in the NVT ensemble due to heat exchange with the thermostat. In the NPT ensemble, neither energy nor enthalpy is strictly conserved; instead, an extended Hamiltonian associated with the coupled system–thermostat–barostat dynamics is conserved, whose physical part corresponds to the enthalpy $H = E + P_0 V$. These differences affect only the nature of the

fluctuations, while the microscopic estimators of thermodynamic and mechanical quantities remain unchanged.

In the present work, instantaneous values of T, P, E, and Π are sampled throughout the simulation, and macroscopic values are obtained by time-averaging over equilibrated trajectory segments. Statistical uncertainties are estimated using block averaging to account for temporal correlations.

3.5 Interatomic potentials

At the core of MD simulations lies the accurate description of atomic interactions, which governs the reliability of predicted material properties such as cohesive energy, lattice constants, elastic moduli, cohesive energy, formation energy of defects, surface energy, and stacking fault energy. These interactions are expressed through an *interatomic potential*, a mathematical function defining the total potential energy $U(\vec{r}_1, \vec{r}_2, \ldots, \vec{r}_N)$ as a function of all atomic positions. The resulting forces driving atomic motion are obtained from the negative gradient of the potential energy (see Eq 3.2), which forms the fundamental basis for Newtonian dynamics in MD simulations.

The interatomic potential includes both the bonding character and energetic stability of materials and thus must reflect the underlying physics of the system, be it van der Waals attraction in inert gases, covalent bonding in semiconductors, or metallic cohesion in transition metals. Fig. 3.7 provides a schematic comparison between two representative potential models: the *Lennard–Jones (LJ)* (Lennard-Jones, 1931) and the *Embedded Atom Method (EAM)* (Foiles et al., 1986), illustrating the evolution from simple pairwise to environment-dependent many-body interactions.

Lennard–Jones Potential: Pairwise Interactions

The simplest and most widely known form of interatomic potential is the Lennard–Jones (LJ) potential, which assumes that the total energy of a system can be represented as the sum of independent pairwise interactions between atoms:

$$U_{\mathrm{LJ}} = \sum_{i<j} V^{\mathrm{LJ}}\left(r_{ij}\right), \tag{3.42}$$

where the pairwise potential is given by

$$V^{\mathrm{LJ}}\left(r_{ij}\right) = 4\varepsilon \left[\left(\frac{\sigma}{r_{ij}}\right)^{12} - \left(\frac{\sigma}{r_{ij}}\right)^{6} \right]. \tag{3.43}$$

Here, ε represents the potential well depth (bond strength), and σ is the finite distance at which the potential equals zero. The first term, $(\sigma/r_{ij})^{12}$, models a steep short-range repulsion that effectively represents Pauli exclusion due to overlapping electron orbitals, while the second

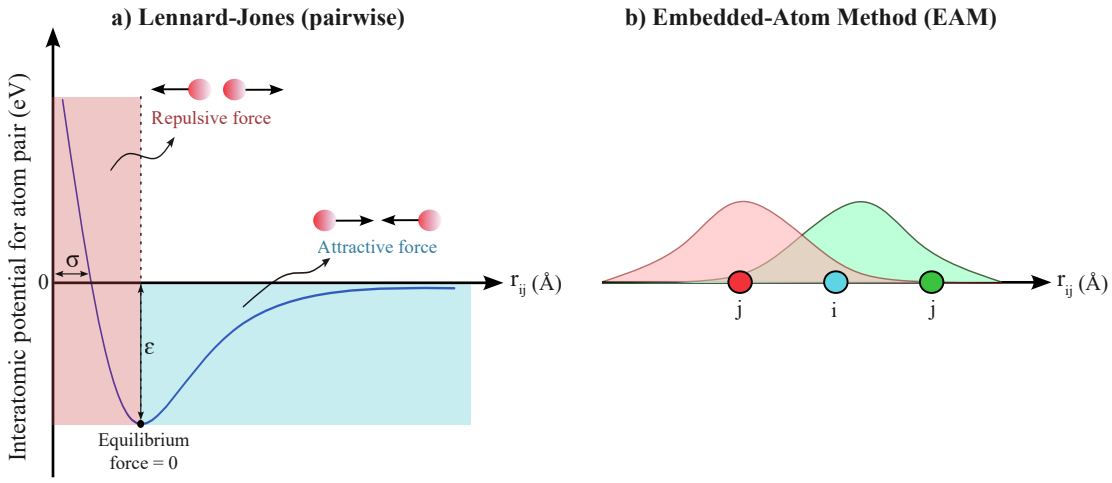

Figure 3.7: Comparison between (a) the pairwise Lennard–Jones potential and (b) the many-body Embedded Atom Method (EAM). The LJ potential models two-body interactions through a balance of short-range repulsion and long-range attraction, while the EAM potential introduces the concept of local electron density, capturing the many-body nature of metallic bonding.

term, $-(\sigma/r_{ij})^6$, represents the long-range *van der Waals attraction*. The potential reaches its minimum at $r = 2^{1/6}\sigma$, where the attractive and repulsive forces balance, corresponding to the equilibrium interatomic distance (Fig. 3.7a).

While computationally efficient and conceptually simple, the LJ potential is limited to systems dominated by weak, isotropic interactions, such as noble gases or molecular fluids. It fails to account for the many-body effects and electron-density dependence that define metallic cohesion and directional bonding, making it inadequate for metals and complex alloys.

Embedded Atom Method: Many-Body Description of Metallic Bonding

In metallic systems, atomic cohesion is governed by delocalized valence electrons that form a collective electron sea rather than localized directional bonds. As a consequence, the bonding strength of an atom depends not only on its nearest neighbors but also on the surrounding atomic environment through the local electron density. The Embedded Atom Method (EAM) (Daw and Baskes, 1984; Bernstein and Hess, 2003; Mishin, 2005) was developed to capture this inherently many-body nature of metallic bonding within an efficient atomistic framework.

Within the EAM formalism, the total potential energy of a system consisting of N atoms is expressed as

$$E_{\text{tot}} = \sum_{i=1}^{N} F_{\alpha_i}(\rho_i) + \frac{1}{2}\sum_{\substack{i,j=1 \\ i\neq j}}^{N} V_{\alpha_i\alpha_j}(r_{ij}), \tag{3.44}$$

where α_i denotes the chemical species of atom i. The second term, $V_{\alpha_i\alpha_i}(r_{ij})$, represents an effective short-range pair interaction between the atomic cores of species α_i and α_j, separated by an interatomic distance r_{ij}. This term primarily accounts for electrostatic repulsion at short

distances and attractive contributions arising from screened ion–electron interactions.

The first term, $F_{\alpha_i}(\rho_i)$, is the *embedding energy* of atom i and constitutes the central many-body contribution of the EAM. It quantifies the energetic cost of inserting an atom of species α_i into the local background electron density ρ_i created by its surrounding neighbors. The local electron density at atom i is defined as

$$\rho_i = \sum_{\substack{j=1 \\ j\neq i}}^{N} f_{\alpha_j}(r_{ij}), \tag{3.45}$$

where $f_{\alpha_j}(r_{ij})$ denotes the electron-density contribution from a neighboring atom j of species α_j evaluated at a distance r_{ij}. In multi-component alloys, this formulation explicitly accounts for the fact that different atomic species contribute differently to the local electron density field.

The embedding function introduces a nonlinear dependence of the atomic energy on the local coordination environment, thereby rendering the total energy intrinsically many-body in nature. Although the electron density ρ_i is constructed as a superposition of pairwise contributions, the functional form of $F_{\alpha_i}(\rho_i)$ couples all neighboring atoms simultaneously, enabling the EAM to reproduce environment-sensitive phenomena that are inaccessible to purely pairwise potentials.

As a result, the EAM provides a physically grounded description of key metallic properties, including elastic constants, surface and interface energies, stacking-fault energies, vacancy and interstitial formation energies, and dislocation core structures. This capability is particularly critical for multi-component alloys, where chemical complexity and local compositional fluctuations strongly influence defect energetics and mechanical response. Conceptually, as illustrated in Fig. 3.7(b), each atom interacts not only through discrete pair forces but is embedded within a continuous electron-density field generated by its neighbors, reflecting the collective nature of metallic bonding.

Comparative Discussion and Physical Implications

The fundamental difference between LJ and EAM potentials lies in their treatment of atomic coordination and bonding environment. The LJ potential assumes additivity of pairwise interactions, which neglects the influence of the surrounding atoms on the bonding strength between a given pair. In contrast, the EAM model incorporates a non-linear dependence on local electron density through $F_i(\rho_i)$, providing a self-consistent response to changes in atomic environment.

This distinction makes EAM particularly suitable for modeling metallic systems, alloys, and radiation-induced processes, where defect formation energies, short-range repulsion, and coordination changes critically control the microstructural evolution.

Furthermore, the EAM framework naturally extends to multi-component alloys through element-specific embedding and density functions, as demonstrated for ternary Fe–Ni–Cr systems investigated in this thesis (Bernstein and Hess, 2003; Mishin, 2005; Bonny et al., 2011).

Table 3.3: Comparison between the Lennard–Jones (LJ) and Embedded Atom Method (EAM) potentials.

Feature	**LJ**	**EAM**
Interaction type	Pairwise additive	Many-body (electron-density dependent)
Cohesion mechanism	van der Waals attraction	Delocalized metallic bonding
Energy dependence	$V(r_{ij})$ only	$F_{\alpha_i}(\rho_i) + V_{\alpha_i\alpha_j}(r_{ij})$
Response to coordination	Fixed pairwise strength	Varies with local electron density
Surface / defect accuracy	Poor	High (coordination-sensitive)
Computational cost	Very low	Moderate
Typical applications	Noble gases, molecular fluids	Metals, alloys

In the present work, the *EAM11 potential* developed by Bonny et al. (2011) was employed due to its robust parameterization against experimental and first-principles data for Fe–Ni–Cr alloys. This potential enables accurate simulation of radiation-induced defect formation under realistic thermodynamic conditions (Béland et al., 2017; Zhou et al., 2023; Ustrzycka et al., 2024), establishing a reliable atomistic foundation for the present MD study.

3.6 Energy minimization and system relaxation

Before initiating dynamic simulations, a robust and mechanically stable initial configuration must be established by performing *energy minimization* and thermal equilibration. These preparatory stages are essential to remove unphysical atomic overlaps, reduce artificial internal stresses, and ensure that the system resides near a stable point on its potential energy surface. Neglecting or poorly executing these steps can lead to artifacts such as unrealistic stress concentrations, non-converging forces, or inaccurate crack initiation mechanisms, particularly in simulations involving irradiation damage and fracture.

Energy minimization in MD corresponds to solving a static optimization problem in which the total potential energy of the system is iteratively reduced by adjusting atomic positions $\vec{r}_i$ until the residual forces satisfy a predefined convergence criterion:

$$\vec{F}_i = -\nabla_i U(\vec{r}_1, \vec{r}_2, \ldots, \vec{r}_N) \approx 0. \tag{3.46}$$

This ensures that the configuration corresponds to a stationary point of the potential energy surface, where $\nabla U = 0$ and $\nabla^2 U > 0$, indicating a local minimum. As depicted in Fig. 3.8, the global minimum corresponds to the most stable state, while local minima represent metastable configurations that may still be physically relevant, particularly in defective or irradiated systems.

Several algorithms are available to achieve energy minimization, each balancing robustness and computational efficiency. The *Steepest Descent (SD)* method (Sheppard et al., 2008) is the

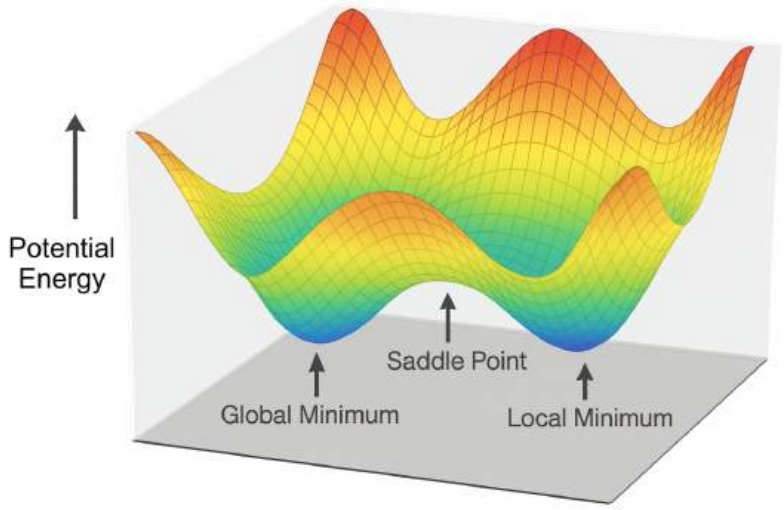

Figure 3.8: Schematic representation of a potential energy surface illustrating the minimization process. The system evolves from high-energy configurations toward local or global minima by following the negative gradient of the potential energy. The *global minimum* represents the most stable configuration, while a *local minimum* corresponds to a metastable equilibrium state separated by a *saddle point*. Adapted from Kumar et al. (2022)

simplest approach, where atomic coordinates are updated along the direction of the negative energy gradient:

$$\vec{r}_{n+1} = \vec{r}_n - \alpha_n \nabla U(\vec{r}_n), \tag{3.47}$$

with α_n as the step size. This method guarantees a monotonic decrease in energy and is well-suited for removing large atomic overlaps, although it converges slowly near minima due to gradient flattening.

To accelerate convergence, the *Conjugate Gradient (CG)* algorithm (Bitzek et al., 2006; Sheppard et al., 2008) introduces memory of previous search directions, avoiding redundant oscillations and achieving near-quadratic convergence near equilibrium. The new search direction $\vec{p}_{n+1}$ is defined as:

$$\vec{p}_{n+1} = -\nabla U(\vec{r}_{n+1}) + \beta_n \vec{p}_n, \tag{3.48}$$

where β_n is a weighting factor (e.g., Fletcher–Reeves or Polak–Ribiere formulation) that ensures conjugacy of successive directions. CG is particularly efficient for crystalline and defect-free systems with a smooth potential energy landscape.

For highly disordered or irradiated systems, the *Fast Inertial Relaxation Engine (FIRE)* method (Guénolé et al., 2020) provides improved robustness by combining MD integration with adaptive damping:

$$m_i \ddot{\vec{r}}_i = \vec{F}_i - \gamma \vec{v}_i, \tag{3.49}$$

where γ is an adaptive damping coefficient that varies with the projection of the force on the velocity, $P = \sum_i \vec{F}_i \cdot \vec{v}_i$. When $P > 0$, velocities are aligned with forces and the system

accelerates toward the minimum; when $P < 0$, motion is damped and velocities are reset. This adaptive mechanism enables FIRE to handle complex energy landscapes with rapid and stable convergence.

In practice, energy minimization in this thesis was performed using the `minimize` command in LAMMPS, employing the CG algorithm with strict convergence tolerances on both energy and force magnitudes, typically 10^{-12} eV and 10^{-6} eV/Å, respectively. For example, Zhu et al. (2021) applied a similar criterion to relax the atomic structure of single-crystal Fe before tensile loading, while Huang et al. (2023) employed a CG-based relaxation followed by NPT thermal equilibration to stabilize irradiated Fe systems. This multi-stage relaxation ensures that the system begins dynamic simulations from a physically meaningful, mechanically stable, and energetically minimized configuration.

Following the minimization stage, the system must be brought to the desired thermodynamic state through thermal and mechanical relaxation. While minimization ensures that the forces on atoms are near equilibrium, it does not establish a physically meaningful temperature or pressure distribution. Therefore, MD simulations are first performed in the *canonical* (NVT) or *isothermal–isobaric* (NPT) ensemble to relax the system toward equilibrium.

In the NVT ensemble, a thermostat regulates the kinetic energy to maintain a target temperature T_0 while allowing atomic vibrations to develop naturally. This step distributes thermal energy uniformly across the system and eliminates spurious temperature gradients. The equations of motion are modified through a thermostat variable that gently adjusts particle velocities, ensuring that the temperature fluctuates around T_0 with the correct statistical variance.

Mechanical relaxation of residual stresses or volumetric strain is then achieved using the NPT ensemble, in which both temperature and pressure are controlled. A barostat dynamically adjusts the simulation cell dimensions to ensure that the averaged pressure matches the target external pressure, P_0. This procedure is essential in irradiated or defect-containing crystals, where local structural disorder and swelling can generate significant internal stresses. The combined thermostat–barostat approach ensures that both thermal and mechanical equilibrium are achieved before any loading or fracture simulation is performed.

Equilibrium is confirmed by monitoring the time evolution of temperature, pressure, total energy, and system volume. Once these quantities fluctuate around stationary mean values with no systematic drift, the system is considered properly relaxed and ready for subsequent deformation, crack propagation, or irradiation evolution analyses.

3.7 Boundary conditions

Boundary conditions play a central role in MD simulations by defining how the simulation domain interacts with its surroundings. Their proper selection is essential for ensuring physical realism and for minimizing numerical artifacts such as spurious stress reflections, artificial confinement, or non-physical mass loss. This is particularly critical in non-equilibrium sim-

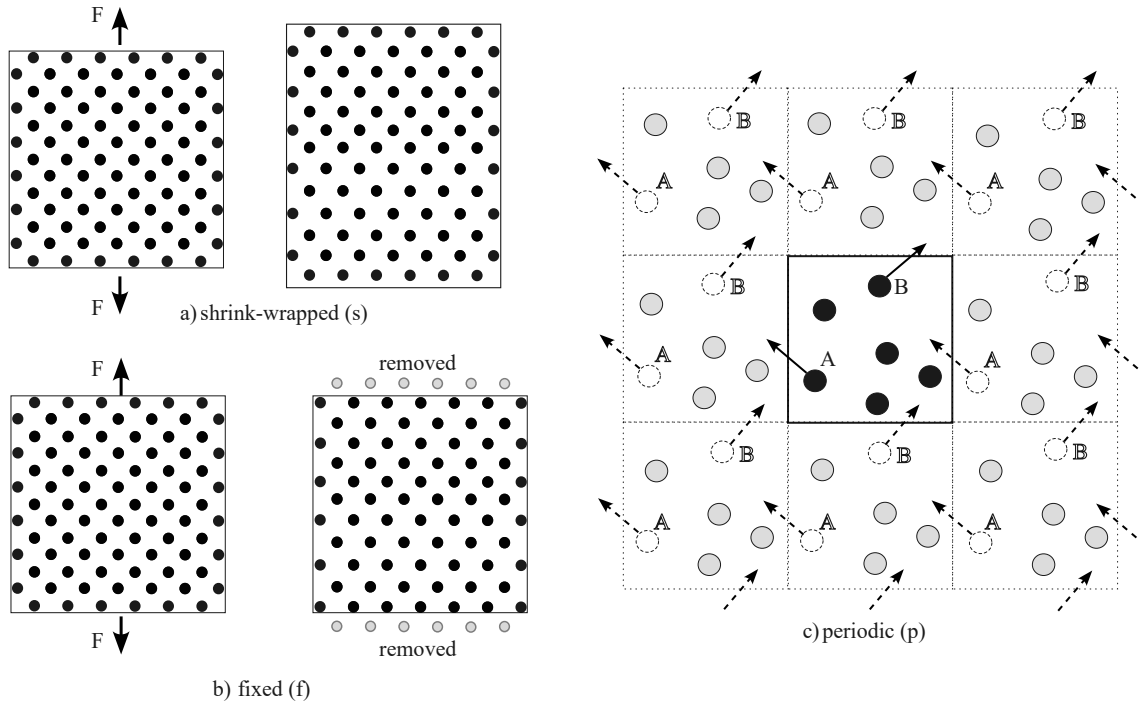

Figure 3.9: Schematic illustration of common boundary conditions used in MD simulations: (a) shrink-wrapped (s), where the simulation box dynamically follows the outermost atoms; (b) fixed (f), where the simulation cell faces remain spatially constant, leading to atom deletion if atoms cross the boundary; (c) periodic (p), where atoms exiting one side of the simulation cell re-enter from the opposite side, reproducing bulk-like behavior.

ulations involving fracture propagation, irradiation damage, and dislocation emission, where long-range stress fields and atomic transport near the boundaries strongly influence the observed mechanisms (Cui and Beom, 2014; Andric and Curtin, 2017).

In MD simulations, three fundamental boundary-condition types are commonly employed: *periodic* (p), *fixed* (f), and *shrink-wrapped* (s). A schematic overview of these boundary conditions and their characteristic behavior is presented in Fig. 3.9.

The shrink-wrapped (s) boundary condition allows the dimensions of the simulation box to adjust dynamically so as to continuously enclose the outermost atoms. This formulation naturally generates free surfaces surrounded by vacuum and permits unconstrained atomic motion without periodic repetition or artificial reflection from rigid boundaries. As a result, shrink-wrapped boundaries are well suited for simulations involving surface evolution, large atomic displacements, and non-equilibrium processes accompanied by volumetric changes.

The periodic (p) boundary condition enforces translational invariance by replicating the simulation cell infinitely along selected directions. Atoms leaving one side of the domain re-enter from the opposite side, thereby eliminating free surfaces and suppressing finite-size effects. This boundary condition is essential for modeling bulk material behavior and for maintaining continuity of stress, structure, and defect populations across the simulation domain.

The defining feature of the fixed (f) boundary condition is the presence of *spatially constant*

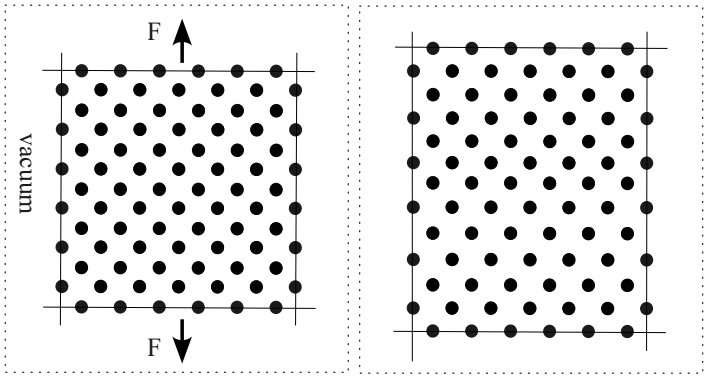

Figure 3.10: Schematic illustration of a fixed boundary (f) condition combined with an explicit vacuum region. The constant simulation-cell faces define the fixed boundary, while the vacuum region prevents atoms from crossing the boundary and being deleted.

simulation-cell faces. Under this boundary condition, the dimensions of the simulation box remain unchanged throughout the simulation, irrespective of atomic motion or deformation within the domain. As a direct and intrinsic consequence of this constraint, atoms that cross a fixed simulation-cell face are removed from the system during neighbor-list updates. This atom deletion behavior is a general characteristic of fixed boundaries and does not depend on the specific atomic constraints applied within the domain.

Because of this property, the use of fixed boundary conditions requires careful consideration in simulations involving large displacements or separation of material regions. To avoid unintended atom loss and to preserve a constant number of atoms, fixed boundaries are commonly combined with explicitly defined vacuum regions. In this approach, portions of the simulation cell are intentionally left unoccupied by atoms, creating space for deformation and separation to occur without atoms reaching the fixed cell faces.

A schematic representation of a fixed boundary condition combined with a vacuum region is shown in Fig. 3.10. In this configuration, the simulation-cell faces remain constant, while the presence of vacuum ensures that atomic motion, surface relaxation, and separation processes can proceed without atom deletion.

It is important to distinguish between boundary conditions and vacuum regions, as they represent independent aspects of the simulation setup. Boundary conditions define the behavior of the simulation-cell faces, whereas vacuum regions arise from the deliberate choice of simulation geometry and atomic distribution. When combined appropriately, fixed boundaries provide numerical stability and controlled loading conditions, while vacuum regions enable physically meaningful deformation and separation without artificial mass loss.

By assigning different boundary conditions along different spatial directions, hybrid configurations can be constructed to balance physical realism and computational stability. Such combinations allow bulk-like behavior to be maintained where required while permitting free

surfaces or constrained directions elsewhere (Allen and Tildesley, 2017; Thompson et al., 2022).

In this work, boundary conditions are selected based on the following general principles to ensure stable numerical behavior, conservation of mass, and a physically consistent representation of deformation and fracture processes. The chosen configuration enables controlled mechanical loading while allowing free-surface evolution and crack opening to occur without unphysical atom deletion, thereby ensuring that the observed response reflects intrinsic material behavior rather than boundary-induced artifacts.

3.8 Simulation framework and data processing pipeline

The simulation methodology in this thesis follows a structured, multistage workflow designed to investigate irradiation-assisted fracture in austenitic Fe–Ni–Cr alloys. As illustrated in Fig. 3.11, the approach integrates atomistic model construction, irradiation-defect generation through overlapping PKA cascades, mechanical characterization, and fracture analysis. This framework ensures physically realistic microstructures, statistically meaningful irradiation conditions, and reliable extraction of atomistic fracture metrics.

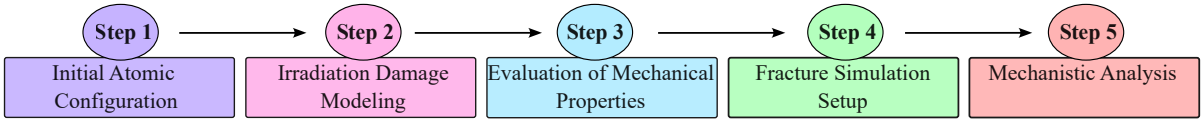

Figure 3.11: Overall simulation workflow: atomistic model generation, cascade-based irradiation, mechanical testing and fracture simulations, followed by post-processing and analysis.

The pre-processing step in the MD simulation involves constructing the atomic structure of the target material. To generate the atomic configuration, Atomsk (Hirel, 2015), a versatile open-source tool, is employed due to its robust capabilities in creating complex atomic structures. Atomsk is used to define a single-crystal structure with precise lattice constants and crystallographic orientations tailored to the material's properties. In this work, the lattice constant of pure Fe, based on its higher composition in the alloy, was used as the reference for generating the initial single-crystal sample, which was subsequently modified in Large-scale Atomic/Molecular Massively Parallel Simulator (LAMMPS) package to achieve the desired Fe–Ni–Cr composition based on the selected material for this research. This procedure ensures consistency with reported alloy structures while maintaining computational efficiency. Beyond single-crystal generation, Atomsk facilitates the introduction of various defects critical for irradiation and fracture studies, including vacancies, interstitials, dislocations, grain boundaries, and twinning. This flexibility ensures the creation of realistic atomic models that reflect the structural complexities of irradiated materials. Fig. 3.12 provides illustrative examples of Atomsk-generated atomic structures, such as bcc, fcc, and hcp lattices, inclusion of Cu in the iron matrix, dislocation generation, and 3D polycrystal structures.

All MD simulations were executed with LAMMPS (Thompson et al., 2022). Following the overall simulation workflow shown in Fig. 3.11, the study begins with the generation of relaxed initial atomic configurations (Step 1). Radiation damage was then introduced via repeated primary knock-on atom (PKA) events with randomized directions and species selection to reach dpa-equivalent damage states (Step 2). Subsequently, mechanical loading simulations were performed to evaluate the elastic and inelastic response of both pristine and irradiated configurations (Step 3). Fracture simulations were then carried out to investigate crack-tip processes and crack propagation behavior (Step 4). Finally, trajectories and thermodynamic outputs generated by LAMMPS were processed for visualization and quantitative analysis (Step 5).

To extract meaningful insights from atomistic simulations, it is essential to employ robust post-processing techniques that can characterize defects, deformation modes, and structural transformations at the atomic scale. In this work, such analyses were performed using the Open Visualization Tool (OVITO), an open-source software specifically developed for the visualization and interpretation of MD simulation data (Stukowski and Albe, 2010). OVITO enables the mapping of atomistic configurations onto physically interpretable features, such as dislocations, stacking faults, voids, grain boundaries, and local crystal symmetry, thereby facilitating an understanding of the underlying deformation and fracture mechanisms.

Among the key analysis tools used in OVITO are the Dislocation Extraction Algorithm (DXA) and the Common Neighbor Analysis (CNA), both of which provide complementary information about the microstructural evolution of irradiated and loaded materials. Fig. 3.13 illustrates an example of a data processing pipeline in OVITO, as presented in the original software paper (Stukowski and Albe, 2010). The pipeline demonstrates the step-by-step transformation of raw atomic data into a visualized grain boundary structure. Starting from the initial atomic configuration, processing steps such as coordination analysis, selection of mis-coordinated atoms, deletion of bulk atoms, and ambient occlusion shading are applied to highlight the grain boundary network in a nanocrystalline material.

The DXA reconstructs full dislocation lines from atomistic data by identifying atomic

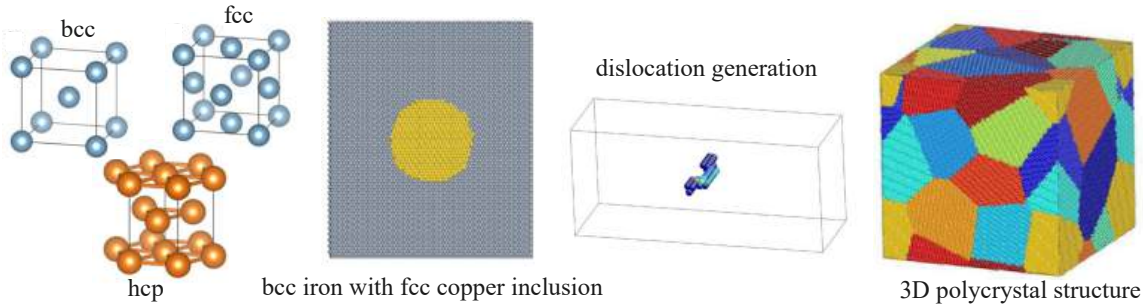

Figure 3.12: Examples of atomic structures generated with Atomsk: crystal lattices, defect seeding (dislocations, vacancies), and polycrystalline samples suitable for MD simulations.

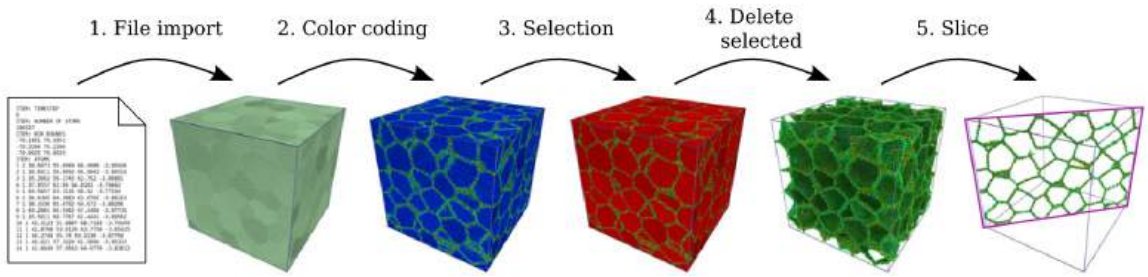

Figure 3.13: Example of a data processing pipeline in OVITO for visualizing grain boundaries in a nanocrystalline structure, as shown in the original reference (Stukowski and Albe, 2010). The pipeline includes steps such as coordination analysis, selection of low-coordinated atoms, deletion of bulk atoms, and application of ambient occlusion shading to enhance depth perception.

displacements that deviate from the ideal lattice and classifying line defects based on Burgers vector content and slip geometry (Stukowski et al., 2012). The method utilizes the concept of local lattice distortion, matching regions of distorted atoms to reference crystal structures, and tracing dislocation lines by locating strings of defective atoms with consistent topology. This enables the identification of perfect dislocations, partial dislocations, sessile locks, and dislocation loops. As shown in Zhang and Ghosh (2013), DXA is capable of capturing complex dislocation interactions during crack propagation, including dislocation nucleation at the crack tip, loop formation from void collapse, and dislocation absorption by stacking faults. In irradiated fcc systems, where SFTs and interstitial loops evolve dynamically, DXA provides critical insights into how these defects interact with the crack tip stress field and contribute to local hardening or embrittlement.

The CNA, on the other hand, is used to classify the local atomic structure around each atom. It distinguishes between different crystal symmetries, such as fcc, hcp, bcc, and disordered environments, such as amorphous or defect cores, by analyzing the bonding topology among nearest neighbors (Honeycutt and Andersen, 1987). CNA is especially useful for identifying stacking faults, grain boundaries, and the extent of plastic zones near crack tips. During deformation, atoms that deviate from perfect fcc symmetry are typically associated with stacking fault ribbons, twin boundaries, or shear bands. This allows for the visualization of slip activity, twin formation, and phase transitions under tensile or shear loading.

The combined use of DXA and CNA allows for a comprehensive interpretation of the physical response of the system. This approach, as demonstrated by Zhang and Ghosh (2013), provides insight into key fracture-controlling mechanisms such as crack-tip shielding, dislocation pinning, and defect–slip interactions.

Quantitative metrics complemented these observations, allowing systematic evaluation of the mechanical response under varying irradiation levels. These included crack growth rate, stress-strain behavior across different dpa levels, and energy-based measures of embrittlement. Specifically, plastic work is computed globally, while localized traction–separation (T–S) laws

are employed to quantify DBT behavior at the crack tip.

Simulation outputs were stored in standard LAMMPS dump and log files, containing atomic positions, virial stresses, system energies, and all requested data at each timestep. These data were post-processed using Python (Van Rossum and Drake Jr, 1995) scripts to extract the desired metrics, such as crack length evolution, stress-strain curves, and energy release calculations. This workflow enabled a systematic and reproducible assessment of the influence of radiation-induced defects on fracture resistance in the desired Fe–Ni–Cr alloy.

Chapter 4

Radiation-induced embrittlement

This chapter is extracted from the following publication:

A. Ustrzycka, H. Mousavi, F. J. Dominguez-Gutierrez, and S. Stupkiewicz.
Atomistic study of radiation-induced ductile-to-brittle transition in austenitic steel.
International Journal of Mechanical Sciences, 303 (2025) 110567.

4.1 Significance of radiation-induced embrittlement in Fe–Ni–Cr alloys

As established in Chapter 2, irradiation critically affects the long-term mechanical performance of structural alloys in nuclear environments. This chapter focuses specifically on radiation-induced ductile-to-brittle transition (DBT) in austenitic Fe–Ni–Cr alloys, with emphasis on how irradiation-driven microstructural evolution alters crack-tip deformation and fracture resistance.

Fe–Ni–Cr alloys with an fcc structure are widely used in fission and fusion reactor components due to their favorable mechanical and environmental properties. However, irradiation fundamentally modifies their fracture response by introducing defect populations that progressively suppress plastic deformation. As a result, these alloys can exhibit pronounced embrittlement despite their nominally ductile behavior, making them an ideal system for investigating irradiation-induced DBT mechanisms at the atomic scale.

Building on the irradiation challenges discussed in Section 2.1, the present study examines a ternary Fe–Ni–Cr alloy representative of 310S stainless steel. The model composition $Fe_{55}Ni_{19}Cr_{26}$ was selected based on experimentally reported chemical compositions and reflects alloys used in reactor applications (Musiał et al., 2022). The simulations and analyses presented in this chapter constitute a dedicated atomistic investigation of irradiation-assisted fracture behavior in this alloy system.

Radiation-induced embrittlement manifests as a progressive reduction in ductility and fracture toughness, ultimately giving rise to a DBT. In the classical case, fracture behavior is controlled by temperature, where decreasing temperature promotes DBT, while increasing temperature induces the reverse brittle–to-ductile transition (BDT) through enhanced plastic accommodation. In contrast, irradiation-induced DBT occurs at nominally constant temperature and is governed primarily by the accumulation of radiation-induced defects. This distinction is illustrated schematically in Fig. 4.1, which emphasizes the analogy between decreasing temperature and increasing irradiation dose (dpa), both of which shift the fracture response toward brittle behavior

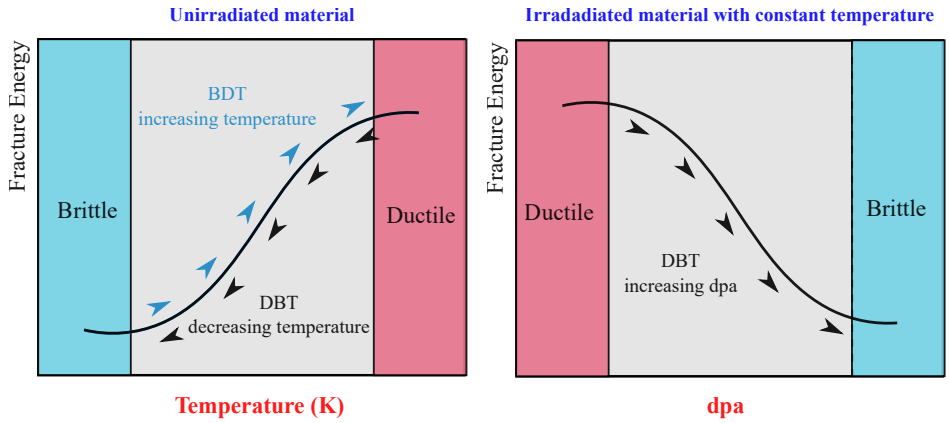

Figure 4.1: Schematic comparison of fracture transition behavior controlled by temperature and irradiation damage. In unirradiated materials (left panel), fracture behavior is governed by temperature, exhibiting a BDT with increasing temperature and a DBT with decreasing temperature. In irradiated materials (right panel), DBT occurs at nominally constant temperature as a function of increasing dpa, highlighting the distinct roles of thermal activation and radiation-induced defect accumulation.

by suppressing plastic energy dissipation.

The macroscopic signature of radiation-induced DBT is illustrated in Fig. 4.2, where increasing displacement-per-atom (dpa) results in pronounced hardening accompanied by a drastic reduction in uniform elongation (Nowak et al., 2023). This response reflects the loss of strain-hardening capacity and the premature onset of fracture caused by irradiation-induced defects that hinder dislocation activity.

The trends observed in Figs. 4.1 and 4.2 originate from atomistic-scale interactions between radiation-induced defects and crack-tip plasticity. Defects such as dislocation loops, voids, and

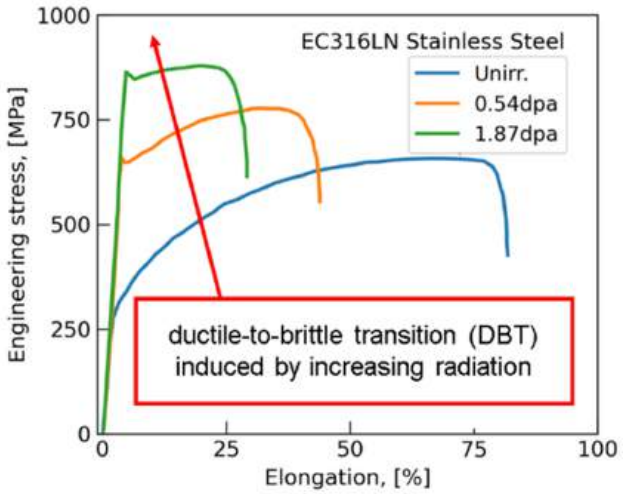

Figure 4.2: Representative stress–strain curves of EC316LN stainless steel at different irradiation doses, illustrating irradiation-induced DBT. Increasing dpa leads to higher yield stress and severely reduced elongation to failure (Nowak et al., 2023).

stacking fault tetrahedra act as strong barriers to dislocation motion, limiting crack-tip blunting and promoting localized deformation and crack advance. To resolve how these mechanisms govern the transition from stable, ductile crack growth to brittle-like fracture, MD simulations are employed in this work.

MD simulations provide direct insight into crack–defect interactions that are inaccessible to continuum approaches. In pristine configurations, cracks are blunted through dislocation emission and associated energy dissipation. In irradiated configurations, MD reveals suppressed dislocation activity, void-assisted crack advance, and increasingly tortuous crack paths. These atomistic mechanisms collectively underpin the reduction in fracture resistance and the emergence of irradiation-induced DBT observed at the macroscopic scale.

From a fracture mechanics perspective, irradiation shifts the balance between crack-tip energy dissipation and crack propagation. In unirradiated alloys, significant plastic work is expended at the crack tip, delaying fracture. Under irradiation, defect-induced restriction of dislocation mobility reduces plastic dissipation, allowing crack advance to dominate. This shift represents a fundamental change in fracture behavior and forms the central focus of the present chapter.

The motivation of this study is therefore to establish a quantitative and mechanistic link between radiation-induced defect evolution and DBT in fcc Fe–Ni–Cr alloys. By combining MD-based crack propagation simulations with energy-based fracture analyses, this chapter clarifies the atomistic origins of irradiation-assisted DBT in $Fe_{55}Ni_{19}Cr_{26}$, providing insight relevant to the assessment and design of radiation-tolerant structural materials for nuclear applications.

4.2 Simulation methodology

This section outlines the MD simulation approach used to investigate the effects of radiation-induced defects on fracture behavior in $Fe_{55}Ni_{19}Cr_{26}$ alloy. It is divided into two main parts: first, the preparation of irradiated samples with controlled displacement damage levels is described; second, the methodology for simulating crack propagation in these pre-defected samples is presented.

4.2.1 Simulation setup for irradiated samples

The irradiated configurations employed in this study were generated through MD simulations using the LAMMPS package (Plimpton, 1995; Thompson et al., 2022). Interatomic interactions were described by the EAM potential parameterized by Bonny et al. (Bonny et al., 2011) with Ziegler–Biersack–Littmark (ZBL) short-range corrections. This potential has been widely validated for Fe–Ni–Cr systems and offers reliable reproduction of defect energetics, stacking-fault energies, and mechanical behavior under irradiation (Béland et al., 2017; Dominguez-Gutierrez et al., 2022; Zhou et al., 2023; Ustrzycka et al., 2024). Its accuracy in capturing defect formation and short-range atomic interactions makes it particularly suited for modeling radiation damage in face-centered cubic (fcc) materials over a broad temperature range (0–900 K).

The alloy composition was selected as $Fe_{55}Ni_{19}Cr_{26}$, representative of the nominal chemistry of 310S stainless steel discussed in Section 2.1. A single-crystal cell oriented along primary (001) orientation was constructed using the Atomsk tool (Hirel, 2015) to provide the reference structure for irradiation and subsequent fracture simulations. The dimensions of the simulation box were determined through convergence tests, following approaches reported in earlier studies (Ustrzycka et al., 2024). This ensured that the chosen cell size was sufficiently large to accommodate the complete development of displacement cascades while minimizing artificial interactions between defects and their periodic images. Periodic boundary conditions were applied in all three directions during irradiation to reproduce bulk-like conditions and to eliminate surface effects, allowing the resulting defect populations to be representative of realistic irradiation behavior.

Irradiation was introduced using the PKA approach following procedures reported in previous studies (Nordlund et al., 2018b; von Toussaint et al., 2021; Zhou et al., 2023; Dominguez-Gutierrez et al., 2022; Ustrzycka et al., 2024). In each cascade, a randomly selected atom from the Fe, Ni, or Cr sublattice was assigned an initial kinetic energy of 10 keV, with recoil velocities scaled according to atomic mass. The velocity corresponding to this energy was computed using the Fe atomic mass and assigned in a randomly chosen direction. The simulations were performed under NVT conditions during each collision cascade, and following each cascade, the excess kinetic energy was dissipated using a Langevin thermostat to restore and stabilize the system temperature at 300 K. Following each cascade, the system was equilibrated to allow stabilization of surviving Frenkel pairs and defect clusters. Repeated cascades with randomized directions and positions were applied to generate statistically representative microstructures at increasing irradiation doses. In this study, a constant displacement threshold energy of $E_d = 40$ eV was used for all species, consistent with values reported for Fe, Ni, and Cr (Sellami et al., 2019; Anderson et al., 2024). While element-specific E_d values could be employed, this uniform choice ensured computational consistency across the ternary alloy.

Representative snapshots of the irradiated $Fe_{55}Ni_{19}Cr_{26}$ samples are shown in Fig. 4.3. To reach doses of 0.008, 0.038, 0.152, and 0.266 dpa, a total of 20, 100, 400, and 700 cascades were introduced, respectively. The progression from a pristine lattice to heavily irradiated states highlights the gradual buildup of a complex defect landscape, including vacancy clusters, dislocation loops, and void precursors. These defect structures form the essential link between cascade-induced microstructural changes and the mechanical response of the alloy under load.

To systematically quantify the microstructural changes, the evolution of defect densities was analyzed using the DXA to identify and classify dislocations, and a Voronoi-based tessellation method to detect and characterize voids, as implemented in OVITO (Stukowski and Albe, 2010). Fig. 4.4 shows the calculated densities of dislocation loops and voids as a function of irradiation dose. At low damage levels, the defect density increases gradually, reflecting the early stages of cascade recovery in which Shockley partial dislocations and small interstitial clusters dominate. Perfect dislocations are absent at 0.008 dpa, appearing only at higher doses as overlapping

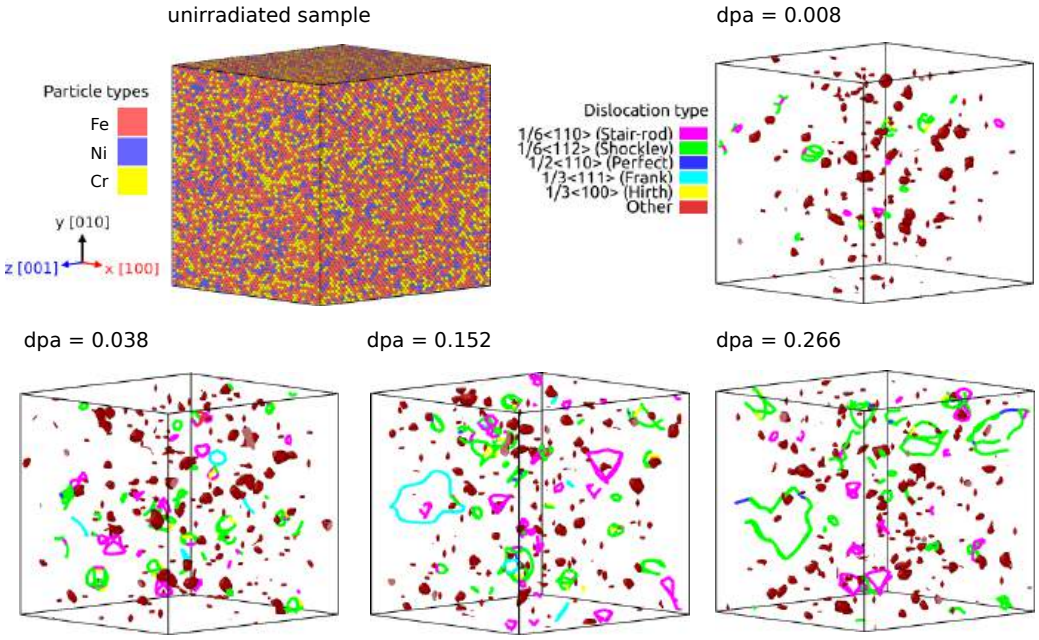

Figure 4.3: Representative snapshots of $Fe_{55}Ni_{19}Cr_{26}$ single-crystal cells after irradiation at different damage levels: (a) pristine, (b) low-dose, and (c) high-dose. Irradiation generates a hierarchy of defects, including vacancy clusters, dislocation loops, and voids.

cascades drive the transformation of partials into stable dislocation structures. The void density likewise increases steadily, beginning with isolated vacancy clusters and evolving into larger voids as cascades accumulate. The analysis accounts for voids of all sizes, capturing both nucleation sites and larger stable cavities.

At higher dpa levels, the accumulation of overlapping cascades produces a more interconnected defect network, characterized by the coexistence of perfect dislocations, partial

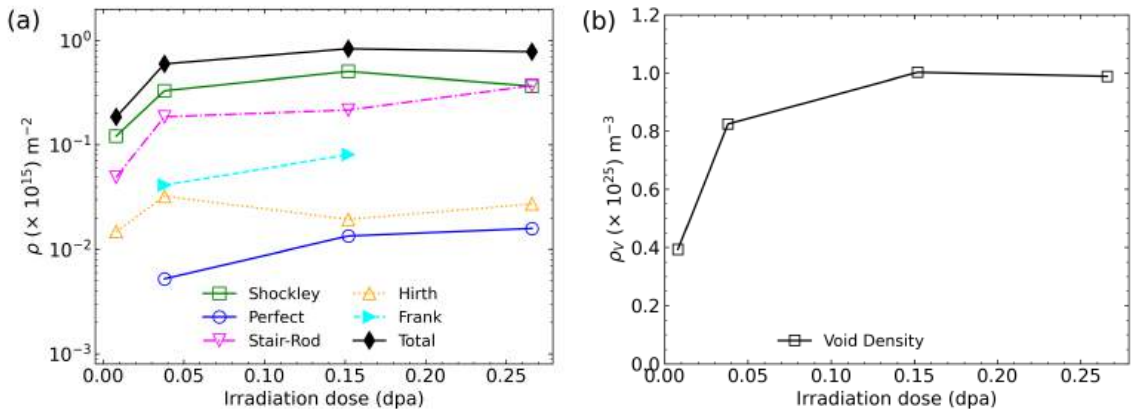

Figure 4.4: Evolution of radiation-induced defect densities in $Fe_{55}Ni_{19}Cr_{26}$ obtained from MD simulations of displacement cascades: (a) dislocation loop density and (b) void density as a function of irradiation dose. The results demonstrate a progressive increase in both dislocation and void populations with increasing dose, reflecting the accumulation and interaction of defects that underpin irradiation-induced embrittlement.

dislocations, and voids. The simultaneous growth of these populations results in defect–defect interactions, dislocation entanglement, and the emergence of complex defect topologies. Such features significantly impede dislocation motion, reduce available slip systems, and provide preferential sites for crack initiation and propagation.

Understanding how radiation-induced defects affect the elastic and mechanical properties of Fe–Ni–Cr alloys is crucial for establishing the relationship between defect accumulation and the resulting embrittlement behavior. Elastic constants not only describe the intrinsic stiffness and anisotropy of the lattice but also reflect the extent to which radiation-induced defects perturb interatomic bonding. To evaluate these effects quantitatively, the elastic constants and derived mechanical moduli of irradiated $Fe_{55}Ni_{19}Cr_{26}$ were computed using the Born matrix (BM) method, as detailed in Appendix A. The BM approach enables accurate determination of temperature-dependent elastic properties from atomistic simulations by combining the static lattice response with thermal stress fluctuations. The results reveal that increasing irradiation dose leads to a slight yet systematic reduction in the material's overall stiffness, indicating a mild elastic softening associated with the accumulation of radiation-induced defects. Despite these localized distortions, the fundamental mechanical integrity of the alloy remains largely preserved. This behavior suggests that the elastic response of the irradiated system is only marginally affected, demonstrating the alloy's resilience under irradiation and confirming the reliability of the Born matrix approach in capturing subtle changes in mechanical behavior.

The evolution of these microstructural features establishes the microscopic foundation of irradiation-induced embrittlement. By correlating defect accumulation with changes in elastic response, the irradiated configurations provide both structural and mechanical input for the subsequent fracture simulations. This integrated approach offers a direct connection between the microstructural evolution and the resulting fracture behavior under irradiation.

4.2.2 Simulation of fracture

The irradiated configurations obtained in the previous section were used to construct atomic-scale fracture models. A three-dimensional representation of the specimen geometry is shown in Fig. 4.5. To achieve the target dimensions required for fracture simulations, the irradiated cells were replicated along the x- and y-directions, resulting in a simulation box of $275 \times 282 \times 148$ Å^3. This system size was verified to be sufficient for resolving crack-tip plasticity, dislocation activity, and defect–crack interactions without introducing significant boundary artifacts, while maintaining computational efficiency.

After replicating each irradiated sample, a relaxation step was performed to ensure system stability under desired conditions. Initially, the atomic configuration was energy-minimized to reduce potential energy and relax internal stresses. This was followed by equilibration using a canonical NPT ensemble for 100 ps at zero pressure and a temperature of 300 K, allowing the system to adjust both atomic positions and box dimensions. This step allowed the system to

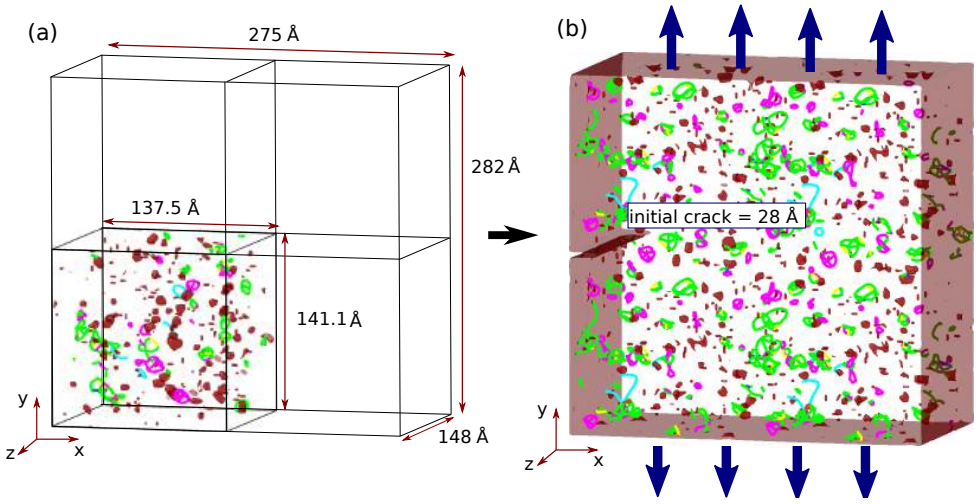

Figure 4.5: Schematic representation of the atomistic fracture model: (a) simulation box prepared by replicating an irradiated sample along the x- and y-axes, and (b) model with an initial crack introduced at the midplane and subjected to uniform tensile loading along the y-direction.

equilibrate under the target conditions before proceeding with crack creation and the subsequent deformation process.

The boundary conditions employed in the crack propagation simulations follow the constrained lateral support configuration established through a systematic boundary-condition analysis (see Appendix B). Periodic boundary conditions were applied along the thickness direction (z), whereas non-periodic boundaries were imposed along the x- and y-directions, corresponding to the crack propagation and applied loading directions, respectively (Krull and Yuan, 2011; Zeng et al., 2018; Xie et al., 2023). This mixed boundary-condition setup enables realistic crack opening while avoiding artificial interactions across free surfaces.

Tensile loading was imposed through two rigid grip layers located at the top and bottom of the specimen, each with a thickness of $2a$ (where $a = 3.526$ Å is the lattice constant). These layers were constrained to move as rigid bodies during deformation. Additional lateral stabilization was achieved by constraining atoms within side layers of thickness $1a$ at the left and right edges of the specimen, restricting their motion in the x-direction while allowing free movement in the y- and z-directions. This boundary configuration was selected based on a comparative assessment of alternative setups, including fully periodic, free, and shrink-wrapped boundary conditions, which demonstrated that lateral constraints are necessary to suppress residual deformation and prevent edge necking in the highly ductile alloy considered here (Appendix B).

Following equilibration and application of the boundary conditions, fracture simulations were conducted under the canonical (NVT) ensemble at 300 K to provide a stable thermal environment during deformation. The use of the NVT ensemble ensures controlled dissipation of the energy released at the crack tip and prevents unphysical temperature rise that could otherwise influence dislocation activity and bond-breaking processes.

A sharp Mode-I pre-crack of length 28 Å, corresponding to approximately 1/10 of the total

specimen length, was introduced at mid-depth from the left edge of the specimen by removing interatomic bonds (see Fig. 5.5). This crack-introduction method does not introduce artificial stress concentrations or structural artifacts before mechanical loading. This crack-to-length ratio lies within the range commonly adopted in molecular dynamics studies of tensile fracture, where the initial crack length is selected as a fraction of the specimen dimension (typically 1/10, 1/5, 1/4, or 1/3) (Ma et al., 2022). The crack extended through the entire thickness of the specimen along the z-direction, enabling a constrained three-dimensional representation of Mode-I fracture (Krull and Yuan, 2011).

Tensile deformation was applied along the y-direction by prescribing equal and opposite velocities to the top and bottom rigid grip layers, corresponding to a global strain rate of 10^9 s^{-1} (grip velocity 0.142 Å/ps). This symmetric loading configuration preserves Mode-I opening conditions and minimizes spurious bending or shear components. A time step of 1 fs was employed throughout the simulations, consistent with established molecular dynamics studies of crack propagation and dynamic fracture (Buehler, 2008; Krull and Yuan, 2011; Wang et al., 2015; Lu et al., 2020; Xie et al., 2023; Wang et al., 2021).

4.3 Physical basis of fracture mechanisms

After preparing the irradiated configurations and establishing the fracture simulation setup, we analyzed how radiation–induced defects modify the material response by combining atomistic visualization with defect mapping. The goal here is qualitative: to elucidate how crack–defect interactions differ between unirradiated and irradiated states, how these differences evolve with increasing irradiation dose through changes in defect spatial distribution and density, and how specific defect types such as voids, dislocation loops, and rigid obstacles influence the crack path and morphology. To that end, this section is organized into three parts. First, we examine the overall fracture behavior of unirradiated and irradiated structures to identify characteristic modes of crack growth across representative dpa levels. Second, we analyze the influence of specific, isolated defect types by embedding voids, dislocation loops, and rigid inclusions within otherwise identical samples to distinguish their individual roles in facilitating or impeding crack propagation. Finally, we synthesize these observations to interpret the governing mechanisms of defect-driven fracture and their contribution to the radiation-induced ductile-to-brittle transition (DBT) in the desired alloy.

4.3.1 Irradiated structure under crack propagation

Crack propagation results for both unirradiated (pristine) and irradiated specimens are illustrated in Fig. 4.6. In the pristine sample, crack advance is accompanied by extensive dislocation activity at the crack tip, which absorbs strain energy, blunts the crack front, and promotes stable crack growth. By contrast, the irradiated specimen (0.152 dpa) exhibits markedly different behavior: pre-existing defects generated during irradiation increase the dislocation density throughout the

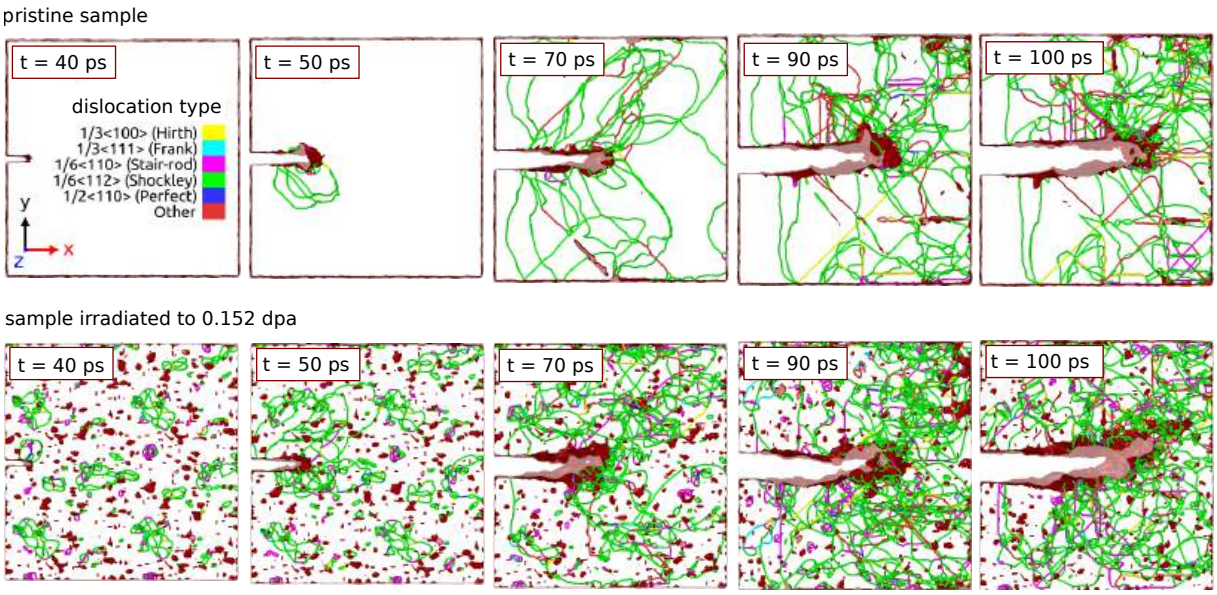

Figure 4.6: Snapshots of crack propagation under Mode-I loading at 300 K: (top) unirradiated sample showing extensive crack-tip plasticity and dislocation emission; (bottom) irradiated sample (0.152 dpa) showing reduced plasticity and accelerated crack advance.

crystal and constrain dislocation mobility near the crack tip. As a result, crack propagation occurs more rapidly, with localized void coalescence and reduced crack-tip blunting. These mechanisms reflect the irradiation-induced reduction in plastic dissipation, highlighting the microstructural origin of DBT in $Fe_{55}Ni_{19}Cr_{26}$ alloy.

To gain deeper insight into the deformation processes in both unirradiated and irradiated models, the equivalent shear strain distributions are illustrated in Fig. 4.7. The equivalent

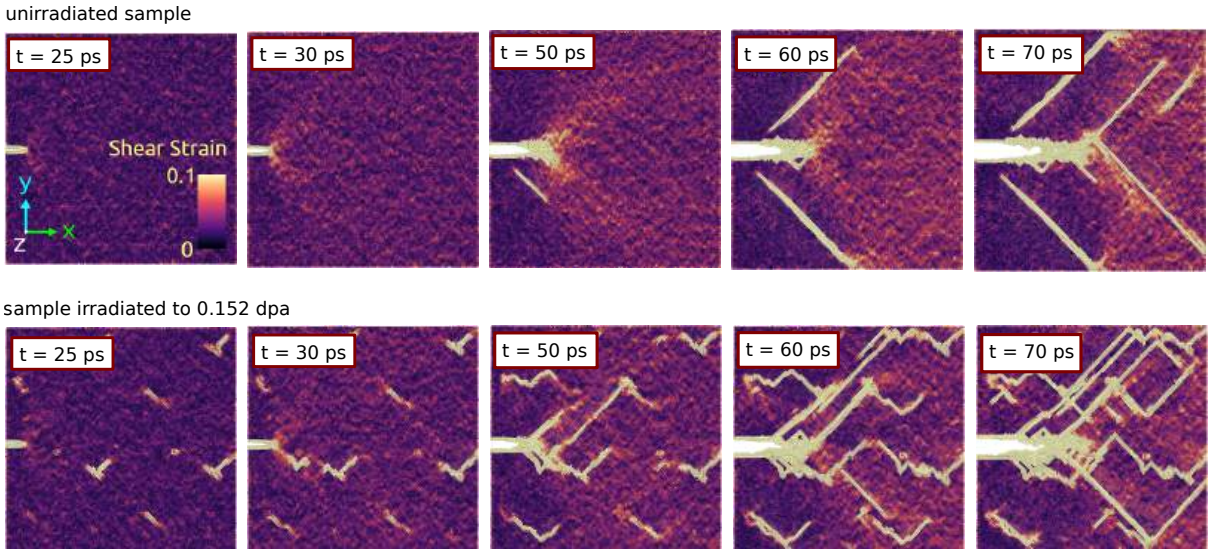

Figure 4.7: Evolution of the equivalent shear strain (von Mises invariant of the Green–Lagrangian strain tensor (Stukowski and Albe, 2010)) in a selected cross-section of unirradiated (top) and 0.152 dpa irradiated (bottom) samples.

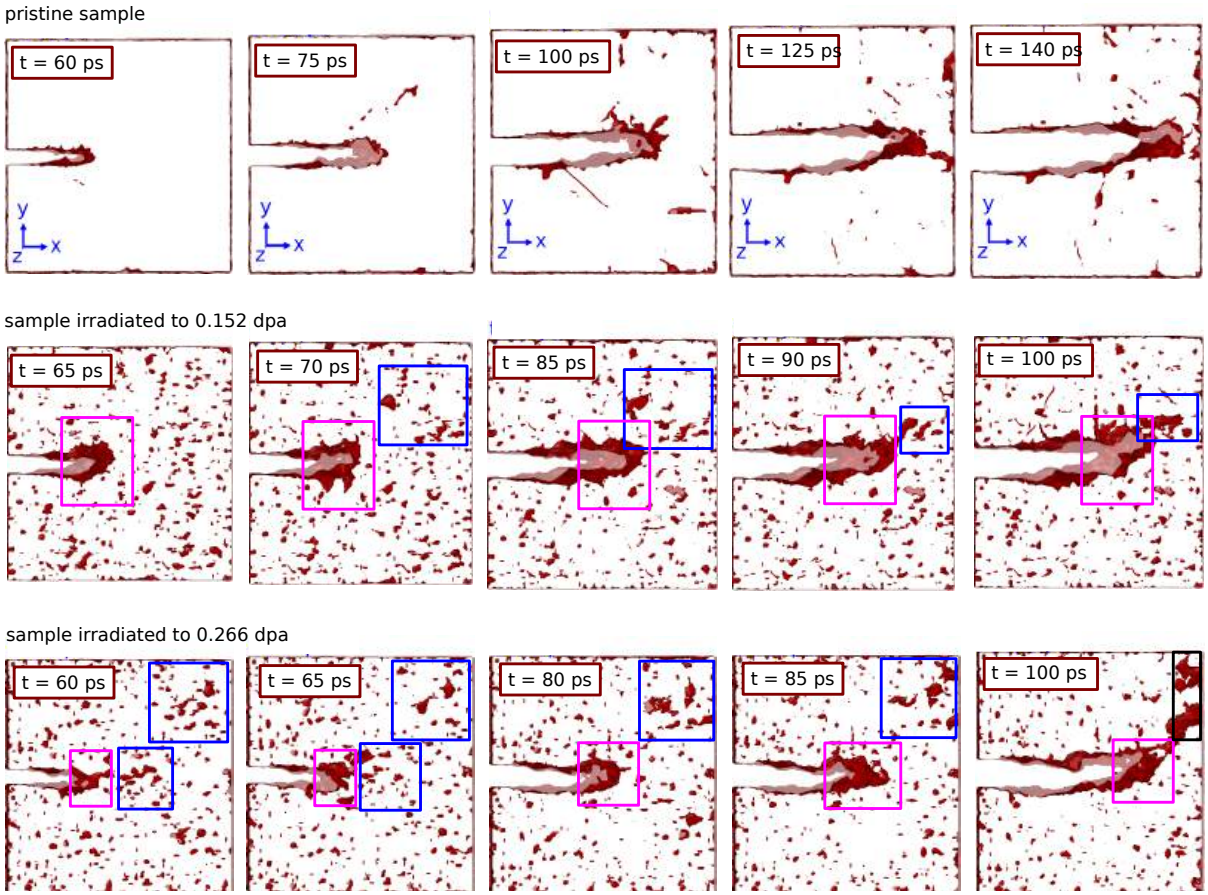

Figure 4.8: Influence of radiation-induced voids and dislocation obstacles on crack growth paths. The coalescence of voids is highlighted with a blue frame, the amorphous zone with a pink frame, and the formation of secondary cracks with a black frame.

shear strain, calculated in OVITO as the von Mises invariant of the Green–Lagrangian strain tensor (Stukowski and Albe, 2010), provides a quantitative measure of local plastic deformation. As shown in Fig. 4.7, the unirradiated sample exhibits a relatively uniform strain distribution, whereas the irradiated sample shows pronounced strain localization around radiation-induced defects, indicating that these defects act as strong stress concentrators and significantly influence the crack-tip deformation behavior.

Representative cases of crack evolution in pristine and irradiated samples are shown in Fig. 4.8, which illustrates the complex mechanisms governing crack advance in the presence of radiation-induced defects. The comparison highlights how irradiation modifies the fracture response, shifting it from a dislocation-mediated ductile regime toward void-assisted brittle fracture.

In the pristine sample (top row of Figs 4.6 and 4.8), the crack propagates smoothly with minimal resistance, accompanied by a well-developed plastic zone at the crack tip. Dislocation emission occurs actively from the tip region, where these dislocations accommodate the applied strain through localized plastic deformation. This process reduces the local stress intensity,

effectively impeding crack advance. This dislocation activity contributes to crack tip blunting (Fig. 4.8: at 75 to 100 ps), as evidenced by the gradual widening of the crack tip and the formation of a diffuse plastic zone (Fig. 4.6: at 70 to 100 ps).

In irradiated samples, however, the dynamics are altered significantly. At 0.152 dpa (middle row of Fig. 4.8), the crack path is frequently redirected by radiation-induced defects. Unlike the pristine sample, where dislocations are primarily emitted from the crack tip, the irradiated system exhibits additional dislocation activity originating at defect clusters. These defects both concentrate local strain and restrict the mobility of dislocations, thereby limiting plastic deformation and modifying the crack trajectory. As a result, an amorphous zone with a width of 2–5 nm develops at the crack tip (pink frame in Fig. 4.8), evolving dynamically as the crack propagates. Simultaneously, radiation-induced voids expand and coalesce under load, forming larger cavities that connect to the crack front (blue frames). These merged voids create weakened corridors that accelerate crack propagation and drive branching, much like void coalescence mechanisms reported in ductile metals (Tvergaard, 2011).

At a higher irradiation level of 0.266 dpa (bottom row of Fig. 4.8), the competition between blocking and acceleration becomes even clearer. Dense defect fields hinder crack advance by generating extended amorphous zones at the tip (pink frame), while large void clusters promote rapid crack growth by linking with the front (blue frame). In addition, a secondary crack emerges on the opposite side of the specimen (black frame), initiating around coalescing voids and eventually merging with the primary crack. This process yields a highly irregular crack path, with enhanced branching and roughness compared to both pristine and lower-dose cases.

Another critical mechanism is the interaction of the crack front with clusters of radiation-induced dislocation loops, illustrated in Fig. 4.9. These loops form entangled structures that act as strong barriers, reducing dislocation mobility and temporarily halting crack advance. When the crack front encounters these barriers, localized zones of increased resistance develop, which can block or deflect the crack tip. At higher doses, the competing effects of void coalescence and loop accumulation coexist, such that the main crack may be obstructed. In contrast, secondary cracks initiate in nearby void-rich regions (Figs. 4.8 and 4.9).

The above analysis highlights the contrasting roles of voids and dislocation loops in crack

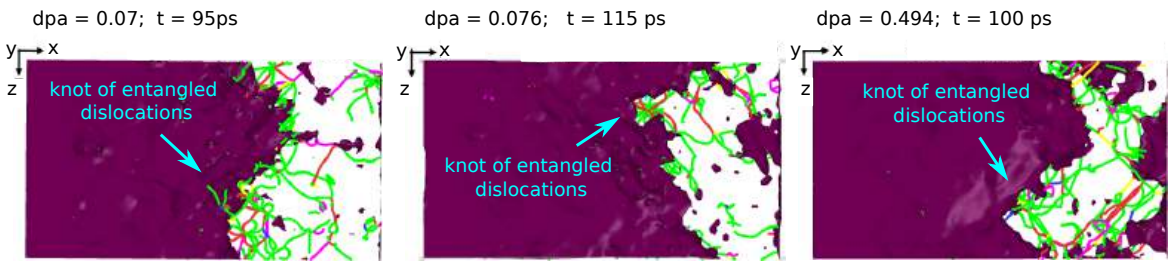

Figure 4.9: Clustering of radiation-induced dislocation loops near the crack front. The burgundy color indicates a cross-section of the crack in the x–z plane, highlighting a cross-sectional view of the crack.

propagation. Voids facilitate crack advance by reducing local cohesion, while dislocation loops act as barriers that slow down or block the crack front. At higher dpa levels, these effects can coexist—crack branching may occur when the main crack is obstructed by loop accumulations, while secondary cracks initiate in weakened regions around radiation voids (see Figs. 4.8 and 4.9). Together, these competing mechanisms contribute to the complex fracture morphology observed in irradiated materials.

4.3.2 Isolated defects impact on crack propagation

To better understand how specific radiation-induced defects influence crack dynamics, additional simulations were performed in which isolated defects were embedded within the fracture model. This approach allowed us to decouple individual mechanisms from the collective behavior observed in irradiated samples and to examine their effect on crack propagation under controlled conditions. The analysis considered representative defect types commonly reported in irradiated Fe–Ni–Cr alloys, including small and large voids, dislocation loops, and rigid inclusions. These defects were constructed using the Atomsk (Hirel, 2015) and LAMMPS (Thompson et al., 2022) packages by selectively removing atoms to generate voids of prescribed sizes, inserting extra half-planes or interstitial configurations to form dislocation loops, and embedding immobile atomic regions to represent rigid inclusions. Each defect type was introduced into a simulation cell of $275 \times 282 \times 148$ Å^3, consistent with the fracture setup described earlier in Section 4.2.2. The chosen geometries reflected typical defect dimensions observed experimentally: small voids with a diameter of 2.5 nm, large voids with a diameter of 5 nm, dislocation loops spanning 5 nm, and rigid inclusions with a diameter of 5 nm. In this framework, rigid inclusions were introduced as simplified models of highly entangled dislocation structures, acting as immobile barriers to crack advance.

The results, shown in Fig. 4.10, highlight the distinct roles of these defects in shaping crack behavior. When the crack front encountered small voids (top row), the voids acted as localized weak points in the lattice, reducing local cohesion and providing stress concentrators that accelerated crack advance. The crack preferentially links to the voids, lowering the effective fracture resistance and enabling growth along paths of least resistance. Larger voids (second row) intensified this effect: their increased size created extended weak regions that disrupted the crack path. As the crack merged with these voids, the advance was significantly accelerated, producing a more irregular morphology compared to the small-void case.

By contrast, dislocation loops (third row) displayed an opposite effect. These loops acted as barriers to crack motion, obstructing dislocation glide in the vicinity of the crack tip and temporarily halting propagation. When the crack front impinged on a loop, localized stress concentrations developed, increasing resistance and sometimes forcing the crack to deviate. Although additional dislocation activity was triggered near the loop, the overall effect was to slow or redirect the crack front. Rigid inclusions (bottom row) produced a similar but stronger

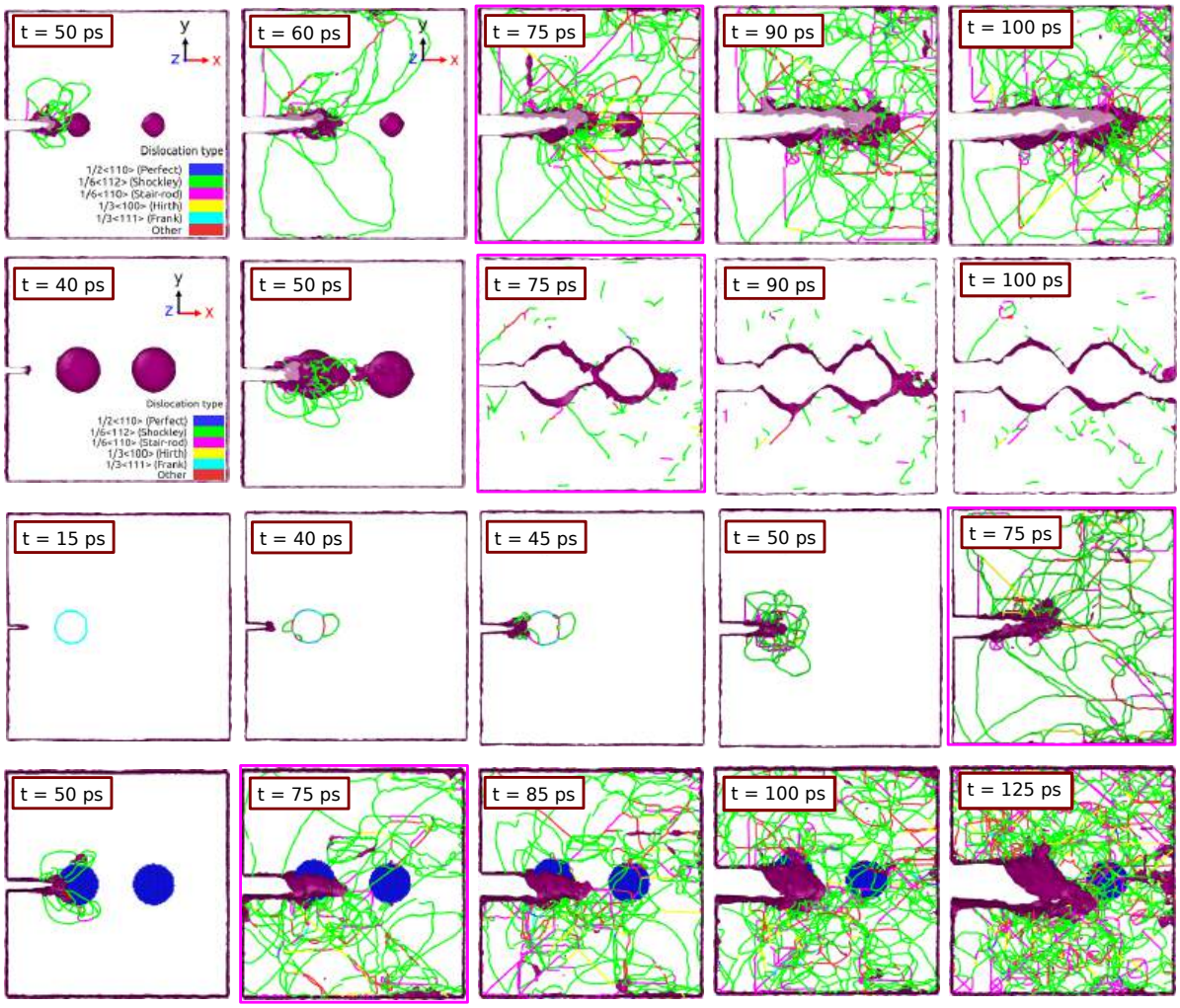

Figure 4.10: Fundamental mechanisms of isolated defect–crack interactions. Rows correspond to small voids (top), large voids, dislocation loop, and rigid inclusion (bottom). Frames outlined in pink correspond to the same simulation time (75 ps).

blocking effect. Since the inclusions were constrained against deformation, they behaved as immovable obstacles, forcing the crack to circumvent them. This led to highly tortuous and branched paths, accompanied by enhanced dislocation activity in the surrounding lattice.

These observations demonstrate the contrasting effects of different defect types. Voids act as facilitators of fracture, accelerating crack advance by reducing local cohesion and creating weak pathways. Dislocation loops and rigid inclusions, on the other hand, increase resistance at the crack tip, impeding or diverting the front. The comparison across defect types underscores the competition between facilitation and obstruction in irradiated materials: while voids promote brittle-like advance, loops and inclusions contribute to local hardening and path deflection. Together, these mechanisms illustrate how the microstructural landscape introduced by irradiation governs the macroscopic fracture morphology.

Importantly, these isolated-defect analyses complement the collective results presented in Section 4.3.1. While irradiated samples exhibit the combined effects of void growth, coalescence,

and loop entanglement, the isolated cases reveal the fundamental mechanisms at play. This dual approach provides a more complete understanding of how radiation-induced defects drive the DBT in the alloy.

4.3.3 Interpretation of defect-driven fracture mechanisms in irradiated materials

Building directly on the fracture simulations reported above, we now interpret how radiation-induced defects reorganize the crack-tip process zone and steer the transition from ductile to brittle response in Fe–Ni–Cr alloys. The atomistic results reveal that fracture is governed not by a single dominant mechanism, but by a competition among defect-facilitated and defect-impeding processes that co-evolve as dose increases. In what follows, we synthesize the salient interactions observed at the crack tip and along the evolving crack path, emphasizing the roles of voids, dislocation loops, defect-mediated dislocation nucleation, amorphization, and branching.

First, voids consistently act as local weakening agents that lower the resistance to advance. By reducing the local stress required for bond rupture, isolated voids provide "easy" corridors for the crack, while clusters of voids further diminish cohesion through coalescence ahead of the tip. This coalescence accelerates growth and corrugates the fracture surface as the crack repeatedly links with nearby cavities and follows paths of least resistance. The same tendency toward void-assisted advance has been reported in atomistic studies of artificially introduced porosity, where void spacing and size were shown to modulate tip shielding or focusing effects (Wang et al., 2015); related work in Al demonstrated that vacancy clusters alter stress fields and promote crack-tip blunting or reorientation (Chandra et al., 2016). In our simulations, this facilitation manifests as faster local velocities and more tortuous trajectories wherever the void density is high.

By contrast, dislocation loops predominantly impede the crack. Formed by clustered interstitials, these sessile defects obstruct dislocation glide in the crack-tip region, intensify local stress concentrations, and can transiently arrest the front. The impingement of the crack on a loop often triggers additional dislocation emission from the tip, providing limited plastic dissipation. However, the mobility of those emitted dislocations is curtailed by surrounding defects (other loops, nearby voids), which curbs the efficacy of plastic flow and biases the response toward a brittle-like advance. Earlier atomistic studies on ideal crystals captured elements of this interplay, such as crack–dislocation interactions, cross-slip, and plastic-zone development near the tip (Bitzek and Gumbsch, 2008; Sheng et al., 2023a,b), yet did not include the dense, irradiation-generated loop populations that are fundamental to the hindered plasticity observed here. In our irradiated microstructures, loop clusters can act like rigid inclusions, deflecting the path and promoting roughness and branching.

A third, dual-action role of radiation defects emerges through defect-mediated dislocation nucleation. Void and loop clusters serve as preferred sites for dislocation emission under load, raising the local dislocation density while simultaneously cluttering glide pathways. This

"source–obstacle" duality reduces net plastic accommodation at the tip and biases the energy budget toward crack advance rather than dissipation. Our prior shear-deformation simulations of irradiated $Fe_{55}Ni_{19}Cr_{26}$ alloy exhibited the same behavior, nucleation at defect clusters coupled to restricted mobility (Ustrzycka et al., 2024), underscoring that the mechanism persists across loading modes.

A fourth feature is the development of amorphous, highly disordered zones at and just ahead of the advancing tip, particularly in defect-dense regions. These zones transiently absorb energy and can delay advance, but they also suppress conventional crystalline plasticity and promote secondary damage initiation. Similar amorphization-assisted shielding has been identified under high contact stresses in Si, where local disorder reconfigures the stress state and suppresses crack advance (Li et al., 2024). In the present fcc alloy, the net effect is mixed: short-lived shielding followed by local embrittlement once the amorphous pocket connects to neighboring weak sites such as voids.

Finally, elevated defect densities (especially loop clusters interspersed with voids) promote crack branching and the nucleation of secondary cracks that subsequently coalesce with the main front. This produces irregular surfaces and a larger fractured area. Such branching is well known in brittle MD systems (Nakano et al., 1995; Luo et al., 2021) and, under specific cyclic or constrained conditions, even in nominally ductile metals (Liu et al., 2024). In our irradiated Fe–Ni–Cr, branching is the macroscopic signature of the microstructural competition: loop barriers divert and slow the front, while adjacent void-rich corridors invite rapid local advance, spawning side cracks that later merge.

Taken together, these mechanisms explain the irradiation-assisted DBT captured in our simulations. Where the pristine alloy relies on sustained dislocation emission and tip blunting to dissipate energy, the irradiated microstructure replaces this capacity with a heterogeneous landscape of weak (void) and strong (loop/inclusion-like) sites. The former accelerate advance and roughen the path; the latter restricts plasticity and redirects the tip. The ensuing reduction in effective plastic dissipation shifts the balance toward cleavage-like propagation, elevates crack velocities locally, and increases branching probability. Thus, embrittlement in Fe–Ni–Cr alloys under irradiation is not merely a matter of higher strength or reduced uniform elongation; it is the emergent outcome of coupled, dose-dependent defect–crack interactions that reconfigure the fracture process zone and reweight the competition between crack driving forces and dissipative mechanisms.

4.4 Energy-based fracture analysis: critical energy release rate

Following the detailed atomistic analysis of defect–crack interactions, it is useful to express the observed mechanisms in terms of a global energetic measure that quantifies the fracture resistance of irradiated $Fe_{55}Ni_{19}Cr_{26}$ alloy. The *critical energy release rate* (G_c) serves this purpose by integrating the local effects of void coalescence, dislocation-loop blocking, and

amorphization into a single parameter that reflects the total energy required for crack advance. This approach provides a direct atomistic interpretation of irradiation-induced embrittlement and the ductile-to-brittle transition (DBT) in energetic terms.

4.4.1 Framework for energy-based fracture analysis

In an ideal brittle material, crack propagation is governed solely by the energy required to create new surfaces as atomic bonds are broken. The energy balance in this case is given by the Griffith relation, where the critical energy release rate equals twice the surface energy, $G_c = 2\gamma_s$. Here, γ_s represents the surface energy per unit area associated with the formation of two new free surfaces during fracture.

However, in metallic systems such as Fe–Ni–Cr alloys, fracture rarely occurs without plasticity. Crack propagation is accompanied by dislocation nucleation, glide, and interactions near the crack tip, which dissipate additional energy. To capture this behavior, Orowan (1945), Jokl et al. (1980), and Beltz and Rice (1992) expanded the energy balance by introducing a plastic work term, w_p, that accounts for irreversible energy dissipation associated with dislocation motion and local deformation. The total fracture resistance can therefore be expressed as:

$$G_c = 2\gamma_s + w_p, \tag{4.1}$$

where $2\gamma_s$ represents the intrinsic energy of atomic bond rupture and w_p denotes the energy dissipated through dislocation-mediated plasticity.

The competition between cleavage and dislocation emission at the crack front, as formulated by Beltz and Rice (1992), establishes a natural link between atomic-scale mechanisms and fracture energy. The unstable stacking fault energy defines the threshold for dislocation emission, while radiation-induced defects strongly modify this balance by either suppressing or facilitating local plasticity. In irradiated alloys, these defects act simultaneously as dislocation sources and obstacles, altering w_p and thereby controlling the effective fracture resistance.

Building on this concept, Xu and Demkowicz (2020) and Barik et al. (2024) proposed a practical atomistic formulation for calculating G_c directly from MD simulations. In this approach, the critical energy release rate is determined as the increment of dissipated energy per increment of crack surface area:

$$G_c = \frac{\partial E_{dis}}{\partial A_{crack}} \approx \frac{dW - dU}{dA_{crack}}, \tag{4.2}$$

where dW is the incremental external work applied to the system and dU is the corresponding change in the total internal energy (potential plus kinetic). The term $(dW - dU)$ thus represents the energy dissipated through irreversible atomic processes, including bond breaking, plastic flow, and defect rearrangement.

Under isothermal conditions maintained by a thermostat, the dissipated energy increment can be related to the change in Helmholtz free energy, $dE_{dis} = dW - dF$, where $dF = dU - T\,dS$.

Because the entropy change dS cannot be computed in the present framework, it is commonly assumed that $dF \approx dU$, following Xu and Demkowicz (2020) and Barik et al. (2024). This assumption implies that most of the plastic work is converted to heat and removed by the thermostat, while only a minor fraction remains stored in the lattice (Kositski and Mordehai, 2021; Stimac et al., 2022). Consequently, Eq. (4.2) provides an effective way to evaluate G_c from MD simulations by monitoring both the external work and internal energy variations during controlled crack propagation.

4.4.2 Effects of radiation on fracture energy

Radiation-induced defects modify fracture behavior by simultaneously weakening atomic cohesion (affecting surface energy, γ_s) and impeding dislocation motion (affecting plastic work, w_p). The spatial distribution, type, and density of these defects determine their cumulative effect on fracture resistance, defining the competition between brittle bond rupture and plastic energy dissipation during crack growth.

The critical energy release rate can therefore be expressed as a function of irradiation dose (dpa) and temperature, which control defect density and thermal activation, respectively:

$$G_\mathrm{c}(\mathrm{dpa}, T) = 2\gamma_\mathrm{s}(\mathrm{dpa}, T) + w_\mathrm{p}(\mathrm{dpa}, T). \tag{4.3}$$

While temperature primarily influences w_p through thermally activated dislocation glide, irradiation governs it through the accumulation of defects that restrict dislocation mobility and alter deformation pathways. This interplay defines the irradiation-induced DBT, where reduced plastic dissipation leads to a brittle fracture response.

To quantify the surface energy term $\gamma_\mathrm{s}(\mathrm{dpa}, T)$, a lower bound can be estimated from the separation energy $2\gamma_\mathrm{sep}(\mathrm{dpa}, T)$:

$$2\gamma_\mathrm{s}(\mathrm{dpa}, T) \geq 2\gamma_\mathrm{sep}(\mathrm{dpa}, T), \tag{4.4}$$

where γ_{sep} represents the idealized surface creation energy under perfect cleavage conditions, without atomic relaxation or plastic rearrangement.

An upper bound for γ_s can be obtained from simulations at absolute zero ($T = 0$ K), where thermal activation and plasticity are suppressed ($w_\mathrm{p} \approx 0$):

$$2\gamma_\mathrm{s}(\mathrm{dpa}, T) \leq G_\mathrm{c}(\mathrm{dpa}, 0K). \tag{4.5}$$

At finite temperatures ($T > 0$ K), the plastic work contribution can then be determined as:

$$w_\mathrm{p}(\mathrm{dpa}, T) = G_\mathrm{c}(\mathrm{dpa}, T) - 2\gamma_\mathrm{s}(\mathrm{dpa}, T), \quad 2\gamma_\mathrm{sep}(\mathrm{dpa}, T) \leq 2\gamma_\mathrm{s}(\mathrm{dpa}, T) \leq G_\mathrm{c}(\mathrm{dpa}, 0\mathrm{K}). \tag{4.6}$$

This formulation isolates the energy dissipated by dislocations as they interact with radiation-induced defects, providing a direct atomistic measure of plastic accommodation under irradiation.

Thus, radiation-induced DBT can be described as a decrease in $w_{\mathrm{p}}(\mathrm{dpa}, T)$ with increasing irradiation dose (dpa). Radiation-induced defects constrain dislocation motion and reduce the extent of plastic deformation at the crack tip, shifting the fracture mechanism toward bond-dominated propagation. Two characteristic regimes emerge:

- *High* $w_{\mathrm{p}}(\mathrm{dpa}, T)$ – *ductile regime:* dislocation activity dominates; the crack tip is shielded by emitted dislocations, resulting in gradual crack advance and extensive blunting.
- *Low* $w_{\mathrm{p}}(\mathrm{dpa}, T)$ – *brittle regime:* defect hardening severely limits dislocation motion; the crack propagates primarily by atomic bond rupture, producing a sharp and accelerated advance.

This energetic analysis complements the mechanistic findings from MD simulations, showing that irradiation-induced embrittlement in Fe–Ni–Cr alloys originates from a progressive reduction in the plastic energy dissipation term w_{p}, while the intrinsic bond-breaking energy $2\gamma_{\mathrm{s}}$ remains comparatively stable.

4.4.3 Energy dissipation in irradiated materials

Building on the preceding analysis of $G_{\mathrm{c}}(\mathrm{dpa}, T)$, we now quantify how irradiation modifies the balance between surface creation and plastic dissipation during crack advance, using only atomistic quantities extracted from the simulations. By tracking the internal energy U, the external work W, and the stress–strain response, we evaluate the dissipated energy and relate it to the projected crack area to obtain G_{c}, and then decompose it into $2\gamma_{\mathrm{s}}$ and w_{p}.

To estimate the plastic work $w_{\mathrm{p}}(\mathrm{dpa}, T)$ via Eq. (4.6), we require the near-zero-temperature reference $G_{\mathrm{c}}(\mathrm{dpa}, 0\ K)$. Practically, we approximate this quantity by performing fracture simulations at $T = 10\ K$:

$$G_{\mathrm{c}}(\mathrm{dpa}, 10\,K) \approx G_{\mathrm{c}}(\mathrm{dpa}, 0\,K)\,, \tag{4.7}$$

which suppresses thermally activated dislocation processes and yields a near-brittle reference consistent with isolating the surface-energy contribution in Eq. (4.6). In turn, comparing G_{c} at $T = 10\ K$ and at a higher temperature (here $T = 300\ K$) enables us to quantify the additional dissipation attributable to plasticity.

Fig. 4.11 contrasts the equivalent shear strain fields for specimens irradiated to 0.07 dpa at 300 K (top row) and 10 K (bottom row). At 300 K, deformation spreads broadly with pronounced localization around the crack tip and radiation-induced defects, consistent with thermally assisted dislocation motion and enhanced dissipation. At 10 K, strain concentrates sharply near the tip and at defect sites, while the surrounding crystal remains largely undeformed, indicating restricted

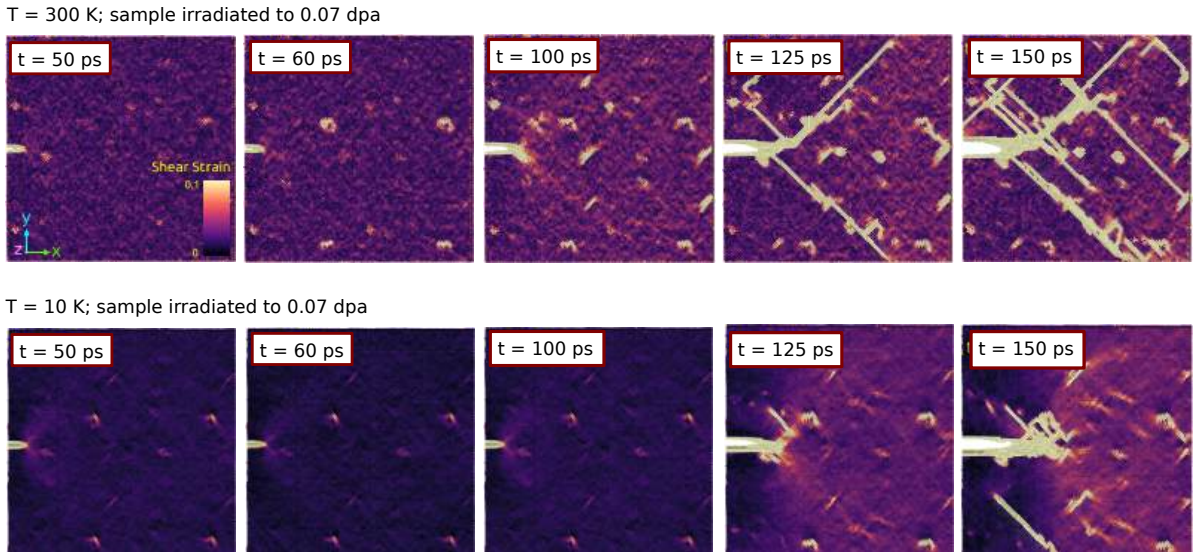

Figure 4.11: Evolution of the equivalent shear strain (von Mises invariant of the Green–Lagrangian strain tensor (Stukowski and Albe, 2010) in a selected cross-section of the samples irradiated to 0.07 dpa at 300K (top) and 10K (bottom).

dislocation mobility and a more brittle response. This comparison supports the use of γ_{sep} and low-T simulations as a near-brittle reference for approximating $G_c(\mathrm{dpa}, 0\ K)$ in Eq. (4.6).

The evolution of internal energy $\Delta U = U - U_0$ (red), external work W (blue), and stress–strain response (black) for unirradiated and irradiated samples (0.008, 0.038, 0.152 dpa) at 300 K

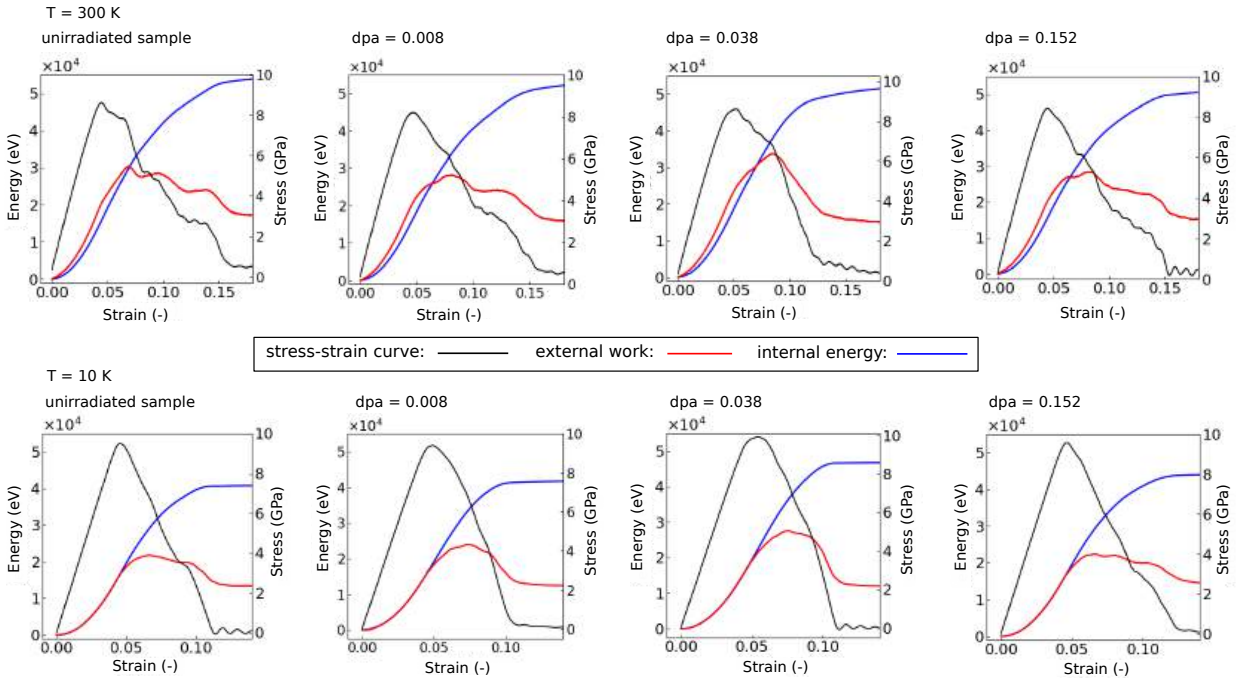

Figure 4.12: Stress–strain curves and energy evolution for different irradiation levels at 300 K (top) and 10 K (bottom), showing internal energy ΔU (red), external work W (blue), and stress–strain response (black).

and 10 K is shown in Fig. 4.12. At 300 K, the post-peak stress–strain curves often exhibit discrete drops, reflecting transient arrests when the crack front meets entangled dislocation structures (cf. Fig. 4.9), accompanied by corresponding features in ΔU as energy is reallocated between bond rupture and dislocation activity. The unirradiated case shows a post-yield plateau indicative of a well-developed plastic zone. With irradiation, especially at 0.008 and 0.152 dpa, stress drops after yielding become sharper, signaling defect-dominated fracture with curtailed plastic dissipation.

A brief remark on the energy balance under isothermal conditions: during the initial elastic regime, ΔU can slightly exceed W due to the thermostat supplying heat ($Q = \Delta U - W > 0$) to maintain the target temperature under the NVT ensemble. Once inelastic processes initiate (overall strain $\gtrsim 0.04$), the sign reverses ($Q < 0$), and heat is extracted by the thermostat as plastic dissipation develops. At 10 K, ΔU tracks W closely in the elastic regime and the thermostat exchange is negligible.

Fig. 4.13 plots the heat extracted by the thermostat, $-Q = W - \Delta U$, versus the projected crack surface area A (projection on the x–z plane), for all dpa levels at 300 K and 10 K. The initial drop in $-Q$ at 300 K (absent at 10 K) corresponds to the purely elastic stage, during which A remains constant while the thermostat supplies heat ($Q > 0$). Following Xu and Demkowicz (2020), in the quasi-steady propagation regime the heat removed equals the dissipated energy, $dE_{\text{dis}} = -dQ$, so that the slope $d(-Q)/dA$ gives G_c via Eq. (4.2). We exclude the initial (blue) interval, which contains transient plastic-zone build-up, and the terminal (pink) interval, where the front interacts with the simulation boundary.

The resulting G_c values are summarized in Fig. 4.14(a) for 300 K (red) and 10 K (blue).

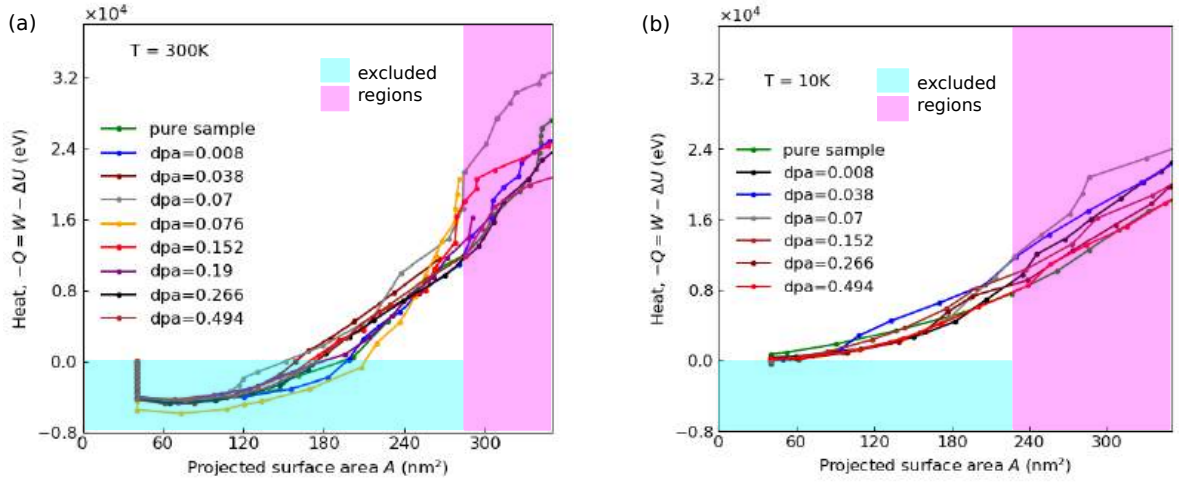

Figure 4.13: Heat taken from the system $(-Q = W - \Delta U)$ versus projected crack surface area A for various dpa levels at (a) 300 K and (b) 10 K. Blue and pink shaded regions denote excluded intervals corresponding to initial plastic zone development and final boundary effects, respectively. The initial drop in $-Q$ observed at 300 K (but absent at 10 K) corresponds to the elastic deformation stage.

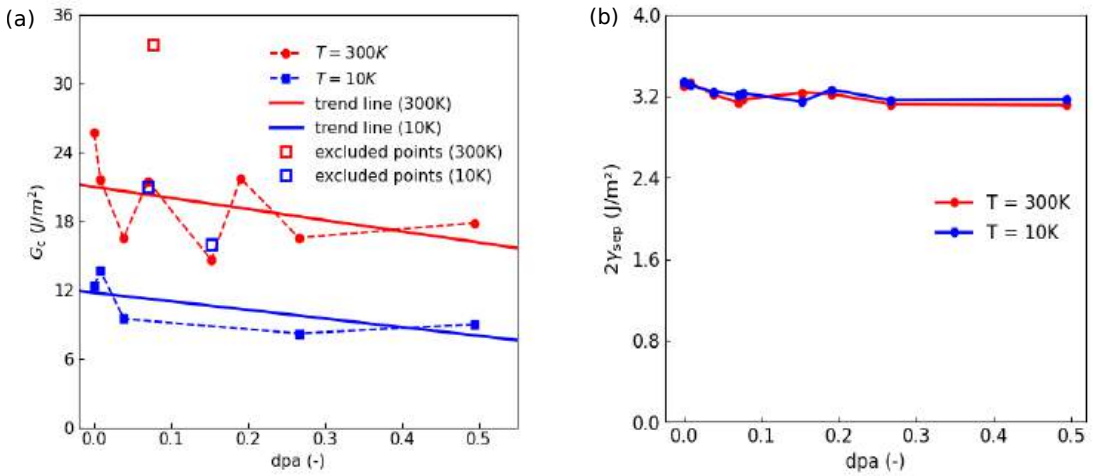

Figure 4.14: (a) Critical energy release rate G_c as a function of irradiation level (dpa) at different temperatures: 300K (dashed red line) and 10K (dashed blue line), with solid lines indicating approximation curves. (b) Separation energy $2\gamma_{sep}$ for crack surface formation as a function of dpa.

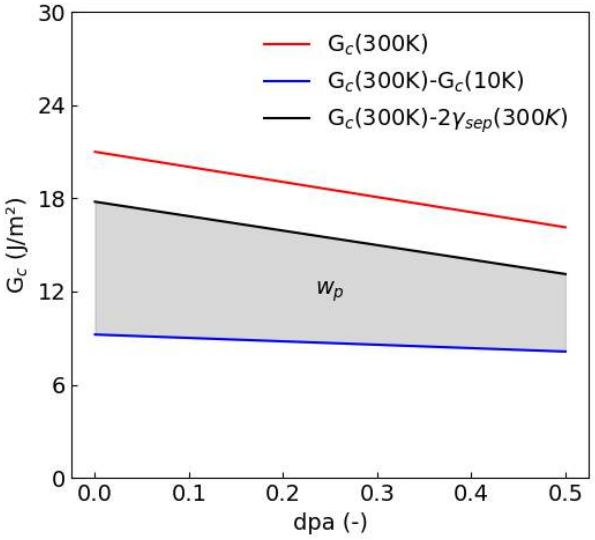

Figure 4.15: Plastic work, w_p, as a function of the irradiation dose. The red curve represents $G_c(300K)$, the blue curve shows the difference between the total critical energy release rate at T=300K and the critical energy release rate at T=10K, and the black curve denotes $G_c(300K) - 2\gamma_{sep}(300K)$, see Fig. 4.14. The shaded region highlights the estimated range of values of the plastic work, w_p.

Solid lines denote linear trends; outliers (empty squares) correspond to rare events where strong defect clusters (e.g., loop entanglements) cause anomalously high resistance (cf. Fig. 4.9). Overall, G_c decreases with dpa, revealing a progressive loss of fracture resistance as irradiation accumulates. Fig. 4.14(b) shows $2\gamma_{sep}$ versus dpa; its weak temperature and dose dependence indicates that the intrinsic separation energy remains comparatively stable, while the dominant irradiation effect acts through the dissipation channel.

Finally, Fig. 4.15 aggregates these results to bound the plastic work $w_p(dpa, T)$. The red curve is $G_c(300\,K)$ (total energy for advance at 300 K). The blue curve, $G_c(300\,K) - G_c(10\,K)$,

provides a lower bound on w_p, while the black curve, $G_c(300\,K) - 2\gamma_{sep}(300\,K)$, gives an upper bound. The shaded band between these curves shows that w_p declines systematically with dpa, quantifying the irradiation-induced suppression of dislocation-mediated dissipation that underpins the DBT identified in the mechanism-level analysis.

4.5 Comprehensive discussion of radiation-induced fracture behavior

This chapter provides a comprehensive atomistic investigation of the fracture behavior of irradiated $Fe_{55}Ni_{19}Cr_{26}$ alloy, elucidating how radiation-induced defects govern the progressive transition from ductile to brittle failure. The simulated microstructures reproduce the characteristic damage accumulation observed under neutron irradiation, enabling direct examination of how dispersed radiation-induced defects influence crack propagation and restrict plastic deformation (Ayanoglu and Motta, 2022; Pareige et al., 2022). Although the limited defect density achievable in atomistic simulations prevents the observation of fully brittle failure, the observed embrittlement trends capture the essential physical mechanisms that drive this transition in irradiated materials.

The results reveal that the fracture process in irradiated alloys is controlled by a complex interplay of mechanisms, as detailed in Section 4.3. Radiation-induced voids act as local weak zones, promoting crack advance by lowering the cohesive strength and forming preferential paths for coalescence. Dislocation loops, in contrast, serve as barriers that impede dislocation motion, deflect crack trajectories, and encourage crack branching. At higher irradiation levels, the accumulation of defect clusters and the formation of amorphous zones at crack tips suppress plasticity and promote cleavage-like fracture. The presence of dense defect networks leads to secondary cracking and coalescence, producing irregular fracture surfaces and enhanced roughness. Additionally, localized stress concentrations generated by defects intensify crack-tip stresses, further influencing the morphology and kinetics of crack growth. Collectively, these mechanisms shift the balance between plastic deformation and bond rupture toward the latter, producing an irradiation-induced embrittlement response.

The combination of atomistic simulations and energy-based fracture analysis demonstrates that irradiation embrittlement arises from a suppression of plastic dissipation, mediated by the evolving defect structure that constrains dislocation mobility and alters crack propagation dynamics. To quantify this effect, the total fracture resistance is expressed through the critical energy release rate, G_c, which is decomposed into two key contributions: (i) the surface energy, γ_s, representing the intrinsic energy required for atomic bond rupture and new surface formation, and (ii) the plastic work, w_p, associated with dislocation activity and other inelastic deformation processes.

The intrinsic surface energy γ_s was estimated using two bounding approaches: the ideal separation energy ($2\gamma_{sep}$), which represents the lower limit corresponding to purely brittle cleavage, and the critical energy release rate at low temperature (G_c at 10 K), which approximates the

upper limit corresponding to near-brittle conditions with minimal plasticity. At 10 K, dislocation mobility is highly restricted, allowing $G_c(10K)$ to serve as a near-brittle reference. The plastic work w_p was determined by comparing the fracture energy at 300 K, where thermally activated dislocation motion contributes to energy dissipation, with the low-temperature reference at 10 K. This comparison isolates the portion of the total fracture energy attributed to plastic deformation and dislocation-mediated processes as they interact with irradiation-induced defects.

This energy-based interpretation provides a robust and transferable framework for evaluating irradiation embrittlement. The approach is not restricted to any specific temperature pair, as long as the lower temperature captures near-brittle behavior and the higher temperature preserves active plasticity. The results demonstrate that with increasing irradiation dose, the plastic contribution w_p diminishes significantly, reflecting a direct link between irradiation hardening, defect accumulation, and the loss of dislocation-mediated energy dissipation. Consequently, the overall fracture energy G_c decreases, signifying reduced crack resistance and the onset of a ductile-to-brittle transition. This quantitative framework establishes a clear correlation between microstructural damage and the macroscopic manifestation of radiation-induced embrittlement.

Key contributions and insights:

- *Defect-driven fracture pathways:* The study identifies and categorizes the principal mechanisms governing crack propagation in irradiated microstructures. Voids act as facilitators of fracture, accelerating crack advance through coalescence and stress concentration, whereas dislocation loops impede propagation by obstructing slip and deflecting the crack front. This competition between facilitation and obstruction underpins the transition from ductile tearing to brittle cleavage as dpa increases.

- *Microstructural–mechanical linkage:* A direct correlation is established between defect density, crack morphology, and energy dissipation. This connection links atomistic defect evolution to the macroscopic response, providing a unified interpretation of how irradiation modifies fracture resistance through microstructural reconfiguration.

- *Energy-based embrittlement criterion:* Building on the atomistic formulation of Xu and Demkowicz (2020), the critical energy release rate G_c is decomposed into its brittle (γ_s) and plastic (w_p) components to quantify how irradiation redistributes the fracture energy balance. This methodology introduces an energetically grounded criterion for assessing embrittlement in irradiated alloys.

- *Quantitative characterization of irradiation-induced DBT:* The progressive reduction in both G_c and w_p with increasing dpa provides a quantitative description of the irradiation-induced ductile-to-brittle transition. Although the effect is moderate in the present MD simulations due to the limited defect densities achievable, higher irradiation doses typical of reactor conditions are expected to amplify this transition substantially.

These results pertain specifically to austenitic Fe–Ni–Cr alloys with fcc lattice, in which defect distributions are relatively isotropic due to uniform displacement threshold energies and minimal channeling effects. In contrast, ferritic–martensitic steels used in advanced nuclear systems possess a body-centered cubic (bcc) structure with low nickel content to mitigate transmutation and helium accumulation. While such structural and compositional differences influence the details of defect evolution and slip behavior, the fundamental embrittlement mechanisms identified here, dislocation pinning, void coalescence, and crack branching, remain universally relevant. Consequently, the findings presented for fcc $Fe_{55}Ni_{19}Cr_{26}$ alloy extend the mechanistic understanding of irradiation-induced embrittlement to a broader class of structural materials used in nuclear environments.

4.6 Statement of author contributions

The work presented in this chapter forms part of a collaboratively developed research project and builds upon results reported in a co-authored publication, with the analysis presented here stemming from Ustrzycka et al. (2025).

The computational fracture framework developed in this chapter constitutes a major original scientific contribution of this thesis and was fully conceived, implemented, and executed by the author.

This includes the development of the complete atomistic crack-propagation framework, the design and implementation of boundary conditions and loading protocols, the selection and physical justification of the statistical ensemble for fracture simulations, and the execution of all crack propagation calculations using a dedicated LAMMPS-based simulation workflow developed by the author.

The complete simulation script, authored and fully implemented by the author, together with the boundary and loading specifications employed in these fracture simulations, is documented in Appendix G. All supplementary material presented in Appendices A–C was prepared by the author as part of this thesis.

Appendices A and C represent original extensions beyond the published article, while Appendix B is based on material reported in Ustrzycka et al. (2025) and is reproduced here for completeness and coherence.

All numerical testing related to fracture was performed by the author, including convergence studies, strain-rate sensitivity analysis, evaluation of boundary-condition artifacts, assessment of thermostat effects, and stabilization of crack propagation behavior under controlled loading conditions.

Post-processing and quantitative analysis of the fracture response were also conducted by the author. This includes the extraction of stress–strain relations, determination of crack length evolution and crack velocity, calculation of dissipated energy and critical energy release rates, and systematic comparison of fracture behavior in the presence of isolated defects and distributed

radiation-induced defect populations.

The physical interpretation of fracture mechanisms, including crack–defect interactions, void coalescence, dislocation-loop blocking, amorphization near crack tips, and crack branching, was developed through detailed analysis of atomistic simulation results and refined through scientific discussion with the supervisor and co-authors.

The energy-based fracture analysis and the mechanistic interpretation of crack–defect interactions were performed in close collaboration with the co-authors. The author actively participated in these analyses through numerical data generation, post-processing, and interpretation of atomistic simulation results.

The irradiation simulations themselves were not performed by the author; however, the underlying irradiation methodology, including the collision cascades overlapping method, is fully understood at a conceptual level. The author can fully justify all aspects related to the design of irradiated specimens and the interpretation presented in this chapter.

Chapter 5

Anisotropic effects in radiation embrittlement

This chapter is extracted from the following publication:

H. Mousavi, S. Stupkiewicz, and A. Ustrzycka.
Molecular Dynamics Study of the Role of Anisotropy in Radiation-Driven Embrittlement.
International Journal of Plasticity, under review (2026).

5.1 Importance of crystallographic orientations in radiation-induced fracture behavior

Building on the atomistic analysis of radiation-induced embrittlement presented in the Chapter 4, this chapter extends the investigation to the role of crystallographic orientation in governing fracture behavior under irradiation. This study investigated irradiation-assisted fracture behavior in fcc $Fe_{55}Ni_{19}Cr_{26}$ alloy with a particular focus on the role of crystallographic orientation.

Structural components in nuclear fission and fusion systems are inherently anisotropic at the grain scale, owing to their crystalline nature and thermo-mechanical processing history (Was, 2007; Zinkle, 2012). As a result, their mechanical response depends not only on the accumulated radiation damage but also on the crystallographic orientation of individual grains relative to applied loads (Klueh and Alexander, 1997; Zinkle and Was, 2013).

In polycrystalline reactor alloys, grains of different orientations coexist within the same component and are subjected to identical irradiation environments. Despite experiencing comparable defect populations, these grains may exhibit markedly different mechanical responses due to crystallographic constraints on deformation and fracture. This orientation dependence has important implications for structural integrity assessments, as local fracture resistance and crack propagation behavior may vary significantly from grain to grain, even under uniform macroscopic loading conditions (Wang et al., 2020; Li et al., 2022; Huang et al., 2024).

Orientation also influences the evolution of fracture mechanisms under irradiation, specifically crack-path selection, the onset and extent of strain localization, and the balance between plastic accommodation and cleavage. Consequently, the ductile-to-brittle transition (DBT) in irradiated materials is expected to be orientation sensitive (Klueh and Alexander, 1997; Barik et al., 2023; Lin et al., 2025; Ustrzycka et al., 2025).

At the same time, the mechanisms driving radiation-induced DBT, such as defect accumulation, nano-void absorption, and dislocation pinning, differ in character from temperature-

driven DBT and depend strongly on how the lattice directs dislocations relative to defect fields (Barik et al., 2023; Ustrzycka et al., 2025). Our previous assessment focused on the (001) orientation and examined how radiation-induced defects influence crack-tip plasticity and fracture behavior within this specific crystallographic configuration (Ustrzycka et al., 2025). Motivated by the orientation-dependent response observed at the polycrystal scale in austenitic stainless steels, it is crucial to clarify how crystallographic orientation governs deformation and fracture under irradiation. Here, we extend this perspective by systematically comparing single crystals of $Fe_{55}Ni_{19}Cr_{26}$ in the (001), (011), and (111) orientations using MD simulations, examining how radiation-induced defects couple with orientation-dependent slip geometry, dislocation interactions, and crack-tip deformation processes (Zhou, 2003; Shimokawa et al., 2005; Bitzek and Gumbsch, 2008; Wang et al., 2015; Cui et al., 2017; Tsugawa et al., 2022; Bao et al., 2022; Lin et al., 2024a; Ustrzycka et al., 2024). This approach enables a systematic examination of how crystallographic orientation influences deformation mechanisms, crack-tip plasticity, and energy dissipation in irradiated materials, and how these factors collectively govern fracture resistance.

In summary, this chapter addresses a central question: to what extent does crystallographic orientation modulate radiation-induced DBT through its control of slip-system activity, defect–dislocation interactions, and crack-tip plasticity? By combining orientation-controlled MD simulations with a consistent analysis of crack initiation and growth across (001), (011), and (111), this chapter examines the extent to which radiation-induced embrittlement can be understood beyond defect density alone. Rather, it emphasizes the role of an orientation-sensitive coupling between evolving defect structures and the lattice mechanisms available to accommodate stress.

5.2 Orientation-based simulation methodology

Based on the orientation-dependent study, a two-stage MD framework was employed to analyze radiation-induced fracture behavior across different crystallographic orientations. The first stage involved irradiation simulations to generate defected microstructures, followed by crack propagation simulations in the second stage. The approach follows the same basic irradiation method used previously to generate realistic defect structures but was modified to account for different selected orientations in the irradiated samples. These pre-defected configurations were then used in orientation-dependent crack propagation simulations to assess how lattice directionality influences deformation and fracture mechanisms in irradiated $Fe_{55}Ni_{19}Cr_{26}$ alloy.

5.2.1 Generation of orientation-specific irradiated samples

In this part of the study, we employ the same sequential overlapping collision–cascade protocol described in Subection 4.2.1 for $Fe_{55}Ni_{19}Cr_{26}$, and focus only on the orientation selection of the single-crystal cells. The adopted elements proportions correspond to 310S stainless steel. Atomic configurations were constructed with ATOMSK (Hirel, 2015) and aligned along (001), (011), and

Table 5.4: Simulation cell parameters for analyzed crystallographic orientations.

orientation of the simulated sample	x-axis	y-axis	z-axis	dimensions (Å^3)	number of atoms
(001)	[100]	[010]	[001]	138 × 141 × 148	262080
(011)	[100]	[01$\bar{1}$]	[011]	138 × 142 × 147	262314
(111)	[1$\bar{2}$1]	[$\bar{1}$01]	[111]	137 × 142 × 147	261360

(111), as summarized in Table 5.4. These orientations were selected to capture the representative behavior of high-symmetry directions in fcc lattices, providing distinct combinations of active slip systems and allowing evaluation of how crystallographic geometry influences plasticity, defect interactions, and crack propagation under irradiation. The box dimensions in Table 5.4 were chosen following the convergence criteria established previously (Ustrzycka et al., 2024) to avoid interactions between cascades and their periodic images.

Irradiation damage was generated using the established cascade scheme (LAMMPS using EAM11 potential with ZBL modification (Bonny et al., 2011; Thompson et al., 2022), 10 keV PKAs assigned to random Fe, Ni, and Cr atoms with arbitrary directions). For each orientation, 400 cascades produced a dose of 0.152 dpa; additional sets at 0.008, 0.038, and 0.076 dpa (20, 100, and 200 cascades) were also prepared for dpa–response comparisons. Temperature control, boundary conditions, and post-cascade relaxation followed the same settings as in Section 4.2.1 and are not repeated here.

Fig. 5.1 shows representative microstructures (DXA in OVITO (Stukowski, 2010)) for the three orientations in selected irradiated samples. Primary radiation events produce only vacancies and interstitial atoms (see Fig. 2.4). During subsequent collisions, radiation defects evolve and grow; vacancies aggregate into clusters that stabilize into voids, represented in Fig. 5.1 as blue spheres. Helium bubbles, which can form in materials through (n, α) transmutation reactions depending on neutron energy and fluence, are not generated and analyzed in this study. The relatively low stacking fault energy in fcc metals facilitates the formation of stacking fault tetrahedra (SFTs) (Kai Nordlund, 1999). These structures adopt a pyramidal morphology and are visible in Fig. 5.1 as pink-colored pyramidal defects. Self-interstitial atoms, in turn, form clusters that collapse into dislocation loops (Hernández-Mayoral and Caturla, 2010; Ustrzycka, 2021). With continued irradiation, these loops interact, evolve, or annihilate.

Radiation-induced defects in fcc metals exhibit nearly orientation-independent characteristics, primarily due to the weak directional dependence of the threshold displacement energy (TDE), which remains approximately constant in austenitic Fe–Ni-Cr alloys (~ 40 eV (Nordlund et al., 2018b)). Moreover, fcc lattices lack pronounced channeling paths, dominant in more open bcc structures, which strongly reduces the possibility of directionally enhanced defect transport (Mahrous et al., 2025). The dense atomic packing in fcc alloys promotes rapid cascade branching, which suppresses directional transport of defects. As a result, defect production is

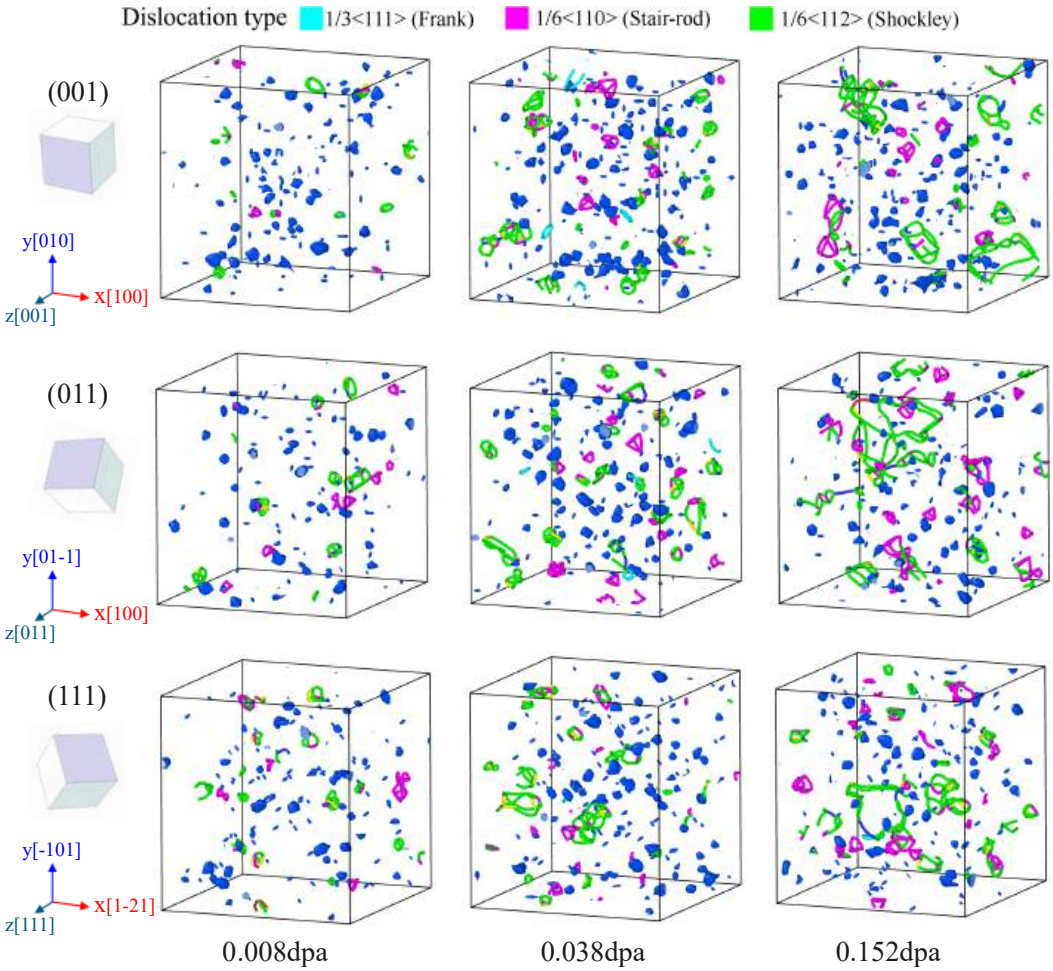

Figure 5.1: $Fe_{55}Ni_{19}Cr_{26}$ samples irradiated using sequential collision cascades at three damage levels (0.008, 0.038, and 0.152 dpa) for the crystallographic orientations (001), (011), and (111). The legend indicates the types of dislocation loops. Voids are marked as blue spheres.

largely independent of lattice orientation.

The qualitative defect morphologies shown in Fig. 5.1 are complemented by a quantitative analysis in Figs. 5.2–5.4. Fig. 5.2 presents the evolution of the total and resolved dislocation densities as a function of the irradiation dose. The results show a rapid nucleation of dislocation loops and voids at low doses, followed by growth and partial saturation of defect densities as the dose increases, a behavior observed in atomistic cascade studies (Nordlund et al., 2018b; Béland et al., 2017; Zhou et al., 2023). The kinetics are very similar for the (001), (011), and (111) orientations, which proves that the defect formation is not affected by the orientation of the MD sample.

Fig. 5.3 presents the corresponding evolution of voids. The left panel shows the void number density, while the right panel shows the cumulative void volume distribution, obtained by sorting voids by size and computing the cumulative sum of their volumes. The latter reveals that all orientations generate void populations with similar cumulative growth, indicating comparable

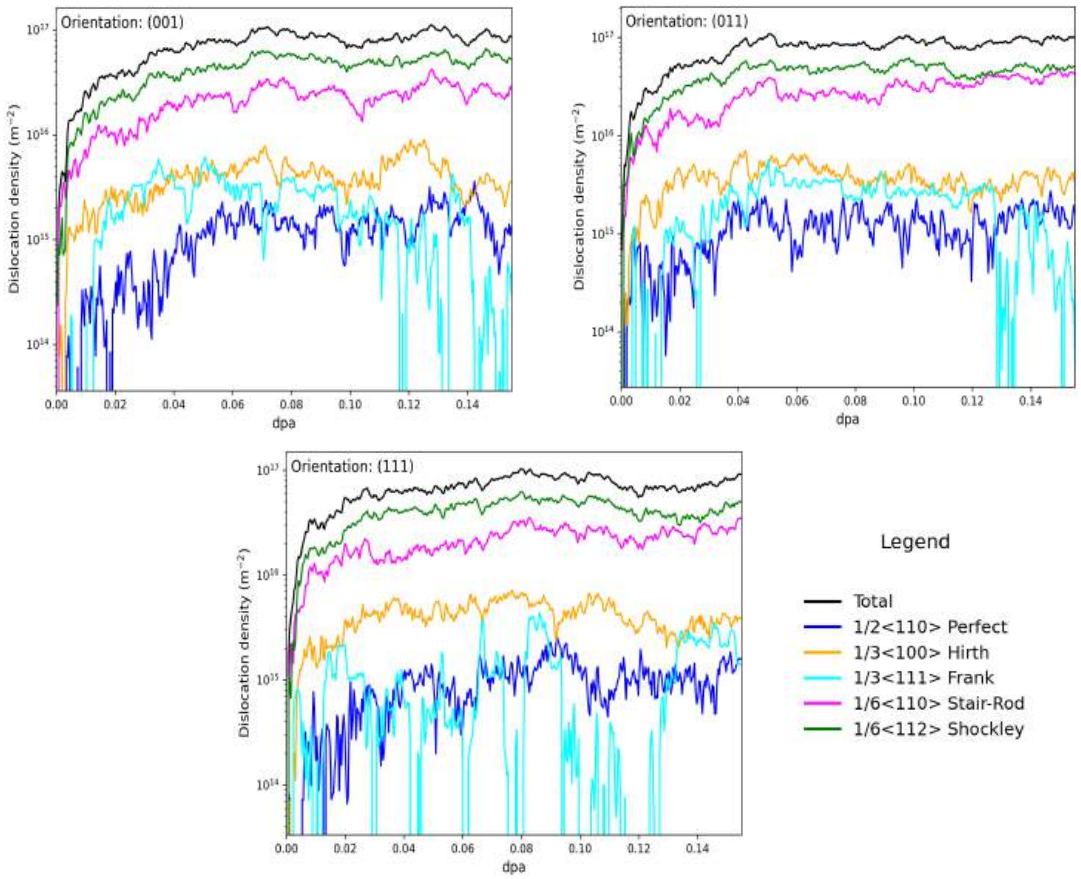

Figure 5.2: Evolution of dislocation density as functions of irradiation dose (dpa) for the (001), (011) and (111) orientations.

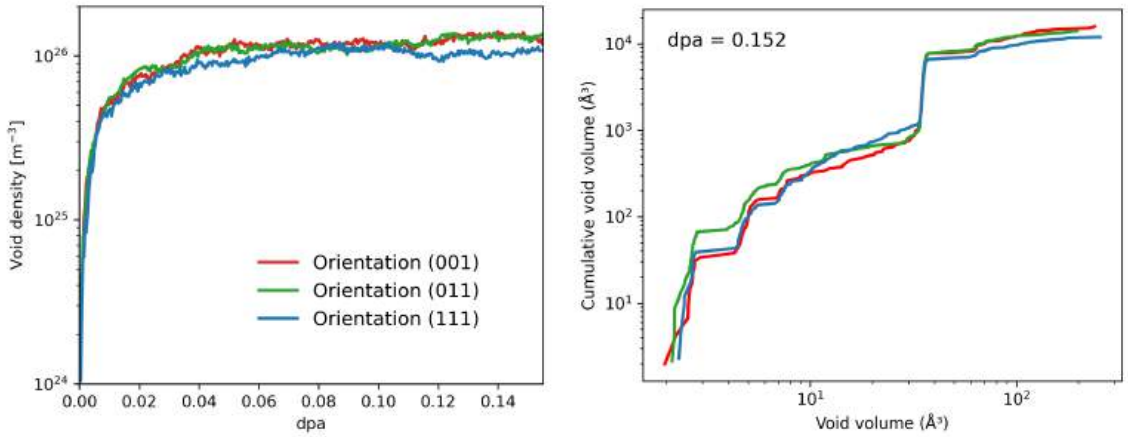

Figure 5.3: Evolution of void number density (left) and cumulative void volume distribution (right) as functions of irradiation dose for the (001), (011), and (111) orientations.

rates of vacancy clustering.

Finally, Fig. 5.4 displays a histogram of the void-size distributions at 0.152 dpa. All three orientations show similarly shaped distributions dominated by small voids, with only minor

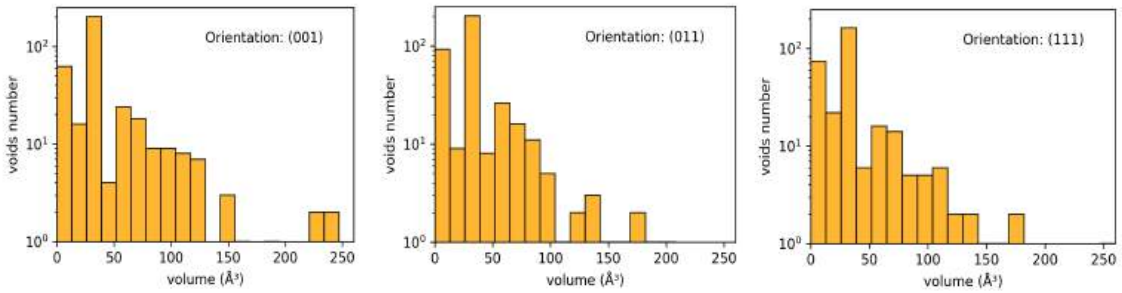

Figure 5.4: Populations of radiation-induced voids at dpa = 0.152 for selected orientations.

variations in the largest voids.

Given the observed defect distribution independent of MD sample orientation (Fig. 5.1) and comparable evolution of defect densities and void volume fractions across the investigated orientations (Figs. 5.1–5.4), the current MD-based framework provides a sufficiently robust representation of radiation-induced defect populations. Therefore, no additional formal statistical analysis of individual collision cascades was considered necessary.

5.2.2 Orientation-dependent mode-I fracture simulation setup

This subsection presents a modified fracture framework relative to Section 4.2.2, tailored for the orientation-dependent study; only modifications and study-specific choices are stated here.

The initial irradiated samples, with three crystallographic orientations as shown in Fig.5.1, were replicated to create three distinct crack growth models. The replication method involved doubling the simulated sample dimensions in the x- and y-directions, while the z-direction remained unchanged. Ultimately, considering the dimensions of the initial irradiated samples, the model with approximate dimensions of $275 \times 282 \times 148$ Å^3 and containing more than 1 million atoms (varying slightly for different orientations due to differing lattice structures) was established.

Fig. 5.5 comprises two views to illustrate the three-dimensional simulated sample fully. The left side of Fig. 5.5 shows the x–y projection of the pre-cracked sample. The right side presents an y-z projection, emphasizing the model's depth along the z-direction. Table 5.5 summarizes the parameters of the replicated crack models, including the crack geometry using the $\{\text{crack plane}\}\langle\text{crack-front direction}\rangle$ notation, loading axis, maximum Schmid factors for slip ($m_{\max}^{\text{slip}}$) and twinning ($m_{\max}^{\text{twin}}$), and cell dimensions. These three crack configurations were chosen to represent crystallographic planes and crack-front directions that probe distinct fracture responses in fcc materials. In particular, they involve different geometric relationships between the crack plane, crack front, and the primary $\{111\}\langle 1\bar{1}0\rangle$ slip systems, which are known to control crack-tip plasticity and dislocation emission.

For all three crystallographic orientations, the maximum Schmid factor for dislocation slip, $m_{\max}^{\text{slip}}$, attains the same value. This enforces crystallographic equivalence of the pri-

Table 5.5: Parameters of replicated pre-cracked simulation cells, including Schmid factors for slip (m_{slip}) and twinning (m_{twin}).

Orientation	Crack geometry {plane}⟨front⟩	Loading axis	$m_{\max}^{\text{slip}}$	$m_{\max}^{\text{twin}}$	Dimensions (Å^3)
(001)	$\{010\}\langle 001\rangle$	[010]	0.408	0.236	$275 \times 282 \times 148$
(011)	$\{01\bar{1}\}\langle 011\rangle$	$[01\bar{1}]$	0.408	0.471	$275 \times 284 \times 147$
(111)	$\{\bar{1}01\}\langle 111\rangle$	$[\bar{1}01]$	0.408	0.471	$274 \times 284 \times 147$

mary $\{111\}\langle 1\bar{1}0\rangle$ slip systems with respect to the applied uniaxial tension along the sample's y-direction, providing a consistent framework for comparing the selected crack geometries. In contrast, the maximum Schmid factor for deformation twinning, $m_{\max}^{\text{twin}}$, varies with orientation, with the (001) configuration exhibiting a lower value than the (011) and (111) cases, reflecting the differing alignment of the $\{111\}\langle 11\bar{2}\rangle$ twinning systems relative to the load. At the same time, only for the (011) orientation, the nominal crack front (parallel to the z-axis) is orthogonal to the shear plane of (two) twinning systems. While fcc steels (except for the high-manganese TWIP steels) plastically deform predominantly via dislocation slip under conventional loading, the highly heterogeneous stress state and local instabilities at the crack tip can nucleate twin-like stacking arrangements, see e.g. Andric and Curtin (2018), as indeed observed in some simulations reported below.

The fracture simulations in this chapter follow the numerical framework, boundary conditions, and loading protocol described in Section 4.2.2, including the procedures for model construction, equilibration, crack introduction, thermostatting, and boundary-condition implementation. These methodological details are therefore not repeated here.

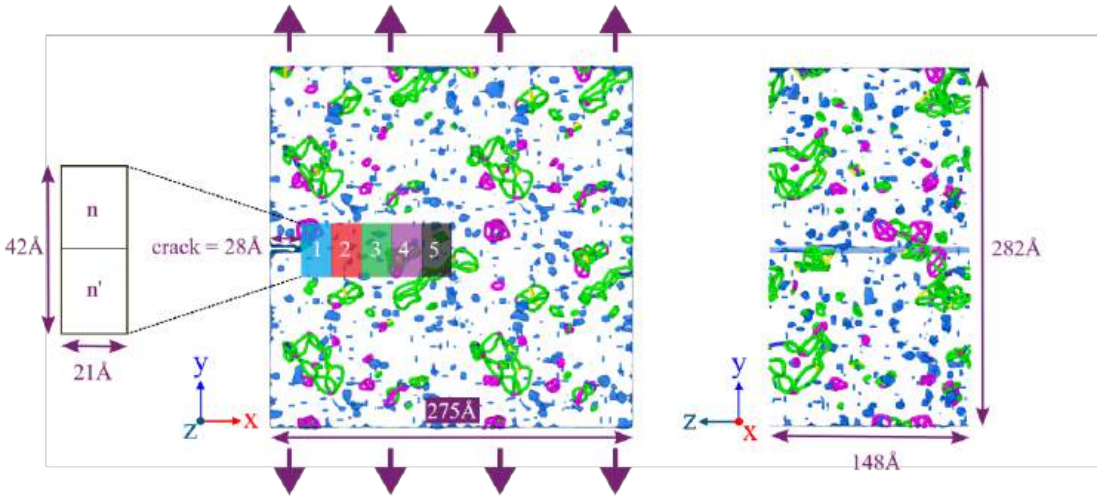

Figure 5.5: Three-dimensional MD model for simulating fracture under tensile loading with a pre-crack, showing the x–y projection on the left, and y–z projection on the right for (001) orientation; five colored boxes indicate subvolumes used to model the material's resistance to crack propagation.

In addition to the reference strain rate of 10^9 s^{-1}, selected simulations for the (001) and (011) orientations were performed at lower strain rates of 10^8 s^{-1} and 5×10^7 s^{-1} to assess strain-rate effects on the dominant deformation mechanisms. Due to the increased computational cost, these simulations were restricted to a maximum applied strain of 6%. A detailed description of the rate-dependent methodology and analysis is provided in Appendix C.

To ensure statistical robustness, crack-propagation simulations were performed on statistically independent irradiated configurations for each crystallographic orientation (four for (011) and three for (001) and (111)). These independent realizations were generated by rotating the samples or by cutting and reassembling different segments of the irradiated volume, thereby modifying the spatial arrangement of defects with respect to the crack front without altering the overall damage level. This procedure ensures that the crack does not accidentally initiate or propagate through an atypical defect cluster, and that the reported responses represent robust trends rather than artifacts of a particular defect configuration.

For subsequent analyses, five fixed subvolumes of size $21 \times 42 \times 148$ $Å^3$ were defined near the crack path (colored boxes in Fig. 5.5) to quantify local resistance to crack advance. The details of this approach will be discussed in Subsection 5.4.2

5.3 Mechanisms of crack growth across crystallographic orientations

This section provides a qualitative analysis of crack propagation in unirradiated and irradiated single crystals oriented along (001), (011), and (111). The focus is on crack–defect interactions and the associated plastic deformation mechanisms. For the irradiated cases, the analysis is conducted at the highest dose considered, 0.152 dpa (400 sequential collision cascades).

Radiation-induced defects originate from energetic collision cascades and evolve under strongly non-equilibrium conditions. Their morphologies and interactions with the crystalline lattice modify local cohesion and slip behavior, shifting the balance between plastic shielding and brittle advance. Clarifying how these defect populations mediate crack initiation and growth is essential for understanding radiation hardening, embrittlement, and DBT behavior.

While the fundamental deformation processes are common across orientations, crystallographic symmetry and the spatial distribution of radiation defects govern their activation pathways and relative prominence. The following subsections detail these orientation-dependent mechanisms and their contributions to the observed fracture response.

5.3.1 Crack-tip plasticity in unirradiated single crystals: orientation effects

Plastic deformation near the crack tip in pristine samples is governed by activation of crystallographically favorable slip systems, determined by the orientation relative to the applied load. Fig. 5.6 presents atomistic snapshots under mode-I tensile loading, capturing dislocation emission, extension of stacking-faulted regions via Shockley partial glide (stacking fault emission), and twinning. To track how plasticity starts at the crack tip, we use CNA together with DXA.

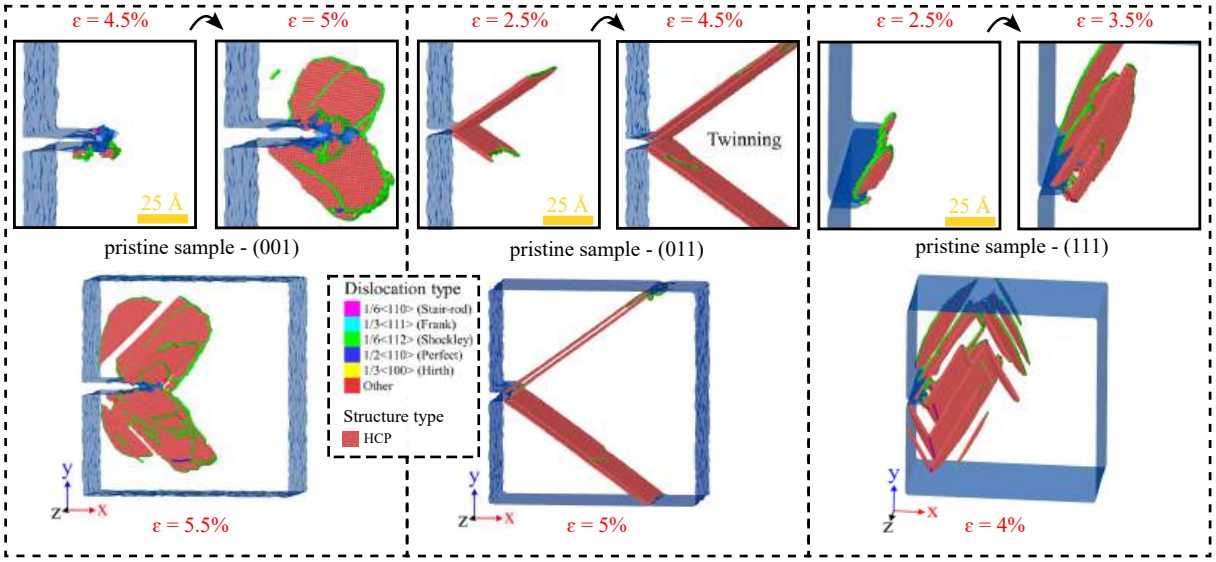

Figure 5.6: Orientation-dependent crack-tip deformation in pristine (001), (011), and (111) samples under mode-I loading. The top row shows close-ups of crack-tip regions, highlighting dislocation activity and twinning. The bottom row presents full-sample views at later stages.

CNA reveals the stacking faults forming at the tip, while DXA identifies the Shockley partial dislocations that create and extend those faults. Together they provide a direct link between fault emission and the responsible dislocations across the unirradiated single-crystals with (001), (011), and (111) orientations. The crack-tip plastic response is strongly orientation dependent under identical loading.

For (001), the nucleation of plasticity is delayed. Stacking faults first appear at about $t \approx 45$ ps and spread only modestly by 50–55 ps, mainly on the two symmetrically equivalent {111} planes. DXA indicates fewer mobile dislocations and a compact plastic zone.

For (011) nucleation occurs earlier, near 25 ps, and growth proceeds more gradually to a wide band by 45–50 ps. Emission includes partials with a pronounced edge character, and successive partials on adjacent {111} planes form a clear twinning band, consistent with the geometry of this orientation.

For (111) more slip systems activate than in the other cases and the response is the fastest. Stacking faults appear by about 25 ps and extend rapidly by 35–40 ps. DXA shows dense emission of Shockley partials on multiple {111} planes, with frequent interactions that thicken the faulted lamellae.

These differences in nucleation timing, slip-system multiplicity, and stacking-fault spread set the size and shape of the plastic zone and explain the greater apparent ductility of (111) compared with (011) and especially (001).

5.3.2 Irradiated sample: (001) orientation

Fig. 5.7 shows the early evolution of a crack in a (001)-oriented sample irradiated to 0.152 dpa, highlighting key interactions with radiation-induced defects. Note that the observed mechanisms are consistent across all analysed doses (0.008, 0.038, 0.076, and 0.152 dpa). Fundamental mechanisms of a single defect–crack interaction governing crack propagation were previously shown in the previous chapter for the (001) orientation.

In Fig. 5.7, frame (a) (pink box) shows the crack front interacting with radiation-induced SFTs, which act as barriers to stacking-fault emission. Frames b (black box) highlight the absorption of irradiation-induced entangled dislocations into the crack-tip plastic zone, altering slip symmetry. Frame c (blue box) shows the interaction with dislocation clusters that impede the propagation of stacking faults, collectively producing an asymmetric plastic field around the crack tip.

Radiation-induced voids further influence crack morphology (Fig. 5.8). The blue regions in the visualization correspond to isosurfaces that capture both crack cavities and radiation-induced voids, with dislocation lines omitted to emphasize crack morphology and its interaction with voids. At low strains (ε from 4% to 5%, purple frames), pre-existing voids locally reduce material strength and are absorbed by the advancing crack, accelerating its growth. At higher strains (ε from 8% to 10%, red frames), void coalescence ahead of the crack connects weakened regions, forcing the crack along a more tortuous path. These results confirm and complement our previous findings in Chapter 4.

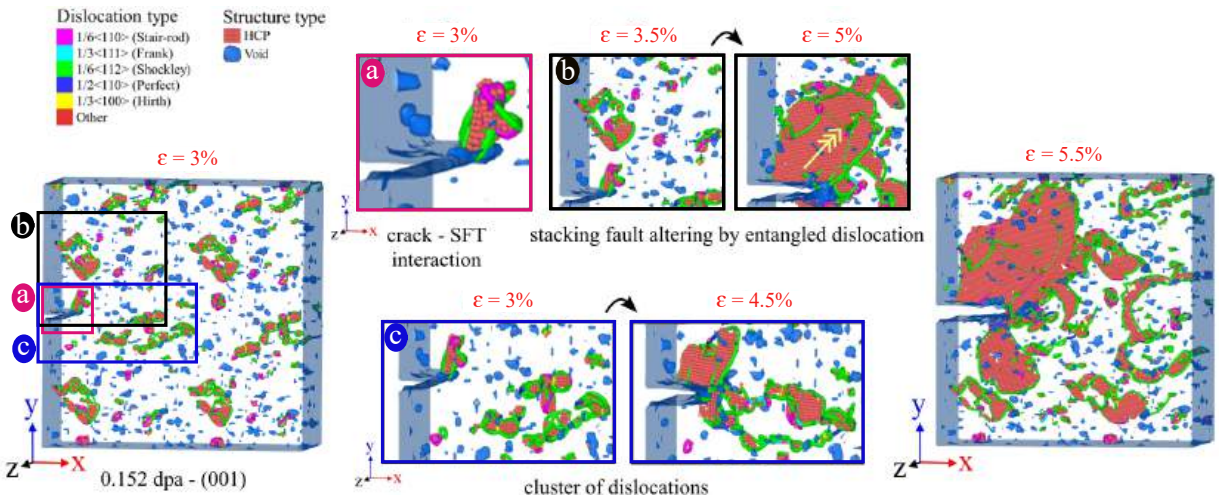

Figure 5.7: Initial crack evolution in a (001)-oriented sample irradiated to 0.152 dpa. Side images show crack positions at 3 and 5.5 % strain, while middle frames highlight active mechanisms near the crack tip: (a) interaction of crack tip with radiation-induced SFT (30 ps; purple frame), (b) absorption of entangled dislocations into the crack-tip plastic zone (3.5-5 % strain; black frames), and (c) interaction with dislocation clusters that impede stacking fault emission (i.e., the extension of stacking-faulted regions via glide of Shockley partials) (3-4.5 % strain; blue frames). The yellow arrow indicates the direction of stacking fault emission.

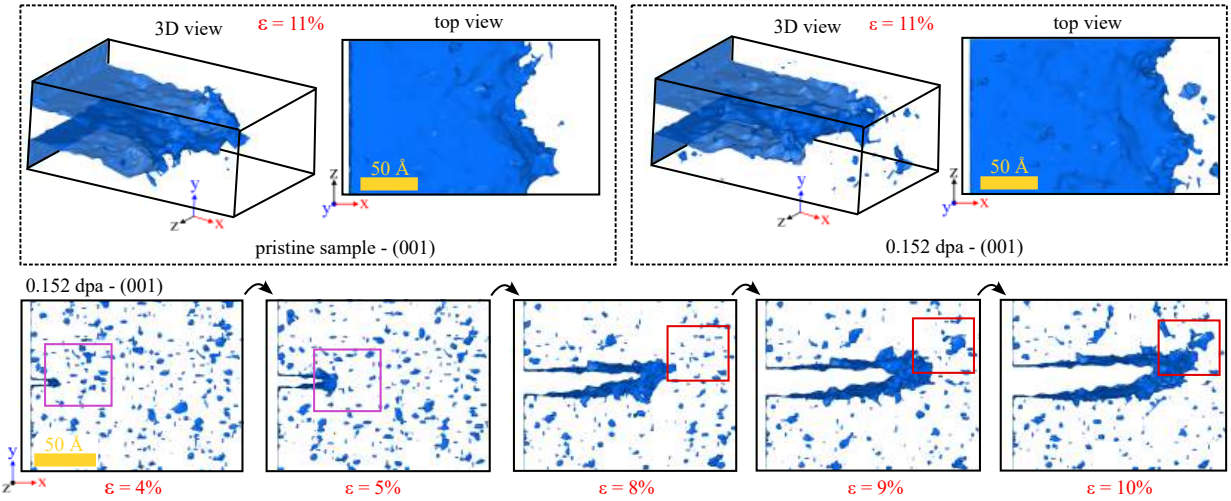

Figure 5.8: Crack propagation in a (001)-oriented sample irradiated to 0.152 dpa, showing the role of radiation-induced voids. Top row: comparison with the pristine sample at the overall strain $\varepsilon = 11\%$ reveals similar crack lengths, with local deviations of crack shape linked to void–crack interactions in the irradiated sample. Bottom row: sequential snapshots (ε varying from 4% to 10%) highlight void absorption at the crack tip (purple rectangles) and subsequent void coalescence ahead of the crack (red rectangles).

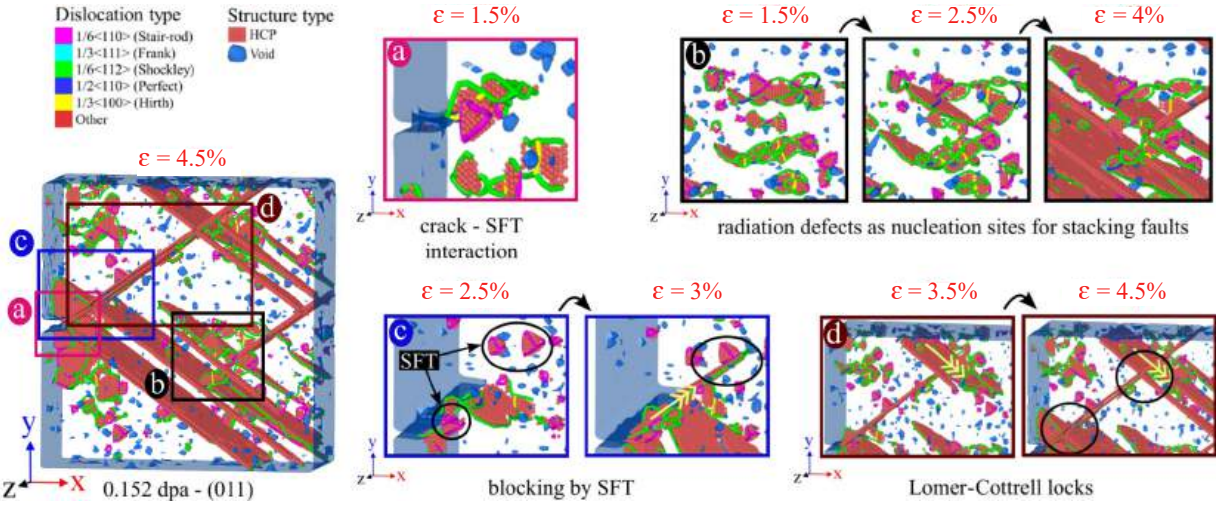

Figure 5.9: Crack evolution in a (011)-orientated sample irradiated to 0.152 dpa. Zoomed-in snapshots show key deformation mechanisms: (a) initial interaction between the crack front and a radiation-induced SFT (15 ps; purple frame), (b) nucleation of plasticity at radiation-induced defects (1.5-4 % strain; black frames), (c) obstruction of stacking fault evolution by SFTs (2.5-3 % strain; blue frames), and (d) formation of Lomer–Cottrell locks at stacking fault intersections near the crack tip (3.5-4.5 % strain; brown frames). Yellow arrows indicate the direction of stacking fault emission.

5.3.3 Irradiated sample: (011) orientation

In a (011)-oriented sample irradiated to 0.152 dpa, shown in Fig. 5.9, crack-tip plasticity develops through successive interactions with radiation-induced defects, fragmenting the coordinated slip observed in the pristine material. In the unirradiated state, as illustrated in Fig. 5.6, intersecting slip systems promote extended stacking faults and twins, leading to effective crack-tip blunting.

Irradiation disrupts this mechanism.

At early times ($t = 15$ ps; purple frame (a) in Fig. 5.9), the crack front interacts with SFTs, triggering localized slip but altering the conditions for fault emission. Between 15 and 40 ps (black frames (b)), deformation initiates from dispersed radiation defect sites, producing a fragmented plastic zone.

At $t = 25-30$ ps (blue frames (c)), SFT blocks dislocation emission and limits the extension of stacking-faulted regions, suppressing forward plasticity along primary slip systems. Later ($35-45$ ps; brown frames (d)), intersecting faults form Lomer–Cottrell locks that restrict slip redistribution. Overall, plastic flow becomes spatially discontinuous and asymmetric.

Similar to the (001) orientation, radiation-induced voids in the (011) promote crack advance by two successive mechanisms: at low strains (ε from 4% to 10%) they are absorbed by the crack front, while at higher strains (ε from 4% to 10%) they coalesce ahead of it, forming weak links that deflect and accelerate propagation. The top row of Fig. 5.10 shows that at $\varepsilon = 9.5\%$ the irradiated (011) sample develops a longer, more tortuous crack path than in the unirradiated state, in contrast to the (001) orientation (see Fig. 5.8), where the crack length remains nearly unchanged by irradiation.

Compared to (001), where the limited number of slip systems remains essentially unaffected by irradiation and allows relatively unhindered crack advance, the irradiated (011) sample shows suppression of twinning and reduced slip activity. Here, the defect-induced reduction of plasticity, combined with void-assisted growth, indicates an irradiation-induced DBT.

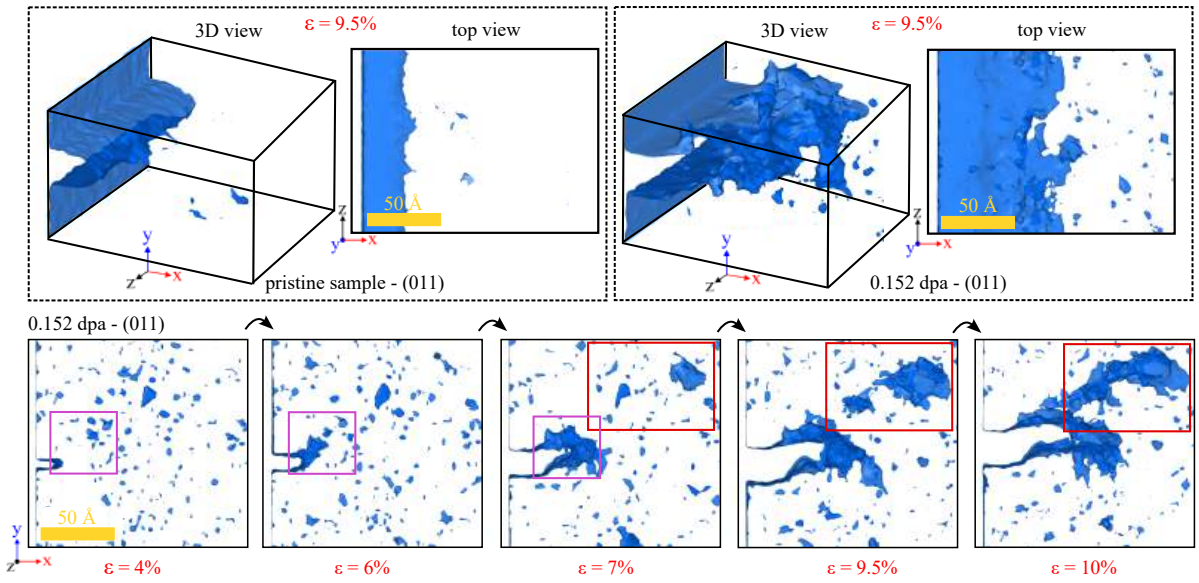

Figure 5.10: Role of radiation-induced voids on crack propagation in (011)-oriented sample irradiated to 0.152 dpa. Top row: comparison of crack length and morphology between pristine and irradiated samples at the same strain level ($\varepsilon = 9.5\%$) highlights void-driven crack advance in the irradiated case. Bottom row: sequence from $\varepsilon = 4\%$ to 10% shows initial absorption of voids near the crack tip (purple rectangles) up to $\varepsilon = 7\%$, followed by void accumulation and coalescence that disrupt the crack front and deflect its path (red rectangles).

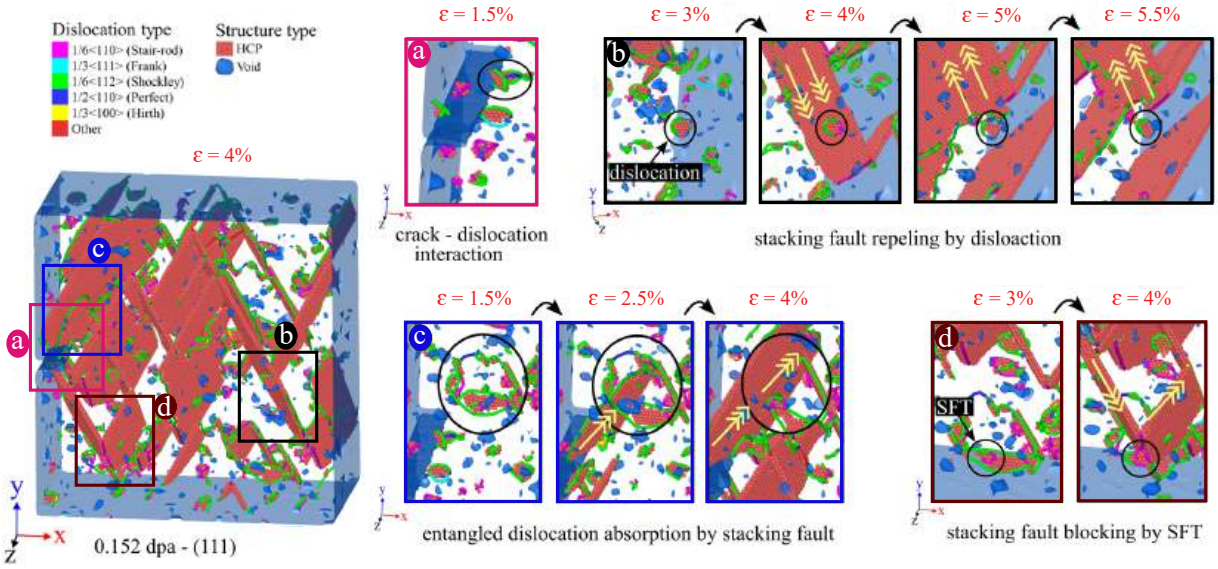

Figure 5.11: Crack evolution in a (111)-oriented sample irradiated to 0.152 dpa, highlighting the interaction between stacking faults and radiation-induced defects. Zoomed-in snapshots illustrate key deformation mechanisms: (a) initial interaction between the crack front and a radiation-induced dislocation loop (1.5 % strain), (b) deflection of stacking faults by radiation dislocations (3-5.5 % strain), (c) absorption of entangled dislocations into stacking faults (1.5-4 % strain), and (d) blocking of stacking fault extension by radiation SFT (3-4 % strain). Yellow arrows indicate the direction of stacking fault emission.

The pronounced DBT effect observed in the (011) orientation appears to be primarily associated with interactions between twins and radiation-induced defects, including the formation of Lomer–Cottrell locks that restrict dislocation motion. At the same time, crystallographic orientation plays an important role by determining which plastic mechanisms, such as twinning or stacking-fault glide, can be activated under stress. Together, these observations suggest that radiation-induced embrittlement reflects both the nature of defect–mechanism interactions and the accessibility of underlying plasticity modes, which vary with orientation. Consequently, similar embrittlement effects could emerge in other orientations if the local plastic mechanisms are similarly engaged.

5.3.4 Irradiated sample: (111) orientation

In a (111)-oriented sample irradiated to 0.152 dpa, crack evolution is dominated by stacking fault emission and dislocation glide along multiple intersecting slip systems. The favorable crystallography ensures highly efficient and spatially distributed plasticity, which remains largely unaffected by radiation-induced defects, consistent with the pristine sample response (compare Fig. 5.6).

Fig. 5.11 illustrates these mechanisms. The full-field image (left) shows the irradiated sample at 40ps, while panels (a)-(d) highlight key defect–fault interactions. At early crack advance (15 ps, purple box), the front interacts with dislocation loops, initiating stacking fault emission. Subsequently (30-55 ps, black box), emitted faults encounter loops that locally repel propagation

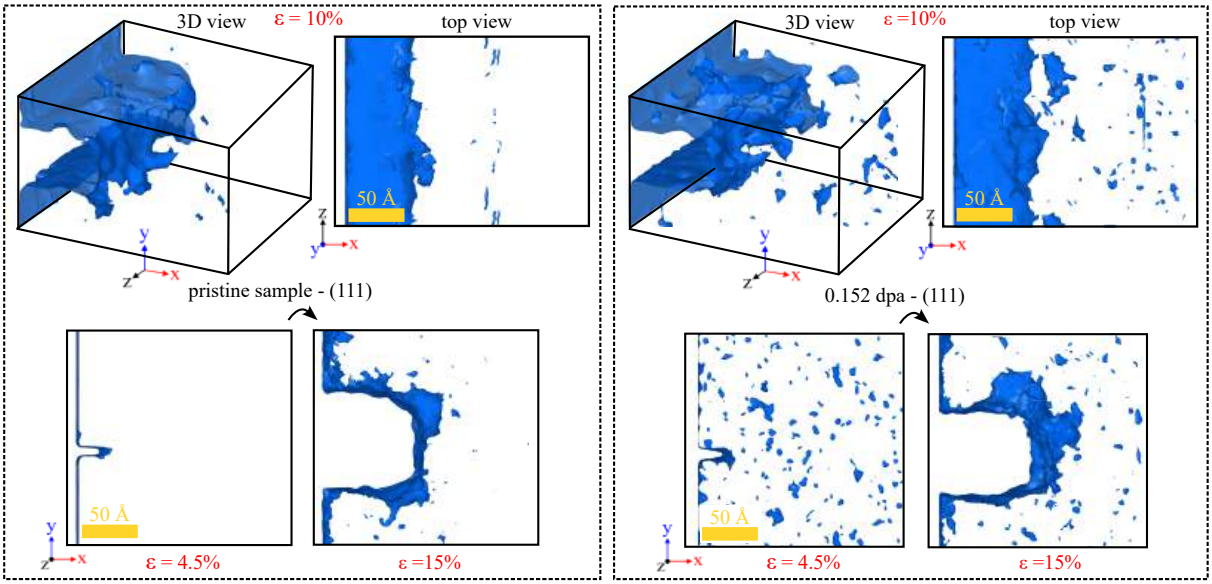

Figure 5.12: Comparison of crack behavior in a (111) orientation before and after irradiation (0.15 dpa), highlighting the limited influence of radiation-induced voids and the role of crack-tip blunting. Top row: crack surface morphology in pristine (left) and irradiated (right) samples at the same strain level ($\varepsilon = 10\%$) reveals enhanced plastic deformation and blunting. Bottom row: evolution of crack tip structure from $\varepsilon = 4.5\%$ to 15% demonstrates sustained plasticity and delayed crack advance with crack tip blunting in both conditions.

but do not impede plastic flow. Radiation-entangled dislocations are then absorbed into stacking faults (15-40 ps, blue box), integrating defects into the plastic front. Finally, limited fault blockage by SFTs occurs (30-40 ps, brown box), yet continuous deformation is maintained.

Fig. 5.12 shows the limited influence of radiation-induced voids in the (111) orientation. At a strain of $\varepsilon = 10\%$, the crack morphology in the irradiated sample is similar to that of the pristine case, with both exhibiting pronounced blunting, indicating that voids have little effect on the local crack-tip response. Snapshots at $\varepsilon = 4.5\%$ and 15% (lower row) confirm the minimal impact of voids on crack propagation in this orientation.

5.3.5 Dislocation density evolution during crack propagation

Fig. 5.13 presents the evolution of the total dislocation density during crack propagation for the three analyzed crystallographic orientations, evaluated in both pristine and irradiated states (0.038 and 0.152 dpa). Across all orientations, at zero strain, irradiation establishes the initial dislocation content, reflecting the presence of radiation-induced defects. As deformation progresses and the crack advances, all orientations show a systematic increase in dislocation density, reflecting continued crack-tip emission and interactions with the pre-existing defect population.

The dislocation evolution exhibits a coupled dependence on the crack geometry (orientation) and irradiation dose.

The $\{010\}\langle 001\rangle$ configuration develops the lowest dislocation densities across the examined strain range. This behavior is consistent with the restricted set of operative slip systems available

to accommodate crack-tip plasticity, as discussed in Subsection 5.3.2. Even at $\varepsilon = 5.5\%$, the dislocation density remains below $\sim 1.0 \times 10^{17} \mathrm{m}^{-2}$, underscoring the strongly constrained plastic response characteristic of this orientation.

The $\{01\bar{1}\}\langle 011\rangle$ orientation displays an intermediate increase in dislocation density under irradiation. In the pristine state, dislocations nucleated at the crack tip move away efficiently along the available glide systems, leaving the near-tip region with only a small residual dislocation content. Irradiation fundamentally changes this mechanism. Radiation-induced defect clusters act as strong obstacles, reducing dislocation mean free paths, promoting trapping, and increasing local pile-up dislocations consistent with established observations of radiation-induced embrittlement. As detailed in Subsection 5.3.3, this leads to a substantial elevation of local dislocation density for both irradiation levels, in stark contrast to the pristine case where most dislocations escape the crack vicinity.

The $\{\bar{1}01\}\langle 111\rangle$ orientation shows the highest dislocation accumulation, reaching $\sim 1.5 \times 10^{17}, \mathrm{m}^{-2}$ at 5.5% strain for 0.152 dpa. This pronounced buildup is consistent with the high symmetry and multiplicity of slip systems intersecting the $\langle 111\rangle$ crack-front direction. These crystallographic conditions favor extensive crack-tip plasticity, dislocation emission, and enhanced cross-slip, as discussed in Subsection 5.3.4. Irradiation amplifies these trends by increasing dislocation, defect interactions, and limiting the escape of emitted dislocations, resulting in the highest defect-assisted storage among all examined orientations.

The results indicate that irradiation amplifies dislocation storage in a strongly orientation-dependent manner. These results correlate with the distinct crack-tip deformation mechanisms.

5.4 Quantitative assessment of fracture behavior

Building upon the qualitative analysis of deformation mechanisms presented in the previous section, this part offers a quantitative assessment of how irradiation affects fracture behavior in samples with (001), (011), and (111) orientations under mode-I tensile loading with a pre-existing

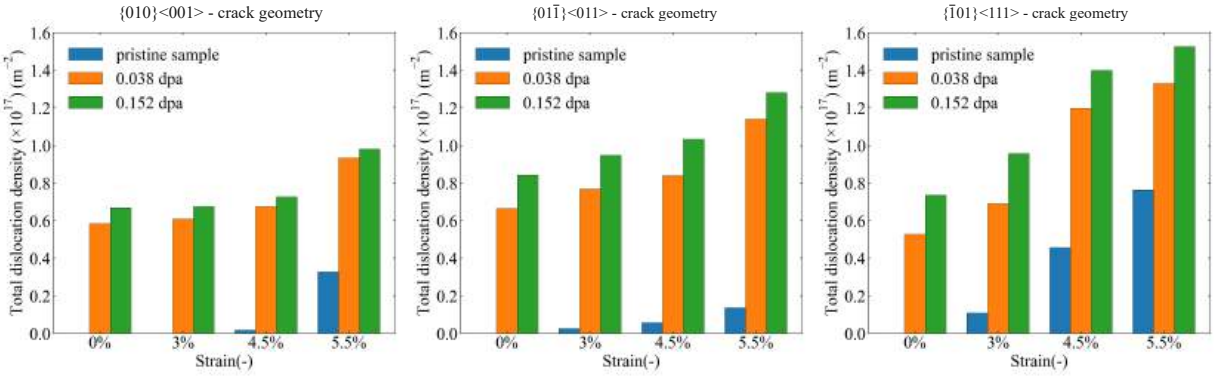

Figure 5.13: Evolution of total dislocation density during crack propagation as a function of applied strain for pristine and irradiated samples in the three crystallographic orientations.

crack. The evaluation is based on stress–strain responses, crack propagation characteristics, and traction–separation (T–S) curves extracted from MD simulations.

5.4.1 Stress–strain response and crack length evolution

Fig. 5.14 presents orientation-resolved stress–strain curves for pristine and irradiated (0.152 dpa) samples. The extent of irradiation-induced mechanical degradation is orientation dependent. Among the three orientations, (011) shows the most pronounced loss of ductility and a clear reduction in peak stress, indicating a radiation-induced DBT. As detailed in Section 5.3, this transition arises from the combined effect of dislocation pinning by SFTs, the formation of Lomer–Cottrell locks, and the fragmentation of stacking faults, which together suppress plastic strain redistribution (Fig. 5.9). Additionally, void absorption and coalescence further facilitate crack propagation. The (111) orientation exhibits minimal sensitivity to irradiation: both yielding and early-stage hardening remain essentially unchanged, as multiple slip systems continue to accommodate plastic flow. As shown in Section 5.3, absorption of defects into stacking faults and repulsive interactions between mobile and radiation-induced dislocations prevent strain localization, preserving ductility (Fig. 5.11). For (001), where slip activity is intrinsically limited, irradiation produces only marginal additional effects, and the stress–strain response remains essentially unchanged (Fig. 5.14). A detailed comparison of the crack-tip stress fields for all orientations and selected irradiation levels is provided in Appendix E, offering additional insight into the orientation-dependent plastic zone development and stress localization discussed in this section. Moreover, the serrated features in the curves arise from intermittent plastic events at the crack tip: stress rises as crack propagation is temporarily blocked by entangled dislocations and stacking faults, followed by drops corresponding to barrier breaking and crack advance. Peaks also reflect successive stages of void nucleation and growth near the crack front, periodically relieving local stresses.

Crack length evolution across all crystallographic orientations is presented in Fig. 5.15. Crack length was estimated by projecting the evolving crack surface onto the propagation (x-z)

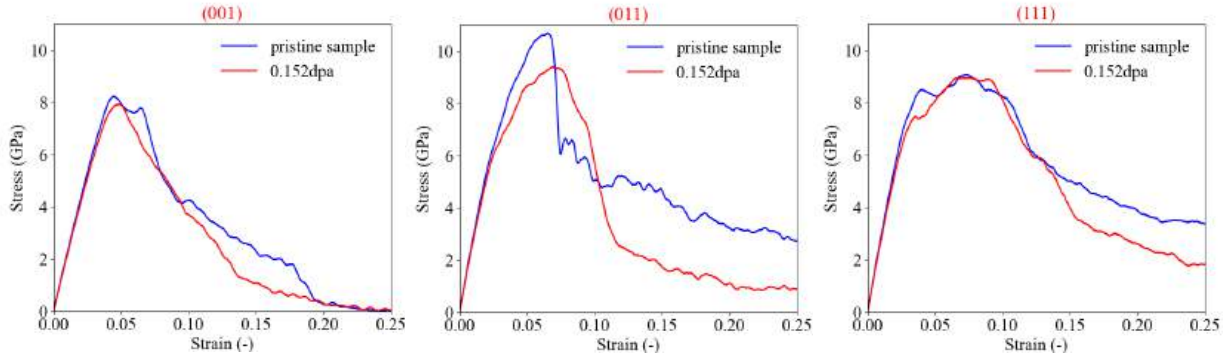

Figure 5.14: Orientation-dependent stress–strain responses for pristine and samples irradiated to 0.152 dpa.

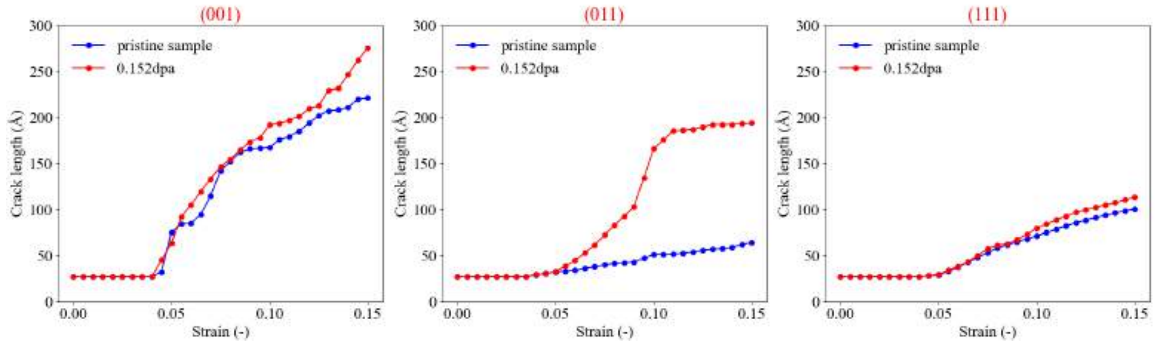

Figure 5.15: Crack length evolution as a function of strain for the (001), (011), and (111) orientations, comparing pristine and irradiated (0.152 dpa) samples.

plane and the mean projected crack length along the propagation direction, which minimizes sensitivity to local crack-front deviations across the specimen thickness. In the pristine samples, crack growth is most limited for the (011) orientation because its geometry favors activation of two intersecting {111} slip systems, producing localized plasticity, stacking faults, and early twinning at the crack tip. This concentrated deformation blunts the crack and efficiently shields the crack tip. In contrast, (001) exhibits limited slip activity, and (111) distributes plasticity across multiple planes rather than concentrating it near the crack tip, resulting in longer cracks. The strongest irradiation effect is observed for (011), where restricted slip activity, combined with void absorption at the crack front, promotes accelerated crack advance. The (001) samples show nearly identical crack extension in pristine and irradiated states, but with a relatively fast crack growth over time due to limited plasticity. For the (111) orientation, crack propagation remains strongly suppressed, irrespective of irradiation, as the efficient activation of multiple slip systems sustains plastic redistribution and blunts the crack tip.

5.4.2 Traction–separation analysis

To further quantify the effect of irradiation on fracture resistance and to complement the global stress–strain analysis, T–S law is used to characterise the fracture behavior at the atomic scale. The T–S curve, widely used to analyse fracture processes in MD simulations (Krull and Yuan, 2011; Barrows et al., 2016; Ding et al., 2020), defines the relationship between the normal traction transmitted across the crack surfaces and the corresponding crack opening displacement. In this framework, fracture is described as a progressive reduction of cohesive traction with increasing crack opening displacement. A detailed theoretical formulation of the cohesive–zone framework and the T-S law is provided in Appendix F.

In our simulations, five distinct regions were distinguished near the crack tip, as shown in Fig. 5.5. A consistent and physically meaningful evaluation of the T–S response requires selecting representative subvolumes along the crack path (Barrows et al., 2016; Ding et al., 2020; Zhu et al., 2021), from which local traction and crack opening displacement are obtained. The

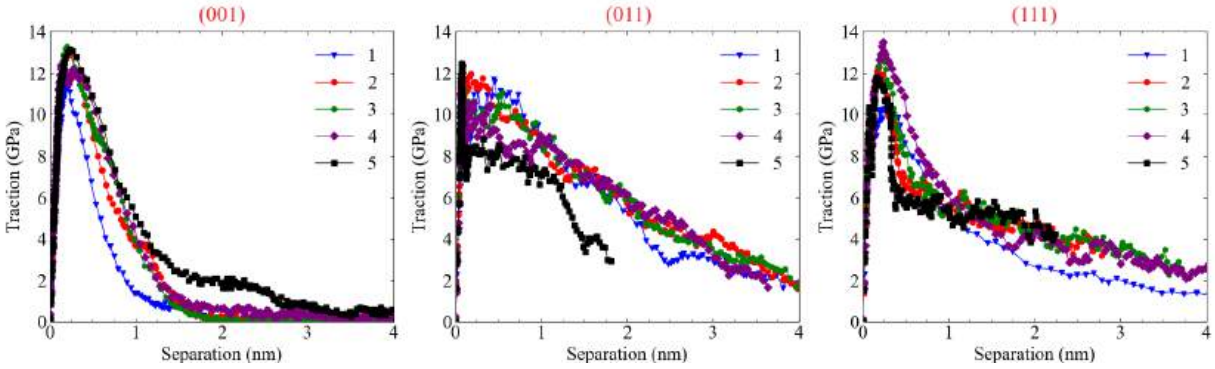

Figure 5.16: T–S curves for pristine samples in the (001), (011), and (111) orientations, derived from discrete sub-volumes (boxes 1-5) along the crack propagation path.

normal traction component is obtained by averaging the stress distribution within two adjacent subvolumes: the upper region (n), and the lower region (n′), positioned on opposite sides of the crack plane (compare Fig. 5.5). The crack opening displacement is determined by computing the relative displacement between these two regions, specifically by subtracting the average atomic displacement of the upper region (n) from that of the lower one (n′) in the loading direction.

Among the five subvolumes defined along the crack path (see Fig. 5.5), boxes 3 and 4 are selected for further analysis based on the T–S curves shown in Fig. 5.16, as they correspond to regions of relatively stable crack propagation and exhibit well-defined separation behavior, including a clear peak and post-peak softening. Boxes 1 and 2 are excluded because they are located too close to the crack tip, where rapid crack advance results in artificially low traction values. Box 5 corresponds to a region behind the active crack front, where defect accumulation and dislocation activity can distort the local mechanical response. For these reasons, boxes 3 and 4 provide the most reliable basis for quantifying orientation-dependent fracture behavior.

Fig. 5.17 presents the T–S responses for all analyzed crystallographic orientations, extracted from boxes 3 and 4. Each row corresponds to a specific crystallographic orientation, with curves for increasing irradiation levels arranged from left to right within the row.

The (011) orientation (second row in Fig. 5.17) exhibits a pronounced DBT under irradiation. With increasing dose, the pre-failure crack opening decreases and the post-peak T–S slope steepens, reflecting constrained plastic dissipation and enhanced crack driving due to irradiation-induced defects. The (001) orientation (first row in Fig. 5.17) shows minimal changes in maximum traction and failure displacement. The (111) orientation (third row in Fig. 5.17) maintains a relatively stable T–S response, with gradual post-peak softening. Interestingly, the maximum traction ($T_{\max}$), a key T–S parameter, does not consistently correlate with irradiation. Consequently, post-peak softening and total separation displacement offer a more reliable metric for assessing irradiation-induced embrittlement (Xie et al., 2023).

5.4.3 Energy-based assessment of radiation-induced embrittlement

In this subsection, the atomic-scale fracture energy (g_f) is evaluated as a quantitative measure of fracture resistance, obtained directly from the T–S response of small subvolumes at the crack tip.

This energetic approach is related to the extended Griffith model for fracture in ductile materials (Orowan, 1945; Jokl et al., 1980; Beltz and Rice, 1992), in which the critical energy release rate (G_c) is expressed as a sum of the energy associated with surface formation, γ_s, and the the plastic work per unit crack area resulting from dislocation activity, w_p, such that $G_c = 2\gamma_s + w_p$. Due to the finite size of the simulated volumes, MD captures only a small fraction of the crack-tip plastic zone, so that the plastic work contribution is underestimated and the resulting G_c values cannot be interpreted as representative macroscopic quantities. However, the MD-based estimates of G_c may serve as qualitative indicators of some physical phenomena, e.g., the DBT induced by temperature (Lin et al., 2025) or by irradiation embrittlement (Ustrzycka et al., 2025).

In our work,the atomic-scale fracture energy (g_f) is defined as the area under the T–S curve, see Fig. 5.18, and represents the local interface formation energy required to open a crack in the MD subvolumes. Unlike the continuum-scale G_c, which accounts for both surface formation and

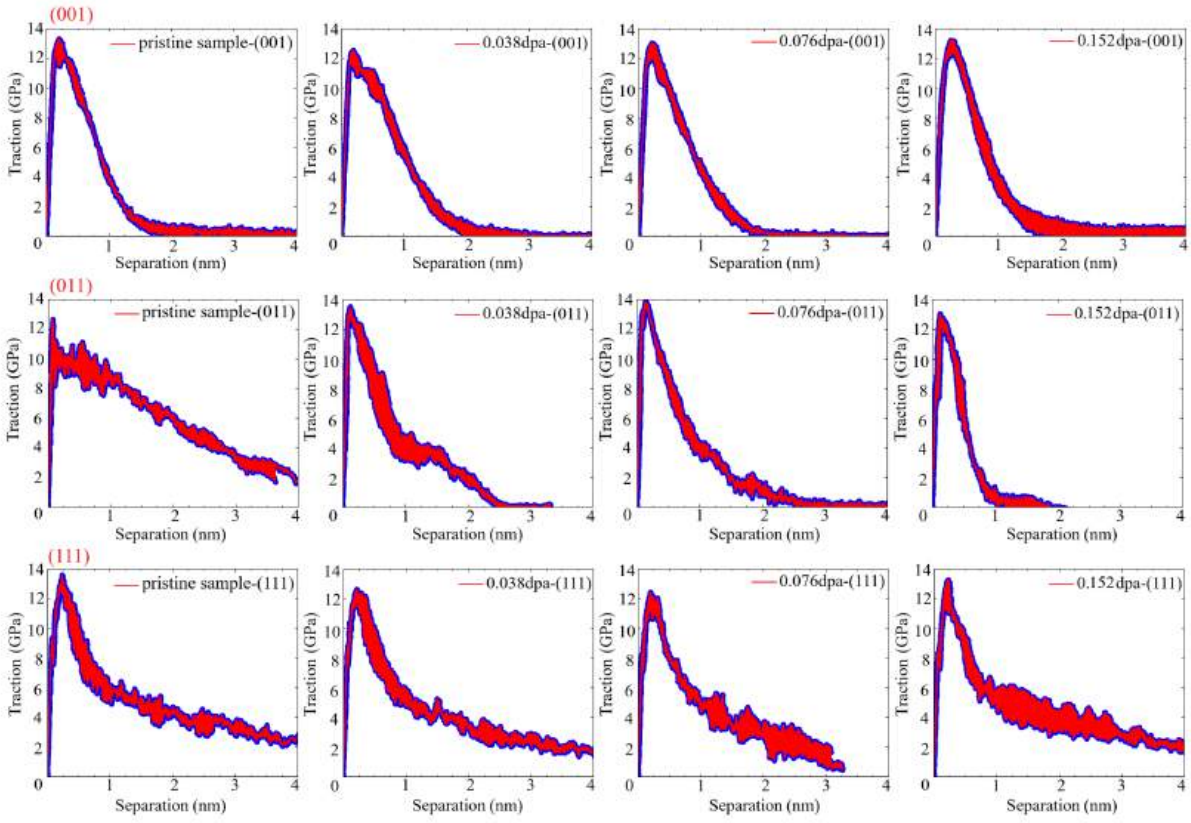

Figure 5.17: T–S responses extracted from two representative subvolumes (boxes 3 and 4) identified as representative regions along the crack path. Columns correspond to increasing irradiation levels, from pristine to 0.152 dpa; rows show orientation-dependent behavior: (001) (top), (011) (middle), and (111) (bottom).

bulk plastic dissipation, (g_f) predominantly reflects the energy of creating new fracture surfaces, with only a minor contribution from plastic work due to the limited portion of the crack-tip plastic zone covered by the MD subvolumes.

T–S responses shown in Fig. 5.17 for (111) orientation and the unirradiated (011) sample retain nonzero tractions at the maximum separation. This indicates that in these cases, the crack propagation was arrested before reaching complete material separation. This behavior is attributed to progressive crack tip blunting, where intensive dislocation activity near the crack front inhibits further crack opening. As a result, the separation process remains incomplete. To ensure a consistent, energy-based assessment across all configurations, an extrapolated contribution to the energy release rate, denoted g_f^{ext}, is introduced for cases in which T–S response does not reach zero traction within the simulated separation range. The terminal part of the T–S curve is extended by a linear extrapolation from the last available data point to an assumed final separation, δ_f, at which the traction vanishes. This procedure, illustrated in Fig. 5.18(b), enables estimation of the energy associated with the unobserved segment of the response, corresponding to the final phase of material separation not captured in the simulation. The fracture energy, (g_f), is then composed of two contributions: the numerically integrated part of the curve, g_f^{int}, and the extrapolated segment, g_f^{ext}, according to equation: $g_f = g_f^{int} + g_f^{ext}$.

Fig. 5.19 shows in (a) the fracture energy, g_f, and in (b) the separation energy, $2\gamma_{sep}$, calculated for the three orientations as a function of the irradiation dose.

The separation energy, $2\gamma_{sep}$, represents the energy required to break atomic bonds and create two planar free surfaces in the absence of plastic deformation. It thus provides a lower bound for

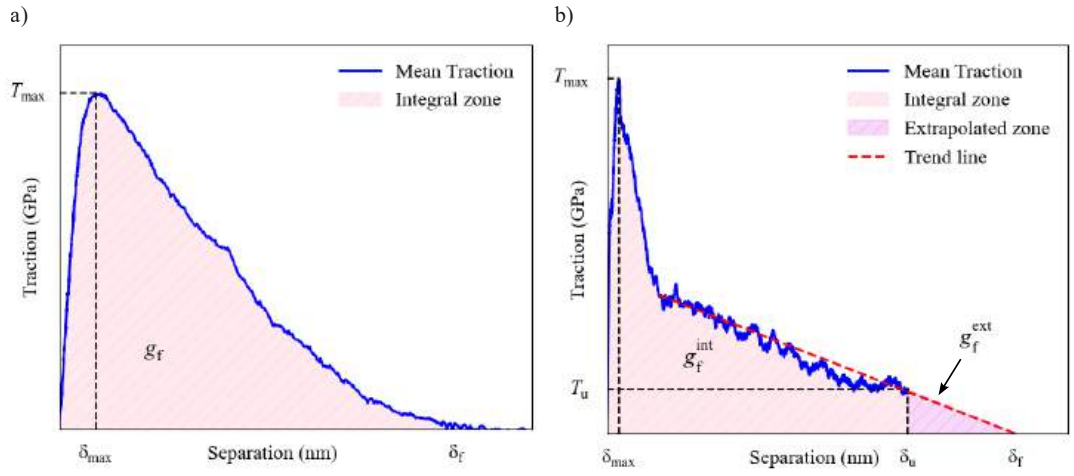

Figure 5.18: Schematic representation of the fracture energy (g_f) obtained from traction–separation behavior. (a) Complete T–S curve; the blue line shows the mean traction response, and the shaded pink area corresponds to the integrated fracture energy ($g_f = g_f^{int}$). (b) Incomplete T–S curve requiring extrapolation; the solid blue line represents the computed mean traction, the light pink area indicates the integrated portion (g_f^{int}), and the red dashed line shows the linear extrapolation used to estimate the remaining contribution (g_f^{ext}, dark pink area), so that $g_f = g_f^{int} + g_f^{ext}$.

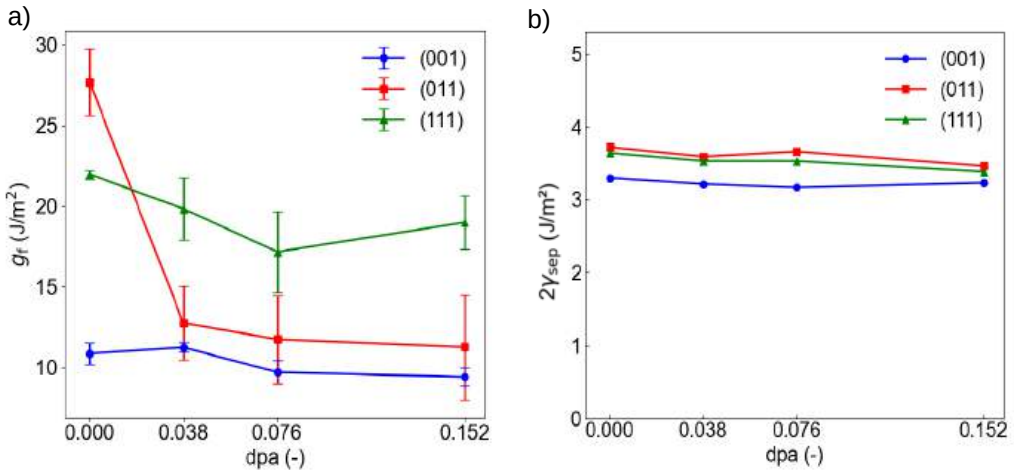

Figure 5.19: (a) Fracture energy, g_f, and (b) separation energy, $2\gamma_{sep}$, as a function of irradiation dose for different orientations.

the energy of surface formation in a fracture process, $2\gamma_s$, which is the dominant contribution to g_f. The nearly constant values of $2\gamma_{sep}$ across irradiation levels confirm that radiation defects have little effect on the intrinsic surface energy. Moreover, for both the (011) and (111) orientations, the free surface (nominal fracture surface) is a {011}-type plane, see Table 5.4, so the respective separation energies should be identical, which is confirmed in Fig. 5.19(b).

Since $2\gamma_{sep}$ remains essentially unchanged, the irradiation-induced reduction of g_f reflects the progressive suppression of plastic dissipation, w_p, in the MD subvolumes at the crack tip. Although w_p is only a minor contribution due to the limited extent of the captured plastic zone, its reduction with increasing dpa provides a meaningful indicator of irradiation-induced embrittlement. Among the analyzed orientations, see Fig. 5.19(a), the (011) exhibits the most pronounced decrease in g_f, pointing to a strong suppression of crack-tip plasticity. The (001) orientation consistently shows the lowest fracture energies, while the (111) maintains the highest resistance to fracture under irradiation. For each irradiation level, g_f values were obtained from several statistically independent realizations, generated by varying the initial distribution of radiation defects through sample rotation or by cutting and reordering the segments to modify the internal defect arrangement. The reported results represent mean values with corresponding standard deviations, based on four realizations for the (011) orientation and three for (001) and (111).

5.5 Integrated analysis of orientation effects on fracture

This section synthesizes the orientation-resolved findings of this chapter into a consolidated, mechanism-to-metrics narrative. We connect the qualitative defect–crack interactions with the quantitative mechanical responses such as stress–strain, crack length, and T–S curves, and interpret the resulting trends through an energy-based perspective (local fracture energy g_f and separation energy $2\gamma_{sep}$). The goal is to establish how crystallography dictates the balance

between plastic accommodation and cleavage in irradiated $Fe_{55}Ni_{19}Cr_{26}$, thereby modulating the radiation-induced DBT. For this comparative analysis, three representative crystallographic orientations were selected based on their distinct slip geometries and deformation characteristics, providing a comprehensive basis for evaluating orientation-dependent fracture behavior under irradiation.

The (001) crystals exhibit delayed plasticity onset and a compact plastic zone even in the pristine state. Under irradiation, SFTs and dislocation clusters intermittently obstruct Shockley-partial mediated fault growth, while voids are readily absorbed or coalesce ahead of the crack. Because the number of active slip systems is inherently limited in this orientation, irradiation does not drastically change the overall response: crack advance remains comparatively fast with modest blunting, and the qualitative morphology is similar to the pristine case (Fig. 5.8).

The (011) orientation demonstrates the most complex and irradiation-sensitive fracture behavior among the analyzed directions. In the pristine state, this orientation possesses a favorable geometry for cross-slip and twinning, which enables coordinated stacking-fault thickening, efficient stress redistribution, and pronounced crack-tip blunting. Under irradiation, however, this coordinated plasticity becomes severely disrupted. Radiation-induced SFTs act as strong barriers that block the forward extension of stacking faults, while the intersection of multiple faults promotes the formation of Lomer–Cottrell locks, which pin dislocations and restrict further glide. At the same time, dispersed defect clusters nucleate localized slip events away from the crack tip, fragmenting the plastic zone and reducing its continuity. In parallel, void absorption and coalescence occur ahead of the advancing crack, locally weakening the ligament and facilitating rapid connection of neighboring cavities. These combined effects lead to a highly irregular and tortuous crack path, characterized by alternating segments of obstruction and weak-linking (see Fig. 5.10). This interplay between blocked slip and void-assisted advance represents the clearest microstructural signature of irradiation-induced DBT among the three orientations.

The (111) orientation exhibits the most ductile response among the analyzed directions, characterized by the rapid activation of multiple {111} slip systems that sustain a wide and highly distributed plastic zone. Under irradiation, stacking faults emitted from the crack tip interact dynamically with radiation-induced dislocations and loops; while loops may locally deflect the faults, they do not arrest plastic flow. Similarly, SFTs occasionally hinder stacking-fault motion, but their blocking effect remains limited and short-ranged. Radiation-induced voids have only a marginal influence, most are absorbed or bypassed without significantly altering the crack trajectory, so the crack front stays strongly blunted with a delayed extension (see Fig. 5.12). Despite the coexistence of various interaction mechanisms in the irradiated state, the high density of activated slip planes inherent to this orientation ensures efficient stress redistribution and continuous plastic accommodation, rendering the influence of individual defects practically negligible on the overall fracture behavior.

The mechanisms explained above explain the quantitative trends:

- *Stress–strain:* (011) shows the largest irradiation-induced loss of ductility and lowered peak stress; (001) changes little (already limited plasticity); (111) is the most robust, retaining yielding/hardening characteristics (Fig. 5.14).
- *Crack length evolution:* (011) advances fastest under irradiation due to void-assisted linking and impeded redistribution of plasticity; (001) is fast in both states with small irradiation effect; (111) remains slow due to sustained blunting (Fig. 5.15).
- *T–S behavior:* (011) exhibits a steeper post-peak softening, and reduced failure opening with dose, indicating curtailed dissipation; (001) is comparatively insensitive; (111) maintains gradual softening with incomplete separation (arrest/blunting) in several cases (Fig. 5.17).

The atomic-scale fracture energy (g_{f}) extracted from T–S curves consolidates these trends:

1. $2\gamma_{\mathrm{sep}}$ is nearly orientation/dose-independent (and identical for (011)/(111) where the nominal fracture plane is $\{011\}$), indicating that intrinsic surface creation energy is weakly affected by irradiation.
2. The dose-dependent decline of g_{f} therefore reflects the loss of plastic dissipation captured within the T–S subvolumes. Among orientations, (011) shows the strongest drop, (001) remains lowest in absolute magnitude, and (111) sustains the highest g_{f}.
3. Interpreted in the extended-Griffith sense ($G_{\mathrm{c}} = 2\gamma_{\mathrm{s}} + w_{\mathrm{p}}$), the orientation trends in g_{f} are consistent with a reduction of w_{p} under irradiation that is *largest* for (011), *moderate/minor* for (001), and *smallest* for (111).

While g_{f} samples only a fraction of the crack-tip process zone and thus underestimates macroscopic dissipation, its orientation- and dose-dependence provides a reliable *local* indicator of an irradiation-induced DBT.

5.6 Statement of author contributions

The research presented in this chapter builds upon the results reported in Mousavi et al. (2026), of which the author is the first author.

The central hypothesis of this work, that irradiation-assisted fracture behavior can be quantitatively assessed using a traction–separation framework, was proposed by the author and formed the foundation of the study.

The author designed the orientation-dependent fracture investigation, which included the selection of crystallographic orientations, the definition of crack geometries, and the formulation of a local traction–separation (T–S) analysis strategy to quantify anisotropic fracture behavior.

The introduction and implementation of the local T–S law at the crack front for irradiated atomistic simulations represent a key methodological contribution of this chapter.

All MD simulations related to fracture were carried out by the author. This includes the preparation of simulation models, execution of crack propagation simulations across different crystallographic orientations, and generation of the complete set of fracture-related results used in the study.

The quantitative analysis of fracture behavior, including orientation-dependent stress–strain responses, crack growth characteristics, T–S relations, critical energy release rates, and anisotropic energy dissipation mechanisms, was performed by the author. Nearly all figures associated with fracture simulations and results were produced by the author and refined through scientific consultation with the supervisor.

The physical interpretation of irradiation-induced anisotropic fracture mechanisms, including orientation-specific crack-tip plasticity, defect-mediated crack shielding or acceleration, and differences in local energy dissipation, was developed through detailed analysis of atomistic simulation results and refined through discussion with the co-authors.

The first version of the manuscript was prepared by the author, including the presentation of results and discussion of physical mechanisms, and the final version was prepared collaboratively by all co-authors.

All aspects related to scientific motivation, fracture methodology, numerical implementation, quantitative analysis, and physical interpretation presented in this chapter can be fully and independently defended by the author.

Chapter 6

Summary, conclusions, and future research

Irradiation-induced degradation of structural materials remains a critical challenge for nuclear energy systems, where fracture resistance and lifetime are governed by complex interactions between microstructural damage and mechanical response. While numerous studies have documented the presence of radiation-induced defects and their macroscopic consequences, a clear mechanistic understanding that directly links atomistic defect processes to fracture behavior has remained incomplete. In particular, the justification of fracture response in terms of physically meaningful mechanical quantities at the atomic scale has not been systematically established. This thesis addresses this gap by providing an atomistic perspective on irradiation-assisted fracture, emphasizing the need to consistently link defect-level mechanisms with quantitative mechanical response. In doing so, the work establishes a unified framework that integrates qualitative insight into defect-controlled fracture processes with quantitative mechanical characterization, while explicitly accounting for the role of crystallographic orientation, thereby offering a physically and mechanically consistent interpretation of radiation-induced embrittlement and the associated ductile-to-brittle transition.

6.1 Summary

This thesis addresses the research objectives formulated in Section 1.2 by developing an atomistic framework to clarify how radiation-induced defects govern crack propagation, fracture resistance, and the ductile-to-brittle transition in fcc $Fe_{55}Ni_{19}Cr_{26}$ alloy. Motivated by the need to identify the mechanisms that either accelerate or decelerate crack growth under irradiation, the work focuses on resolving the competing roles of voids and dislocation loops and on determining the conditions under which each mechanism dominates the fracture response.

To address these questions, the study adopts a structured, atomistically informed framework that consistently links radiation-induced defect populations, crack-tip deformation processes, and energy-based fracture analysis. In the initial stage of the work, defect configurations representative of accumulated irradiation damage are analyzed to identify the dominant physical mechanisms governing crack–defect interactions. This analysis clarifies the respective roles of voids and dislocation loop clusters in either facilitating crack advance or locally shielding the crack tip through constrained plastic deformation. At this stage, the fracture response is examined in the (001) crystallographic orientation, allowing the defect-controlled mechanisms governing crack propagation to be identified.

However, the crystalline nature of the alloy and the strong dependence of plastic deformation on slip-system activity imply that defect–crack interactions cannot be fully characterized without considering crystallographic orientation. The effectiveness of crack-tip plasticity, stress redistribution, and defect shielding is inherently orientation-dependent, as these processes are governed by the availability and activation of crystallographic slip systems. This consideration motivates the second part of the thesis, in which crystallographic orientation is introduced as a governing parameter to systematically assess its influence on fracture behavior under irradiation.

Building on this foundation, the study systematically examines how differences in crystallographic orientation influence defect–crack interactions by modifying slip-system activity and the capacity for crack-tip plastic deformation. These effects govern the balance between defect-assisted crack acceleration and defect-induced crack shielding during crack propagation under irradiation. By extending the analysis in this manner, the thesis establishes that identical radiation-induced defect populations can lead to markedly different fracture responses depending on the crystallographic orientation, providing a physically grounded basis for understanding anisotropic irradiation-induced embrittlement.

Across both stages, fracture behavior is evaluated using mechanically meaningful indicators that quantify deformation mechanisms and energy dissipation during crack propagation. This sequential approach ensures that qualitative observations of defect-controlled fracture processes are consistently supported by quantitative measures of mechanical response. In this way, the thesis establishes a coherent link between atomistic-scale mechanisms and fracture-relevant behavior, providing a unified basis for interpreting radiation-induced embrittlement and its orientation-dependent ductile-to-brittle transition.

6.2 Conclusions

The analysis presented in this thesis demonstrates that fracture behavior in irradiated fcc $Fe_{55}Ni_{19}Cr_{26}$ alloy is governed by competing interactions between radiation-induced defect populations and crack-tip plastic deformation mechanisms. The results show that irradiation does not introduce a single dominant embrittlement mechanism; instead, fracture resistance and crack propagation behavior emerge from the balance between defect-assisted crack acceleration and defect-induced crack shielding. The dominance of either mechanism is controlled by defect evolution and by the crystallographic constraints that regulate plastic accommodation at the crack tip. This competition provides a unifying physical basis for interpreting radiation-induced degradation across different defect populations, irradiation levels, and crystallographic orientations.

In the first stage, the fracture behavior is examined under irradiation without explicit consideration of crystallographic variability, allowing the dominant defect-controlled mechanisms to be isolated. This analysis demonstrates that irradiation fundamentally reduces the material's ability to accommodate plastic deformation at the crack tip. Vacancy-type defects, particularly radiation-

induced voids, play a central role in this process by acting as weak zones that locally reduce lattice cohesion and promote crack advance through absorption and linkage mechanisms. As irradiation progresses, the accumulation and spatial connectivity of voids increasingly facilitate crack propagation, driving a gradual transition from ductile crack-tip blunting toward more brittle fracture behavior. At the same time, interstitial-type defect clusters impede dislocation motion and restrict plastic flow, further limiting the capacity for crack-tip stress relaxation. Together, these effects establish radiation-induced embrittlement as a consequence of defect-mediated suppression of plastic deformation rather than changes in intrinsic bond strength. At increasing irradiation levels, this analysis demonstrates that void populations progressively become the dominant contributors to crack acceleration, while the influence of interstitial clusters transitions from crack-shielding to plasticity-suppressing behavior.

A key outcome of this first stage is the identification of plastic energy dissipation as the controlling factor governing fracture resistance under irradiation. By decomposing the fracture response into physically interpretable contributions, the analysis shows that embrittlement is directly associated with a progressive loss of plastic work at the crack tip, while the energy associated with crack surface formation remains largely unaffected. This finding provides a quantitative basis for translating atomistic defect effects into fracture-relevant mechanical response and confirms that irradiation-induced ductile-to-brittle transition is fundamentally a plasticity-controlled phenomenon. Accordingly, the transition from defect-shielded to brittle fracture regimes can be quantitatively traced through reductions in plastic work extracted from stress–strain response, traction–separation behavior, and energy-based fracture metrics.

The second stage of the thesis extends this mechanistic understanding by explicitly accounting for crystallographic orientation. This extension reveals that the fracture response of irradiated material cannot be described solely by defect density or defect type, but is strongly governed by the orientation-dependent capacity of the lattice to accommodate plastic deformation. The same radiation-induced defect populations give rise to markedly different fracture behaviors depending on the available slip systems and the associated crack-tip deformation pathways.

In orientations with inherently limited slip activity, such as (001), plastic relaxation remains constrained even in the absence of significant irradiation damage, resulting in consistently low fracture resistance. In this case, irradiation primarily reinforces an already brittle response. In contrast, orientations that rely on coordinated slip activity, such as (011), exhibit pronounced sensitivity to irradiation. Here, defect-induced obstruction of stacking fault propagation and the formation of immobile dislocation junctions sharply suppress plastic dissipation, leading to a rapid degradation of fracture resistance and an accelerated transition to brittle fracture. Conversely, orientations that activate multiple slip systems, exemplified by (111), retain a greater capacity to incorporate radiation-induced defects into extended deformation structures. This enables sustained crack-tip plasticity and elevated energy dissipation, allowing these orientations to resist embrittlement even in irradiated conditions. These results demonstrate that

crystallographic orientation governs not only the rate of embrittlement, but also the irradiation dose window over which crack-shielding mechanisms remain operative.

These orientation-dependent responses demonstrate that interstitial defect clusters can act as effective crack-shielding features under specific conditions, delaying crack advance and contributing positively to material lifetime despite their role in radiation hardening. However, this beneficial effect is conditional and persists only while sufficient plastic accommodation remains available. As irradiation advances and void populations grow and coalesce, void-assisted crack acceleration ultimately dominates, overwhelming defect-induced shielding and driving the fracture response toward a brittle regime. Interstitial defect clusters can therefore be regarded as beneficial to material lifetime only at low to intermediate irradiation levels and in orientations capable of sustaining distributed slip, beyond which their hardening effect accelerates embrittlement.

Taken together, the results establish that radiation-induced fracture in fcc alloys is governed by a competition between defect-assisted crack acceleration and defect-induced crack shielding, with the dominant mechanism controlled by defect evolution and crystallographic orientation. The ductile-to-brittle transition emerges not as a single intrinsic fracture process, but as a progressive shift in the balance between these competing mechanisms, mediated by the orientation-dependent capacity for plastic deformation and energy dissipation at the crack tip. This progression provides a mechanistic definition of the irradiation-induced ductile-to-brittle transition in terms of evolving defect populations and diminishing plastic energy dissipation.

By consistently linking qualitative observations of crack-defect interactions with quantitative measures of fracture energy dissipation, this thesis provides a unified, atomistically grounded interpretation of radiation-induced embrittlement. The resulting framework clarifies how radiation-induced defects, slip-system activity, and fracture energetics collectively govern crack propagation and lifetime-limiting behavior in irradiated structural alloys. Within this framework, the governing mechanisms of irradiation-assisted fracture are explicitly resolved through stress–strain response, traction–separation laws, and energy-based fracture metrics, providing a physically consistent answer to the central research questions posed in this thesis.

6.3 Future research directions

The results of this thesis open several avenues for further investigation aimed at extending the understanding of irradiation-assisted fracture in structural materials. One natural extension of the present work is the exploration of austenitic stainless steels with different chromium and nickel contents. Variations in alloy chemistry modify stacking-fault energy, solute–defect interactions, and deformation mechanisms, all of which can influence defect evolution and fracture response under irradiation. Systematic studies across related compositions would help assess the generality of the mechanisms identified here and provide guidance for the design of embrittlement-resistant alloys.

Beyond fcc systems, extending the analysis to body-centered cubic (bcc) materials represents an important direction for future research. Structural alloys with bcc crystal structures, including reduced-activation ferritic–martensitic (RAFM) steels relevant for fusion applications, exhibit fundamentally different slip behavior, defect mobility, and irradiation response. Comparative investigations between fcc and bcc systems would clarify which aspects of irradiation-assisted fracture are universal and which are strongly structure-dependent, thereby strengthening the predictive capability of atomistically informed fracture models.

Another critical aspect that warrants further attention is the role of helium-related damage. Addressing this problem will require the development or extension of interatomic potentials that can accurately describe Fe–Ni–Cr–He and Fe–Cr–He systems, as no suitable potentials currently exist for these alloy–helium combinations. Helium accumulation under irradiation can strongly affect defect stability, void nucleation, and bubble growth, with significant consequences for crack-tip plasticity and fracture behavior. Incorporating helium effects into atomistic simulations would enable detailed analysis of bubble–defect and bubble–crack interactions and provide a more realistic representation of service conditions in nuclear environments.

The present work is limited to single-crystal configurations, whereas real engineering materials are polycrystalline and contain grain boundaries that interact strongly with both irradiation-induced defects and propagating cracks. Extending the framework to bicrystalline and polycrystalline systems would allow investigation of how grain boundary character, cohesion, and irradiation-induced boundary weakening influence fracture mechanisms and lifetime-limiting behavior under irradiation.

Finally, closer integration with experimental investigations would significantly enhance the impact of the present findings. Validation through in-situ transmission electron microscopy, micro-mechanical testing, and controlled irradiation experiments would strengthen confidence in the atomistic predictions and facilitate their incorporation into multiscale modeling frameworks. Such combined experimental–computational efforts are essential for translating atomistic insight into reliable, engineering-relevant predictions of irradiation-induced embrittlement and fracture.

Appendix A

Elastic properties and moduli

Irradiation generates lattice defects that may influence the elastic response of crystalline materials. Understanding the elastic properties of irradiated materials is therefore essential for predicting their mechanical behavior under service conditions. An experimental measurement of elastic constants over a wide range of irradiation conditions (e.g., varying dpa) is often impractical due to cost, time, and technical limitations. Atomistic simulation methods such as the Born matrix (BM) method provide a powerful alternative for evaluating the elastic response of both pristine and irradiated materials.

The Born matrix method determines elastic constants by analyzing the system's response to small applied infinitesimal strains. It captures the second derivative of the potential energy with respect to strain and can include thermal contributions, thus allowing the evaluation of temperature-dependent elastic constants in equilibrium MD simulations.

In this framework, the elastic stiffness tensor C_{ijkl} is defined as:

$$C_{ijkl} = \left.\frac{\partial^2 U}{\partial \varepsilon_{ij} \partial \varepsilon_{kl}}\right|_{\varepsilon=0}, \tag{A.1}$$

where U is the total potential energy of the system, and ε_{ij} represents the components of the infinitesimal strain tensor. The Born term corresponds to the static contribution from the potential energy landscape, capturing the inherent stiffness of the relaxed lattice.

For finite-temperature simulations, the BM method is extended to include contributions from stress fluctuations and dynamic atomic displacements. This enables more realistic predictions of elastic constants for both defect-free and irradiated configurations, especially when defects perturb the local bonding environment. The full temperature-dependent elastic constants is expressed as:

$$C_{i,j} = \langle C^{B}_{i,j} \rangle + \frac{V}{k_B T} \left(\langle \sigma_i \sigma_j \rangle - \langle \sigma_i \rangle \langle \sigma_j \rangle \right) + \frac{N k_B T}{V} \left(\delta_{i,j} + (\delta_{1,i} + \delta_{2,i} + \delta_{3,i})(\delta_{1,j} + \delta_{2,j} + \delta_{3,j}) \right), \tag{A.2}$$

where $\langle C^{B}_{i,j} \rangle$ denotes the Born contribution, $\langle \sigma_i \sigma_j \rangle$ are the stress tensor fluctuations, and the last term accounts for kinetic contributions at finite temperature. Here, k_B is the Boltzmann constant, T is the temperature, V is the system volume, N is the number of atoms, and δ represents the Kronecker delta.

For cubic systems such as the fcc Fe–Ni–Cr alloys studied here, the elastic behavior is fully

characterized by three independent elastic constants: C_{11}, C_{12}, and C_{44}. Once obtained from atomistic simulations, these constants can be used to derive several macroscopic mechanical parameters under the Voigt approximation (Hill, 1952), which assumes a uniform strain distribution throughout the crystal.

The first of these is the bulk modulus, B_{V}, which quantifies the material's resistance to uniform volumetric compression. For cubic crystals, it is expressed as:

$$B_{\mathrm{V}} = \frac{C_{11} + 2C_{12}}{3}. \tag{A.3}$$

A higher bulk modulus indicates a stiffer response to hydrostatic loading, reflecting strong interatomic bonding.

The tetragonal shear modulus, C', measures the material's ability to resist shear deformation on $\{110\}$ planes along $\langle 1\bar{1}0\rangle$ directions. It is given by:

$$C' = \frac{C_{11} - C_{12}}{2}. \tag{A.4}$$

This parameter is particularly sensitive to changes in bonding symmetry and is often affected by point defects or alloying.

The overall resistance to shear deformation can be represented by the shear modulus G_{V}, which in the Voigt scheme is a weighted combination of C' and C_{44}:

$$G_{\mathrm{V}} = \frac{3C_{44} + 2C'}{5}. \tag{A.5}$$

Here, C_{44} corresponds to simple shear on $\{100\}$ planes along $\langle 010\rangle$ directions, while C' captures tetragonal shear, making G_{V} an effective descriptor of the crystal's average shear resistance.

From the bulk and shear moduli, the Young's modulus E_{V} can be derived as:

$$E_{\mathrm{V}} = \frac{9B_{\mathrm{V}}G_{\mathrm{V}}}{3B_{\mathrm{V}} + G_{\mathrm{V}}}. \tag{A.6}$$

Young's modulus represents the stiffness of the material in uniaxial loading and is a key indicator of its ability to elastically store energy.

Similarly, the Poisson's ratio ν_{V}, defined as:

$$\nu_{\mathrm{V}} = \frac{3B_{\mathrm{V}} - 2G_{\mathrm{V}}}{2(3B_{\mathrm{V}} + G_{\mathrm{V}})}, \tag{A.7}$$

describes the ratio of transverse contraction strain to longitudinal extension strain under uniaxial loading. This quantity is linked to the material's ductility, with higher values generally indicating greater plastic deformability.

Finally, the Zener anisotropy ratio (Zener and Sidney, 1949), A_r, is calculated as:

$$A_r = \frac{C_{44}}{C'}. \tag{A.8}$$

This dimensionless quantity measures the degree of elastic anisotropy in cubic crystals. A value of $A_r = 1$ corresponds to elastic isotropy, while deviations from unity indicate direction-dependent stiffness, often amplified by defects or compositional inhomogeneities.

In this study, the mechanical properties of the irradiated $Fe_{55}Ni_{19}Cr_{26}$ alloy in the (001) orientation were analyzed using the BM method, which evaluates elastic constants based on the energy-strain relationship. This approach accounts for static lattice stiffness, represented by the Born term, while also incorporating contributions from stress fluctuations due to thermal vibrations, allowing for the determination of elastic constants at finite temperatures (Workum et al., 2006). A comparative analysis was conducted to ensure the reliability of the computational approach used in this study, specifically the BM method employed. The elastic constants of a structurally similar material, $Fe_{70}Ni_{10}Cr_{20}$, were computed using the BM method and compared with EAM11 potential results using the uniform deformation method (UD method)

Table A.1: Elastic constants of non-irradiated $Fe_{70}Ni_{10}Cr_{20}$ alloy computed using the Born matrix (BM), compared with experimental data (cited in Bonny et al. (2011)) and EAM11 potential results reported in Bonny et al. (2011).

	C_{11} (GPa)	C_{12} (GPa)	C_{44} (GPa)	B_V (GPa)	G_V (GPa)	A_r
Experimental data	204–226	132–134	111–122	157–164	81–92	2.4–3.5
EAM11 – UD method	214	136	129	162	93	3.3
Born–matrix (present work)	214.0	135.1	128.2	161.4	92.7	3.3

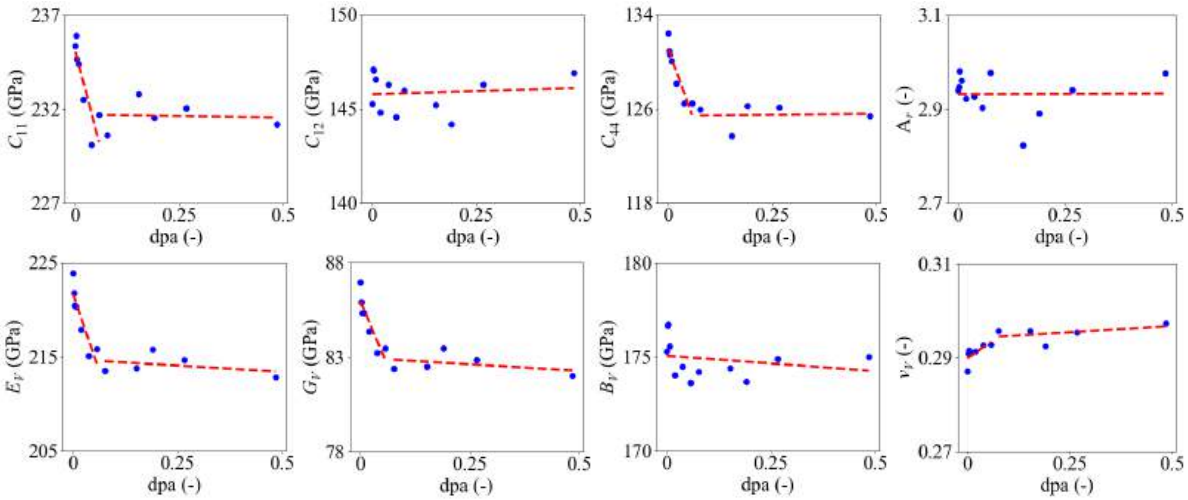

Figure A.1: Evolution of elastic constants (C_{11}, C_{12}, C_{44}) and mechanical properties: Zener anisotropy ratio (A_r), Young's modulus (E_V), shear modulus (G_V), bulk modulus (B_V), and Poisson's ratio (ν_V)) of irradiated Fe-Ni-Cr alloy as a function of dpa. Blue dots represent computed values at discrete dpa levels, while red dashed lines indicate trend fits.

and experimental measurements reported in Bonny et al. (2011). As shown in Table A.1, the computed elastic constants exhibit strong agreement with both EAM11 and experimental data, confirming the robustness and accuracy of the adopted methodology.

As shown in Fig. A.1, the elastic properties of $Fe_{55}Ni_{19}Cr_{26}$ alloy exhibit systematic changes as a function of dpa. C_{11} and C_{44} display a bilinear decrease, indicating an initial rapid softening due to defect accumulation, followed by a more gradual decline as the evolution of defect structures stabilizes. This trend suggests that at low dpa levels, the formation of radiation-induced voids primarily contributes to elastic softening. In contrast, at higher dpa, the increased presence of dislocation loops and SFTs leads to a more stabilized response. C_{12} component remains relatively unchanged.

E_V and G_V follow a similar, slightly decreasing trend, reflecting a minor reduction in the alloy's resistance to tensile and shear deformation. The A_r shows a constant trend toward increased dpa, implying that directional dependence on mechanical behavior is largely preserved. The overall analysis reveals that irradiation induces only minor changes in the mechanical behavior of the alloy, with the elastic response remaining largely unchanged.

Appendix B

Boundary condition analysis

To systematically evaluate how different boundary constraints influence the accuracy and realism of crack propagation in MD simulations, three representative configurations were tested: (i) the shrink-wrapped and surface-fixed setup (`ssp`), (ii) the fully fixed with vacuum padding configuration (`ffp`), and (iii) the fully periodic boundary setup (`ppp`). All simulations were performed under uniaxial tensile loading, and representative deformation snapshots are presented in Fig. B.1. Such configurations have been extensively used in previous studies to investigate fracture behavior in crystalline materials, including `ppp` (Singh et al., 2019), `ffp`, and `ssp` systems (Krull and Yuan, 2011; Xu and Demkowicz, 2020; Ding et al., 2020; Barik et al., 2023). **(A) Shrink-wrapped surface-fixed (`ssp`) configuration:** Panel A shows two variations of

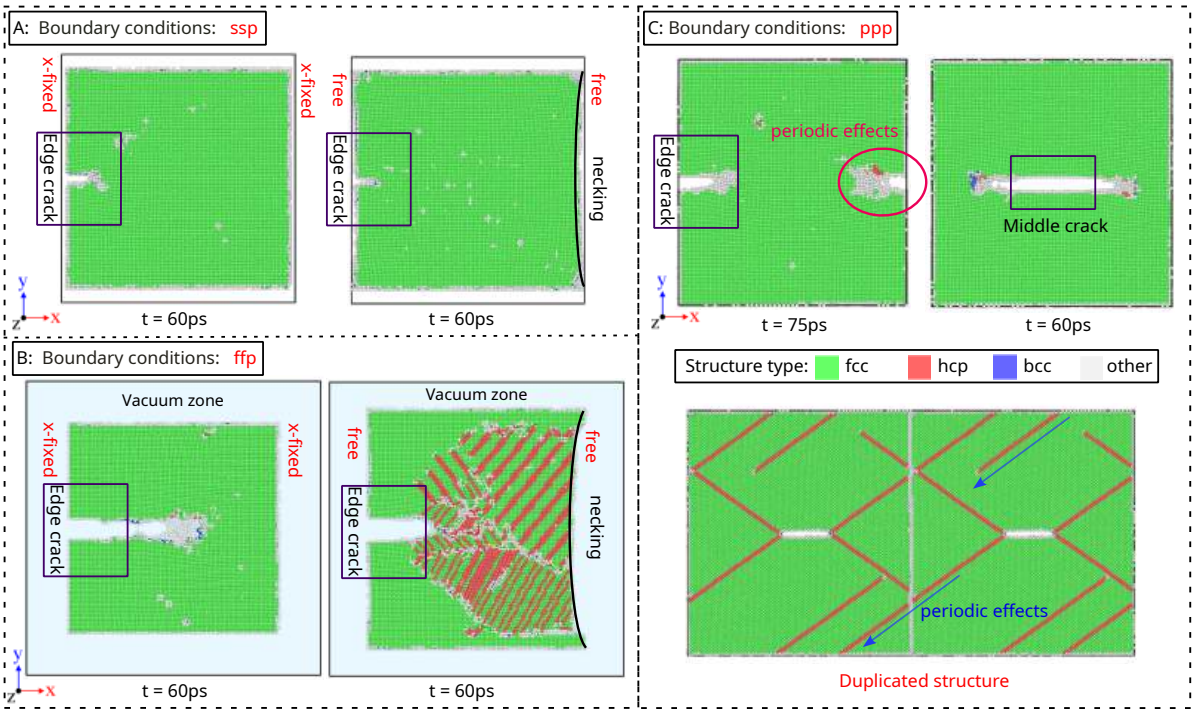

Figure B.1: Comparative analysis of boundary conditions on crack propagation behavior. Panel A illustrates the `ssp` configuration under uniaxial tension, panel B shows the `ffp` setup, and panel C represents the `ppp` configuration. All snapshots correspond to equivalent time steps (t = 60–75 ps) and are color-coded by atomic structure: fcc (green), hcp (red), bcc (blue), and others (gray). (A) Two `ssp` variants: with fixed lateral boundaries (left) and with free sides (right). (B) Two `ffp` cases: with constrained x-edges and vacuum padding (left), and without lateral constraints (right), both showing necking near free surfaces. (C) `ppp` setups: edge crack (left) and middle crack (right), showing mirrored cracks and duplicated structures due to periodic effects.

the ssp boundary scheme. In the left image, the lateral edges in the *x*-direction are fixed to suppress transverse motion, representing the configuration adopted throughout this study. This constraint mimics an experimental tensile test with clamped grips at the top and bottom, ensuring that deformation is transmitted through the lattice without artificial relaxation at the sides. In contrast, the right image depicts an identical setup with lateral edges released. The absence of *x*-constraints allows lateral strain release, resulting in strong necking near the edges and premature crack arrest. The local narrowing and lateral contraction modify the stress distribution at the crack front, impeding its forward propagation and altering the fracture morphology.

(B) Fully fixed with vacuum padding (ffp) configuration: Panel B compares two representative ffp setups. In the left image, the *x*-edges are fixed, and a vacuum zone (light-blue region in the figure) is added to prevent atom deletion at the free surfaces. This setup enforces affine deformation by globally scaling the simulation box, creating a nearly homogeneous strain field across the sample. Although numerically stable and efficient, this uniform loading accelerates crack opening and failure, leading to earlier decohesion and reduced plastic accommodation. Moreover, it tends to suppress local deformation modes such as dislocation emission or shear band formation, which are critical for understanding ductile response. The right image in panel B shows the same configuration without *x*-constraints, where the free lateral boundaries cause enhanced necking and asymmetry near the fracture zone. Such a setup better reflects bulk-like conditions but fails to capture realistic free-surface relaxation essential for surface-driven fracture mechanisms.

(C) Fully periodic (ppp) configuration: The right panel C presents the ppp configuration for two cases—one with the crack located at the edge (top-left subpanel) and one at the center (top-right subpanel). Because of the periodicity in all directions, mirrored cracks form on the opposite side of the simulation cell (highlighted in purple in the figure), and duplicated structural features appear periodically along the *x*-axis (indicated in blue). These mirrored effects distort the actual stress field and interfere with the evolution of the crack tip, often resulting in artificial interactions between periodic images. While such boundary conditions are suitable for bulk plastic deformation and defect studies, they are not ideal for simulating free-surface fracture processes or crack propagation, where boundary relaxation plays a dominant role.

Based on the comparative analysis, the constrained ssp configuration was selected as the most balanced approach. It maintains physically realistic plasticity, dislocation emission, and crack-tip evolution while avoiding unphysical global deformation or mirrored periodic effects. Hence, the ssp setup used in this work provides a reliable representation of Mode-I crack propagation under tensile loading in finite atomistic systems.

Appendix C

Ensemble Selection for Fracture Simulations

In MD simulations, the choice of statistical ensemble determines the thermodynamic constraints imposed on the system and therefore influences the interpretation of both radiation-damage evolution and mechanically driven fracture processes. All commonly used ensembles, including NVE, NVT, and NPT, are valid and well-established frameworks within MD; however, their suitability depends on the specific physical problem being addressed and on the quantities of interest.

In this work, the NVT ensemble was adopted during the irradiation stage, consistent with numerous previous studies (Nordlund et al., 2018b; von Toussaint et al., 2021; Zhou et al., 2023; Dominguez-Gutierrez et al., 2022; Ustrzycka et al., 2024). Under irradiation conditions, NVT provides controlled thermal dissipation while maintaining a fixed simulation volume, enabling stable relaxation of cascade-induced defects. In continued application of this framework, it is necessary to examine whether the same ensemble remains appropriate for the mechanically loaded fracture stage, where crack initiation and propagation introduce additional thermomechanical requirements.

Accordingly, this appendix presents a comparative assessment of the NVE, NVT, and NPT ensembles in the context of Mode-I tensile crack propagation in irradiated materials. The objective is not to rank the ensembles in a general sense, but rather to identify the ensemble that best satisfies the specific requirements of the fracture problem addressed in this thesis.

To ensure a consistent comparison, a middle-crack model with identical geometry and dimensions was employed for all simulations. A representative irradiated sample with the (011) crystallographic orientation was selected for this assessment. For the NVE and NVT simulations, boundary conditions were defined as *shrink-wrapped* in the crack-propagation direction (x), *non-periodic* in the loading direction (y), and *periodic* in the thickness direction (z). This configuration allows crack opening and free-surface formation while preserving continuity in the out-of-plane direction.

For the NPT ensemble, global pressure control was applied. In order to ensure a well-defined pressure response under this control scheme, fully periodic boundary conditions were employed in all three directions. As discussed in Appendix B, such fully periodic configurations suppress free-surface formation and introduce interactions between periodic images, which limit their suitability for analyzing localized crack-tip mechanisms. Nevertheless, this configuration allows the intrinsic response of the NPT ensemble under pressure-controlled conditions to be evaluated consistently.

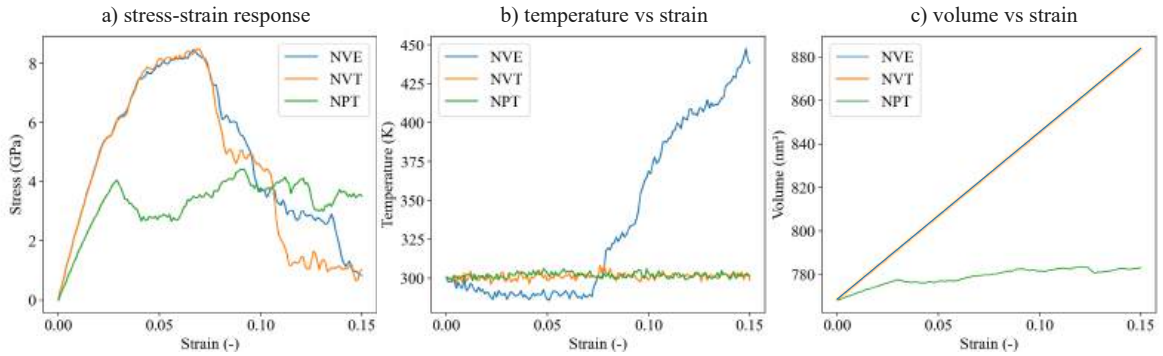

Figure C.1: Comparison of (a) stress–strain response, (b) temperature–strain evolution, and (c) volume–strain behavior for NVE, NVT, and NPT ensembles in the (011) orientation.

To examine the thermomechanical response of each ensemble, stress–strain, temperature–strain, and volume–strain curves were extracted under identical loading conditions, as shown in Fig. C.1. The NVE and NVT ensembles exhibit comparable elastic behavior and similar stress evolution up to the onset of plasticity. The NPT ensemble, by contrast, reflects the influence of active pressure regulation throughout deformation.

The stress–strain response under NPT conditions is characterized by a smooth and stable evolution of stress, accompanied by a relatively constant volume, as shown in Fig. C.1a and c. This behavior arises from the pressure-control mechanism, which continuously adjusts the simulation cell to maintain the prescribed pressure state. While such stabilization is appropriate for equilibrium or bulk deformation studies, it limits the accumulation of localized stresses at the crack tip.

In fracture simulations, crack initiation and propagation depend on the development of pronounced stress concentrations within a confined crack-tip process zone. Under NPT conditions, deformation is redistributed through global cell adjustments, reducing the degree of stress localization required to drive crack advance. Consequently, although the NPT ensemble provides consistent pressure and temperature control, it does not fulfill the mechanical requirements needed to resolve crack-tip stress fields in the present fracture problem.

The temperature–strain response further highlights the intrinsic differences among the ensembles. Under NVE conditions, no explicit temperature control is imposed, and irreversible processes associated with crack-tip plasticity lead to a gradual increase in kinetic energy, resulting in a rising temperature during deformation (Fig. C.1b). This temperature increase enhances thermally activated deformation mechanisms and influences the timing and extent of plastic activity near the crack tip.

In contrast, the NVT ensemble regulates temperature through coupling to a thermostat, maintaining stable thermal conditions throughout loading. This enables the mechanical response to be analyzed at a prescribed temperature, facilitating comparison across different deformation stages. The NPT ensemble also maintains temperature control; however, this occurs simultaneously with

pressure regulation, leading to global volume adjustments that influence the stress distribution and deformation mode.

These differences are most clearly reflected in the volume–strain behavior (Fig. C.1c). Under NVT conditions, the simulation volume remains fixed, consistent with the imposed boundary conditions and with the mechanical constraints of a tensile fracture test. Under NPT conditions, the volume evolves with strain as part of the pressure-control process, introducing additional deformation pathways that complicate the interpretation of crack-related mechanical response.

From an energy-based perspective, consistent thermodynamic constraints are essential for interpreting fracture metrics such as mechanical work input, internal energy evolution, and energy dissipation during crack propagation. Under NVE conditions, the progressive increase in temperature modifies the balance between kinetic and potential energy contributions, influencing the relative contribution of thermally activated plasticity during fracture. Under NPT conditions, volume changes associated with pressure regulation introduce additional work contributions related to cell rescaling, which affect the partitioning of energy during deformation.

By contrast, the NVT ensemble maintains controlled temperature while enforcing fixed-volume conditions, allowing mechanical work, internal energy changes, and dissipated energy to be evaluated consistently throughout the fracture process. This combination enables a clear separation of energy contributions directly associated with crack propagation, supporting reliable extraction of fracture-related quantities such as critical energy release rates and traction–separation relationships.

Qualitative inspection of atomic-scale deformation provides further support for this assessment. Fig. C.2 presents atomic configurations at $\varepsilon = 6.5\%$ and $\varepsilon = 10\%$ for the three ensembles. Under both NVE and NVT conditions, dislocation emission and slip-band formation occur near the crack tip in a manner consistent with deformation mechanisms expected in fcc metals. Under NVE conditions, elevated temperature accelerates local plastic activity and promotes earlier void nucleation near the crack tip. In contrast, under NVT conditions, void nucleation occurs at higher strain levels, following sufficient mechanical stress accumulation.

Under NPT conditions, the presence of full periodicity and pressure regulation leads to deformation dominated by global cell adjustments rather than localized crack opening. As a result, crack-tip separation and slip activity are suppressed relative to the other ensembles, limiting the ability to resolve fracture mechanisms relevant to free-surface crack propagation.

In summary, all three ensembles examined in this appendix are valid and applicable within their respective domains. The NVE ensemble captures deformation under conditions where no explicit temperature control is imposed, allowing the system temperature to evolve naturally in response to mechanical work and irreversible processes. The NPT ensemble provides pressure-controlled deformation suitable for bulk response, and the NVT ensemble offers controlled thermal conditions at fixed volume. Based on the specific requirements of Mode-I fracture simulations, including stable temperature control, fixed-volume constraints, free-surface crack

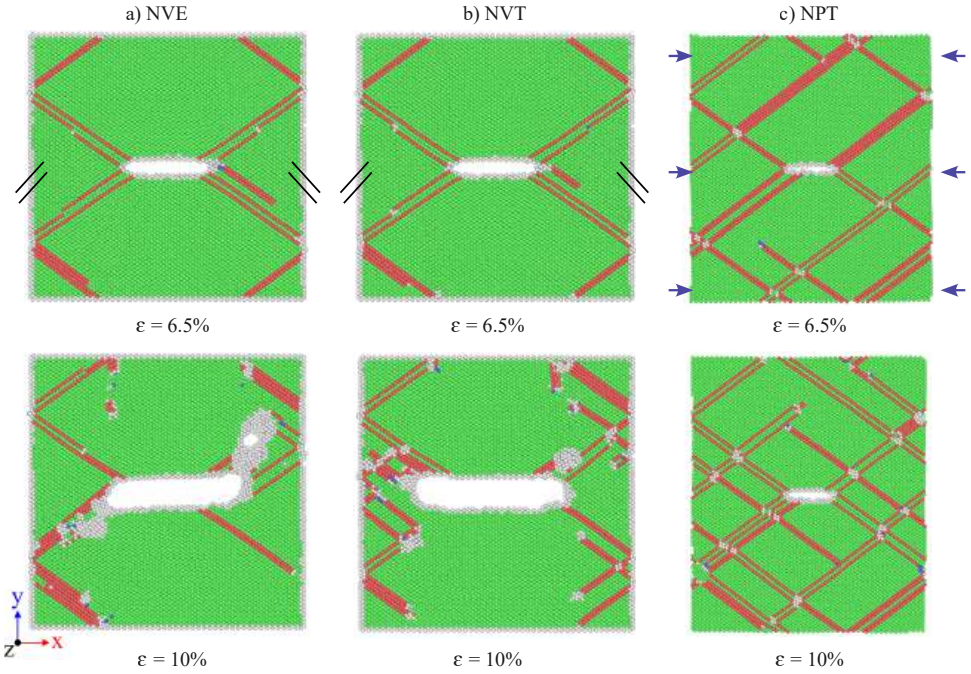

Figure C.2: Qualitative comparison of crack-tip deformation mechanisms in the (011) orientation at $\varepsilon = 6.5\%$ and $\varepsilon = 10\%$ for NVE, NVT, and NPT ensembles.

opening, and resolvable stress localization, the NVT ensemble provides the most suitable framework for the fracture analyses performed in this thesis.

Appendix D

Strain-rate effects on fracture mechanisms

The fracture mechanisms identified in Sections 5.3.2, 5.3.3, and 5.3.4 indicate that radiation-induced defects markedly influence crack-tip plasticity via orientation-dependent interactions with evolving deformation fields. These mechanisms were characterized under the high strain-rate conditions typical of MD simulations ($\dot{\varepsilon} = 10^9$ s^{-1}). However, the physics of dislocation nucleation, defect mobility, and crack-tip shielding is known to be sensitive to the applied deformation rate (Zhang and Jiang, 2017; Zhao et al., 2025). At elevated rates, reduced time for defect relaxation may suppress thermally activated processes, alter slip activity, and stabilize irradiation-induced obstacles that would otherwise be absorbed or bypassed.

It is therefore essential to verify whether the main mechanisms remain operative across a broader range of loading rates. Demonstrating their rate-independence is crucial for confirming their physical relevance beyond the constraints of MD-specific conditions.

The simulation set at $\dot{\varepsilon} = 10^9$ s^{-1} was extended to include two additional loading rates:

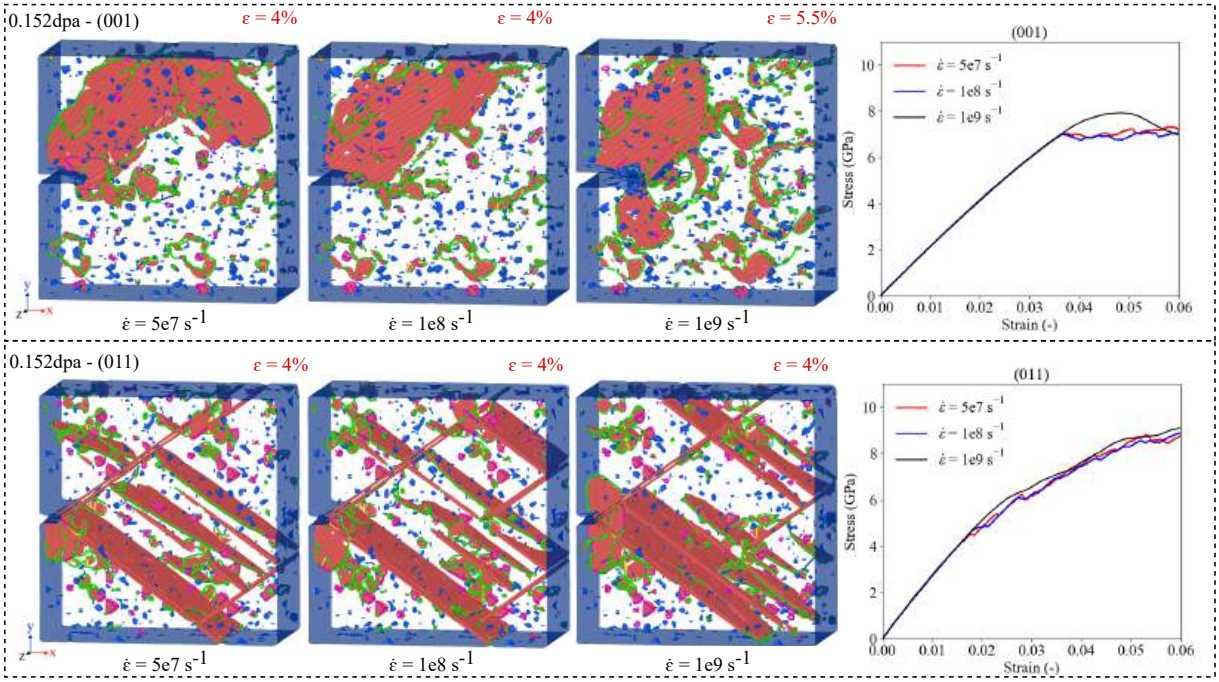

Figure D.1: Strain rate-dependent crack propagation in irradiated samples for two orientations: (001) (top row) and (011) (bottom row). Simulations are conducted at $\dot{\varepsilon} = 5 \times 10^7$ s^{-1}, 10^8 s^{-1}, and 10^9 s^{-1}. Morphologies are captured at $\varepsilon = 4\%$ except for (001)-10^9 s^{-1} case, where $\varepsilon = 5.5\%$ was needed due to delayed plasticity. The consistent appearance of dislocation clusters, void coalescence, and defect-stacking fault interactions confirms the convergence of underlying physical mechanisms across strain rates.

10^8 s^{-1} and 5×10^7 s^{-1}, for the (001) and (011) orientations, as shown in Fig. D.1. The (111) orientation was not considered, as dominant plasticity in this case renders the effect of radiation-induced defects negligible. Due to high computational cost, the simulations were performed over a reduced strain range up to $\varepsilon = 6\%$. Crack-tip morphologies were evaluated at $\varepsilon = 4\%$, except for the (001) sample at $\dot{\varepsilon} = 10^9$ s^{-1}, where delayed plasticity required extension to $\varepsilon = 5.5\%$. This confirms the strain-rate sensitivity of dislocation nucleation in orientations with limited slip activity. Despite this shift, key deformation mechanisms, such as SFT-crack front interactions, stacking fault deflection, and asymmetric plastic zones, remain qualitatively consistent across the considered strain rates.

Appendix E

Evaluation of crack-tip stress distributions

The supplementary stress-field maps in this appendix provide additional insight into the orientation-dependent mechanisms discussed in Sections 5.3 and 5.4.

Each set of figures presents the crack-tip σ_{yy} distributions for three irradiation levels, including pristine sample, 0.038 dpa, and 0.152 dpa, evaluated at two strain levels specific to each crystallographic orientation. For the (001) orientation, the stress fields are shown at $\varepsilon = 4.5\%$ and 5.5% in Fig. E.1; for the (011) orientation at $\varepsilon = 3.0\%$ and 4.0% in Fig. E.2; and for the (111) orientation at $\varepsilon = 2.5\%$ and 3.5% in Fig. E.3. These results illustrate how irradiation alters the spatial distribution of σ_{yy} for the three crystallographic orientations and their corresponding crack configurations. To enhance the clarity of the crack-tip stress contours, the σ_{yy} fields shown in these results were post-processed using a neighbor-mean stress calculation, in which atomic stresses were smoothed over a 5 Å radial neighborhood to reduce local noise and highlight the underlying spatial trends.

For the (001) orientation, the stress fields in Fig. E.1 reveal a consistently sharp and highly localized tensile peak positioned directly ahead of the crack tip. With increased irradiation dose, this peak intensifies and becomes progressively narrower. The minimal lateral spreading of stress contours highlights the inherently limited plastic relaxation capacity of the (001) system. Irradiation amplifies this limited plasticity by further constraining dislocation mobility, in agreement with the mechanisms discussed in Subsections 5.3.2 and 4.4.1, where defect–slip interactions were shown to suppress crack-tip plasticity and produce the pronounced hardening and reduced ductility observed in the stress–strain responses.

The (011) orientation exhibits the most pronounced radiation-induced transformation among the three, as shown in Fig. E.2. While the pristine configuration already displays a relatively confined tensile zone, higher irradiation levels significantly sharpen the crack-tip stress peak and generate asymmetric secondary hotspots. These features indicate strong obstruction of slip by radiation-induced defects, leading to severe local stress accumulation and a highly constrained plastic zone. This response is fully consistent with the behavior reported in Subsection 5.3.3, where the (011) system was shown to be particularly susceptible to defect clustering and slip inhibition. Moreover, the strong localization of stress correlates directly with the steep hardening and reduced plastic flow observed in the stress–strain curves of Subsection 4.4.1, as well as with the accelerated crack advance and higher crack velocity exhibited by irradiated (011) samples.

In contrast, the (111) orientation preserves the broadest and most diffuse crack-tip stress field, as illustrated in Fig. E.3. Even with increasing irradiation levels, the tensile hotspot sharpens

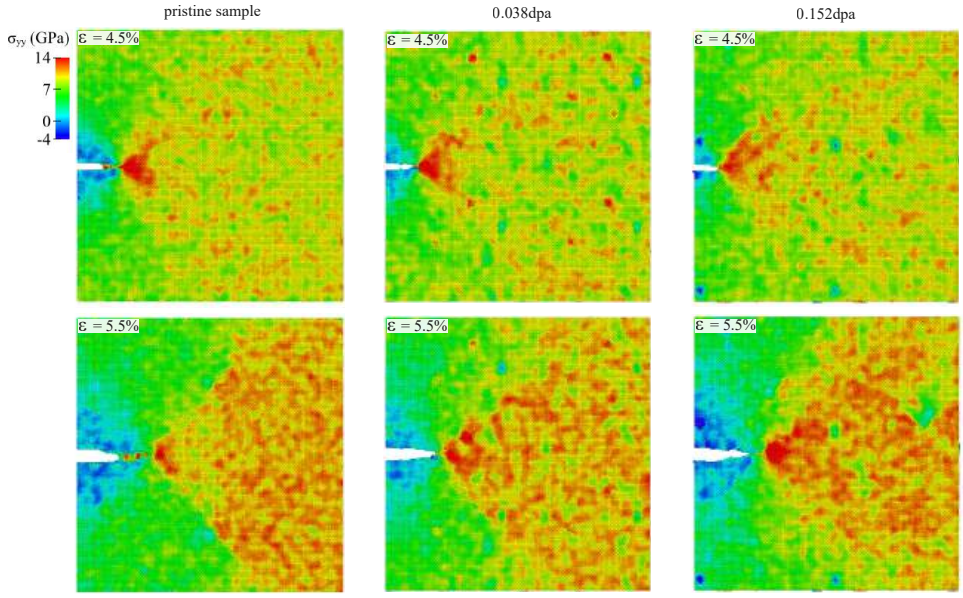

Figure E.1: Stress field distribution (σ_{yy}) in pristine and irradiated samples with the (001) crystallographic orientation during crack propagation, corresponding to the $\{010\}\langle 001\rangle$ crack configuration.

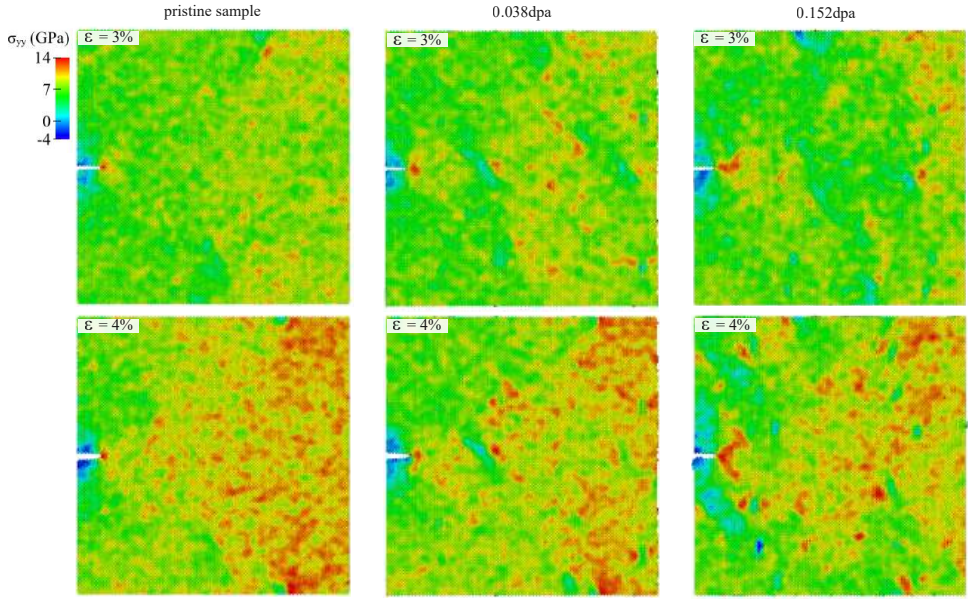

Figure E.2: Stress field distribution (σ_{yy}) in pristine and irradiated samples with the (011) crystallographic orientation during crack propagation, corresponding to the $\{01\bar{1}\}\langle 011\rangle$ crack configuration.

only slightly, and the stress contours continue to extend laterally, indicating that the plastic zone remains comparatively large and well developed. This behavior reflects the high availability of favorably oriented slip systems on the (111) plane, which promotes efficient stress redistribution and enables dislocations to relax the crack tip, consistent with the slip-activation mechanisms discussed in Subsection 5.3.4. The smooth stress gradients and lack of significant secondary hotspots also align with the mechanical response described in Subsection 4.4.1, where the (111) samples exhibited the mildest hardening rate and the most stable stress–strain behavior.

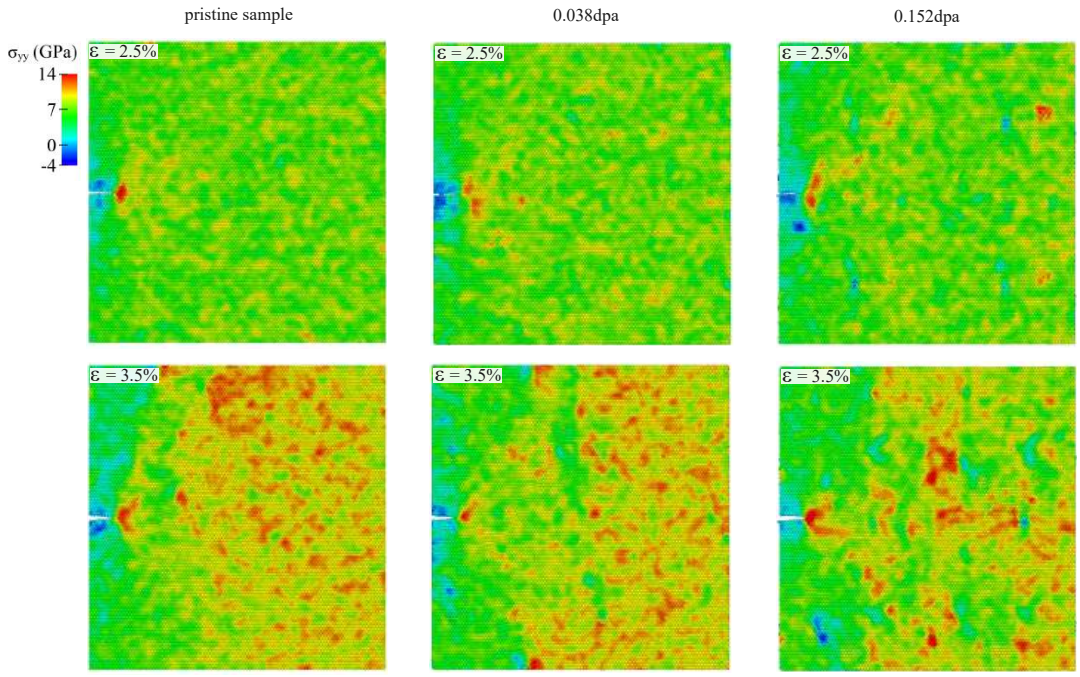

Figure E.3: Stress field distribution (σ_{yy}) in pristine and irradiated samples with the (111) crystallographic orientation during crack propagation, corresponding to the $\{\bar{1}01\}\langle 111\rangle$ crack configuration.

A comparison of the three orientations highlights a clear hierarchy in irradiation sensitivity, stress localization, and DBT behavior. The (001) orientation exhibits inherently limited plasticity, with stress localization that intensifies under irradiation and promotes an early shift toward brittle-like crack advance. The (011) orientation exhibits the most severe irradiation-driven stress concentration, developing sharply focused tensile peaks and secondary hotspots that reflect strong defect–crack interactions and accelerate the onset of DBT. In contrast, the (111) orientation maintains the broadest tensile distribution and the most effective plastic relaxation even at elevated dpa levels, delaying the DBT and preserving a more ductile response under irradiation.

Appendix F

Cohesive–zone model and traction–separation law

The description of fracture at the continuum scale has traditionally relied on classical linear elastic fracture mechanics (LEFM), in which the crack-tip stress field exhibits a square–root singularity,

$$\sigma_{ij}(r) \sim \frac{K}{\sqrt{x}}, \tag{F.1}$$

where K is the mode-I stress–intensity factor and x denotes the distance from the crack tip. Although Eq. (F.1) correctly captures the far-field behaviour, it becomes unphysical at small length scales because it predicts an infinite stress as $x \to 0$. Atomistic simulations, including those performed in the present work, demonstrate that the region immediately ahead of the crack is governed by nonlinear mechanisms such as bond stretching, local cleavage, atomic rearrangements, and dislocation emission. These processes regularize the singularity and give rise to a finite fracture process zone (FPZ), invalidating the notion of a mathematically sharp crack tip.

This conceptual shortcoming of LEFM was first addressed in the pioneering works of Dugdale (1960) and Barenblatt (1962), who introduced the notion of a cohesive zone in which opposing crack faces remain partially bonded and transmit a finite traction. Modern cohesive–zone models (CZM) build upon this foundation by prescribing a constitutive relationship between the traction transmitted across the separating surfaces and the corresponding displacement jump. Such T–S relations have been widely adopted in continuum fracture modelling because of their physical transparency and flexibility in representing material softening behaviours.

A schematic illustration of these concepts is shown in Fig. F.1, depicting (a) the transition from the LEFM singular field to a bounded cohesive field inside the FPZ, (b) the distribution of cohesive tractions acting over a finite cohesive length u_c, and (c) a representative traction–separation (T–S) response. As emphasized in classical cohesive-zone studies and more recent interface-fracture analyses, the T–S curve provides a direct link between micromechanical separation mechanisms and the macroscopic fracture energy.

Within the cohesive-zone framework, the interface response is described by a constitutive relation between the cohesive traction T and the crack-opening displacement δ:

$$T = T(\delta), \tag{F.2}$$

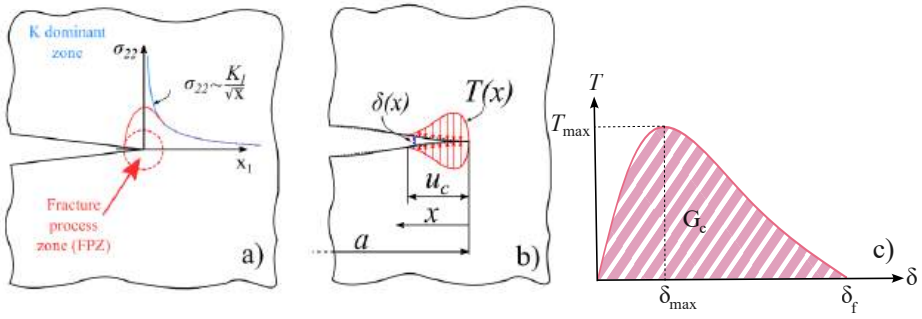

Figure F.1: Schematic illustration of cohesive-zone concepts: (a) transition from the LEFM singular field to a finite-strength FPZ; (b) cohesive traction distribution $T(x)$ acting over a finite cohesive length u_c; (c) traction–separation (T–S) relation, where the fracture energy G_c corresponds to the shaded area under the curve. Figure reproduced from (Andric, 2019).

subject to the physically motivated conditions

$$T(0) = 0, \qquad T(\delta_{\max}) = T_{\max}, \qquad T(\delta_f) = 0, \tag{F.3}$$

where $\delta_{\max}$ denotes the displacement at peak traction and δ_f the final opening at which complete separation occurs.

The energy associated with full interface decohesion is obtained as the work of separation:

$$G_{\mathrm{c}} = \int_0^{\delta_{\mathrm{f}}} T(\delta)\,\mathrm{d}\delta, \tag{F.4}$$

which represents the critical energy release rate in continuum CZM formulations.

In these models, G_{c} must be provided as a material parameter, and the T–S shape (bilinear (Dugdale, 1960), exponential (Barenblatt, 1962), polynomial (Needleman, 1990), or smooth multi-parameter forms (Tvergaard and Hutchinson, 1992)) is chosen a priori. While versatile, such phenomenological laws require calibration and may not fully capture microstructure-dependent fracture behaviour.

In our work, the atomic-scale fracture energy g_{f} is defined as the area under the MD-extracted T–S curve, see Fig. 5.18. This quantity reflects the local interface formation energy required to separate the crack surfaces inside a nanoscale MD subvolume. Unlike the continuum-scale G_{c}, which combines surface-formation energy γ_{s} with the full macroscopic plastic dissipation w_{p}, the atomistic fracture energy $g_{\mathrm{f}} = 2\gamma_{\mathrm{s}}^{\mathrm{local}} + w_{\mathrm{p}}^{\mathrm{local}}$ is dominated by surface creation, as MD captures only a small portion of the crack-tip plastic zone. Thus, the measured g_{f} primarily quantifies local decohesion energetics, with only a minor fraction attributed to crack-tip plasticity. This distinction is essential when interpreting radiation-induced trends, since irradiation suppresses local plasticity and hence directly affects the MD contribution to g_{f}.

MD provides a fundamentally different route to constructing cohesive-zone relations. Instead of postulating a functional form, the entire T–S behaviour emerges directly from interatomic

forces. As the two crack faces are displaced in a controlled manner, the cohesive traction is calculated using virial stresses or boundary reaction forces, while the separation δ is obtained from the relative displacements of the crack surfaces. This atomistic procedure, widely employed in cohesive-parameter extraction (Yamakov et al., 2006; Krull and Yuan, 2011; Wang et al., 2021), reproduces the full evolution of bond stretching, peak traction $T_{\max}$, post-peak softening, and ultimate decohesion at δ_f without phenomenological assumptions.

Because MD explicitly resolves defect interactions, dislocation emission, and local disorder around the crack tip, the resulting g_{f} captures the combined effects of surface formation and the limited plasticity present in the simulation cell. This makes MD-derived T–S relations particularly valuable for studying orientation effects, defect–crack coupling, and irradiation-induced changes in local fracture resistance.

Although MD provides a direct, assumption-free separation response, the simulated T–S curves do not always reach $T(\delta_{\mathrm{f}}) = 0$. In ductile orientations or configurations exhibiting strong crack-tip blunting, separation may arrest prematurely due to intensive dislocation activity, resulting in T–S curves that terminate with nonzero traction.

Since the fracture energy requires integration up to δ_{f}, the incomplete tail must be supple-

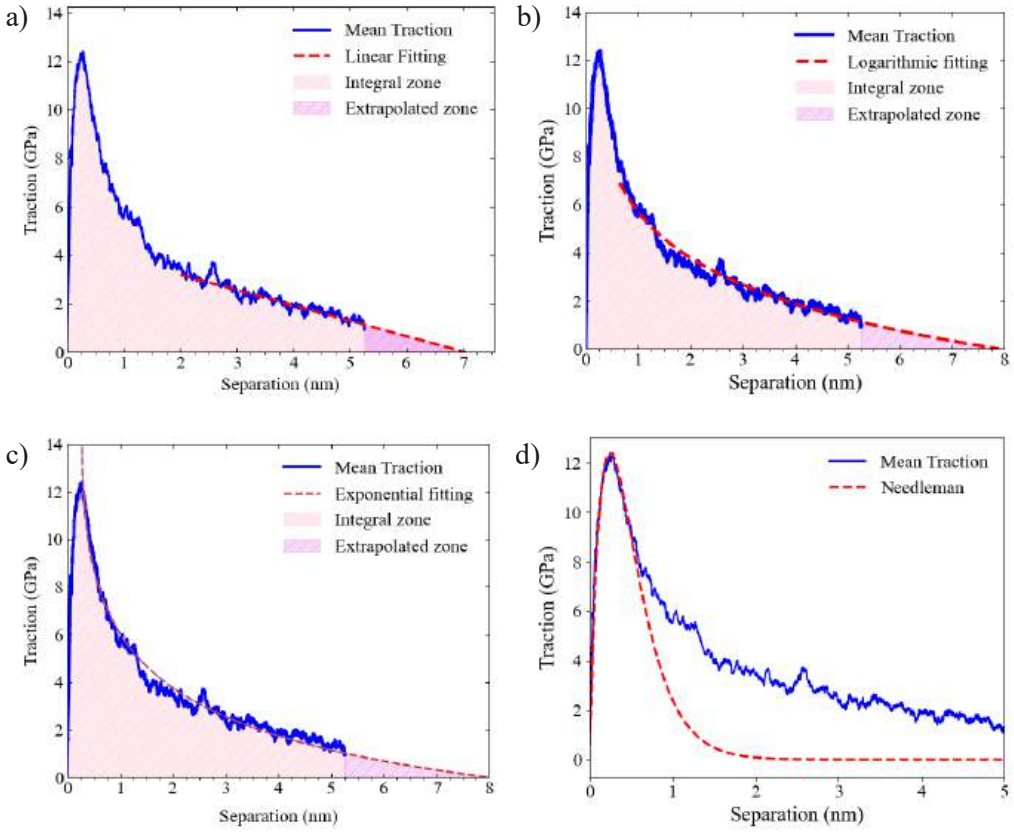

Figure F.2: Comparison of extrapolation strategies for the (111)-oriented (0.038 dpa) sample: (a) linear; (b) logarithmic; (c) stretched exponential; (d) Needleman model. The pink region denotes the directly integrated zone $g_{\mathrm{f}}^{\mathrm{int}}$, while the purple region indicates the extrapolated tail $g_{\mathrm{f}}^{\mathrm{ext}}$.

mented by an extrapolated softening branch. The continuation is anchored at the last MD data point, decays monotonically to zero traction, and represents the final stage of material separation not captured within the MD window.

To ensure consistency across all configurations, the total fracture energy is decomposed as

$$g_{\mathrm{f}} = g_{\mathrm{f}}^{\mathrm{int}} + g_{\mathrm{f}}^{\mathrm{ext}}, \tag{F.5}$$

where $g_{\mathrm{f}}^{\mathrm{int}}$ is the MD-integrated portion and $g_{\mathrm{f}}^{\mathrm{ext}}$ the decay tail added analytically.

Three nonlinear continuation methods were tested to estimate $g_{\mathrm{f}}^{\mathrm{ext}}$:

(i) Logarithmic decay

$$T_{\log}(\delta) = a\ln(\delta) + b, \tag{F.6}$$

with

$$a = \frac{T_{\max}}{\ln(\delta_{\max}) - \ln(\delta_{\mathrm{f}})}, \tag{F.7}$$

$$b = -a\ln(\delta_{\mathrm{f}}); \tag{F.8}$$

(ii) Stretched–exponential decay

$$T_{\exp}(\delta) = A\left[e^{-B(\delta-\delta_{\max})^n} - e^{-B(\delta_{\mathrm{f}}-\delta_{\max})^n}\right]; \tag{F.9}$$

(iii) Needleman cohesive law (Needleman, 1990)

$$T_{\mathrm{Need}}(\delta) = T_{\max}\frac{16e^2}{9\delta_{\mathrm{f}}}\delta\exp\left(-\frac{16e}{9\delta_{\mathrm{f}}}\delta\right). \tag{F.10}$$

All continuations were constrained to match the last MD data point and satisfy $T(\delta_{\mathrm{f}}) = 0$. Figure F.2 demonstrates that the linear, logarithmic, and stretched-exponential continuations agree closely with the measured softening branch, while the Needleman model deviates for highly ductile responses.

Across all tested methods, the extrapolated energies were:

$$\begin{aligned} g_{\mathrm{f}}^{\mathrm{ext}} &= 1.13\ \mathrm{J/m^2} \quad \text{(linear)},\\ g_{\mathrm{f}}^{\mathrm{ext}} &= 1.34\ \mathrm{J/m^2} \quad \text{(logarithmic)},\\ g_{\mathrm{f}}^{\mathrm{ext}} &= 1.22\ \mathrm{J/m^2} \quad \text{(stretched exponential)}. \end{aligned}$$

Because the directly integrated portion $g_{\mathrm{f}}^{\mathrm{int}}$ is identical in all cases, the small spread in $g_{\mathrm{f}}^{\mathrm{ext}}$ confirms that the tail contributes only a minor fraction of the total fracture energy. This demonstrates that the simplified linear continuation used in the main work is fully justified and that the reported g_{f} values are robust with respect to the extrapolation procedure.

Appendix G

MD implementation of crack propagation

This appendix documents the MD implementation used to simulate mode-I crack propagation in the $Fe_{55}Ni_{19}Cr_{26}$ alloy. The simulations were performed using the LAMMPS package and were designed to accommodate both pristine and irradiated configurations, apply loading conditions according to the prescribed deformation protocol, and extract the relevant mechanical and fracture-related quantities for post-processing analysis. The purpose of this appendix is to provide transparency and technical clarification of the numerical procedures employed in the main chapters.

The fracture simulation input script is organized into modular segments, each corresponding to a specific stage of the MD workflow. For clarity, the implementation is presented below using structured blocks, followed by a concise explanation of the physical and numerical role of each segment.

G.1: Global variables and simulation control

```
variable   Temp        equal 300.0
variable   atom_file   string Sample.data
variable   NumSteps    equal 150000
```

As shown in G.1, the global variables controlling the MD simulation are defined at the beginning of the input script. These include the target temperature (300 K), the input data file containing the equilibrated atomic configuration, and the total number of MD steps used during the fracture simulation. Defining these quantities as variables ensures consistency throughout the script, facilitating reproducibility and parametric studies.

G.2: Initialization and boundary conditions

```
units            metal
boundary         s s p
atom_style       atomic
read_data        $atom_file
neighbor         1.0 bin
neigh_modify     every 1 delay 0 check yes
timestep         0.001
```

The initialization of the simulation domain and the applied boundary conditions are presented in G.2. The simulation is executed using metal units, which define the internal unit system for time (ps), length (Å), energy (eV), and mass in atomic mass units. Boundary conditions are specified as non-periodic (s) in the loading and crack propagation directions and periodic (p) along the out-of-plane direction.

The atomic configuration of the specimen is introduced using the `read_data` command, which reads a data file containing atomic positions, atom types, and the simulation box dimensions. This enables the use of pre-equilibrated atomic structures as initial configurations for the fracture simulations.

Neighbor lists are constructed using a bin-based method with a skin distance of 1.0 Å. The neighbor list is rebuilt at every MD step without delay to ensure that interatomic interactions are updated consistently during the simulation. The `timestep` command specifies the integration time step used for advancing the MD equations of motion, which are set to 0.001 in metal units, corresponding to a time increment of 1 fs.

G.3: Geometric parameters and crack region definition

```
variable  lattice    equal 3.527
variable  crack_l    equal 0.1*(xhi-xlo)
variable  region_h   equal 6*${lattice}
variable  crack_m    equal (yhi-ylo)/2
variable  crack_low  equal ${crack_m}-${region_h}
variable  crack_up   equal ${crack_m}+${region_h}
```

The geometric parameters defining the crack and crack-tip regions are introduced in G.3. The crack length and crack-tip position are expressed relative to the simulation box dimensions, ensuring scalability with specimen size. The upper and lower crack-tip regions are constructed using LAMMPS variable substitution, enabling direct evaluation of crack opening displacement during loading.

G.4: Geometric parameters and crack region definition

```
region  1           block INF ${crack_l} ${crack_m} ${leftup} INF INF units box
group   abovecrack  region 1
region  2           block INF ${crack_l} ${leftlow} ${crack_m} INF INF units box
group   belowcrack  region 2
```

In G.4, two auxiliary regions are defined to identify atoms located above and below the initial crack plane. These regions are bounded in the crack propagation direction by the crack length variable and in the loading direction by the crack center and auxiliary offset variables.

G.5: Region and group definitions

```
region  3         block INF INF INF ${ylo0} INF INF units box
group   lower     region 3
region  4         block INF INF ${yhi0} INF INF INF units box
group   upper     region 4
region  5         block ${xhi0} INF ${ylo0} ${yhi0} INF INF units box
group   right     region 5
region  6         block INF ${xlo0} ${ylo0} ${yhi0} INF INF units box
group   left      region 6
group   boundary  union upper lower right left
group   mobile    subtract all boundary
```

The spatial regions and atom groups defined in G.5 specify the geometric partitioning of the simulation domain and the corresponding group assignments. Rectangular regions are defined using LAMMPS `block` commands to represent the lower, upper, left, and right portions of the domain. Atom groups are then assigned to each region and combined to form a single boundary group. The mobile group is constructed by subtracting the boundary atoms from the full system.

G.6: Crack initialization

```
neigh_modify  exclude  group abovecrack belowcrack
```

The initial sharp crack is introduced in G.6 by excluding interatomic interactions across a predefined crack plane. This approach preserves atomic positions while removing cohesive forces, resulting in a well-defined crack tip without introducing artificial voids or mass loss.

G.7: Group definitions for mobile and T–S regions

```
group  boundary  union upper lower right left
group  mobile    subtract all boundary
group  tsregion  union upperTS lowerTS
```

Additional atom groups required to distinguish mobile atoms from fixed boundaries and to construct the traction–separation measurement region are defined in G.7. This grouping strategy enables localized evaluation of traction and crack opening displacement ahead of the crack tip.

G.8: Variables defining T–S region partitions

```
variable  point0  equal ${crack_l}
variable  point1  equal ${point0}+${region_h}
variable  point2  equal ${point1}+${region_h}
variable  point3  equal ${point2}+${region_h}
...
```

The variables defined in G.8 specify a sequence of reference positions used to partition the T–S region along the crack propagation direction. The variable `point0` is initialized using the crack length variable, which serves as the starting coordinate of the T–S region.

Subsequent variables `point1` through `point6` are defined recursively by incrementing the previous point by the characteristic length ${region_height}. Each variable, therefore, represents the boundary of a consecutive sub-region with equal extent. These variables are later used as positional limits for defining multiple adjacent regions in the input script.

G.9: T–S sub-region and group definitions

```
region  7       block ${point0} ${point1} ${crack_m} ${crack_up} INF INF units box
group   TSup-1  region 7
region  8       block ${point0} ${point1} ${crack_low} ${crack_m} INF INF units box
group   TSlo-1  region 8
...
```

The region and group definitions summarized in G.9 describe the partitioning of the T–S domain into multiple sub-regions. Spatial bounds along the crack propagation direction are specified using predefined point variables, while the loading-direction limits are defined relative to the crack-center coordinate. Each sub-region is assigned to a corresponding atom group, and the same construction pattern is applied to all subsequent intervals indicated by the abbreviated entries.

G.10: Interatomic potential

```
pair_style       eam/alloy
pair_coeff   * *  FeNiCr.eam.alloy Fe Ni Cr
```

The interatomic interactions employed in the MD simulations are specified in G.10 using an embedded atom method (EAM) potential parameterized for Fe–Ni–Cr alloys. This potential captures metallic bonding, defect energetics, and deformation mechanisms relevant to irradiation-assisted fracture.

G.11: Stress, strain, and displacement computations

```
compute   stress_atoms  all stress/atom NULL virial
compute   mob           mobile reduce sum c_stress_atoms[*]
compute   ts            tsregion reduce sum c_stress_atoms[*]
compute   dis           mobile displace/atom
```

The computation of stress, strain, and displacement quantities is summarized in G.11. Atomic-level virial stress is spatially averaged over selected regions, while crack opening displacement is obtained from relative atomic displacements across the crack plane. These quantities form the basis for constructing stress–strain curves and T–S relations.

G.12: Strain rate and loading parameters

```
variable  srate   equal 1.0e9
variable  srate1  equal ${srate}/1.0e12
variable  Vel     equal (${srate1}*${L0y})/2
```

The strain rate and loading parameters employed in the MD simulations are defined in G.12. A constant nominal strain rate is prescribed, and the corresponding boundary velocity is computed to ensure symmetric displacement-controlled loading.

G.13: Boundary loading and thermostat

```
fix  1  lower move linear 0.0 -${Vel} 0.0 units box
fix  2  upper move linear 0.0 ${Vel} 0.0 units box
fix  3  right move linear 0.0 NULL NULL units box
fix  4  left move linear 0.0 NULL NULL units box
fix  5  mobile nvt temp ${Temp} ${Temp} 0.1
```

The commands defined in G.13 specify the prescribed motion of selected atom groups and the time integration applied to mobile atoms. The first two `fix` commands assign linear displacement to the `lower` and `upper` groups, respectively, with velocities determined by the variable ${Vel}. The motion is applied along the loading direction, while the remaining velocity components are set to zero.

The subsequent `fix` commands apply `fix move linear` to the `right` and `left` groups, where `NULL` entries indicate that no prescribed motion is imposed along the corresponding directions. These commands define the boundary motion behavior for the associated atom groups during the simulation.

Finally, the `fix nvt` command applies a Nose–Hoover thermostat to the `mobile` atom group, maintaining the target temperature defined by ${Temp} using the specified thermostat

damping parameter.

G.14: Output and data logging

```
fix     def1         all print 100 output.txt screen no
dump    dump_stress  mobile custom 5000 dump.stress id type x y z
thermo               1000
run                  ${NumSteps}
```

The output and data logging procedures defined in G.14 specify the generation of text-based and atomic-level output files during the MD simulation. Selected global and group-based quantities related to stress, strain, energy, and traction–separation parameters are written at prescribed intervals for post-processing and visualization. The simulation is subsequently executed for the total number of time steps defined by the run control parameters. All output files generated by this script are intended for subsequent post-processing, visualization, and extraction of fracture metrics described in the main chapters.

Bibliography

Aidhy, D. S., Lu, C., Jin, K., Bei, H., Zhang, Y., Wang, L., and Weber, W. J. (2016). Formation and growth of stacking fault tetrahedra in Ni via vacancy aggregation mechanism. *Scripta Materialia*, 114:137–141.

Allen, M. P. and Tildesley, D. J. (2017). *Computer Simulation of Liquids*. Oxford University Press.

Andersen, H. C. and Chandler, D. (1970). Mode expansion in equilibrium statistical mechanics. I. general theory and application to the classical electron gas. *The Journal of Chemical Physics*, 53(2):547–554.

Anderson, S., Khafizov, M., and Chernatynskiy, A. (2024). Threshold displacement energies and primary radiation damage in AlN from molecular dynamics simulations. *Nuclear Instruments and Methods in Physics Research Section B: Beam Interactions with Materials and Atoms*, 547:165228.

Anderson, T. L. (2005). *Fracture mechanics: fundamentals and applications*. CRC press.

Andric, P. (2019). *The mechanics of crack-tip dislocation emission and twinning*. PhD thesis, Ecole Polytechnique Fédérale de Lausanne.

Andric, P. and Curtin, W. (2017). New theory for mode I crack-tip dislocation emission. *Journal of the Mechanics and Physics of Solids*, 106:315–337.

Andric, P. and Curtin, W. (2018). New theory for crack-tip twinning in fcc metals. *Journal of the Mechanics and Physics of Solids*, 113:144–161.

Ashby, M. F. and Jones, D. R. (2012). *Engineering materials 1: an introduction to properties, applications and design*, volume 1. Elsevier.

Ayanoglu, M. and Motta, A. (2022). Emulation of neutron-irradiated microstructure of austenitic 21Cr32Ni model alloy using dual-ion irradiation. *Journal of Nuclear Materials*, 570:153944.

Bacon, D., Gao, F., and Osetsky, Y. N. (1999). Computer simulation of displacement cascades and the defects they generate in metals. *Nuclear Instruments and Methods in Physics Research Section B: Beam Interactions with Materials and Atoms*, 153(1-4):87–98.

Bao, H., Xu, H., Li, Y., Bai, H., and Ma, F. (2022). The interaction mechanisms between dislocations and nano-precipitates in CuFe alloys: A molecular dynamic simulation. *International Journal of Plasticity*, 155:103317.

Barenblatt, G. I. (1962). The mathematical theory of equilibrium cracks in brittle fracture. In Dryden, H. L., von Kármán, T., Kuerti, G., van den Dungen, F. H., and Howarth, L., editors, *Advances in Applied Mechanics*, volume 7, pages 55–129. Elsevier.

Barik, R. K., Ghosh, A., and Chakrabarti, D. (2023). Fundamental insights on ductile to brittle transition phenomenon in ferritic steel. *Materialia*, 27:101667.

Barik, R. K., Jayasree, T., Biswal, S., Ghosh, A., and Chakrabarti, D. (2024). Investigating the ductile to brittle transition phenomenon in binary Fe-Ni systems using molecular dynamics simulation. *Journal of the Mechanics and Physics of Solids*, 187:105624.

Barrows, W., Dingreville, R., and Spearot, D. (2016). Traction–separation relationships for hydrogen induced grain boundary embrittlement in nickel via molecular dynamics simulations. *Materials Science and Engineering: A*, 650:354–364.

Beltz, G. and Rice, J. (1992). Dislocation nucleation at metal-ceramic interfaces. *Acta Metallurgica et Materialia*, 40:S321–S331. Proceedings of the International Symposium on Metal-Ceramic Interfaces.

Bernstein, N. and Hess, D. W. (2003). Lattice trapping barriers to brittle fracture. *Phys. Rev. Lett.*, 91:025501.

Bhandarkar, V. V., Shahare, H. Y., Mall, A. P., and Tandon, P. (2025). An overview of traditional and advanced methods to detect part defects in additive manufacturing processes. *Journal of Intelligent Manufacturing*, 36(7):4411–4446.

Bitzek, E. and Gumbsch, P. (2008). Atomistic simulations of dislocation-crack interaction. *Journal of Solid Mechanics and Materials Engineering*, 2(10):1348–1359.

Bitzek, E., Koskinen, P., Gähler, F., Moseler, M., and Gumbsch, P. (2006). Structural relaxation made simple. *Phys. Rev. Lett.*, 97:170201.

Boisson, M., Legras, L., Andrieu, E., and Laffont, L. (2019). Role of irradiation and irradiation defects on the oxidation first stages of a 316L austenitic stainless steel. *Corrosion Science*, 161:108194.

Bonny, G., Terentyev, D., Pasianot, R. C., Poncé, S., and Bakaev, A. (2011). Interatomic potential to study plasticity in stainless steels: the FeNiCr model alloy. *Modelling and Simulation in Materials Science and Engineering*, 19(8):085008.

Briceño, M., Fenske, J., Dadfarnia, M., Sofronis, P., and Robertson, I. (2011). Effect of ion irradiation-produced defects on the mobility of dislocations in 304 stainless steel. *Journal of Nuclear Materials*, 409(1):18–26.

Buehler, M. J. (2008). *Atomistic modeling of materials failure*. Springer.

Bukonte, L., Djurabekova, F., Samela, J., Nordlund, K., Norris, S., and Aziz, M. (2013). Comparison of molecular dynamics and binary collision approximation simulations for atom displacement analysis. *Nuclear Instruments and Methods in Physics Research Section B:*

Beam Interactions with Materials and Atoms, 297:23–28.

Béland, L. K., Tamm, A., Mu, S., Samolyuk, G. D., Osetsky, Y. N., Aabloo, A., Klintenberg, M., Caro, A., and Stoller, R. E. (2017). Accurate classical short-range forces for the study of collision cascades in Fe–Ni–Cr. *Computer Physics Communications*, 219:11–19.

CERN (n.d.). CERN – The European Organization for Nuclear Research, https://home.cern.

Chandra, S., Kumar, N., Samal, M., Chavan, V., and Patel, R. (2016). Molecular dynamics simulations of crack growth behavior in Al in the presence of vacancies. *Computational Materials Science*, 117:518–526.

Chang, L., Kitamura, T., and Zhou, C.-Y. (2020). Atomic simulation of the orientation effects on crack tip behavior in titanium single crystal. *Theoretical and Applied Fracture Mechanics*, 110:102791.

Chauhan, A., Yuan, Q., Dethloff, C., Gaganidze, E., and Aktaa, J. (2021). Post-irradiation annealing of neutron-irradiated EUROFER97. *Journal of Nuclear Materials*, 548:152863.

Chen, W.-Y., Miao, Y., Gan, J., Okuniewski, M. A., Maloy, S. A., and Stubbins, J. F. (2016). Neutron irradiation effects in Fe and Fe-Cr at 300°C. *Acta Materialia*, 111:407–416.

Christian, J. and Mahajan, S. (1995). Deformation twinning. *Progress in Materials Science*, 39(1):1–157.

Clausius, R. (1870). XVI. On a mechanical theorem applicable to heat. *The London, Edinburgh, and Dublin Philosophical Magazine and Journal of Science*, 40(265):122–127.

Cui, C. and Beom, H. (2014). Molecular dynamics simulations of edge cracks in copper and aluminum single crystals. *Materials Science and Engineering: A*, 609:102–109.

Cui, W., Liu, W., and Cui, Y. (2024). Does the decoration of irradiation defects induce hardening? *Acta Mechanica Sinica*, 40(2):423031.

Cui, Y., Po, G., and Ghoniem, N. (2017). Does irradiation enhance or inhibit strain bursts at the submicron scale? *Acta Materialia*, 132:285–297.

Daw, M. S. and Baskes, M. I. (1984). Embedded-atom method: Derivation and application to impurities, surfaces, and other defects in metals. *Physical Review B*, 29(12):6443–6453.

Ding, J., Zheng, H.-r., Tian, Y., Huang, X., Song, K., Lu, S.-q., Zeng, X.-g., and Ma, W.-S. (2020). Multi-scale numerical simulation of fracture behavior of nickel-aluminum alloy by coupled molecular dynamics and cohesive finite element method (CFEM). *Theoretical and Applied Fracture Mechanics*, 109:102735.

Domínguez-Gutiérrez, F. and von Toussaint, U. (2020). On the detection and classification of material defects in crystalline solids after energetic particle impact simulations. *Journal of Nuclear Materials*, 528:151833.

Dominguez-Gutierrez, F. J., Ustrzycka, A., Xu, Q. Q., Alvarez-Donado, R., Papanikolaou, S., and Alava, M. J. (2022). Dislocation nucleation mechanisms during nanoindentation

of concentrated FeNiCr alloys: unveiling the effects of Cr through molecular simulations. *Modelling and Simulation in Materials Science and Engineering*, 30(8):085010.

Dugdale, D. (1960). Yielding of steel sheets containing slits. *Journal of the Mechanics and Physics of Solids*, 8(2):100–104.

EUROfusion (n.d.). DEMO Fusion Power Plant, https://www.euro-fusion.org/programme/demo/.

Foiles, S. M., Baskes, M. I., and Daw, M. S. (1986). Embedded-atom-method functions for the fcc metals Cu, Ag, Au, Ni, Pd, Pt, and their alloys. *Phys. Rev. B*, 33:7983–7991.

Frenkel, D. and Smit, B. (2023). *Understanding molecular simulation: from algorithms to applications*. Elsevier.

Frenkel, J. (1931). On the transformation of light into heat in solids. I. *Phys. Rev.*, 37:17–44.

Fu, R., Rui, Z., Du, J.-P., Zhang, S., Meng, F.-S., and Ogata, S. (2025). Temperature and loading-rate dependent critical stress intensity factor of dislocation nucleation from crack tip: Atomistic insights into cracking at slant twin boundaries in nano-twinned TiAl alloys. *Journal of Materials Science & Technology*, 222:290–303.

Fukumoto, K.-i., Umehara, K., and Yabuuchi, K. (2022). Dynamic interaction between dislocation and irradiation-induced defects in stainless steels during tensile deformation. *Metals*, 12(5):762.

Griffith, A. A. (1921). VI. The phenomena of rupture and flow in solids. *Philosophical transactions of the royal society of london. Series A, containing papers of a mathematical or physical character*, 221(582-593):163–198.

Griffiths, M., Xu, S., and Ramos Nervi, J. E. (2022). Swelling and He-embrittlement of austenitic stainless steels and Ni-alloys in nuclear reactors. *Metals*, 12(10):1692.

Guiqiu, X., Fang, W., Bo, S., Junliang, C., Jin, W., and Xiangguo, Z. (2021). Grain size dependence of cracking performance in polycrystalline NiTi alloys. *Journal of Alloys and Compounds*, 884:161132.

Gupta, P., Katakam, K. C., Katakareddi, G., and Yedla, N. (2020). Crack and its interaction with defects in Al coated with $Cu_{50}Zr_{50}$ metallic glass thin film: an MD simulation study. *Journal of Molecular Modeling*, 26(4):82.

Guénolé, J., Nöhring, W. G., Vaid, A., Houllé, F., Xie, Z., Prakash, A., and Bitzek, E. (2020). Assessment and optimization of the fast inertial relaxation engine (FIRE) for energy minimization in atomistic simulations and its implementation in LAMMPS. *Computational Materials Science*, 175:109584.

Haile, J. M. (1992). *Molecular dynamics simulation: elementary methods*. John Wiley & Sons, Inc.

Hasanzadeh, A., Hamedani, A., Alahyarizadeh, G., Minuchehr, A., and Aghaei, M. (2019). The role of chromium and nickel on the thermal and mechanical properties of FeNiCr austenitic

stainless steels under high pressure and temperature: a molecular dynamics study. *Molecular Simulation*, 45(8):672–684.

Hernández-Mayoral, M. and Caturla, M. (2010). 8 - Microstructure evolution of irradiated structural materials in nuclear power plants. In *Understanding and Mitigating Ageing in Nuclear Power Plants*, Woodhead Publishing Series in Energy, pages 189–235. Woodhead Publishing.

Hill, R. (1952). The elastic behaviour of a crystalline aggregate. *Proceedings of the Physical Society. Section A*, 65(5):349.

Hirel, P. (2015). Atomsk: A tool for manipulating and converting atomic data files. *Computer Physics Communications*, 197:212–219.

Hirth, J. and Lothe, J. (1992). *Theory of Dislocations*. Krieger Publishing Company.

Honeycutt, J. D. and Andersen, H. C. (1987). Molecular dynamics study of melting and freezing of small Lennard-Jones clusters. *The Journal of Physical Chemistry*, 91(19):4950–4963.

Hoover, W. G. (1985). Canonical dynamics: Equilibrium phase-space distributions. *Physical Review A*, 31(3):1695–1697.

Hosemann, P., Frazer, D., Fratoni, M., Bolind, A., and Ashby, M. (2018). Materials selection for nuclear applications: Challenges and opportunities. *Scripta Materialia*, 143:181–187.

Howard, C., Judge, C., Poff, D., Parker, S., Griffiths, M., and Hosemann, P. (2018). A novel in-situ, lift-out, three-point bend technique to quantify the mechanical properties of an ex-service neutron irradiated Inconel X-750 component. *Journal of Nuclear Materials*, 498:149–158.

Huang, X., Ding, J., Song, K., Lu, S., Zhang, Z., and Wang, L. (2023). Crystal orientation effect on the irradiation mechanical properties and deformation mechanism of α-Fe: molecular dynamic simulations. *Journal of Materials Engineering and Performance*, 32(18):8063–8074.

Huang, Y., Li, P., Yao, S., Wang, K., and Hu, W. (2024). Orientation-dependent deformation mechanisms of alpha-uranium single crystals under shock compression. *International Journal of Plasticity*, 177:103991.

Hull, D. and Bacon, D. J. (2011). *Introduction to dislocations*, volume 37. Elsevier.

Irving, J. H. and Kirkwood, J. G. (1950). The statistical mechanical theory of transport processes. *The Journal of Chemical Physics*, 18:817–829.

ITER Organization (n.d.). ITER – The Way to New Energy, https://www.iter.org.

Jia, P., Huang, K., Yu, H., Shimada, T., Guo, L., and Kitamura, T. (2022). A novel atomic J-integral concept beyond conventional fracture mechanics. *Theoretical and Applied Fracture Mechanics*, 121:103531.

Jokl, M., Vitek, V., and McMahon, C. (1980). A microscopic theory of brittle fracture in deformable solids: A relation between ideal work to fracture and plastic work. *Acta Metallurgica*, 28(11):1479–1488.

Jung, S.-P., Kwon, Y., Lee, C. S., and Lee, B.-J. (2018). Influence of hydrogen on the grain boundary crack propagation in bcc iron: A molecular dynamics simulation. *Computational Materials Science*, 149:424–434.

Kai Nordlund, F. G. (1999). Formation of stacking fault tetrahedra in collision cascades. *Applied Physics Letters*, 74(18):2720–2722.

KEK (n.d.). High Energy Accelerator Research Organization (KEK), https://www.kek.jp/en/.

Kim, H., Kim, S., and Kim, S. (2021). Lattice-based J-integral for a steadily moving dislocation. *International Journal of Plasticity*, 138:102949.

Kinchin, G. H. and Pease, R. S. (1955). The displacement of atoms in solids by radiation. *Reports on Progress in Physics*, 18(1):1.

Klimenkov, M., Möslang, A., Materna-Morris, E., and Schneider, H.-C. (2013). Helium bubble morphology of boron alloyed EUROFER97 after neutron irradiation. *Journal of Nuclear Materials*, 442:S52–S57.

Klueh, R. and Alexander, D. (1997). Neutron irradiation effects on the ductile-brittle transition of ferritic/martensitic steels. Technical report, Oak Ridge National Lab. (ORNL), Oak Ridge, TN (United States).

Kositski, R. and Mordehai, D. (2021). Employing molecular dynamics to shed light on the microstructural origins of the taylor-quinney coefficient. *Acta Materialia*, 205:116511.

Krull, H. and Yuan, H. (2011). Suggestions to the cohesive traction–separation law from atomistic simulations. *Engineering Fracture Mechanics*, 78(3):525–533. Meso-Mechanical Modelling of Fatigue and Fracture.

Kumar, G., Mishra, R. R., and Verma, A. (2022). *Introduction to Molecular Dynamics Simulations*, pages 1–19. Springer Nature Singapore, Singapore.

Le, H., Sutcliffe, M., Wang, P., and Burstein, G. (2004). Surface oxide fracture in cold aluminium rolling. *Acta Materialia*, 52(4):911–920.

Lennard-Jones, J. E. (1931). Cohesion. *Proceedings of the Physical Society*, 43(5):461.

Li, P., Huang, Y., Wang, K., Xiao, S., Wang, L., Yao, S., Zhu, W., and Hu, W. (2022). Crystallographic-orientation-dependence plasticity of niobium under shock compressions. *International Journal of Plasticity*, 150:103195.

Li, X., Li, W., Irving, D. L., Varga, L. K., Vitos, L., and Schönecker, S. (2020). Ductile and brittle crack-tip response in equimolar refractory high-entropy alloys. *Acta Materialia*, 189:174–187.

Li, X., Rincón Bonilla, M., Lu, M., and Huang, H. (2024). Atomistic understanding of ductile-to-brittle transition in single crystal Si and GaAs under nanoscratch. *International Journal of Mechanical Sciences*, 282:109689.

Li, Y., Qi, Z., Bhattacharya, A., and Zinkle, S. J. (2025). Temperature and dose effects on dislocation loops in self-ion irradiated high-purity iron. *Acta Materialia*, 296:121235.

Lin, P., feng Nie, J., dong Cui, W., He, L., gang Cui, S., and peng Lu, Y. (2024a). Comparative analysis of irradiation-stimulated hardening in the austenite and ferrite phases of F321 stainless steel. *Acta Materialia*, 281:120409.

Lin, P., Nie, J., Cui, S., and Lu, Y. (2025). Molecular dynamics study on the ductile-to-brittle transition in W-Re alloy systems. *Acta Materialia*, 285:120684.

Lin, P., Nie, J., Cui, W., He, L., Cui, S., Xiang, L., Lu, Y., and Xiao, G. (2024b). Experimental and modeling study on irradiation effect of A508-III steel. *International Journal of Mechanical Sciences*, 277:109371.

Lin, Y.-R., Chen, W.-Y., Tan, L., Hoelzer, D. T., Yan, Z., Hsieh, C.-Y., Huang, C.-W., and Zinkle, S. J. (2021). Bubble formation in helium-implanted nanostructured ferritic alloys at elevated temperatures. *Acta Materialia*, 217:117165.

Little, E. (1986). Fracture mechanics evaluations of neutron irradiated type 321 austenitic steel. *Journal of Nuclear Materials*, 139(3):261–276.

Liu, X., Chang, L., Ma, T., and Zhou, C. (2024). Molecular dynamics simulation of effects of loading parameters on fatigue crack growth behavior in titanium single crystal. *Fatigue and Fracture of Engineering Materials and Structures*, 47:1715–1730.

Lu, M., Wang, F., Zeng, X., Chen, W., and Zhang, J. (2020). Cohesive zone modeling for crack propagation in polycrystalline NiTi alloys using molecular dynamics. *Theoretical and Applied Fracture Mechanics*, 105:102402.

Lucon, E., Benoit, P., Jacquet, P., Diegele, E., Lässer, R., Alamo, A., Coppola, R., Gillemot, F., Jung, P., Lind, A., Messoloras, S., Novosad, P., Lindau, R., Preininger, D., Klimiankou, M., Petersen, C., Rieth, M., Materna-Morris, E., Schneider, H.-C., Rensman, J.-W., van der Schaaf, B., Singh, B., and Spaetig, P. (2006). The european effort towards the development of a demo structural material: Irradiation behaviour of the european reference rafm steel eurofer. *Fusion Engineering and Design*, 81(8):917–923. Proceedings of the Seventh International Symposium on Fusion Nuclear Technology.

Luo, J., Deng, B., Vargheese, K., Tandia, A., DeMartino, S., and Mauro, J. (2021). Atomic-scale modeling of crack branching in oxide glass. *Acta Materialia*, 216:117098.

Ma, L., Deng, Y., Ren, Y., and Hu, W. (2022). Influence of orientation on crack propagation of aluminum by molecular dynamics. *The European Physical Journal B*, 95:25.

Mahrous, M., Abdelghany, M., Farag, H., and Jasiuk, I. (2025). Irradiation effects on additively manufactured porous 316H stainless steel: A molecular dynamics study. *Computational Materials Science*, 258:113985.

Mansur, L. (1994). Theory and experimental background on dimensional changes in irradiated alloys. *Journal of Nuclear Materials*, 216:97–123.

Mattei, G. and Mazzone, A. (1996). Multiple cascades regime in fcc metals. molecular dynamics

simulations and calculated HREM imaging. *Nuclear Instruments and Methods in Physics Research Section B: Beam Interactions with Materials and Atoms*, 114(3):293–301.

Max Planck Institute for Plasma Physics (n.d.). Wendelstein 7-X Stellarator, https://www.ipp.mpg.de/wendelstein7x.

Mishin, Y. (2005). *Interatomic Potentials for Metals*, pages 459–478. Springer Netherlands, Dordrecht.

Monnet, G. and Mai, C. (2019). Prediction of irradiation hardening in austenitic stainless steels: Analytical and crystal plasticity studies. *Journal of Nuclear Materials*, 518:316–325.

Mousavi, H., Stupkiewicz, S., and Ustrzycka, A. (2026). Molecular dynamics study of the role of anisotropy in radiation-driven embrittlement. *International Journal of Plasticity*. Under review.

Musiał, S., Maj, M., Urbański, L., and Nowak, M. (2022). Field analysis of energy conversion during plastic deformation of 310S stainless steel. *International Journal of Solids and Structures*, 238:111411.

Nakano, A., Kalia, R., and Vashishta, P. (1995). Dynamics and morphology of brittle cracks: A molecular-dynamics study of silicon nitride. *Physical Review Letters*, 75:3138–3141.

Needleman, A. (1990). An analysis of decohesion along an imperfect interface. *International Journal of Fracture*, 42(1):21–40.

Nordlund, K. (2019). Historical review of computer simulation of radiation effects in materials. *Journal of Nuclear Materials*, 520:273–295.

Nordlund, K., Zinkle, S. J., Sand, A. E., Granberg, F., Averback, R. S., Stoller, R., Suzudo, T., Malerba, L., Banhart, F., Weber, W. J., et al. (2018a). Improving atomic displacement and replacement calculations with physically realistic damage models. *Nature communications*, 9(1):1084.

Nordlund, K., Zinkle, S. J., Sand, A. E., Granberg, F., Averback, R. S., Stoller, R., Suzudo, T., Malerba, L., Banhart, F., Weber, W. J., Willaime, F., Dudarev, S. L., and Simeone, D. (2018b). Primary radiation damage: A review of current understanding and models. *Journal of Nuclear Materials*, 512:450–479.

Norgett, M., Robinson, M., and Torrens, I. M. (1975). A proposed method of calculating displacement dose rates. *Nuclear engineering and design*, 33(1):50–54.

Nosé, S. (1984). A molecular dynamics method for simulations in the canonical ensemble. *Molecular Physics*, 52:255–268.

Nowak, M., Mulewska, K., Azarov, A., Kurpaska, L., and Ustrzycka, A. (2023). A peridynamic elasto-plastic damage model for ion-irradiated materials. *International Journal of Mechanical Sciences*, 237:107806.

Ohr, S. (1987). Dislocation-crack interaction. *Journal of Physics and Chemistry of Solids*,

48(11):1007–1014.

Orowan, E. (1945). *Notch Brittleness and the Strength of Metals*. Institution of Engineers and Shipbuilders in Scotland.

Orowan, E. (1949). Fracture and strength of solids. *Reports on progress in physics*, 12(1):185.

Ortner, S. (2023). A review of structural material requirements and choices for nuclear power-plant. *Frontiers in Nuclear Engineering*, 2.

Osetsky, Y., Stoller, R., and Matsukawa, Y. (2004). Dislocation–stacking fault tetrahedron interaction: what can we learn from atomic-scale modelling. *Journal of Nuclear Materials*, 329–333:1228–1232.

Pareige, C., Etienne, A., Gueye, P.-M., Medvedev, A., Kaden, C., Konstantinovic, M., and Malerba, L. (2022). Solute rich cluster formation and Cr precipitation in irradiated Fe-Cr-(Ni,Si,P) alloys: Ion and neutron irradiation. *Journal of Nuclear Materials*, 572:154060.

Park, N.-Y., Kim, Y.-C., Seok, H.-K., Han, S.-H., Cho, S., and Cha, P.-R. (2007). Molecular dynamics simulation of irradiation damage in tungsten. *Nuclear Instruments and Methods in Physics Research Section B: Beam Interactions with Materials and Atoms*, 265(2):547–552.

Parrinello, M. and Rahman, A. (1980). Crystal structure and pair potentials: A molecular-dynamics study. *Phys. Rev. Lett.*, 45:1196–1199.

Parrinello, M. and Rahman, A. (1981). Polymorphic transitions in single crystals: A new molecular dynamics method. *Journal of Applied Physics*, 52(12):7182–7190.

Plimpton, S. (1995). Fast parallel algorithms for short-range molecular dynamics. *Journal of computational physics*, 117(1):1–19.

Rapaport, D. C. (2004). *The art of molecular dynamics simulation*. Cambridge university press.

Renault-Laborne, A., Hure, J., Malaplate, J., Gavoille, P., Sefta, F., and Tanguy, B. (2018). Tensile properties and deformation microstructure of highly neutron-irradiated 316 stainless steels at low and fast strain rate. *Journal of Nuclear Materials*, 508:488–504.

Schmid, E. and Boas, W. (1968). *Plasticity of Crystals: With Special Reference to Metals*. Chapman & Hall.

Sellami, N., Debelle, A., Ullah, M. W., Christen, H. M., Keum, J. K., Bei, H., Xue, H., Weber, W. J., and Zhang, Y. (2019). Effect of electronic energy dissipation on strain relaxation in irradiated concentrated solid solution alloys. *Current Opinion in Solid State and Materials Science*, 23(2):107–115.

Sheng, Y., Yang, H., Ma, W., and Jiang, X. (2023a). Interaction between cracks and dislocations in body-centered cubic crystals under mixed loads. *Engineering Fracture Mechanics*, 292:109588.

Sheng, Y., Yang, H., Zhang, J., and Jiang, X. (2023b). The interaction of crack and dislocations in cyclic loading in the body-centered cubic (bcc) crystal. *Engineering Fracture Mechanics*,

292:109558.

Sheppard, D., Terrell, R., and Henkelman, G. (2008). Optimization methods for finding minimum energy paths. *The Journal of Chemical Physics*, 128(13):134106.

Shimokawa, T., Kinari, T., Shintaku, S., Nakatani, A., and Kitagawa, H. (2005). Defect-induced anisotropy in mechanical properties of nanocrystalline metals by molecular dynamics simulations. *Modelling and Simulation in Materials Science and Engineering*, 13(8):1217.

Singh, D., Sharma, P., Jindal, S., Kumar, P., Kumar, P., and Parashar, A. (2019). Atomistic simulations to study crack tip behaviour in single crystal of bcc niobium and hcp zirconium. *Current applied physics*, 19(1):37–43.

Song, H., Wang, Z.-j., He, X.-d., and Duan, J. (2017). Self-healing of damage inside metals triggered by electropulsing stimuli. *Scientific Reports*, 7(1):7097.

Stepanova, L. and Mushankova, K. (2024). Atomistic and continuum ascertainment of the crack tip stress fields in anisotropic elastic cubic media. *Theoretical and Applied Fracture Mechanics*, 133:104613.

Stephenson, K. J. and Was, G. S. (2015). Comparison of the microstructure, deformation and crack initiation behavior of austenitic stainless steel irradiated in-reactor or with protons. *Journal of Nuclear Materials*, 456:85–98.

Stimac, J., Bertin, N., Mason, J., and Bulatov, V. (2022). Energy storage under high-rate compression of single crystal tantalum. *Acta Materialia*, 239:118253.

Stoller, R. E. (2012). Primary radiation damage formation. *Comprehensive nuclear materials*, 1:293–332.

Stork, D., Agostini, P., Boutard, J.-L., Buckthorpe, D., Diegele, E., Dudarev, S. L., English, C., Federici, G., Gilbert, M. R., Gonzalez, S., Ibarra, A., Linsmeier, C., Puma, A. L., Marbach, G., Packer, L. W., Raj, B., Rieth, M., Tran, M. Q., Ward, D. J., and Zinkle, S. J. (2014). Materials R&D for a timely DEMO: Key findings and recommendations of the EU roadmap materials assessment group. *Fusion Engineering and Design*, 89(7):1586–1594. Proceedings of the 11th International Symposium on Fusion Nuclear Technology-11 (ISFNT-11) Barcelona, Spain, 15-20 September, 2013.

Stukowski, A. (2010). Visualization and analysis of atomistic simulation data with OVITO-the Open Visualization Tool. *Modelling and simulation in materials science and engineering*, 18(1).

Stukowski, A. and Albe, K. (2010). Extracting dislocations and non-dislocation crystal defects from atomistic simulation data. *Modelling and Simulation in Materials Science and Engineering*, 18(8):085001.

Stukowski, A., Bulatov, V. V., and Arsenlis, A. (2012). Automated identification and indexing of dislocations in crystal interfaces. *Modelling and Simulation in Materials Science and*

Engineering, 20(8):085007.

Subramaniyan, A. K. and Sun, C. (2008). Continuum interpretation of virial stress in molecular simulations. *International Journal of Solids and Structures*, 45(14):4340–4346.

Tadmor, E. B. and Miller, R. E. (2011). *Modeling materials: continuum, atomistic and multiscale techniques*. Cambridge university press.

Thompson, A., Aktulga, H. M., Berger, R., Bolintineanu, D. S., Brown, W. M., Crozier, P. S., in 't Veld, P. J., Kohlmeyer, A., Moore, S. G., Nguyen, T. D., Shan, R., Stevens, M. J., Tranchida, J., Trott, C., and Plimpton, S. J. (2022). LAMMPS - a flexible simulation tool for particle-based materials modeling at the atomic, meso, and continuum scales. *Comp. Phys. Comm.*, 271:108171.

Tsai, D. H. (1979). The virial theorem and stress calculation in molecular dynamics. *The Journal of Chemical Physics*, 70(3):1375–1382.

Tsugawa, T., Hayakawa, S., Iwase, Y., Okita, T., Suzuki, K., Itakura, M., and Aichi, M. (2022). Molecular dynamics simulations to quantify the interaction of a rigid and impenetrable precipitate with an edge dislocation in Cu. *Computational Materials Science*, 210:111450.

Tuckerman, M. E. (2023). *Statistical mechanics: theory and molecular simulation*. Oxford university press.

Tuckerman, M. E. and Martyna, G. J. (2000). Understanding modern molecular dynamics: Techniques and applications. *The Journal of Physical Chemistry B*, 104(2):159–178.

Tvergaard, V. (2011). Void shape effects and voids starting from cracked inclusion. *International Journal of Solids and Structures*, 48(7):1101–1108.

Tvergaard, V. and Hutchinson, J. W. (1992). The relation between crack growth resistance and fracture process parameters in elastic-plastic solids. *Journal of the Mechanics and Physics of Solids*, 40(6):1377–1397.

Ustrzycka, A. (2021). Physical mechanisms based constitutive model of creep in irradiated and unirradiated metals at cryogenic temperatures. *Journal of Nuclear Materials*, 548:152851.

Ustrzycka, A., Dominguez-Gutierrez, F., and Chromiński, W. (2024). Atomistic analysis of the mechanisms underlying irradiation-hardening in Fe–Ni–Cr alloys. *International Journal of Plasticity*, 182:104118.

Ustrzycka, A., Mousavi, H., Dominguez-Gutierrez, F., and Stupkiewicz, S. (2025). Atomistic study of radiation-induced ductile-to-brittle transition in austenitic steel. *International Journal of Mechanical Sciences*, 303:110567.

Van Rossum, G. and Drake Jr, F. L. (1995). *Python reference manual*. Centrum voor Wiskunde en Informatica Amsterdam.

Vázquez, H., Kononov, A., Kyritsakis, A., Medvedev, N., Schleife, A., and Djurabekova, F. (2021). Electron cascades and secondary electron emission in graphene under energetic ion

irradiation. *Phys. Rev. B*, 103:224306.

Velilla-Díaz, W. and Zambrano, H. R. (2021). Crack length effect on the fracture behavior of single-crystals and Bi-Crystals of aluminum. *Nanomaterials*, 11(11).

Vo, H., Reichardt, A., Frazer, D., Bailey, N., Chou, P., and Hosemann, P. (2017). In situ micro-tensile testing on proton beam-irradiated stainless steel. *Journal of Nuclear Materials*, 493:336–342.

von Toussaint, U., Domínguez-Gutiérrez, F., Compostella, M., and Rampp, M. (2021). FaVAD: A software workflow for characterization and visualizing of defects in crystalline structures. *Computer Physics Communications*, 262:107816.

Wang, L., Liu, Q., and Shen, S. (2015). Effects of void–crack interaction and void distribution on crack propagation in single crystal silicon. *Engineering Fracture Mechanics*, 146:56–66.

Wang, Q., Cochrane, C., Skippon, T., Wang, Z., Abdolvand, H., and Daymond, M. R. (2020). Orientation-dependent irradiation hardening in pure Zr studied by nanoindentation, electron microscopies, and crystal plasticity finite element modeling. *International Journal of Plasticity*, 124:133–154.

Wang, R., Han, J., Mao, J., Hu, D., Liu, X., and Guo, X. (2021). A molecular dynamics based cohesive zone model for interface failure under monotonic tension of 3D four direction SiCf/SiC composites. *Composite Structures*, 274:114397.

Warner, D. H., Curtin, W. A., and Qu, S. (2007). Rate dependence of crack-tip processes predicts twinning trends in f.c.c. metals. *Nature Materials*, 6(11):876–881.

Was, G. S. (2007). *Fundamentals of radiation materials science: metals and alloys*. Springer.

Will, A. (2021). *Damage mechanisms in superconductors due to the impact of high energy proton beams and radiation tolerance of cryogenic diodes used in particle accelerator magnet systems*. PhD thesis, Karlsruhe Institute of Technology (KIT). CERN-THESIS-2021-187.

Wilson, M. A., Grutzik, S. J., and Chandross, M. (2019). Continuum stress intensity factors from atomistic fracture simulations. *Computer Methods in Applied Mechanics and Engineering*, 354:732–749.

Workum, K. V., Gao, G., Schall, J. D., and Harrison, J. A. (2006). Expressions for the stress and elasticity tensors for angle-dependent potentials. *The Journal of Chemical Physics*, 125(14):144506.

Xiao, X. (2019). Fundamental mechanisms for irradiation-hardening and embrittlement: a review. *Metals*, 9(10):1132.

Xie, G., Wang, F., Lai, X., Xu, Z., and Zeng, X. (2023). Atomistic study on crystal orientation-dependent crack propagation and resultant microstructure anisotropy in NiTi alloys. *International Journal of Mechanical Sciences*, 250:108320.

Xu, C., Zhang, X., Chen, Y., Li, M., Park, J.-S., Kenesei, P., Almer, J., and Yang, Y. (2018).

In-situ high-energy X-ray characterization of neutron irradiated HT-UPS stainless steel under tensile deformation. *Acta Materialia*, 156:330–341.

Xu, D., Wang, H., Yang, R., and Sachdev, A. K. (2014). Molecular dynamics simulation of asymmetric nucleation and motion of $\langle 011 \rangle$ superdislocations in TiAl. *Chinese Science Bulletin*, 59(15):1725–1737.

Xu, G. and Demkowicz, M. (2020). Computing critical energy release rates for fracture in atomistic simulations. *Computational Materials Science*, 181:109738.

Yamakov, V., Saether, E., Phillips, D., and Glaessgen, E. (2006). Molecular-dynamics simulation-based cohesive zone representation of intergranular fracture processes in aluminum. *Journal of the Mechanics and Physics of Solids*, 54(9):1899–1928.

Yang, H. (2022). Anisotropic effects of radiation-induced hardening in nuclear structural materials: A review. *Journal of Nuclear Materials*, 561:153571.

Zener, C. and Sidney, S. (1949). Elasticity and anelasticity of metals. *The Journal of Physical Chemistry*, 53(9):1468–1468.

Zeng, X., Han, T., Guo, Y., and Wang, F. (2018). Molecular dynamics modeling of crack propagation in titanium alloys by using an experiment-based Monte Carlo model. *Engineering Fracture Mechanics*, 190:120–133.

Zhang, J. and Ghosh, S. (2013). Molecular dynamics based study and characterization of deformation mechanisms near a crack in a crystalline material. *Journal of the Mechanics and Physics of Solids*, 61(8):1670–1690.

Zhang, Y. and Jiang, S. (2017). Molecular dynamics simulation of crack propagation in nanoscale polycrystal nickel based on different strain rates. *Metals*, 7(10):432.

Zhao, S., Osetsky, Y., Stocks, G. M., and Zhang, Y. (2019). Local-environment dependence of stacking fault energies in concentrated solid-solution alloys. *npj Computational Materials*, 5(1):13.

Zhao, X., Liu, S., Xie, Z., Liu, Z., Wang, D., and Luo, L. (2025). Effects of temperature and strain rate on crack propagation in NiCoCr multi-principal element alloys: A molecular dynamics simulation. *Materials Today Communications*, 43:111667.

Zhou, M. (2003). A new look at the atomic level virial stress: on continuum-molecular system equivalence. *Proceedings of the Royal Society of London. Series A: Mathematical, Physical and Engineering Sciences*, 459:2347–2392.

Zhou, X., Foster, M., and Sills, R. (2023). Enabling molecular dynamics simulations of helium bubble formation in tritium-containing austenitic stainless steels: An Fe-Ni-Cr-H-He potential. *Journal of Nuclear Materials*, 575:154232.

Zhu, J., He, X., Yang, D., Bie, Z., Mei, H., and Tian, X. (2021). A peridynamic model for fracture analysis of polycrystalline bcc-fe associated with molecular dynamics simulation.

Theoretical and Applied Fracture Mechanics, 114:102999.

Zinkle, S. (2012). 1.03-radiation-induced effects on microstructure. *Comprehensive nuclear materials*, 1:65–98.

Zinkle, S. and Singh, B. (2006). Microstructure of neutron-irradiated iron before and after tensile deformation. *Journal of Nuclear Materials*, 351(1):269–284. Proceedings of the Symposium on Microstructural Processes in Irradiated Materials.

Zinkle, S., Terrani, K., and Snead, L. (2016). Motivation for utilizing new high-performance advanced materials in nuclear energy systems. *Current Opinion in Solid State and Materials Science*, 20(6):401–410. the COSSMS Twentieth Anniversary Issue.

Zinkle, S. and Was, G. (2013). Materials challenges in nuclear energy. *Acta Materialia*, 61(3):735–758. The Diamond Jubilee Issue.

Zinkle, S. J. and Busby, J. T. (2009). Structural materials for fission & fusion energy. *Materials Today*, 12(11):12–19.

Zinkle, S. J. and Ghoniem, N. M. (2011). Prospects for accelerated development of high performance structural materials. *Journal of Nuclear Materials*, 417(1):2–8. Proceedings of ICFRM-14.